Fluorescent nanodiamonds as siRNA vectors : in vitro efficacy evaluation and high-content/high-resolution quantifications of their distribution in vivo

Sandra Claveau

NNT : 2018SACLS119

Thèse de doctorat

Fluorescent nanodiamonds as siRNA vectors: *in vitro* efficacy evaluation and high-content/high-resolution quantifications of their distribution *in vivo*

Thèse de doctorat de l'Université Paris-Saclay
préparée à l'Université Paris-Sud

École doctorale n°569 **Innovation thérapeutique du fondamental à l'appliqué**

Spécialité de doctorat: Pharmacotechnie et Physico-chimie Pharmaceutique

Thèse présentée et soutenue à Villejuif, le 25 mai 2018, par

Sandra Claveau

Composition du Jury :

Sylvie Chevillard Directrice de Recherche, CEA Paris-Saclay (Institut de Radiobiologie Cellulaire et Moléculaire, Fontenay-aux-Roses)	Présidente
Nathalie Mignet Directrice de Recherche, CNRS (UMR8258, Paris)	Rapportrice
Cécilia Ménard-Moyon Chargée de Recherche, CNRS (UPR3572, Strasbourg)	Rapportrice
Roser Lòpez Alemany Chargée de Recherche, IDIBELL (Bellvitge Biomedical Research Institute, Barcelone)	Examinatrice
Didier Bazile Chercheur, Sanofi, Gentilly	Examinateur
Jean-Rémi Bertrand Ingénieur de Recherche, INSERM (UMR8203, Villejuif)	Examinateur
Lluis M Mir Directeur de Recherche, CNRS (UMR8203, Villejuif)	Directeur de thèse
François Treussart Professeur, ENS Paris-Saclay (UMR9188, Orsay)	Co-Directeur de thèse
Claude P Malvy Professeur émérite, Univ. Paris-Sud (UMR8203, Villejuif)	Invité

« Le rôle de l'infiniment petit est infiniment grand. »

Louis Pasteur

Acknowledgment

Ce manuscrit vient conclure trois années de thèse effectuées entre le Laboratoire de Vectorologie et thérapeutique anticancéreuses sous la direction du Pr. Claude Malvy puis du Dr. Lluis M Mir, et le Laboratoire Aimé Cotton sous la direction du Pr. François Treussart. Je commencerai donc par remercier mes différents directeurs de thèse, Claude puis Lluis et François pour m'avoir offert l'opportunité de réaliser ma thèse sur un sujet alliant nanoparticules et cancer, deux thèmes qui m'étaient chers, à l'interface entre la biologie et la physique. Claude, merci d'avoir eu assez confiance en moi pour mener à bien notre partie du projet européen. Vous m'avez distillé de précieux conseils tout au long du projet. Lluis, je vous suis très reconnaissante d'avoir pris la suite de Claude au milieu de la thèse. C'était un plaisir de travailler à vos côtés, grâce à votre éternelle bonne humeur. Malgré votre distance par rapport au projet, vous avez toujours été présent et bienveillant, notamment sur les derniers mois de travail, malgré vos nombreux projets. Pour finir, je remercie François. J'ai passé les derniers mois de ma thèse à tes côtés, au LAC, ils ont été particulièrement intenses et riches en résultats. J'ai énormément appris grâce à ta rigueur et ton dynamisme à toute épreuve. Ce manuscrit ne serait pas aussi bon sans tes remarques et tes suggestions. Un grand merci donc !

Enfin, je n'aurais pas pu effectuer cette thèse sans la présence quotidienne du Dr. Jean-Rémi Bertrand. C'est d'abord toi Jean-Rémi qui me l'a proposé, merci donc d'avoir cru en mes capacités pour mener à bien ce projet. Tout au long de ces trois années tu as été de bon conseil et tu as été essentiel pour balancer ma vision négative des résultats ! Mais au-delà de nos discussions scientifiques durant lesquelles tes connaissances très diverses, mais toujours très pointues, m'ont toujours impressionnées, je retiens également nos conversations photo et balades, parmi tant d'autres choses.

Je tiens ensuite à remercier les membres du jury : Nathalie Mignet, Cécilia Ménard-Moyon, Sylvie Chevillard, Roser Lopez Alemany et Didier Bazile du temps qu'ils ont consacré à la lecture de mon manuscrit et des remarques constructives qu'ils ont pu émettre lors de ma soutenance.

Ce projet s'est inscrit dans le cadre du projet européen DiamEstar. Je remercie donc l'ANR et le programme EuroNanoMed 2 pour avoir financé l'intégralité de ce projet de thèse. This PhD thesis would never have been possible without the contribution of our partner and

provider of nanodiamonds: the teams of Dr. Jean-Charles Arnault at CEA-List, of Dr. Gregory Pieters at CEA-Saclay and of Dr. Petr Cigler at IOCB, Prague. We had to face many hurdles but we finally made something out all of this! During my PhD, I had the chance to spend two weeks to perform our first in vivo experiments in the team of Dr. Ibane Abasolo, thank you for your warm welcome in Barcelona and for the attempts to teach me Spanish and Catalan, I am sorry I was such a bad learner! Finally, I want to thank the team of Dr. Oscar Tirado, which was always invested in the project and gave smart ideas to move on the in vivo application.

Back to french ! J'ai eu la chance de trouver au sein de l'UMR 8203 de vrais amis, avec qui j'ai pu partager joies et peines mais surtout beaucoup de fous rires, essentiels pour survivre à une thèse, durant la pause-café ou nos soirées mojitos ! Je pense tout particulièrement à Adeline, Florian, Célia, Linda, Marie (la jeune) et Marie (la brune), Céline, Tòmas, Giorgia, Isabelle L., Julia, Charles, Antoine. Merci pour tous les bons moments passés ensemble ! J'ai dû m'isoler quelques temps à Orsay pour obtenir mes derniers résultats, où les membres du LAC m'ont réservé un accueil merveilleux. Merci à Fériel, François, Lucile, Baptise, Timothée, Ferdinand, Margarita et les deux Loïc. Je pense que vous m'avez vu dans une période assez difficile et vous m'avez permis de la passer sans y laisser mon moral.

Une autre équipe dans laquelle j'ai également passé du temps est celle de la Cité des Sciences et de l'Industrie. Sachez que mes journées à la Cité à présenter le microbiote intestinal, la montée des eaux et la théorie de l'évolution de Darwin étaient une expérience incroyable qui m'aura beaucoup apportée. Si vous avez besoin d'un titre d'anim, pas de soucis pour faire ça le vendredi soir, ce sont nos plus gros fous rires je pense !!

Enfin, je dédie ces dernières lignes à tous mes proches. Toute mon équipe de water-polo avec qui j'ai vécu des moments inoubliables. Nos entrainements et tournois étaient de véritables parenthèses essentielles à ma santé mentale !! Maman, Papa, vous m'avez toujours soutenue, aidée et poussée à aller plus loin. Je crois que là je ne peux pas faire mieux ! Je pense bien sûr également à mes sœurs et mes grands-parents. Et enfin, last but not least, merci à toi Mon Chéri pour ton soutien continu. Je pense que tu as fait cette thèse par procuration tant tu étais investi et curieux de mes travaux. Malgré les épreuves, tu as toujours été là pour moi, tu as toujours trouvé les mots justes pour me réconforter et me faire rebondir. Merci !!

TABLE of CONTENT

General introduction

Cancer is a wide-spread disease, considered as the disease of the 21st century. The treatment of the different types of cancer is more and more well managed, but some of rare occurrences are still in the need of more efficient treatments. New therapies are currently developed and tested, such as immunotherapy, combined with the classical approaches (*e.g.* surgery, chemotherapy, radiotherapy, among others).

Among all new technologies and new drugs, nanomedicines represent good alternatives or enhancement of the efficacy of current therapies, potentially enabling the improvement of the drugs' bioavailability and efficiency, and/or to reduce their toxicity.

Ewing Sarcoma is one of the cancer that suffers from a lack of therapeutical progress. This rare pediatric cancer is caused in the majority of cases by a chromosomic translocation: the fusion oncogene *EWS-Fli1*. This chromosomic aberration confers all the hallmarks of cancerous cells, in particular the aberrant cell proliferation and the loss of the apoptotic function. This specificity of the disease has been explored for years as a specific target to help beating this cancer, and we exploit this solution in this work. Furthermore, the high specificity of the junction oncogene to Ewing cells allows to only target the cancerous cells, thus displaying an opportunity to reduce the adverse effects of the current treatments, by a reduction of the prescribed doses.

In order to fulfil the objective of only targeting *EWS-Fli1*, the strategy started in my team at the *Laboratoire de Vectorologie et Thérapeutiques Anticancéreuses* (LVTA) several years ago, consisted in using the siRNA therapy. siRNA is a genetic tool, enabling the inhibition of the expression of a specific gene, presenting great promises for the treatment of several genetic disorder-caused diseases. Unfortunately, this double-stranded oligonucleotide is poorly stable in the circulation, as it is rapidly degraded by the nucleases of the organism. There is thus a need for a vehicle, protecting the siRNA from the circulation and allowing it to reach the cytoplasm of the cell, where it can have its effect.

Several technologies have been tested in LVTA team, under the supervision of Dr Jean-Rémi BERTRAND and Prof. Claude MALVY, by using either organic or inorganic nanovectors. In the latter category, the team used nanodiamonds (NDs) rendered cationic by hydrogenation and coated with different polymers (*e.g.* PEI and PAH) and showed an *in vitro* inhibition efficacy between 60% and 70%. For this project, I have extended this work to a larger variety

of nanodiamonds and to *in vivo* study. I used several nanodiamonds, originating from two different synthesis processes: detonation (DND) or High Pressure High Temperature (ND_{HPHT}). I also used several functionalizations methods: hydrogenation (i) by a plasma-assisted method or (ii) by an annealing method, (iii) cationization by chemical treatments, or (iv) cationisation by a copolymer coating (Cop-ND).

This PhD project took place at the interface of the different work-packages of the European project DiamESTar (ERA-Net EuroNanomed 2). It involved several French teams: the LVTA team (UMR8203) located at Gustave Roussy, Villejuif, the 'Biophotonics" team at *Laboratoire Aimé Cotton* (UMR9188), Orsay and two teams from CEA-Saclay (Dr. Jean-Charles ARNAULT's team at the Diamond Sensors Laboratory, CEA-LIST, and Dr. Gregory PIETER's team at the *Laboratoire de Marquage par le Tritium of the Institut des sciences du vivant Frédéric Joliot*/CEA-Saclay); but also involved two teams in Spain: Dr.Ibane ABASOLO-OLAORTUA's team at the Nanomedicine and Advanced Therapies Research Center (CIBBIM-Nanomedicine) - Vall d'Hebron Institut of Recerca (VHIR), Barcelona and Dr. Oscar TIRADO-MARTINEZ's team at the *Institut d'Investigaciò Biomèdica de Bellvitge* (IDIBELL), Barcelona; and a team in Czech Republic: Petr CIGLER's team at the Institute of Organic Chemistry and Biochemistry (IOCB), Prague.

Most of my PhD work was carried out in LVTA team at Gustave Roussy, Villejuif, where I have realized the *in vitro* characterization of the various nanodiamonds suspensions and treated the mice for the biodistribution assay using fluorescent nanodiamonds as siRNA vectors. The entire analysis of the organ mice sections was carried out at the *Laboratoire Aimé Cotton* using a home-made time-gated microscopy setup developed by Prof. François TREUSSART. I also had the chance to perform some experiments in Dr. Ibane ABASOLO-OLAORTUA's team in Barcelona.

This manuscript contains the work carried out during the three years of my PhD work (April 2015-May 2018), under the supervision, first of Prof. Claude MALVY, then of Dr. Lluis M. MIR and Prof. François TREUSSART. Dr. Jean-Rémi BERTRAND closely supervised my daily work.

This manuscript contains five chapters.

The **first chapter** presents the nanomedicine landscape, by presenting the main advantages and drawbacks of this new technology when applied to the medical field. It also proposes a non-exhaustive analysis of the trends in the pre-clinical publications, clinical trials and

commercialization of nanomedicines products, showing the growing interest for them but also the bottlenecks preventing a wider commercialization.

The **second chapter** introduces the nanodiamond, which is at the heart of this PhD work, presenting the main characteristics of this nanomaterial, the main methods of synthesis, the optical properties that have been exploited during this PhD project and its current biomedical applications. This chapter aims at showing the potential that represents nanodiamonds for a use in medicine.

The **third chapter** presents the targeted disease, Ewing Sarcoma, after a general introduction on cancer. The epidemiology, the causes and the current treatments of Ewing Sarcoma is developed. Then, the target point of our strategy, the oncogene *EWS-Fli1*, is introduced. Finally, I demonstrate how an antisense therapy, by using a siRNA sequence directed towards *EWS-Fli1*, is well adapted to inhibit this oncogene expression, and why it needs a vehicle, such as nanodiamond.

The **fourth chapter** presents the *in vitro* characterization of the different nanodiamond suspensions, synthetized from different methods, detonation (DND) or High Pressure High Temperature (HPHT), and rendered cationic by different functionalizations. This chapter presents these different functionalization methods and their physico-chemical behavior alone or when bound with siRNA. It also shows the variation of the oncogene expression inhibition efficacy, depending on the suspension used. The aim of this chapter is to highlight the optimal synthesis and functionalization methods to obtain a proper inhibition of the *EWS-Fli1* gene *in vitro*.

The **fifth and last chapter** is devoted to the *in vivo* distribution studies conducted with the tritiated DND (^{3}H-DND) and the Cop-ND, made fluorescent by the creation of Nitrogen-Vacancy (NV) color centers (Cop-FND). This chapter first presents the distribution and elimination results obtained by the measurement of the radioactivity in the different organs, urine and feces of mice. Then is displayed the results of the quantitative assessment of the Cop-FND accumulation in the different organs of mice. This work was carried out thanks to a home-build time-gated microscopy imaging setup, based on an amplified picosecond diode laser (built by Xavier DÉLEN, Institut d'Optique Graduate School, Palaiseau), and an automated slide scanner and acquisition setup developed by Imstar S.A. (Paris). This system enabled us to obtain high-content images of whole organ sections, in fluorescence as well as in bright-field (white light illumination), composed of up to 15,000 fields of view recorded at

a 60x magnification. This approach has the sensitivity of the single FND, which has allowed us to precisely detect and quantify the Cop-FND in tissues with a subcellular resolution.

The aim of my PhD project, reported in this manuscript, is to demonstrate (i) the positive value of nanomedicines for rare diseases like Ewing Sarcoma; (ii) the importance of the synthesis and functionalization methods applied to diamond nanocrystals, in order to bind siRNA to obtain a satisfying inhibition of the fusion oncogene *EWS-Fli1 in vitro*; and (iii) the biodistribution trend of the ND:siRNA complexes in the organisms of mice. In addition to the biological results, this manuscript presents an innovative setup for high-content screening of fluorescent nano-complexes distribution in the organism with subcellular localization.

INTRODUCTION

CHAPTER 1

Is nanomedicine the future of medicine?

1.1. Why using nanotechnology in medicine?

Nanotechnologies have been used for centuries, most of the time without even knowing it. The oldest example of the use of nanotechnology has been reported with the famous Lycurgus cup. As pictured in Figure 1.1-1, this cup dating from A.D. 4, was made of dichroic glass, conferring a color change when held up to the light. This effect was achieved by including in the glass meticulously grinded gold and silver dusts, with sizes going down to the nanoscale. This very ancient cup inspired an entire generation in nanoplasmonics research [1].

Figure 1.1-1: Lycurgus cup. Left: no light; Right: exposed to light. Credit: British Museum (London, UK)

Gold and silver dusts were later used during the Middle Ages to obtain the various colors in cathedral's stained-glass windows. It has been characterized and demonstrated in the 1990's that this was the result of the emission from nanoparticle plasmon resonance [2]. The different colors have been associated to the nanoparticles size and shape: Red: Silver (~100 nm, Triangle); Yellow: Gold (~100 nm, Spheres); Green: Gold (~50 nm, Spheres); Light blue: Silver (~90 nm, Spheres); Blue: Silver (~40 nm, Spheres) [3].

It is only in 1959 that Richard FEYNMAN (CalTech Institute, USA) introduces the idea to work at the nanoscale in his famous talk "There's plenty of room at the bottom" [4]. He was the first to raise the idea that nanoscale objects could bring important progresses to all fields. He suggested to improve the resolution of electron microscopes to enable the observation of atom-sized objects, for biology and material science purposes and researches. He was also one the first to think about computer miniaturization. At that time, computers filled entire rooms, so the idea to produce actual portable computers was visionary. He encouraged the young generation to develop new production methods to get down at the nanoscale and produce new machineries.

The term "nanotechnology" was introduced by Professor Norio TANIGUCHI from Tokyo University of Science (Japan) in 1974[a]. He described ultra-high precision manufacturing of semiconductors and more specifically thin film deposition and ion beam milling, that allowed to work on materials at the scale of one atom or one molecule. In the frame of computer miniaturization, the ability to produce smaller semiconductors leads to a faster computing processing and a decreased energy consumption.

Nanotechnology was then very popular in science-fiction series or books, thanks to Eric DREXLER or Star Trek. It was imagined that nano-robots could be introduced in the body to treat diseases or to regenerate organs. Then began a growing interest in this area and massive investment were made by governments, the United States being first in this race, with over 15 billion dollars invested during the last decade. It is forecast that by 2020, this industry would represent $ 75.8 billion[b] and is seen as the next industrial revolution.

Working at the nanoscale is about exploiting characteristics specific to this range. Indeed, when materials are brought down to this size, new phenomena and different physicochemical

[a] N. Taniguchi, "On the Basic Concept of 'Nano-Technology'," Proc. Intl. Conf. Prod. Eng. Tokyo, Part II, Japan Society of Precision Engineering, 1974.

[b] "Global Nanotechnology Market Outlook 2015-2020", http://www.prnewswire.com

properties appear. For instance, gold quantum dots (QD) present different emission spectra depending on their size, due to quantum confinement [5].

Nanomedicine commonly designates the use of nanotechnology or nano-sized objects in health and medicine [6]. The first nanoparticles used for medical applications were magnetic nanoparticles in 1974-77 [7], used as contrast agent in Magnetic Resonance Imaging (MRI). Later in the 1990's, organic nanoparticles were developed, for drug delivery and imaging purposes [8,9]. Nanoparticles' functionalization became more and more controlled over time, allowing a better proficiency. Some of them are currently in clinical trial or even commercialized [10], as it will be presented in Section 1.3. A timeline of the history of nanotechnology in medicine is presented in Figure 1.1-2.

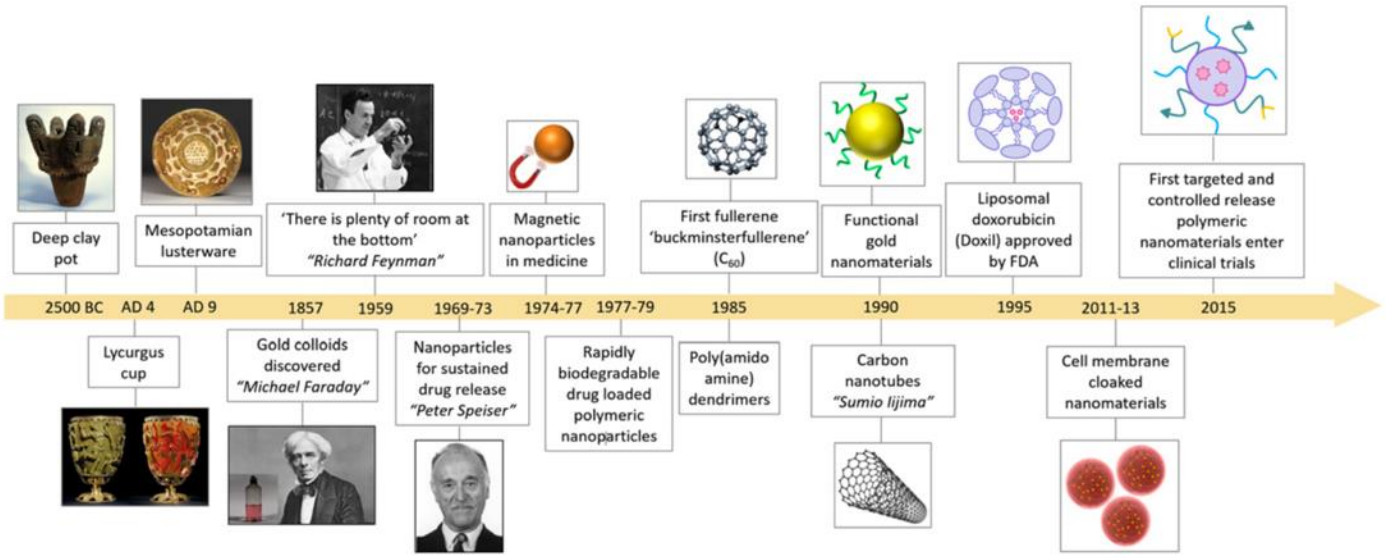

Figure 1.1-2: Evolution of nanomaterials with emphasis on drug delivery. From Ref. [7]

Nanomedicine refers to various fields such as diagnosis [11], treatment [12], a combination of both in theranostic applications [13], nanobiosensing (*e.g.* for temperature fluctuation measurements at subcellular resolution [14] or as immuno sensor [15]), tissue engineering [16] or in miniaturized medical devices [17]. It is forecast that it will revolutionize the healthcare system and the way to practice medicine. Point-of-care sensors are being developed thanks to on-chips molecularly imprinted polymers (MIP) [18], which would enable practitioners to test patients' blood for an immediate and early diagnosis. Nanoparticles (NP) are also being developed to act as contrast agents and tracers, bringing more accuracy and more specificity to medical imaging, in MRI [19], Positron Emission

Tomography (PET) [20] or Computed Tomography (CT) [21]. They also are studied as treatment particles, for magnetic field induced thermotherapy combined with radiotherapy [22] or Near-Infrared light or UV-triggered phototherapy [22,23]. The main advantage of miniaturization is the tremendous increase of surface to volume ratio, as presented in Figure 1.1-3, allowing to load a higher quantity of molecules [24]. This nanometric size also allows a better accessibility to the target in the organism, and potentially an easier excretion from the body [25,26] compared to microparticles.

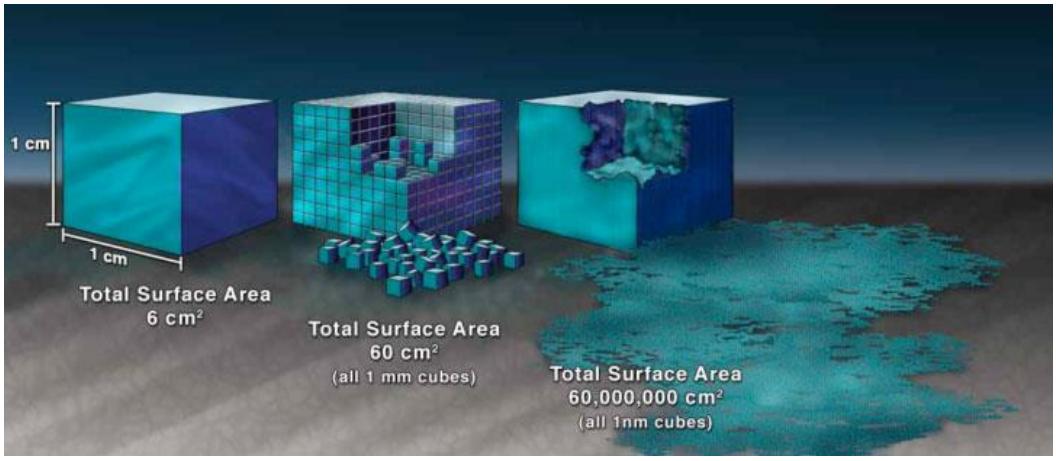

Figure 1.1-3: Effect of the miniaturization on the surface area. From https://www.nano.gov/nanotech-101/special

Besides these promises, nanomedicine is still a young technology and there are still fears related to their potential toxicity, the nanoparticle fate in the organism being not well known yet and varying from one type of particle to another. The increasing use of nanomaterials in cosmetics [27] and medical products raises concerns about their safety, and with very few data regarding their impact on the environment [28]. What makes their major advantage also makes their major drawback: nanoparticle size corresponds to the macromolecular level where biological reactions occur. Thus, they could interfere with these reactions and induce deleterious effects. This matter is still under discussion in the scientific community and new regulations established specific requirements to fulfil for nanomedicines before being commercialized (see EMA and FDA guidelines[c]). Regulations have been put in place for the biomedical field but is still far from being adequate to the massive increase of the use of nanomaterials in all kinds of industries, such as food and cosmetics [29]. Therefore, any

[c]EMA:http://www.ema.europa.eu/ema/index.jsp?curl=pages/regulation/general/general_content_000564.jsp&mid=WC0b01ac05806403e0

FDA: https://www.fda.gov/ScienceResearch/SpecialTopics/Nanotechnology/ucm301114.htm

clinical study involving nanomaterials ought to investigate and monitor their pathways, once introduced in the organism, their biodistribution and their potential effects at the molecular level and at macro-scale by monitoring the inflammation reaction, but also their elimination.

Despite all those concerns, the advent of nanotechnology and associated nanomedicine, allowed medicine to make great advances [6]. This technology has already helped in a better understanding of diseases with the identification of new mechanisms and then the enhancement of some therapies.

Nanomedicine is not utopia anymore, as some nanoparticles are already commercialized, and others are proceeding through clinical trials. The two following sections will give a trend analysis of the various nanoparticles and nano-platforms currently under investigation in pre-clinical studies, under clinical trials and commercialized.

1.2. Trends in pre-clinical studies on nanomedicines

As presented in the previous sub-section, nanomedicine attracts more and more interest from fundamental research and clinical point of views. This trend is highlighted by the number of publications indexed on PubMed (with keyword “nanomedicine”, excluding clinical trials studies and reviews) presented in Figure 1.2-1. This study encompasses a large spectrum of research fields and applications. We can see that the growing interest in this field started in 2005 and steadily developed, which can be related to the increasing number of publications on pre-clinical studies publications.

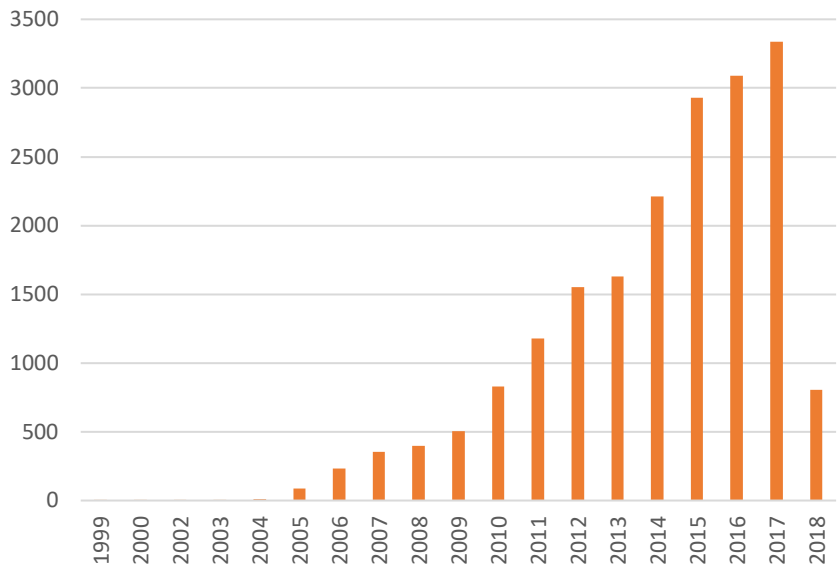

Figure 1.2-1: Number of publications indexed in PubMed on "Nanomedicines"

The advantages of nanoparticles applied to medicine [30] are numerous:

- Improvement of the drug therapeutic index by increasing efficacy and/or decreasing toxicity;
- Targeted delivery of drugs in a tissue or a cell;
- Enhancement of the pharmaceutical properties of therapeutic molecules, *e.g.* stability, solubility, circulating half-life;
- Enabling the sustained or stimulus-triggered drug release;
- Enabling the delivery of biomolecules, such as DNA or siRNA, to intracellular sites of action;
- Co-delivery of several drugs or biomolecules to improve the therapeutic efficacy;
- More sensitive diagnosis and imaging, as contrast agents;
- Miniaturized medical devices for diagnosis, drug screening and delivery;
- Inherent therapeutic properties of some nanoparticles upon stimulation (*e.g.* magnetic NP, gold NP, for imaging or for thermotherapy purposes, respectively);
- Ability to combine optical features and drug delivery or therapy enhancer (hyperthermia) capacity, enabling both the diagnosis or localization of the action site and the direct treatment of the target. The nanoparticle then acts as a theranostic agent.

All the nanomaterial candidates for biomedical applications have to be first tested *in vitro*, on cultured cells or through digital modeling. For nanomedicines, the requirements from authorities are becoming more and more demanding concerning the physico-chemical

parameters and behavior of the material [7]. After having identified a drug or a molecule candidate from convincing results of *in vitro* assays, a pre-clinical testing phase has to be conducted on animals to demonstrate the *in vivo* efficacy and safety, as well as to determine the toxicity profile, first pharmacokinetics and pharmacodynamics assessment, and to identify the appropriate dose ranges [31]. There is a large range of nanomaterials available for biomedical applications, the first hallmarks of these being their biocompatibility and not inducing cytotoxicity. Table 1 summarizes the main nanoplatforms that are used in medical applications, describing the main features, properties and specific applications for each. One can see that both organic (*e.g.* polymer, dendrimer, lipid) and inorganic (*e.g.* QD, gold NP, silica NP, magnetic NP, carbon-based NP) nanoparticles are used.

Table 1: Summary of the different nanoparticle vehicles used in nanomedicine. With a differentiation between organic nanoparticles (top of the table) and inorganic nanoparticles (bottom of the table). From ref. [32]

	Particle type	Composition/structure	Properties	Applications
	Polymer	*e.g.* PLGA, glycerol, chitosan, DNA; monomers, copolymers, hydrogels	Some biodegradability	Drug delivery, passive release (diffusion), controlled release (triggered)
	Dendrimer	PAMAM, etc.	Low polydispersity, biocompatibility	Drug delivery
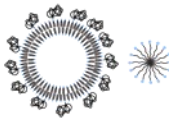	Lipid	Liposomes, micelles	Transport of hydrophobic cargo, biocompatibility	Drug delivery
	Quantum dots	CdSe, CuInSe, CdTe, etc.	Broad excitation, low photo-bleaching, tunable emission	Optical imaging
	Gold	Spheres, rods or shells	Biocompatibility	Drug delivery, hyperthermia therapy
	Silica	Spheres, shells, mesoporous	Biocompatibility	Drug delivery (encapsulation), contrast agents
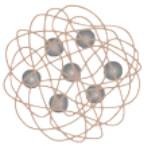	Magnetic	Iron oxide or cobalt-based; spheres, aggregates in dextran or silica	Superparamagnetic, ferromagnetic, superferromagnetic, paramagnetic	Contrast agents (MRI), hyperthermia therapy
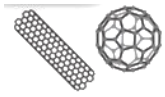	Carbon-based	Carbon nanotubes, buckyballs, graphene, nanodiamonds	Biocompatibility	Drug delivery

Organic vehicles are preferred for drug delivery purposes, their easy degradation in the organism ensuring a better biocompatibility and less long-term toxicity concerns [33]. That is probably the reason why organic nanoparticles were the first materials to be investigated for biomedical applications.

As presented in Figure 1.2-2-A, the number of citations indexed by PubMed for **"Liposome and micelle Nanomedicine"** is the highest of all organic and inorganic nanomedicines, with a beginning in the early 2000's. These types of nanomaterial, composed of a single layer of phospholipids in the case of lipid micelles and of a double layer of lipids for liposomes,

present the simplest methods to encapsulate a drug or a molecule. In the case of lipid micelles, only hydrophobic drugs can be loaded [24], while in the case of liposomes, both hydrophilic, in an aqueous media in the inner compartment of the liposome, and hydrophobic drugs, in between the two lipid layers [34], can be loaded. Liposomes can also be functionalized for active targeting, thanks to the grafting of antibodies or ligands.

"Polymer-based nanomedicines" are the second most studied nanomaterial among organic nanoparticles (cf. Figure 1.2-2-B). They are structured as nanospheres in which a polymeric matrix entraps the drug [35], or as nanocapsules, in which a polymeric membrane is protecting the aqueous or oily inner core [36]. Their synthesis can be straightforward, by using various techniques such as emulsion-solvent evaporation or diffusion, double emulsion or nanoprecipitation [37]. Nevertheless, the most widespread method to encapsulate an hydrophilic drug is the water-in-oil-in-water (W/O/W) double emulsion-solvent evaporation [38]. The main polymer used is Poly(lactic-co-glycolic acid) (PLGA), nevertheless other polymers are also used, among which the copolymer N-(2-Hydroxypropyl)methacrylamide (HPMA) and poly(ethylene glycol) (PEG) [39]. Our team at LVTA also developed nanoparticles transporting siRNA or drugs with polyisobutylcyanoacrylate [40] or with squalene [41]. Although, there is a great number of publications on pre-clinical studies using these polymeric nanomedicines, polymers are more and more used as coating agents on various types of nanoparticles, whether they are organic or inorganic [42,43].

"Dendrimers nanomedicines" are the less studied organic nanomaterial (cf. Figure 1.2-2-C). These nanoparticles with a polymeric treelike structure, *e.g.* composed of Poly(amidoamine) (PAMAM) among others, entrap within their core the drug or molecule of interest [44]. The cargo can either be hydrophobic or hydrophilic thanks to the tunable molecules that can be used to synthetize the dendrimer. This versatility also allows to control the size and the functionalization of the dendrimers [44]. Their development also started early, from the beginning of the 2000's, but seems to be left behind for about four years. This might come from the complexity of synthesis, and the need for outer surface functionalization in order to minimize the toxicity [45].

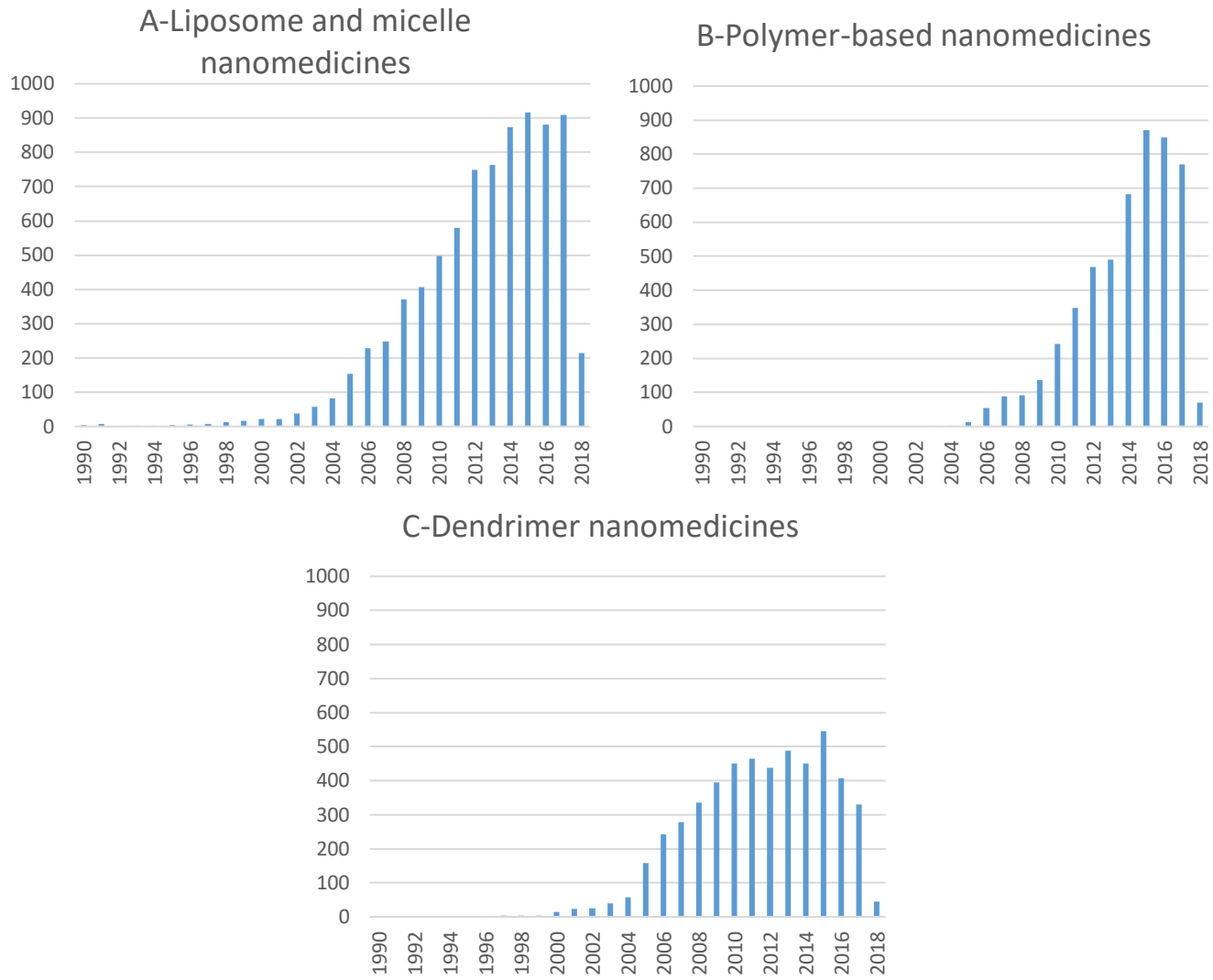

Figure 1.2-2: Number of publications in PubMed dealing with pre-clinical assays with organic nanoparticles, from 1990 to 2018

Just as for organic nanoparticles, inorganic nanoparticles (Figure 1.2-3) are used for drug delivery purposes by encapsulating the drugs [46]. They can also be functionalized in order to be able to graft the molecules or drugs on their surface [47,48] or coated or encapsulated by organic materials such as polymers [49]. They also are used as therapeutic (hyperthermia therapy) or imaging contrast agents.

The most studied inorganic NP are the **"magnetic nanoparticles"** (MNP), mostly used for the improvement of diagnosis imaging [50], theranostic [51] and for enhanced therapies applications [52]. Composed of iron oxide [53] or nickel ferrite, the cytotoxicity of these

nanoparticles is still under investigation but it appeared that the size and shape had a great influence on cell viability and proliferation [54]. In order to prevent a too high toxicity, coatings are realized and have proved to diminish toxicity compared to non-modified MNPs [55]. By taking advantage of their magnetic properties, with a modulation of their spin-spin relaxation time (T_2) [54], they make very suitable MRI contrast agents [56] greatly improving the detection and localization of tumor sites. The magnetic particle can also act as a potentiator of the applied magnetic field, thus locally increasing the temperature, inducing a cellular hyperthermia, leading to death [50]. By combining these two components, magnetic nanoparticles can then be used as theranostic agents, combining in real time the visualization of the target site (*e.g.* tumor site) and the treatment of the target. As it will be presented in the next sub-section, they are the only inorganic nanomaterial being commercialized.

"Gold nanoparticles" are the second most studied inorganic NP. Their applications are wide: they are used as drug [47] or gene [57] delivery agents, with the addition of a surface functionalization; as a necrosis trigger [58], by the production of Reactive Oxygen Species (ROS), at high concentrations [59]; as a thermotherapeutic reagent by converting light to heat, most of the time with a conjugation to another NP, or as a shell to encapsulate other NP (for iron NPs the encapsulation is needed to prevent their fast oxidation [60], or nanodiamonds [61]).

Next comes the **"carbon-based nanomedicines"** including carbon nanotubes (CNT), nanodiamonds and graphene. The pre-clinical studies for biomedical applications began at the beginning of the 2000's. CNT can be used as a reservoir hosting a molecule, within the tube or in between the walls in the case of Multi-Walled Carbon Nanotubes (MWCNT) [62], but it is mostly functionalized by covalent or non-covalent addition of functional groups [63]. It can also be used in scaffolds for stem cells growth [64] or tissue engineering [65]. The cytotoxicity of CNT is still under investigation, but it can be presumed that given their needle-like shape, they can potentially cause unwanted cell damage [66]. However, it has been shown that when properly modified at their surface or functionalized with a polymer, like PEG, their toxicity was reduced [67]. I will not detail nanodiamonds' use here, as it is the topic of the next chapter.

Finally comes the **"Quantum dots"** (QD) and the **"silica nanoparticles"**. The first are mostly investigated for their unique optical properties as biomarkers [68]. Nevertheless, it has been shown that QD presented some cytotoxicity [13], limiting their use in the biomedical field.

Silica is mostly used to encapsulate other nanoparticles [69,70] or to directly encapsulate a drug or a molecule [46,48].

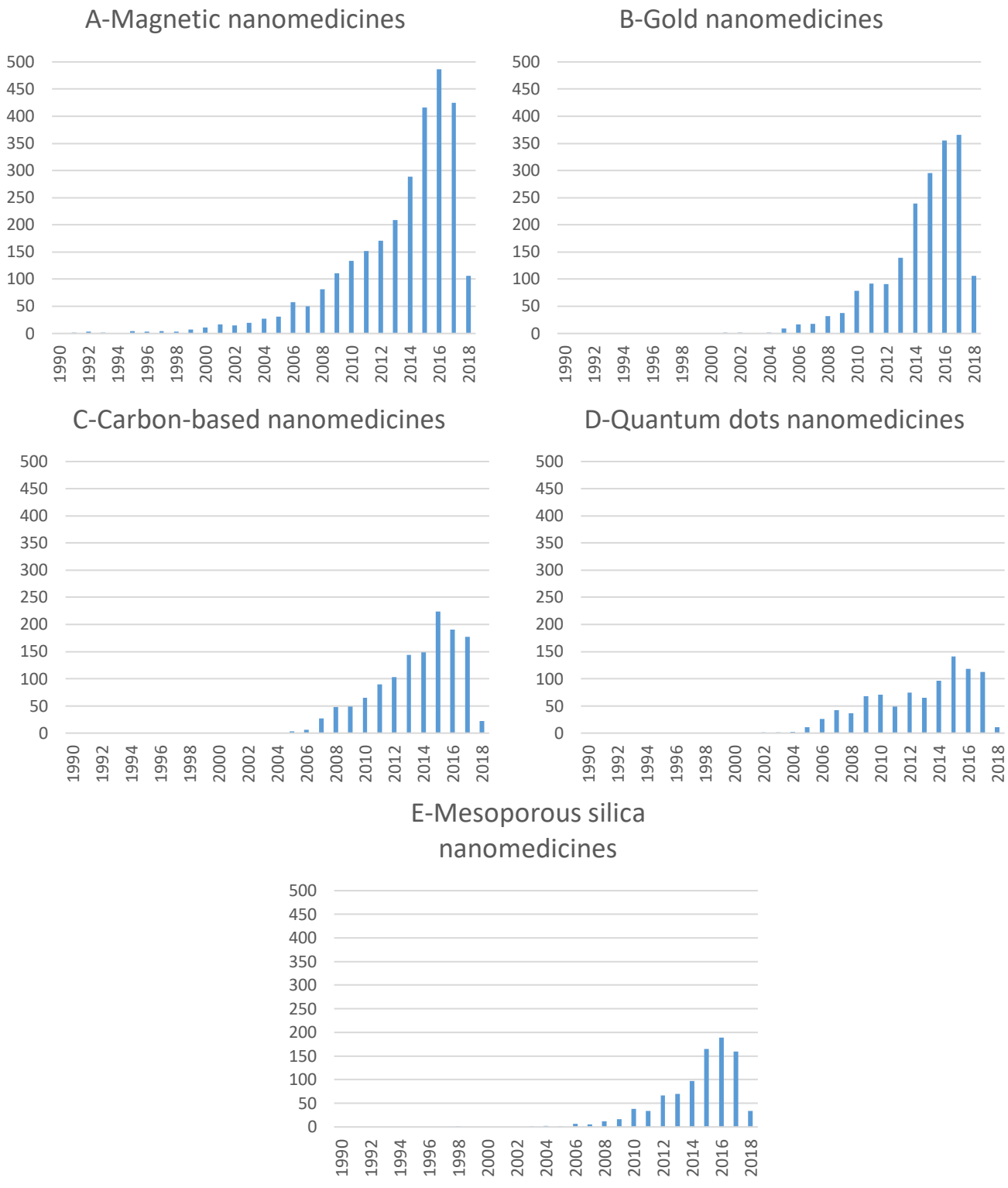

Figure 1.2-3: Number of publications in PubMed dealing with pre-clinical assays with inorganic nanoparticles, from 1990 to 2018

Figure 1.2-2 and Figure 1.2-3 showing the number of publications by nanoplatform types, reveal the diversity of nanomaterials available and under pre-clinical assessment for biomedical applications. We can also see that the forecasts having seen the nanomedicine as a promising field are confirmed, considering the high number of publications on the nanomedicine indexed in this field in 2017. Organic nanoparticles are clearly preferred to inorganic nanoparticles, mainly due to a lower cytotoxicity of the organic platforms and a better excretion from the organism. Nevertheless, great advances have been made on the furtivity of inorganic NPs, thanks to surface functionalization, and this difference tends to decrease.

Despite the fact that there is a fairly high number of publications, with promising pre-clinical results, the number of nanomedicines having passed through clinical trials and being approved for commercialization is still very limited. The various hurdles preventing the nanomedicines to develop more widely and rapidly is presented in the next subsection.

1.3. Trends in approved drugs and clinical trials involving nanoparticles for biomedical applications

Following the in-depth study of the compounds during pre-clinical studies, every new drug request a proper clinical translation, demanding rigorous clinical trials to obtain the authorization to be commercialized. Different phases can be distinguished, each having its purpose in the testing of the compound in the human. I will briefly describe the different phases of a clinical trial, in order to present the complexity and the duration of this process.

Phase I: first phase of testing in human subjects, a small group (20-50) of subjects are selected, including either healthy or palliative care volunteers, depending on the pathology [71]. Typically, in the field of oncology and HIV, the volunteers are at the end-stage of the disease, under treatments to ease symptoms without curing the underlying disease. For any other pathology, this phase is conducted on healthy subjects. This first step allows to assess the safety (pharmacovigilance), tolerability, pharmacokinetics and pharmacodynamics of the drug candidate. This phase also includes a dose-ranging assessment, in order to determine the appropriate dose range for therapeutic use and the maximal tolerable dose before the compound becomes too poisonous to administer [72].

Phase II: performed on larger groups of 20 to 300 volunteers, this phase allows to assess the efficacy of the drug [73]. When a new drug development fails, this is typically the phase when

it is discovered not to work as planned, to have toxic effects in humans or to require a specific protocol of administration not to have an unexpected behavior (mode, site and kinetic of administration). Two sub-phases can be distinguished: Phase IIA, which is specifically designed to assess dosing requirements, the right amount of drug which should be given to obtain a treatment efficacy; Phase IIB intends to study the efficacy of the drug at the prescribed dose. It is not uncommon to combine Phase I and Phase II, to assess at the same time both efficacy and toxicity.

Phase III: this is the largest scale and longer phase of the clinical trial process [73]. This phase consists in a randomized controlled multicenter, if possible worldwide, trial on large patient groups (300-3,000+). This phase is aimed at being the definitive assessment of the efficacy of the drug when compared with the current standard of care. Due to their size and long duration, Phase III trials are the most expensive, time-consuming and difficult trials to design and run. After the completion of this phase, a sales permission can be obtained if no toxicity was observed all along the trial and if a real improved efficacy has been showed.

Phase IV: least known of all phases, it is the post marketing surveillance trial [74]. This is the ongoing pharmacovigilance and technical support of a drug after it received sales permission, and in a way is a phase that never ends. This phase might be required by authorities, to study the interactions with other drugs or with a certain population, that are unlikely to subject themselves to trials (*e.g.* pregnant women). This phase is designed to detect any long-term or rare adverse effects over a large population and a long period of time. If harmful effects are observed during this phase, the drug can be withdraw from the market (8.2% of all drugs in 2015 in USA [75]) or restricted to certain uses. In France, the Mediator (Laboratoire Servier) withdrawal is a well-known case and has raised lots of interrogation on how the pharmacovigilance was conducted. This drug, which was initially prescribed for the treatment of type 2 diabetes from 1976 to 2009, has been observed to induce an increase of valvular heart diseases and of pulmonary hypertension, responsible for over 1,300 deaths [76]. The pharmacovigilance phase is thus a crucial phase during the drug lifecycle and is conducted in order to protect the patients. Nevertheless, every drug can induce an adverse effect, most of the time on a very small fraction of the population, but it is only when the drug is widely used that those adverse effects can be detected [77].

All phases are crucial and bring new information on the behavior, the pharmacokinetics, the pharmacodynamics, the efficacy and the toxicity of the new drug. It is also important to

highlight that each phase tests the drug on a different and increasingly broader population of patients. Even though the pre-clinical trials give very good data on the efficacy of a drug, the behavior in an animal can greatly differ from the behavior in human, inducing the interruption of the development of a majority of compounds, at different stages. Figure 1.3-1 presents the probability of a drug, tested either for an oncologic or for a non-oncologic application, to pass to the following phase of the clinical trials process and to be approved for commercialization. One can see that the proportion of drug for oncology purposes reaching the approval is only of 5%, with an entire clinical trials process duration from 10 to 15 years [31].

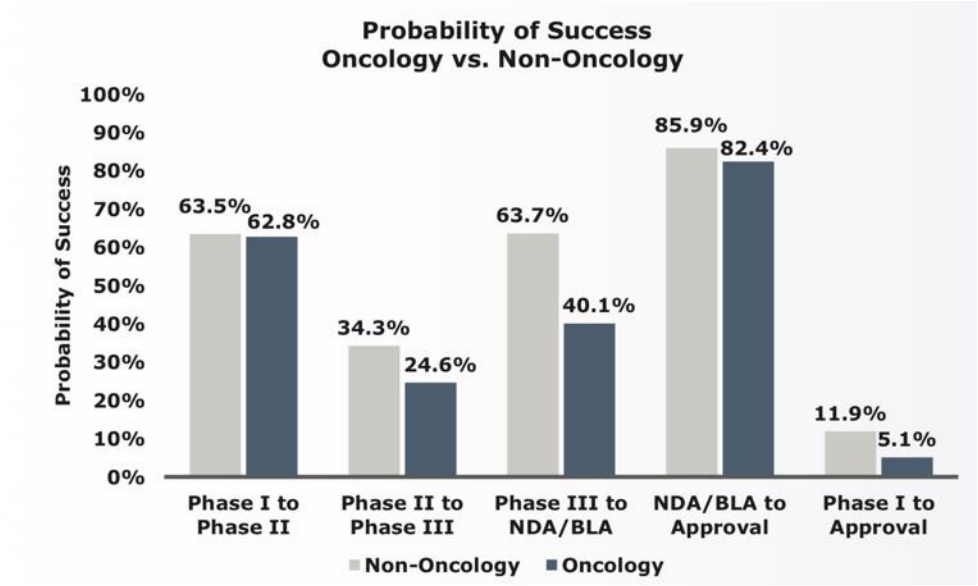

Figure 1.3-1: Probability of success of drug candidates in oncology and in non-oncology applications, data for U.S. FDA in 2015. Abbreviations: NDA: new Drug Application, BLA: Biologic License Application. From "Clinical Development Success Rates 2006-2015", Biotechnology Innovation Organization (BIO), Biomedtracker and Amplion.

Nanomedicine, just like classical drugs or medical devices, must follow the same clinical trials process. Different reviews have observed a 3-fold increase of clinical trials involving nano-sized compounds within the last 5 years [31], with over 200 products involved in trials [7]. The applications and delivery modalities are various and cover:

- Oral delivery of particles for imaging applications [50];
- Local delivery of particles carrying a variety of biologics including peptides and small molecules [78,79];
- Topical application of particles to increase skin penetration [80,81];

- Systemic delivery of particles transporting various molecules for the treatment of cancers or other diseases [7,82].

In 2016, 51 FDA-approved nanomedicines were identified [31], including therapeutic or imaging agents, in which nanoparticles were used to better control the tissue biodistribution, to enhance the efficacy or to reduce toxicity of the vectorized drug or molecule. As presented in Figure 1.3-2-a, the trend shows a clear preference for the development and then the commercialization of liposomal, polymeric and metallic based nanoparticles before the 2000's, following the trend of publications showed in the previous sub-section (Figure 1.2-2 and Figure 1.2-3). From the 2000's, the approvals for commercialization experienced a peak, with a large increase of FDA-approved nanocrystal-based platforms and still a strong presence of polymeric platforms. Since 2005, the number of approved nanomedicines per 5-years period has decreased and then stayed constant, most probably because of the financial crisis in the 2006-2010 period [83]. These observations can be put in parallel to the number of clinical trials which has also dropped at this period. Figure 1.3-2-b clearly shows that "soft" nanomedicines (*e.g.* micelle, liposomes and polymeric-based NP) are preferred and are more likely to pass the clinical trials process. Nevertheless, it is worth noting that nanocrystals and metallic NP (used in radiotherapy or thermotherapy and for imaging purposes, respectively) also occupy a good place in the approved nanomedicines.

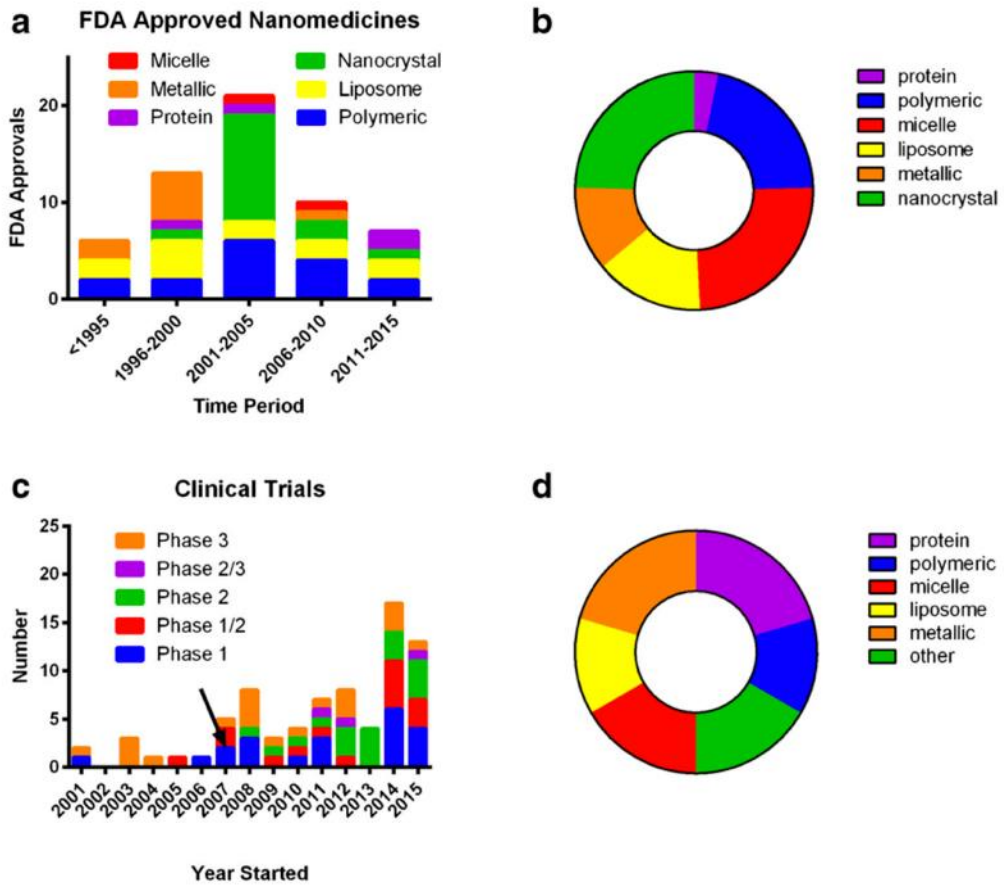

Figure 1.3-2: Trend in the development of nanomedicines from 1990's until 2015. (a) FDA-approved nanomedicine classified by category; (b) FDA-approved nanomedicines classified by category overall; (c) clinical trials identified in clinicaltrials.gov from 2011 to 2015. The arrow indicates the approximate start date of US law (FDAAA 801) requiring the inclusion of the trial in the FDA database. This new regulation explains the large increase of recorded clinical trials in the following years; (d) nanomedicines under clinical trial investigation stratified by category overall. From ref. [31].

The number of clinical trials involving nanomedicine gives precious information on which technology is the most promising and which one fails in human application. First, one can observe that the number of Phase I and Phase II clinical trials are predominant, confirming what was said before: Phase II stage is critical in the development of a new drug. This phase, which allows to test for the first time the drug at a large scale, is the one at which there is the highest probability of failure, as presented in Figure 1.3-1. Thus, it makes sense that only a small number of compounds passes this step. It is also worth highlighting the steadily increase of overall number of clinical trials, 2014 and 2015 being the best years, suggesting that the development pipeline of nanomedicines is thriving.

Interestingly, a large number of protein-based nanomedicines are tested during the clinical trials (Figure 1.3-2-d), but from Figure 1.3-2-b, not much of them obtain FDA-approval, on the contrary of the other platforms.

An exhaustive list of the various FDA-approved or still under clinical trials nanomedicine will not be given here, but several recent reviews have listed them [7,10,30,31]. The trend that can be extracted from these different reviews is that nanomedicines are tested for a great variety of applications: in oncology, in psychiatry, or as bone substitutes, among other application fields. In all cases, the nanoparticle or nano-system allows to either improve the drug bioavailability, or the drug loading or to reduce the drug toxicity, thus enabling an improved treatment and a dose reduction.

Despite the fact that there are more and more pre-clinical studies publications, patent fillings and clinical trials conducted using nanomaterials, there are still bottlenecks to the wide commercialization of nanomedicines [84,85], mainly due to issues inherent to the large-scale production [86]:

- Lack of standard "nano" nomenclature, leading to an imprecise definition of nanomedicines;
- Lack of a precise control over nanoparticles manufacturing parameters;
- Hurdle with the large scale good manufacturing (staying up to date with the current good manufacturing practices, cGMP) production (current compounds not fully 'compatible' with large-scale production);
- Lack of quality control of the produced nanomedicines;
- Scalability complexity: need to enhance the production rate;
- Reproducibility issues;
- High fabrication costs;
- Biocompatibility, biodistribution, toxicity to human and the environment: lack of knowledge regarding the interaction between NP and biosurfaces/tissues;
- Consumer confidence and ethical issues: public's general reluctance to trust innovative medical technologies;
- Big pharma's reluctance to massively invest in nanomedicines; the entire long and cost-consuming process being ensured by small or medium companies (SME), who do not necessarily have the funds.

This might also come from several hurdles in the patenting process, made quite difficult for the nanomedicine field [87]. The patent is the safest way to protect the invention and the conditions to obtain one are to demonstrate:

- the novelty and commercial usefulness of the invention, it is called the "inventive step";
- the "non-obviousness of the invention", from a one skilled in the art point of view;
- the ownership/inventorship of the invention, the "first to invent" law;
- the proof of invention: lab notebooks, archived experiments, ...

The nanomedicine field suffers from a lack of massive investments from big pharma companies, thus making the patenting step even more difficult: public laboratories or SMEs are not necessarily well trained or managed on this matter, nor have the funds to fully finance the process. Thus, the nanomedicine, even though it has showed great *in vitro* results, has difficulties to pass to the step of clinical trials, mostly because of a lack of proper intellectual property protection. Furthermore, the delays to obtain concluding results can be very long, it can take more than a decade before having concluding pre-clinical results and then passing all steps of the clinical trials process. In such cases, the patent might be expired because of the timescale, and the invention then loses all its commercial value.

1.4. Conclusion of Chapter 1

This chapter briefly introduced the history of nanomedicine, a less than two decades old field, the reasons why it is such a promising technology and proposed a focus on the trends of the various nanoparticles that are currently under pre-clinical studies, under clinical trials or commercialized for medical applications. It has been demonstrated that nanomedicine is an active field, with a large number of publications and products already on the market. The clinical trials process being very selective, time and cost-consuming, about only 50 products have been delivered to the market since 1995 (e.g. Doxil, Abraxane) [31]. Nevertheless, the trend tends to demonstrate that the development pipeline of nanomedicines is prosperous, and we can bet that this trend will continue in the next years. A major difference from classical drugs and molecules tested in clinical trials, is that there are more and more SMEs entering the field, rather than the traditional big pharma, who, it seems, are more reluctant to massively invest in this new technology. The trend is that SMEs develop and support the pre-clinical and/or the clinical steps, and the big pharma only enters in the process as a partner or at the end, by buying a license to the SME which developed the technology. It is at the opposite of

the old drugs that were owned from the beginning by the big pharmas and took years and billions of dollars to develop. The nanomedicine field might then reshape the pharmaceutical landscape and might introduce a new process for the development of new therapeutics, with a greater open innovation and a greater partnership between big pharmaceutical companies and public laboratories or SMEs.

Overall, nanomedicine is a very promising field, with a high number of publications, some products being under clinical trials and a few products commercialized. Nanomedicine is an attractive field but still suffers from bottlenecks to truly revolutionize medicine.

After having introduced nanomedicine, let us now focus on the specific nanoparticle which was at the heart of this PhD work: diamond nanocrystal (nanodiamond). Over the past two decades, this material has been first investigated for its specific properties, its very small size (≈ 5 to 70 nm), and for its high affinity for proteins leading to its application in matrix for MALDI-TOF mass spectrometry [88]. Then began the study of its fluorescence and magneto-optical properties originating from embedded nitrogen-vacancy (NV) centers, leading to a large number of applications, mostly in nano-magnetometry and bioimaging.

The next chapter will present the characteristics of nanodiamond, the possibilities of its surface functionalization and the potential and currently studied biomedical applications, showing that nanodiamond is a remarkable tool, which can be used for our specific application, as a traceable vector for a new treatment of a rare pediatric cancer.

CHAPTER 2

Nanodiamond: a promising platform for biomedical applications

Nanodiamond (ND) was discovered in the early 1960's, long before any interest in their nanometric size and just a few years after the first diamond man-made production in 1955 [89]. In the late 1960's, the first colloidal suspension of 4-5 nm individual particles diameter was synthesized, but researchers began to investigate their application for biomedical purposes only years later, in the late 1990's. Researchers also started to take advantage of fluorescent nanodiamonds (FNDs) as a non-toxic and a perfectly photo-stable alternative to

quantum dots in biomedical imaging. From the 2000's, began the tailoring of surface properties of nanodiamonds by several wet [90] and gas [91] chemistry techniques, allowing their use as drug and gene delivery vehicle.

Among all nanoparticles, nanodiamond is considered as the best for numerous applications, thanks to several properties ranked as "the highest among known materials on earth" [92]. This includes exceptional mechanical properties, chemical stability [92], versatile surface functionalization [93], biocompatibility [94] and excellent photo-stability of embedded defects [95] (no bleaching or blinking in the fluorescence spectrum, as it will be detailed in Section 2.2.1). Consequently, aside from their exploitation for their mechanical properties as additives in lubricant for industrial applications [96] or of their NV defects in quantum computing applications [97], nanodiamonds have been investigated for three decades as drug delivery agents, contrast agents in biomedical imaging or as biosensors.

Diamond is composed of carbon atoms in a sp^3 hybridization state, arranged in a face-centered cubic crystal structure, with an additional four atoms in position $(\frac{1}{4}, \frac{1}{4}, \frac{1}{4})$ [98]. This particular arrangement, represented in Figure 2.0-1, is made possible thanks to the very strong covalent binding between its atoms, conferring to this material the highest hardness and thermal conductivity of all materials.

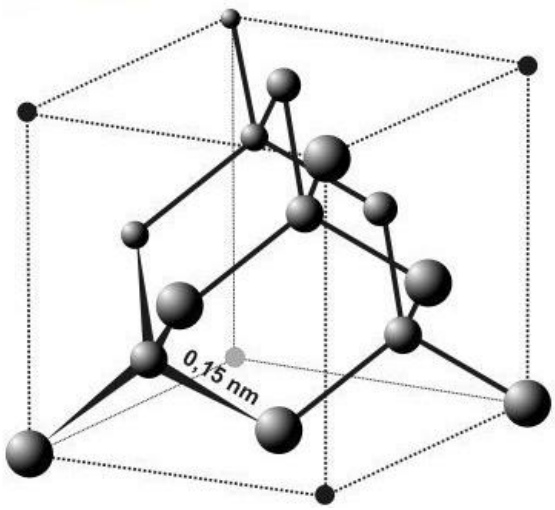

Figure 2.0-1: Diamond lattice. By Anton [GFDL (http://www.gnu.org/copyleft/fdl.html) or CC-BY-SA-3.0 (http://creativecommons.org/licenses/by-sa/3.0/)], via Wikimedia Commons

In this chapter, the main synthetic methods of production of nanodiamonds will be presented. Then the fluorescence properties that can be induced and their applications will be

introduced, and the various surface modifications that can be made on nanodiamonds will be described. Finally, some examples of biomedical applications using nanodiamonds will be given and the different biodistribution and elimination studies conducted on this vector will be presented.

2.1. Nanodiamond's main methods of production

Diamond exists in nature and can be found in the Earth's mantle at a depth >150 km, where the proper high pressure P and high temperature T (P>10 GPa and T>2000 K) for the production of this carbon allotrope are gathered. Diamond can also be found in meteorites craters, where, during the impact, the same extreme conditions for diamond formation are realized. Some studies also show that white dwarf stars have a core mainly composed of diamond [99].

Despite the extreme conditions in which diamonds are produced in nature, synthetic diamond can be produced, and nanoparticle can be obtained from two main techniques: (i) by high-energy milling of diamond microcrystals, synthesized by high-pressure high-temperature process (HPHT) discovered in 1955 [89], and (ii) by detonation reaction developed in the USSR [100] in 1963. Nanodiamonds are now mainly synthesized by those two techniques but also by plasma-assisted chemical vapor deposition (CVD) [101], laser ablation, ion irradiation of graphite, electron irradiation of carbon onions and ultrasound cavitation [93,102,103]. For biomedical applications and more specifically for drug delivery and imaging purposes, the first two production techniques are preferred, producing single particle diamonds of size down to 3 nm for detonation process and of ≈10-20 nm for HPHT synthesis process [93].

2.1.1. Detonation reaction synthesis

Detonation synthesis is the main mean of production of nanodiamonds. It was first experienced by researchers from USSR in 1963, by explosive decomposition of high-explosive mixtures within a negative oxygen balance and a non-oxidizing medium [104]. The most common explosive used is made of a mix of 60 wt% TNT ($C_6H_2(NO_2)_3CH_3$) and 40 wt% hexogen ($C_3H_6N_6O_6$)(RDX) [105]. Those two compounds are detonated in a closed chamber with an atmosphere containing N_2, CO_2 and liquid or solid H_2O [106]. Temperature and pressure extreme conditions are exposed in Figure 2.1-1-b and lead the explosive molecules to disintegrate into atoms. Carbon atoms released by this mean are condensed into amorphous carbon phase, which then undergo diffusion and liquid droplet coalescence, leading to the

formation of diamond, as represented in Figure 2.1-1-c [104]. This reaction produces up to 12% weight soot by incomplete combustion, containing up to 75% weight diamond carbon [92].

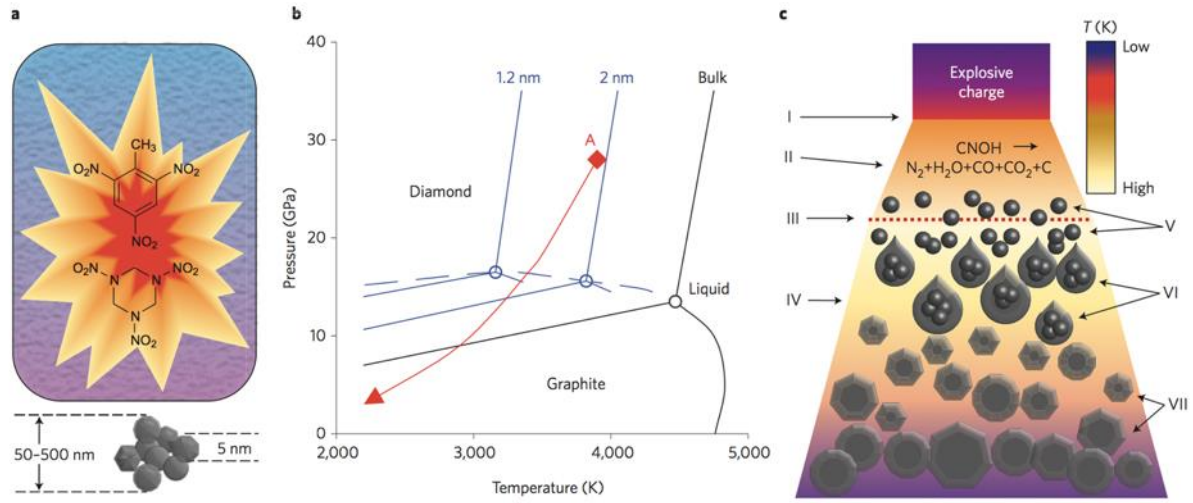

Figure 2.1-1: Diamond nanoparticles production by detonation reaction. (a) Chemical reaction used for the detonation. (b) Carbon phase diagram during detonation reaction. The Jouguet-Chapman condition (point A) corresponds to the situation when the speed of the gas forming the diamond is the same as the speed of sound, leading to a detonation shock wave. While temperature and pressure decrease following the isentrope (red line), carbon atoms condense into nanoclusters. When pressure drops under the carbon-graphite equilibrium line, graphite formation takes place. (c) Different phases of carbon growth during detonation reaction. (I) Shock wave caused by the explosion. (II) Detonation reaction where the molecules of the reaction decompose. (III) Chapman-Jouguet condition (point A on diagram (b)). (IV) Expansion of detonation products. (V) Formation of nanoclusters. (VI) Coagulation into nanodroplets. (VII) Crystallization, growth and agglomeration of nanodiamonds. From Ref. [103]

The product must then be purified of metal impurities from the igniter used for the detonation reaction, and from the steel walls of the detonation chamber [103]. On an industrial scale, purification of the detonation soot is performed with liquid oxidants such as HNO_3, a mixture of H_2SO_4 and HNO_3, $K_2Cr_2O_7$ in H_2SO_4, KOH/KNO_3, Na_2O_3, HNO_3/H_2O_2 under pressure, or $HClO_4$ [104]. The different purification steps are presented in Figure 2.1-2. The products of the soot being under the form of agglutinates of up to 500 nm, they are disintegrated by oxidation and zirconia bead-milling [93]. Primary particle diameter thus obtained is about 4 to 5 nm [107], with the notable presence of a graphitic layer, which can be removed by chemical baths at a later stage. This purification step is hazardous and expensive and is estimated to contribute to up to 40% of the production cost [103]. The nanodiamonds

thus produced are chemically inert and their functionalization can be performed by different means that will be described later.

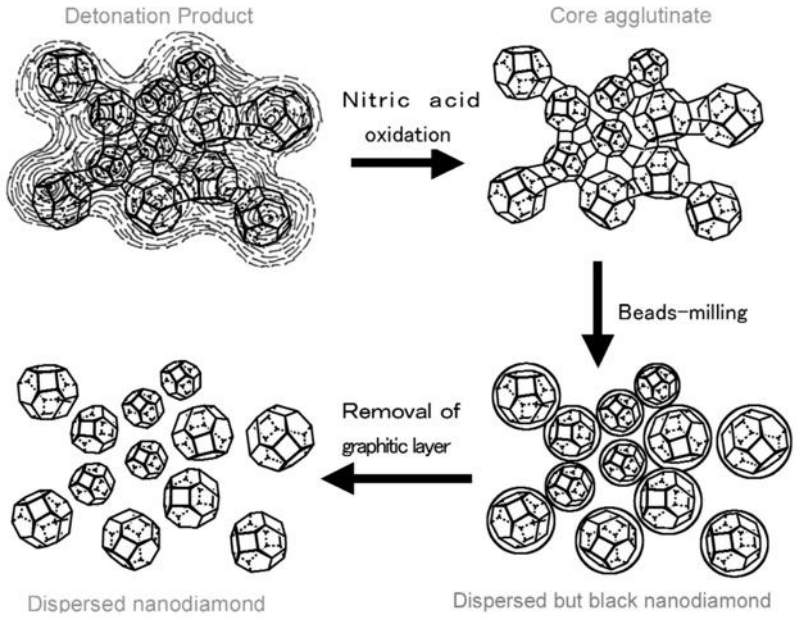

Figure 2.1-2: Purification process of detonation products. From Ref. [92]

2.1.2. High Pressure High Temperature synthesis

Compared to the bottom-up method of detonation reaction, the so-called HPHT nanodiamonds are produced by a top-down method. As presented in Figure 2.1-3, a large hydraulic press is used to produce a high pressure (7-10 GPa) at a high temperature (1500-2000°C), yielding micrometer-sized diamond crystals (100-200 µm). Graphite and catalysts are employed in the hydraulic press for a few hours, in order to induce graphite-diamond conversion. To produce nanodiamond, the microcrystals are commonly milled with very hard beads (*e.g.* made of zirconium). A nano-powder is finally obtained, that needs further size selection by centrifugation after having been dispersed in water. The smallest HPHT ND currently present on the market offers a primary median size of about 18 nm [108]. A similar HPHT powder (with a median size of 25 nm) was reported with 60% of sub-10 nm particles, observed under transmission electron microscopy (TEM) analysis [109]. By using an additional annealing step, which allowed the removal of the amorphous sp^2 carbon at the surface of NDs, it is even possible to obtain HPHT nanodiamonds of a size down to 1 nm [108].

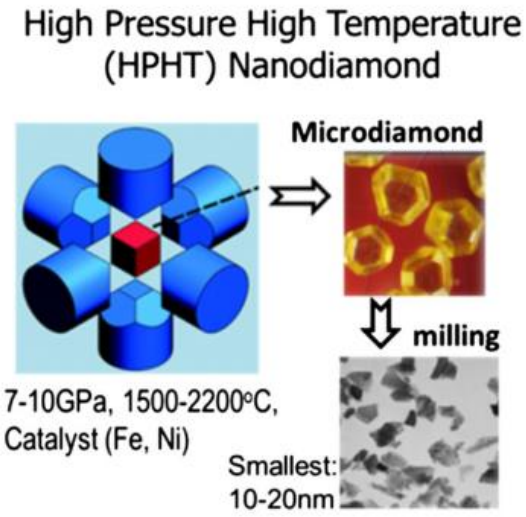

Figure 2.1-3: Schematic representation of HPHT nanodiamond synthesis. From Ref. [110]

Compared to detonation nanodiamond, the size distribution of HPHT NDs is broader, mainly due to the milling step, which is also responsible for the irregular shapes. Also, their surface is harder to modify, due to their lower reactivity and a lower surface/volume ratio, compared to detonation ND [70].

Whatever the mode of production, nanodiamonds can be modified and conferred color centers impurities, inducing fluorescence properties. This characteristic is described in the following subsection.

2.2. Fluorescent nanodiamond: production and properties of nitrogen-vacancy (NV) color centers

2.2.1. Properties of NV centers

Diamond is an optically transparent material over a large band of the electromagnetic spectrum, which does not show any luminescence unless presenting structural defects.

Diamonds are classified based on their nitrogen content and optical absorption: type I are those containing nitrogen impurities while type II are those with no measurable traces of nitrogen [111]. Only type I diamonds are thus suitable for producing high concentration of Nitrogen-Vacancy centers. Two sub-classes of type I diamonds can be distinguished:

- type Ia: most of the natural diamonds, nitrogen is at a concentration of 3,000 ppm and clustered;

- type Ib: most of the synthetic diamonds, nitrogen is at a concentration of about 100 ppm, and impurities are isolated from each other.

Type II diamonds present a very low concentration of nitrogen (<1,020 atoms.cm^3) and can also be divided into two sub-categories. Type IIa is the purest diamond, colorless and free from any impurities. Type IIb contains high quantities of boron atoms, leading to semi-conductor properties.

Type I diamonds fluorescence is then due to the presence of color centers, coming from impurities in the diamond lattice. The most utilized defect is due to a carbon vacancy associated to a substitutional nitrogen atom impurity, as shown in the inset of Figure 2.2-1-a. This defect exists in two charges states: NV^- and NV^0. Other single-photon sources defects can be produced in the diamond lattice, such as silicon-vacancy (SiV^-) centers (738 nm), possibly nickel-related complex NE8 (793-802 nm), chromium-related emitters (750-770 nm) or possibly interstitial carbon-related TR12 center (470 nm), among many others [112].

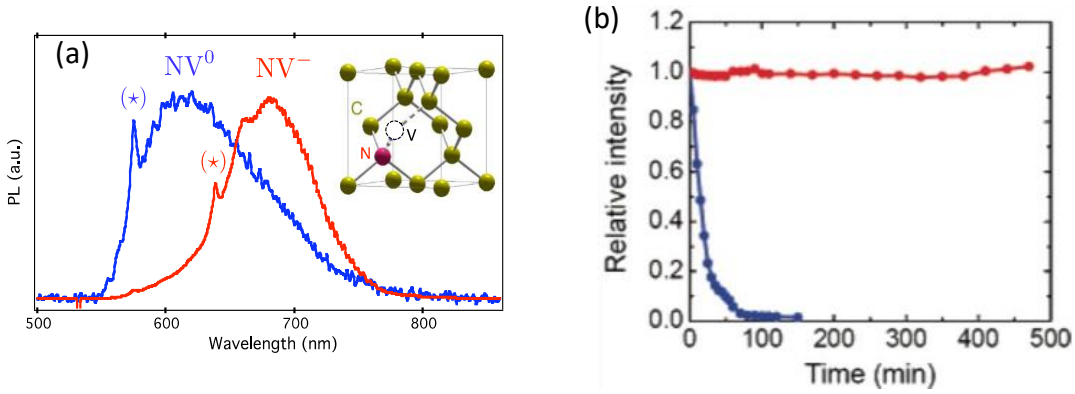

Figure 2.2-1: Structural and emission properties of FNDs. (a) Photoluminescence spectra (normalized from their respective maximum value) of single NV^- (red curve) and NV^0 (blue curve) color centers in nanodiamonds. The inset shows the atomic structure of the NV defect. From Ref. [113]. *(b) Photostability of FND (red) compared to fluorescent polystyrene nanospheres (blue) excited in the same conditions. From Ref.* [114]

The NV^- color center is efficiently excited by a laser beam emitting in the green spectrum (generally 488 nm < λ < 575 nm) and emits in the far red – near infrared spectrum (600–750 nm) with a very stable photo-emission [105], as presented in Figure 2.2-1-b.

2.2.2. Production of Nitrogen-Vacancy centers in diamond lattice

Vacancies are created in diamond by irradiation with high energy particles. When passing through the matter, their kinetic energy is transferred by elastic collision to a lattice carbon

atom, leading to the displacement of this atom from its equilibrium lattice position. The displaced atoms can also induce a cascade of atomic displacements before stopping, after having lost all its kinetic energy [115]. This effect is more or less significant, depending on (i) the heaviness of the incident particle (heavy particles are protons or alpha particles) and on (ii) the energy utilized (a few MeV for electrons for instance).

Several methods of production of these color centers have been reported. The most commonly used ones consist in creating the vacancies by:

- Microcrystals irradiation under a 10 MeV electron beam, followed by an annealing step at 800°C under vacuum, and a final step of milling, to obtain a high yield of fluorescent ND of size 10 nm [116]. Figure 2.2-2 shows the effect of the different steps.
- Placing the nanodiamonds powder under a high energy, 13.9 MeV electron beam [117] or a 40-keV He^+ ions bombardment [95], followed by an annealing process at 800°C, inducing a high concentration of color centers.
- Forming a very thin film of nanodiamonds, and irradiating it with a 3 MeV H^+ or a 40 keV He^+ ion beam, followed by an annealing step at 800°C, to form the NV defects [118].

The thermal annealing step is essential to NV creation as, at such temperature, the vacancies start migrating and eventually stabilize in the adjacent site of the nearest substitutional nitrogen atom, this position being thermodynamically the most favorable one.

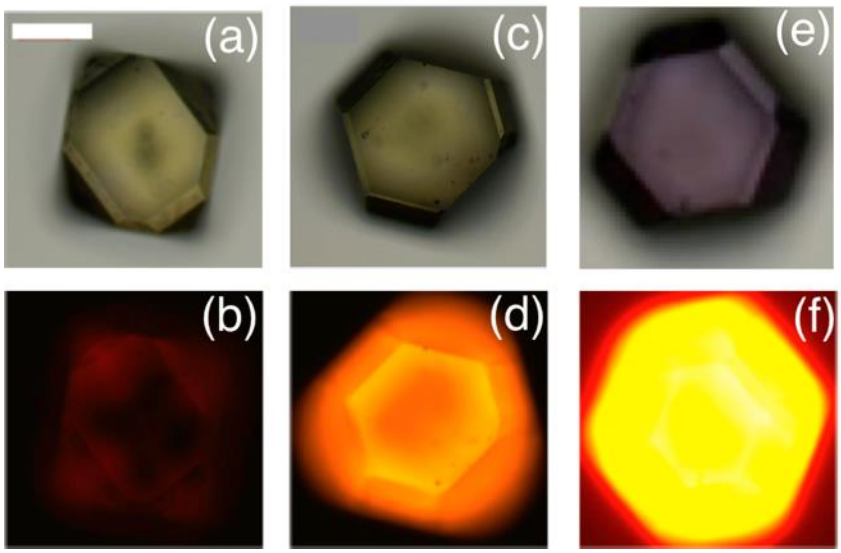

Figure 2.2-2: Microdiamond fluorescence at the different nitrogen-vacancies centers creation steps (a), (c) and (e): White light illumination optical microscopy image of a diamond microcrystal, at different stages of NV

centers creation process: (a) as-received, (c) irradiated with a 8 MeV energy electron beam, at fluence of 2.10^{18} electrons/cm^2, and (e) irradiated and high temperature annealed (800°C, 2 hours, under vacuum) microcrystal. (b), (d) and (f): same microcrystal as in (a), (c) and (e) respectively, observed under epifluorescence microscopy. Epifluorescence microscopy acquisition conditions (same for (b)-(d)-(f)): excitation band wavelength 500-550 nm, detection with a long-pass filter at wavelength above 600 nm, and CCD array detector integration time of 1.5 s. Scale bar: 50 µm. In (f), the high concentration of NV centers from the annealing step induces the saturation of the CCD array. From Ref. [119]

In both cases, a sp^2 graphitic layer is formed after the thermal annealing step, which needs to be removed by oxidation.

The fluorescence of the NDs used in our application is generated by a high energy proton beam (15.5 MeV) [120] followed by an annealing step and several acid cleaning treatments, as detailed in Section 4.3.

2.2.3. Fluorescent nanodiamond imaging and NV centers detection

The fluorescence property of NDs is more and more explored for the biomedical applications, as it will be described in Section 2.4. FND can of course be imaged by conventional confocal microscopy, but NV center is also particularly well suited for more demanding methods like Stimulated Emission Depletion (STED) super-resolution microscopy and time-gated microscopy.

- **Stimulation Emission Depletion** (STED): uses two laser beams at different wavelength: one "low" power beam brings the fluorophore in its exciting state, while the second at much higher power and larger wavelength reduces the fluorescence by stimulated emission. The latter beam is passed through a phase plate to yield a doughnut-like shape at the microscope objective focus, leading to the situation where all molecules except those in the middle of the doughnut gives a fluorescent signal of sub-diffraction size [121]. Due to the high power of the STED beam, the resolution is usually limited by photobleaching with conventional fluorophores. This limitation falls in the case of NV centers that are perfectly stable. STED was first applied to NV center in diamond by RITTWEGER *et al.* in [122], who showed a dramatic improvement of NV centers detection compared to confocal microscopy, as shown in Figure 2.2-3. STED also allows to resolve single NV centers in 40-250 nm-sized nanodiamonds with a resolution of ≈10 nm. This method can detect individual defects from multiple adjacent centers down to a relative distance of ≈15 nm [123].

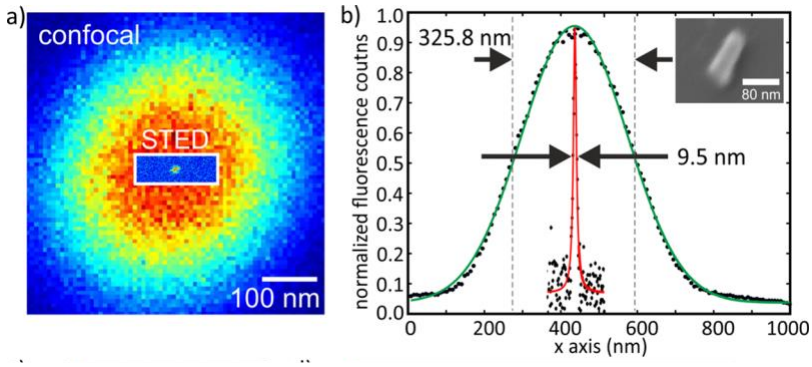

Figure 2.2-3: Stimulated Emission Depletion(STED) microscopy shows a greater resolution for nitrogen-vacancy centers in diamond compared to confocal imaging. (a) Confocally detected image versus STED image in the center inset. (b) Respective side projection of a single NV in a ND. Green curve, signal from confocal image; Red curve, signal from STED image. The inset shows an SEM image of the ND. From Ref. [123]

- **Time-gated imaging:** another characteristic of NV centers in nanodiamond is their long excited state lifetime (≈30 ns) [124] in comparison to the one of dye or to tissue autofluorescence (≈2 ns) as presented in Figure 2.2-4-A. This property has been used to improve the signal/background imaging of FND in a biological environment. FAKLARIS *et al.* in [125] showed that NV centers fluorescence could be distinctly detected from the surrounding tissue autofluorescence, as presented in Figure 2.2-4-B-C, by a pulsed-laser excitation and a time resolved detection.

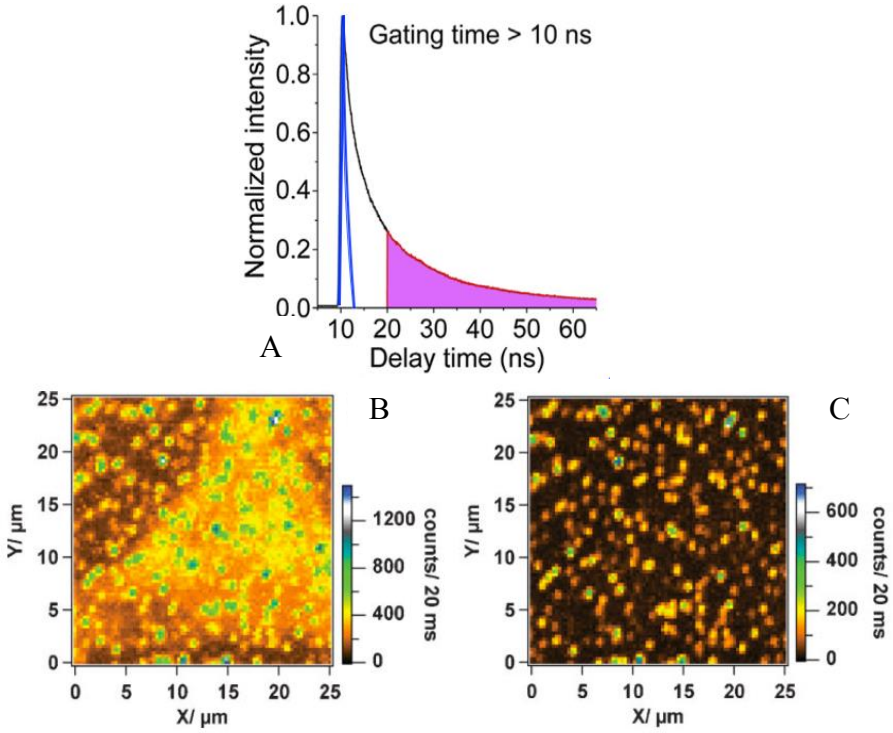

Figure 2.2-4: Time-gated confocal imaging property and usage. A: Fluorescence decay trace of 100-nm FND suspended in water (black curve) and of tissue autofluorescence (blue curve).The area shaded in magenta represents the signal collected after a gated time longer than 10 ns. Adapted from Ref. [126]. *B and C: Application of the time-gated imaging on HeLa cells in the presence of FNDs. B: Image of all detected photons, displaying FND along with cell fluorescence. C: Time-gated raster scan constructed from photons detected between 15 and 53 ns after the laser excitation pulse. From Ref.* [125].

This delayed detection of fluorescence allows to only collect photons from the NV centers. This technique enabled the clear dynamical detection of HeLa cells containing FNDs, when placed in whole blood [127]. During my PhD work, I have used a similar time-delayed microscope setup as in Ref. [127], with some major differences: we used a faster pulsed laser emission rate, a larger magnification, allowing us to obtain very detailed and resolved images (see Section 5.2), and an automatized acquisition setup of millimeter-sized samples (generating up to 10^4 field of views). This setup will be fully described in Section 5.2.

2.3. Surface chemistry of nanodiamonds

2.3.1. Colloidal properties of nanodiamonds

Nanodiamonds offer very good colloidal properties, several studies showing that when prepared properly, their dispersion in water, yields a non-aggregated, very stable suspension over time [128]. As presented before, several complementary steps are employed to reduce

aggregates' sizes after detonation and HPHT production: bead milling of the aggregates [129], strong sonication to break aggregates and centrifugation to only collect small particles in the supernatant [130,131]. These methods allow to eventually obtain dispersed individual particles. These colloidal properties are very interesting, in particular when NDs are used as diamond germs for Chemical Vapor Deposition (CVD) thin layers growth [132].

Such colloidal stability is mainly due to the electrostatic charges present at the surface of single nanodiamonds, inducing electrostatic repulsion between particles. Zeta potential is commonly used to characterize the electrophoretic mobility which is related to the surface charge. In water, these charges can be either positive or negative [133], depending on surface terminations. It also varies with the pH of the solution, as presented in Figure 2.3-1.

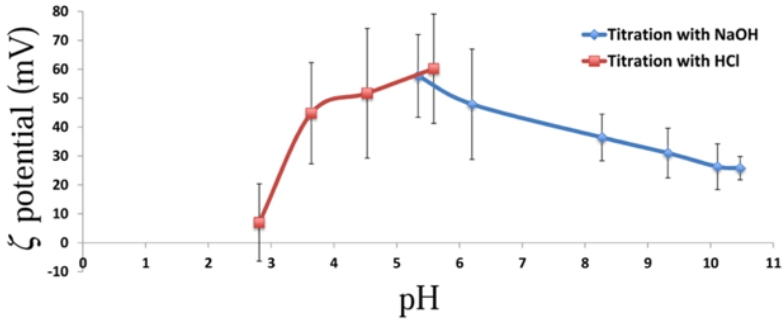

Figure 2.3-1: Zeta potential values of detonation nanodiamond solution depending on pH. From Ref. [106]

This colloidal property is a great advantage over other carbon-based nanomaterials that are naturally hydrophobic and need a chemical functionalization or specific treatments to secure colloidal stability.

2.3.2. Surface modifications

Nanodiamonds have thus a very good colloidal stability and are naturally given electrostatic charges after milling and annealing steps. These charges can be used to directly bind molecules at their surface by electrostatic attraction [88]. Surface chemical groups composition can be modified for example by hydrogenation [134], leading to cationic properties, or oxidation, or by carboxylation which yields negative charges at pH=7 [42].

Surface chemistry of NDs can be of a great diversity and is a tremendous advantage over other inorganic NPs. Several surface cationization methods and a functionalization by the covalent grafting of a copolymer were tested during this PhD project. The various surface modifications that are possible to obtain are described in this subsection.

2.3.2.1. Natural functional groups at the surface of NDs

Most of the commercially available detonation nanodiamonds carry various carbon-oxygen functions, as presented in Figure 2.3-2. It is due to the cooling process used during the detonation step, which involves water or ice, resulting in the reaction of highly reactive hydroxyl species [133]. Carbonyl and carboxyl groups can also be found at the surface of DNDs, as a result of the purification step, executed using oxidizing mineral acids and/or air oxidation [133]. After detonation and the different purification steps, nanodiamonds naturally present three different layers [135]:

- A diamond core, containing 70-90% of the total carbon atoms;
- An intermediate layer of amorphous carbon, containing 10-30% of the total carbon atoms;
- A surface layer composed of diverse functional groups, mainly carbon, oxygen, hydrogen and nitrogen.

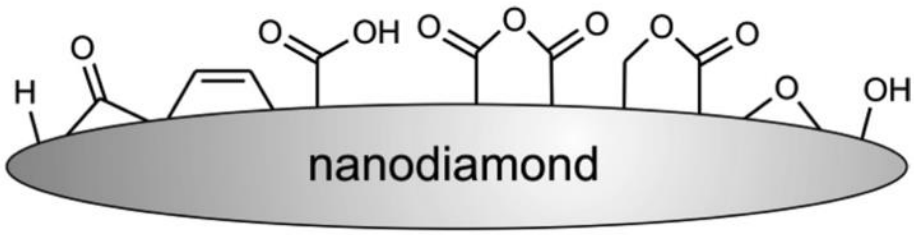

Figure 2.3-2: Surface terminations of detonation nanodiamonds. From Ref. [133]

The nitrogen atoms can be found equally in the three different layers, while the oxygen and hydrogen atoms are most commonly found on the surface layer.

HPHT nanodiamonds present a relatively low concentration of carboxyl groups, compared to detonation ones (≈2 %). Instead, ND-HPHT surface is dominantly populated of hydroxyl groups [136]. The surface functionalization will then be different from DND.

Apart from natural functional groups found after the detonation synthesis and purification steps, the surface of the nanodiamonds can also be modified at will, depending on the application. Two different families of treatment can be distinguished: wet [90] and gas [91] chemical treatments.

2.3.2.2. Wet chemical treatments

Wet chemical treatments are made from successive chemical baths and are purely chemical reactions creating new functional groups at the surface of NDs. Acidic treatments are typical

wet treatments allowing the saturation of the surface layer with carboxyl functions, that appear after nitric (HNO_3), sulphuric (H_2SO_4) or chlorhydric (HCl) acid baths [137], or a mix of the three solutions [104]. Carboxyl groups can also be created by hydrogen peroxide (H_2O_2) treatments, such as the so called "piranha" treatment (hydrogen peroxide and sulphuric acid) [138]. Chemical reduction can also be done after carboxylation, by using reducing compounds, such as borane (BH_3) or hydrures ($LiAlH_4$) [139,140], in order to obtain hydroxyl groups at the surface.

Nanodiamonds with O–H terminations are involved in esterification with acylchlorides yielding ND terminated by long alkyl chains and in silanization [110].

A DND solution of NanoAmando® (NanoCarbon Institute, Japan) was kindly provided by Prof. Eiji OSAWA, at a high stock solution concentration of 20 mg/mL, with a nominal primary particle size of 3.1±0.6 nm and a positive zeta potential of +46.2 mV. The method of cationization will be presented in more details in Section 4.2. Briefly, the positive zeta potential originates from a succession of reduction reactions.

This ultra-small size is a key asset for biomedical applications, as the main concern of the use of nanoparticles is their fate in the body. Thanks to this ultra-small primary particle size, we expect renal clearance and facile excretion from the body.

2.3.2.3. Physico-chemical gas treatments

Physico-chemical modifications with a gas are generally performed under the assistance of microwave plasma or by heating in an oven. One of the major advantage of these techniques is that there is no need for extensive washings after the treatment, contrary to wet treatments. Furthermore, gas that are utilized are pure and thus avoid contamination from other chemical reactives or sub-products coming from the reaction.

Both dry hydrogenation treatments were tested during this PhD project and were realized by Jean-Charles ARNAULT's and Hugues GIRARD's team at the Diamond Sensors Laboratory of CEA-LIST Saclay (Gif-sur-Yvette, France) for plasma-assisted hydrogenation and by Emilie NEHLIG in Gregory PIETER's team at the *Laboratoire de Marquage par le Tritium of Institut des sciences du vivant Frédéric Joliot-CEA Saclay* for hydrogenation by annealing. More details about these methods of hydrogenation used for our application will be presented in Section 4.1. Briefly, these surface treatments allow the removal of non-diamond carbon phases, the elimination of oxygen groups and the formation of C-H terminations on nanodiamond surface [91].

The plasma-assisted and annealing treatments can be made under several atmospheres, such as fluorine [141,142], chlorine [143] or ammonia [144]. The use of these gas induces at the surface of NDs fluorine, chlorine and amine groups, respectively.

Our application required cationic charges at the surface of NDs, plasma and annealing treatments were then made under hydrogen atmosphere on detonation nanodiamond powders [91]. The carboxylic acid groups (COOH groups) present at the surface of NDs were then reduced and oxygens removed leading to hydrogenated diamond [110].

The different surface modifications presented allow the homogenization of the chemical groups located at the surface of ND. The functionalization is then eased and a great variety of grafting, in a covalent or non-covalent manner, can be made.

2.3.3. Grafting functional groups on ND surface

Surface functionalization of nanodiamonds confers new properties and allows new applications. Different grafting routes can be explored, depending on the terminations present at NDs surface and on the molecules that need to be attached to them. There are two main functionalization techniques, as recently detailed by NEBURKOVA *et al.* in [42], for synthetic (*e.g.* polyethylene glycol (PEG), methacrylate derivatives, polyglycerol (PG)) and natural (proteins, polysaccharides, nucleic acids) polymer coatings:

- **Covalent coating**: creates stronger and better-defined bounds between the molecules and ND surface [133]. A distinction should be made between "grafting to" and "grafting from" approaches, represented in Figure 2.3-3. "Grafted to" coatings are synthetized separately from the nanoparticle and then attached *via* covalent binding. In "grafted from" techniques, the polymerization occurs directly at the surface of nanodiamonds. This approach leads to denser and better protecting coatings than "grafting to" approach [120]. Covalent coating of polymer, *e.g.* polyethylene glycol (PEG), is generally realized via amination [145] or esterification [146] reactions.

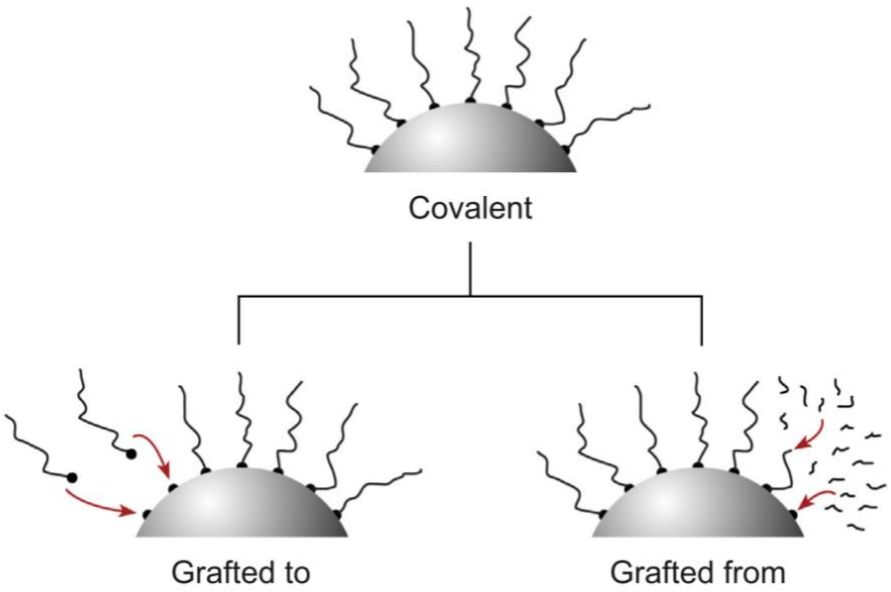

Figure 2.3-3: Polymer covalent grafting. Distinction between "grafted to": polymers are attached to a present surface group; and "grafted from": elongation of the polymer from the surface. From Ref. [42]

- **Non-covalent coating** though electrostatic, hydrophobic, hydrophilic or Van der Waals interactions [42]. This grafting approach is readily made and it allows the immobilization of various proteins (cytochrome c [147], bovine insulin [148] or lysozyme [149]), drugs (doxorubicin [150]) and polymer coating (polyethylene-imine (PEI) [151], poly(allylamine) hydrochloride (PAH)), acting as a shell around NDs or to dispose of new functional groups at their surface and then graft other compounds such as nucleic acids [152].

The method of cationisation tested during this PhD project relied on fluorescent HPHT nanodiamonds that were first covered by a thin silica shell on which a synthetic cationic copolymer has been covalently grafted. This approach will be described in more details in Section 4.3.

Nanodiamonds present the great advantage that they can be functionalized by a broad variety of not too complex methods, conferring very interesting characteristics to the nanoparticles. The next subsection will now present the different biomedical applications, for which nanodiamonds are used.

2.4. Biomedical applications of nanodiamonds

2.4.1. Biocompatibility and biodistribution of nanodiamonds

Nanodiamonds present interesting features, highly suited for various biomedical applications, including a high biocompatibility[d] and a low cytotoxicity. Indeed, several studies showed that nanodiamonds, produced by detonation [153] or HPHT [154] synthesis, have a very limited toxicity, and even no genotoxicity on *C. Elegans* [155]. Nevertheless, complementary experiments would need to be undertaken, first to assess the activation of the complement but also to assess if the presence of ND on cells would induce the production of deleterious products, mostly originating from the surface groups. Note that a study showed that detonation diamonds, hydrogenated under plasma, induced an increased production of hydroxyl radicals under X-ray radiations [156]. It is important to highlight that the surface terminations greatly influence the cytotoxicity, the oxygen-terminated nanodiamonds presenting the highest biocompatibility, compared to H-terminated NDs [157]. Long-term (6 months) *in vivo* studies using detonation NanoAmando® solution (NanoCarbon Research Institute Ltd., Japan) that have been conducted on a non-primate and a rat models [94] showed that for two different doses (15 mg/kg and 25 mg/kg) injected intravenously, no side effects were observed and no dysfunction of any organ appeared. These results confirm *in vitro* studies and demonstrate that nanodiamond is suited for biomedical applications, as a drug delivery agent for instance.

Nanodiamond biodistribution have also been assessed on rodents models, at various time-scales and with various injection routes [158,159]. These studies were mainly conducted with detonation nanodiamonds, displaying various sizes and surface functionalization.

Table 2 summarizes the results obtained.

Table 2: Rodent biodistribution studies of nanodiamonds, established with various detection methods, for different sizes of NDs, at different time-points.

Type of ND	Injection route	Method of detection	Size of injected NDs	Time-scale	Organ of accumulation	Ref.
^{188}Re-	Intratracheal	Radioactivity	2-10 nm	24h	Lung, spleen, liver,	[159]

[d] **Biocompatible**: "compatible with living cells, tissues, organs, or systems, and posing no risk of injury, toxicity or rejection by the immune system". From Mosby's Dental Dictionary, 2nd edition (Elsevier, Inc., 2008).

DND	instillation	measurement	(before injection)	48h	urine	
^{18}F-DND	IV injection	Radioactivity measurement	7-20 nm (before injection); actual size when injected: 300-680 nm	2h	Bladder (small sizes of NDs), lung, liver, spleen. Macrophages of the RES	[160]
^{125}I-DND	IV injection	Short-term assay: Radioactivity measurement. Long-term assay: Raman spectroscopy, UV-Vis absorption.	50 nm	0.5h up to 28 days	Liver (RES), lung, spleen	[158]
^{99}Tc-DND	IV injection	Radioactivity measurement	20-30 up to 220 nm	24h	Liver, spleen, lung. Urine: between 0 and 10h.	[161]

This table shows that the nanodiamonds, displaying sizes between 20 and 700 nm, preferentially accumulate in the liver (in macrophages, *i.e.* the Kupffer cells, that are part of the reticuloendothelial system), the lung and the spleen. Interestingly, short-term analysis shows that the excretion through the urine is made pretty rapidly, typically within 10 hours, and favors the excretion of small-sized DNDs. I will demonstrate in Chapter 5 that we observed a similar trend as the one reported in

Table 2 with both radiolabeled DND and fluorescent HPHT NDs.

2.4.2. Nanodiamonds as a drug/gene delivery platform

As presented in Subsection 2.3.2, the surface of nanodiamonds can be modified and functionalized, allowing to use them as delivery agents.

The different surface groups obtained after the purification steps allow an electrostatic grafting of oligonucleotides or drugs. This basic method was used with the commercial solution of NanoAmando® during this PhD project, and has already been used for the efficient delivery of water-insoluble anti-cancer drugs [150]. Dean HO and Eiji OSAWA used carboxylated nanodiamonds (surface terminations COOH/COO^-) in an aqueous suspension to adsorb doxorubicin (DOX) ions (DOX-NH_3^+) [162] at their surface. The electrostatic

interaction between ND and DOX seems straightforward, nevertheless, an addition of salt was necessary to obtain an enhanced loading (0.5 wt % without salt versus 10 wt % adsorption when salt was added). This “basic” grafting allowed an apoptosis-inducing mechanism driven by the DOX-functionalized ND, on colorectal adenocarcinoma cells.

The same process was used for gene delivery, using a first layer of 800 Da PEI, adsorbed by polar interactions through hydrogen bonding and through electrostatic interactions, on which negatively charged DNA has been immobilized onto positive charges of ND-PEI800 via electrostatic interactions [163], a strategy that was developed in parallel for HPHT ND in our groups [152,164].

In order to efficiently direct the treatment towards desired cells, an active targeting can be implemented, using, among other routes, surface antigens, carbohydrate receptors or transferrin receptors. To this aim, a physical adsorption at the surface of FND of (neo)glycoproteins was made for targeting hepatocytes via carbohydrates receptors [145]. This method was compared to a covalent grafting of streptavidin. This grafting was done in two steps: (i) reaction of the FND carboxyl groups on the amino groups of NH_2-PEG-COOH; (ii) reaction of the carboxyl groups of HOOC-PEG-FND with the primary amine groups (-NH_2) of streptavidin (SA). In both amide bond formation [145], leading to the formation of SA-PEG-FND, to which biotinylated antibodies were conjugated. The study showed that the targeting by one or the other approach induced a specific hepatic cell labeling, offering interesting opportunities to direct drugs to their target with the FND complex. Such combination was realized successfully, by using transferrin covalently conjugated to FND and the addition of doxorubicin anticancer drug, which was physically adsorbed onto the FNDs [146].

Furthermore, a successful covalent attachment of paclitaxel (PTX), anti-cancer drug, was obtained thanks to the use of thiolated drug-oligonucleotides conjugates that was attached to the aminated surface of ND (ND-NH_2) [165]. This complex, combined with thiolated antibody also grafted at the surface of ND, allowed to improve the therapeutic index of PTX [165] on breast adenocarcinoma, and to preserve the mitotic blockage, the apoptosis induction and the anti-tumorigenesis properties of this drug in lung carcinoma cells [166].

2.4.3. Nanodiamonds as a therapeutic potentiator

CHEVILLARD *et al.* demonstrated that hydrogenated nanodiamonds could be used for their negative electronic affinity, *i.e.* photo-emission of low-energy electrons, when irradiated by

ionizing radiations [167]. Indeed, the combination of H-ND, irradiations and dioxygen lead to an increase level of Reactive Oxygen Species (ROS), thus inducing an increased and sustained DNA damage [167]. The potentiating effect of H-ND in forming ROS may allow to reduce the irradiation dose in radiotherapy or/and to circumvent the resistance of certain cells.

More and more complex functionalizations are realized, conferring ND various characteristics. As an example, REHOR *et al.* realized in Ref. [168] a very complex hybrid material, as presented in Figure 2.4-1. This nanostructure is composed of a plasmonic silica-coated nanodiamond core, encapsulated in a gold shell. The latter can be heated through optical excitation at surface plasmon resonance, allowing to thermally ablate cancer cells. The PEG layer confers stealth to the gold-ND structure, thus reducing opsonization. Finally, the grafting of the Alexa Fluor 647 and of the azide-modified Transferrin, acts as labeling and targeting moities, respectively. This platform then combines therapeutic capabilities, with gold shell, allowing to enhance cancer cell thermoablation, complemented with targeting capacity of Transferrin, and the localization component of Alexa Fluor 647, making it a perfect example of an effective therapeutic potentiator and theranostic agent.

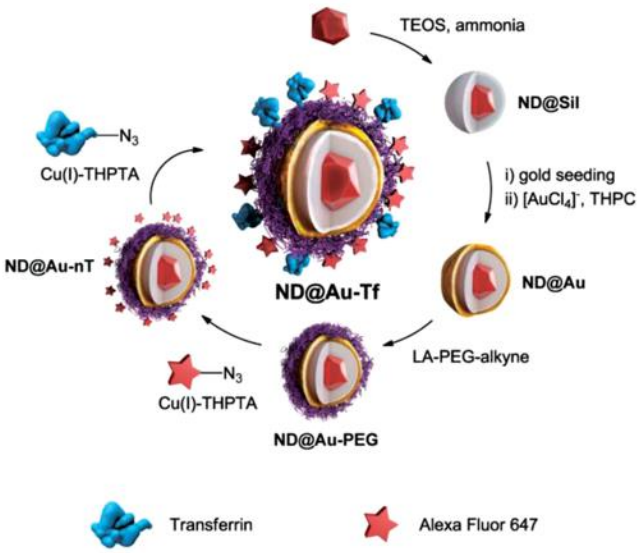

Figure 2.4-1: Schematic representation of the functionalization of ND with different layers. Abbreviations: TEOS: tetraethyl orthosilicate; Sil: silica; THPC: Tetrakis(hydroxymethyl) phosphonium chloride; PEG: polyethylene glycol; THPTA: tris(3-hydroxypropyltriazolylmethyl) amine; Tf: Transferrin. From Ref. [168]

2.4.4. Exploiting the fluorescence of nanodiamonds

A majority of applications take advantage of the fluorescence of NV centers embedded in nanodiamonds. NV center photostability and nanodiamond's very low toxicity represent

significant advantages for biomedical applications, compared to organic dyes or quantum dots, two other nanodevices also commonly used (Table 3).

Table 3: Comparison of fluorescent ND to organic dyes and quantum dots, regarding properties relevant in biomedical applications. FND values are given for NV defects.

PROPERTY	ORGANIC DYES	QUANTUM DOTS	FNDs
SIZE	<1 nm	3-10 nm	From 3 nm [93]
EMISSION SPECTRUM	IR-UV	IR-UV, selected by size	IR, selected by the defect
EMISSION LINE WIDTH (FWHM)	35-100 nm	30-90 nm	Mostly >100 nm [169]
ABSORPTION CROSS SECTION	Typically $1x10^{-16}$ cm²	Typically $3x10^{-15}$ cm²	Typically $1x10^{-16}$ cm² [170]
QUANTUM YIELD	0.5-1.0	0.1-0.8	0.1-0.9
LIFETIME	1-10 ns	10-100 ns	30 ns [171]
PHOTOSTABILITY	Low	High	Extremely high [169]
THERMAL STABILITY	Low	High	Extremely high [172]
TOXICITY	Medium to high	High	Low [173]
COMMERCIALIZATION	Yes	Yes	Yes[e]

Application of FND to whole organisms imaging:

As mentioned in Subsection 2.2.3, common imaging techniques used for FND detection and observation are confocal microscopy [145], integrated scanning Electron Microscopy and cathodoluminescence, allowing to excite fluorescence using a focused electron beam [174,175]. Stimulated Emission Depletion (STED) microscopy also offers imaging of NV centers with a resolution as low as ≈10 nm, well below the diffraction limit. Unfortunately, these imaging techniques cannot be easily extended to imaging through "thick" tissue, due to their auto-fluorescence. To circumvent this hurdle, time-delayed fluorescence imaging, described in Subsection 2.2.3, can be used. This technique, combined with the perfect photostability of FNDs, has allowed, in particular, to trace the intracellular transport of proteins in living *Caenorhabditis elegans* worms [126], as presented in Figure 2.4-2. They

[e] Sold for example by FND Biotech (Taiwan), Adamas Nanotechnologies (Raleigh, USA) and CymarisLabs (Columbus, USA).

showed that FND could be employed as a photostable fluorescence nanoprobe for long-term *in vivo* imaging, in living whole organisms.

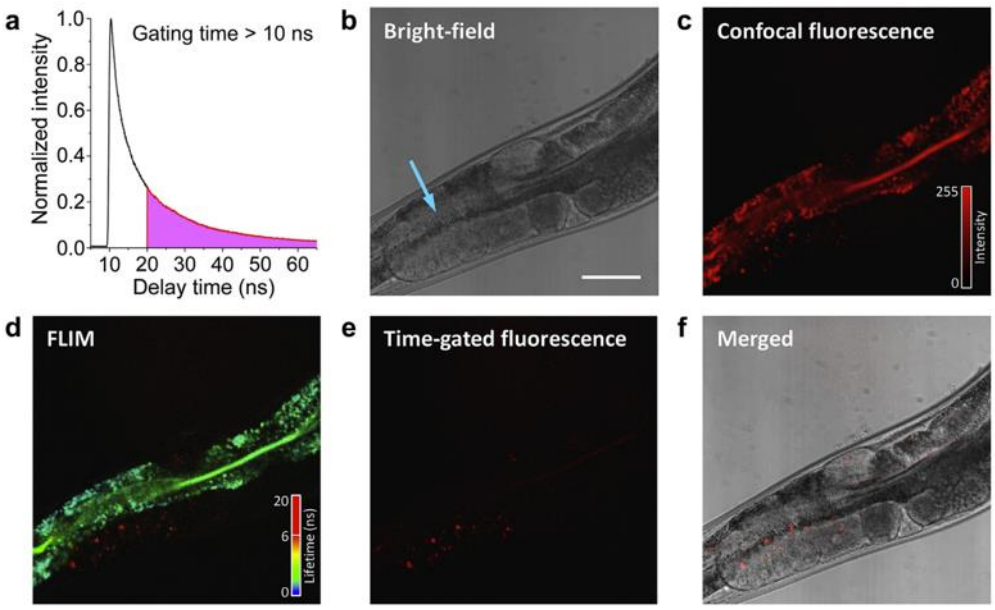

Figure 2.4-2: Observation of GFP:YLC-FNDs in C. elegans by different imaging techniques. (a) Fluorescence decay time trace of 100-nm FNDs suspended in water. The magenta area represents the fluorescence signal collected at the gating time longer than 10 ns. (b) Bright-field, (c) Confocal fluorescence, (d) FLIM, (e) time-gated fluorescence, gating time > 10 ns, (f) merged bright-field and time-gated fluorescence images of a worm microinjected with GFP:YLC-FNDs at the distal gonad. Scale bar: 50 µm. Abbreviation: YLC: yolk lipoprotein complexes; FLIM: Fluorescence-Lifetime Imaging Microscopy. From Ref. [126]

Long term tracking of whole cells:

By using the same property of very long photostability, FNDs have also been used to label whole cells, taking advantage of the efficient cellular uptake and the very low toxicity. This strategy allows to track the labelled cells for a long period of time, even in an organism. To this aim, sized ≈130 nm FNDs have been used to render different cancer cell lines fluorescent [176] with a perfect stability owing to the low exocytosis and photostability of FNDs. By using a microfluidic circuit combined with time-gated fluorescence microscopy, HUI *et al.* [127] were able to image, with a large signal/background ratio, individual FND-labeled cells circulating in whole blood. Moreover, these cells could also be detected in a mouse ear blood vessel *in vivo* after injection in its caudal vein.

FNDs were also used to label quiescent cancer stem cells (CSCs) for their subsequent tracking. CSCs are suspected to be responsible for tumor initiation, growth and recurrence [177]. The study of these cells is not easy, and the use of classical fluorescent dyes does not allow the tracking over a long period of time. Using a mammosphere assay, LIN *et al.* observed that even after 20 days, FNDs could still be detected in a subpopulation of cells, corresponding to slow-proliferating/quiescent cancer stem cells, labelled with FNDs [178].

Intracellular process studies:

Beside whole cell labeling, FNDs can be of interest to track intracellular processes such as endosomal transport. The intraneuronal transport parameters were measured by tracking FND internalized in endocytotic vesicles [179]. This study has shown that the perfect photostability, the high brightness and the very low toxicity of FNDs allow to sense the impact of very small protein concentration changes in relation with neurodegenerative diseases.

2.5. Conclusion of Chapter 2

In this chapter, I have presented the main physico-chemical properties of nanodiamonds, essential for a biomedical application. We have focused on their non-toxicity and their versatile surface chemistry modification, allowing to use them as vectors for drugs, nucleic acids or as theranostic agents.

We also have emphasized that the fluorescence from embedded Nitrogen-Vacancy defects has a perfect photostability that can be exploited to track over a timescale of a few days and in whole organisms, the engraftment of stem cells, or the spread of cancerous cells.

Given all of these outstanding properties, nanodiamond is an attractive platform for many other biomedical applications. Several studies demonstrated their long-term non-toxicity. It seems that they are preferentially taken up by the reticuloendothelial system, in the macrophages of the liver, the lung and the spleen. It has also been demonstrated that small-sized NDs were easily excreted through urine.

Various synthesis processes are available to produce nanodiamonds, I have used and compared four of them during this PhD thesis, for our application as a siRNA delivery platform to Ewing Sarcoma cells and tumor: (i) plasma-assisted hydrogenation, (ii) hydrogenation by annealing, (iii) cationisation by successive chemical processes, (iv) cationisation by the covalent binding of a copolymer onto FND surface. As it will be

presented later in this manuscript, the most efficient one was the last, with which we have made a quantification of the biodistribution in organs of mice.

The next chapter presents the targeted disease of this study: Ewing Sarcoma. I will first propose a general description of cancer, and then focus on Ewing Sarcoma's characteristics and the challenges of its treatment. Finally, I will present the new treatment that is currently developed, relying on siRNA, which needs to be vectorize.

CHAPTER 3

Presentation of the targeted disease, Ewing Sarcoma, and of the inhibition strategy with siRNA

Before introducing Ewing Sarcoma, the disease targeted by the work of this PhD project, this chapter will first briefly describe the hallmarks and characteristics of cancer, to better understand this major illness. Then Ewing Sarcoma will be described, and its main treatments will be presented. Finally, the treatment strategy of this project, using siRNA, will be introduced.

3.1. Cancer: the disease of the 21st century

Cancer is one of the most spread disease and is among the leading cause of death in the world (8.2 million in 2012 [180]). It exists more than a hundred types of cancer and even more subtypes of tumors can be described [181].

Cancer is caused by a series of deregulations, as described in Figure 3.1-1, which cannot be considered as individual and static targets. On the contrary, it is more accurate and essential to describe and consider them as complementary, codependent and responding to an evolutionary dynamic [182].

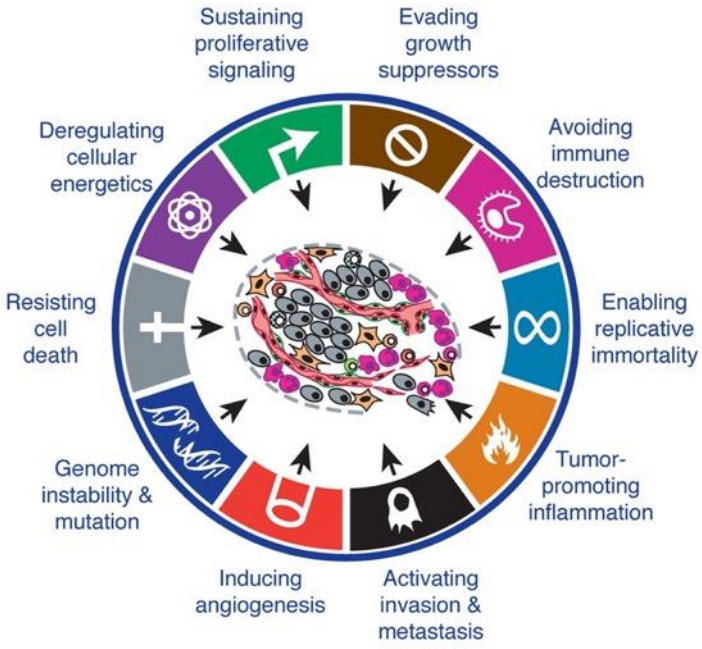

Figure 3.1-1: Acquired hallmarks of cancer. From Ref. [183]

Within the previous figure, one can distinguish six hallmarks that were described in a first review [181]:

- Sustaining proliferative signaling: ability of cancerous cells to multiply indefinitely, without the trigger and signal from extracellular matrix components;
- Evading growth suppressors: normal tissue receives multiple anti-proliferative signals to maintain cellular quiescence and tissue homeostasis, cancerous cells evade these signals and proliferate;
- Resisting cell death: classical programmed cell death, apoptosis, signal is disabled in cancerous cells;
- Enabling replicative immortality: in addition to growth suppressors, apoptosis evasion and to autonomous growth triggers, senescence of cancerous cells is disabled, thus inducing an infinite replication of the cells;
- Inducing angiogenesis: creation of new blood vessels is facilitated in the tumor micro-environment, when it is normally regulated in healthy tissues;

- Activating invasion and metastasis: ability of cancerous cells to escape the primary tumor site and colonize new tissues in the body. In 1996, metastases were the cause for 90% of human cancer deaths.

Two additional emerging hallmarks were later described by HANAHAN and WEINBERG in Ref. [183]:

- Deregulating cellular energetics: expansion of the tumor environment requires an increased energy consumption and cancerous cells show amazing characteristics to circumvent unfavorable conditions such as anaerobic conditions;
- Avoiding immune destruction: it is not yet well understood which percentage of solid tumors escape detection from the immune system nor how many of them can limit, in some extent, immunological killing, thereby circumventing eradication.

In addition, two enabling characteristics, complementary to the cancer hallmarks, were also described in the later review:

- Genome instability and mutation: the various hallmarks described above mainly rely on a succession of alterations of the genome, only possible after a breakdown in one or several components of the genomic integrity maintenance machinery and/or an increased sensitivity to mutagenic agents;
- Tumor-promoting inflammation: pathologists have showed that tumors were infiltrated by both innate and adaptive immune systems cells, first thought to be an immune response to the invasion of cancerous cells. But it later paradoxically appeared that it was not only an immune response but that it also enhanced tumorigenesis and progression.

As demonstrated, all characteristics have to be taken into account globally and not as individual parameters. The described parameters occur at the molecular level, when one look at a more global scale, one can observe that incidence of cancer is also due to three identified triggers:

- Environment: for instance, the increased exposure to air pollution has been linked to an increasing occurrence of lung cancer [184], among other diseases. Also, endocrine disruptors, commonly found on everyday products, have been declared as carcinogens [185];

- Lifestyle: tobacco, alcohol and dietary have been linked to various cancers, among which we can obviously cite lung cancer, liver and colon cancer [186];
- Genetics: some gene alteration can be passed to offspring, but also genetic predisposal to develop certain types of cancer. The *BRCA1* gene is a well-known inherited mutation, inducing a 70% lifetime risk for developing breast or ovarian cancer [186].

Cancer treatment is a very important field of research and development and historically includes the use of chemotherapies, radiotherapies and/or surgery. A growing interest has developed in the last decade over the very promising immunotherapies combined to classical chemotherapies, for a better specificity and efficacy of the treatment.

My PhD project focused on a specific type of pediatric cancer, Ewing Sarcoma, a rare bone cancer, which treatment has not evolved much over the last decades. The following sections will present this cancer, its epidemiology and treatments, and finally will present how this PhD project can lead to an improvement of the disease management.

3.2. Introduction on Ewing Sarcoma

3.2.1. Incidence and epidemiology

Ewing Sarcoma is the second most frequent pediatric primary bone cancer [187], representing about 5% of all child and teenagers cancers [188]. It most occurs in children and young adults, mainly appearing in the second decade of life: approximately 80% of patients diagnosed with Ewing Sarcoma are younger than 20 [189,190], with a median observed at 15 years old. Some patients are over 30 or very young but few data are available for this population. It has been observed that Caucasians were more affected than Asians and Africans, and that males were more affected than females (55:45 ratio) [189]. It was determined that between 1973 and 2004 in the United States, Ewing Sarcoma had occurred in 2.93 child over 1,000,000 [188], thus classifying it as a rare cancer.

3.2.2. Diagnosis

Detection of this cancer is characterized by extreme bone pain, the presence of a mass along the bone, extreme fatigue, unexplained weight loss and intermittent low-grade fever. Magnetic Resonance Imaging is the standard of care for primary tumor detection. As presented in Figure 3.2-1-(a), the mass of the tumor is clearly visible with this imaging modality. PET and CT are also very used methods for the diagnosis of primary tumor in soft

tissues and for metastases localization. Histomorphology, immunohistochemistry and molecular pathology are also conducted on biopsies.

Figure 3.2-1-(b) shows the invading aspect of this cancer on the bone. The picture clearly shows that the tumor grows from the bone and one can understand better the detected mass on MRI or PET scan.

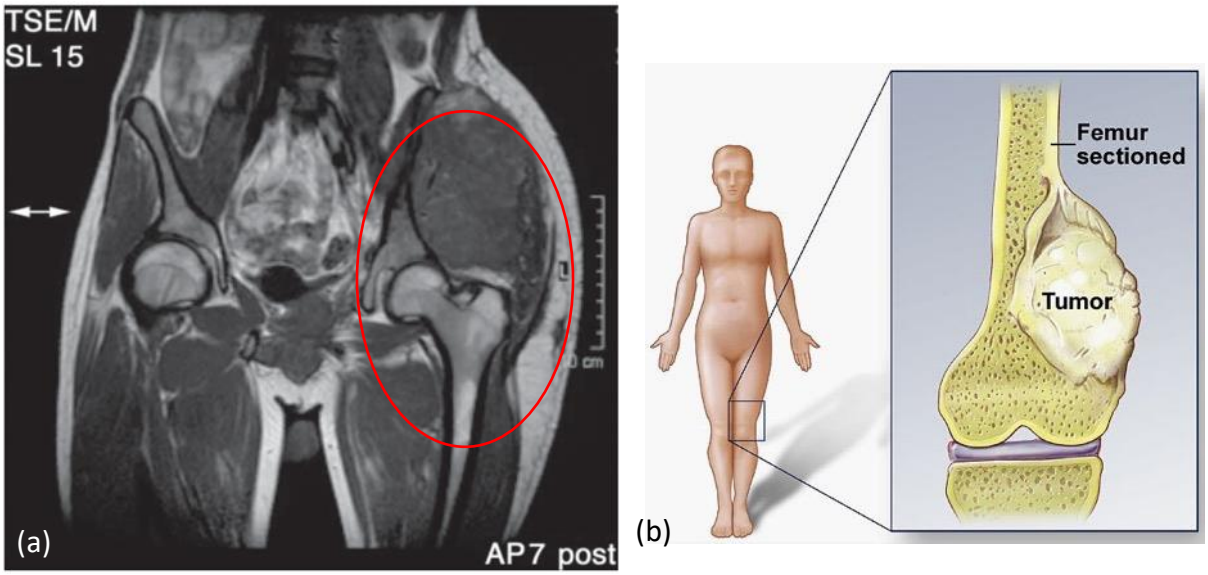

Figure 3.2-1: (a) Magnetic Resonance Image of a pelvic presenting Ewing Sarcoma mass on the left hip. From [187].*(b) Ewing Sarcoma tumor on a femur. From Mayo Foundation for Medical Education Research*

Lower extremities such as pelvis, femur, fibula, tibia or foot are the main primary tumor sites with 44% of occurrences [189]. Then comes the chest wall (23%) and the upper extremities. Ewing sarcoma is classified as a bone cancer but it also can appear in soft tissues, indeed 15% of Ewing Sarcomas arises in soft tissues [188], making its histogenesis poorly defined. When they occur, metastases mainly appear near the central primary tumor (40%), then in the proximal placement of the primary tumor (30%) and finally in the distal placement of the primary tumor (15%). Metastases can also spread to lung and bone marrow. About 25% of the patients are diagnosed with primary metastases, always presenting a low survival rate. Figure 3.2-2 summarizes the different occurring sites of primary tumor and metastases.

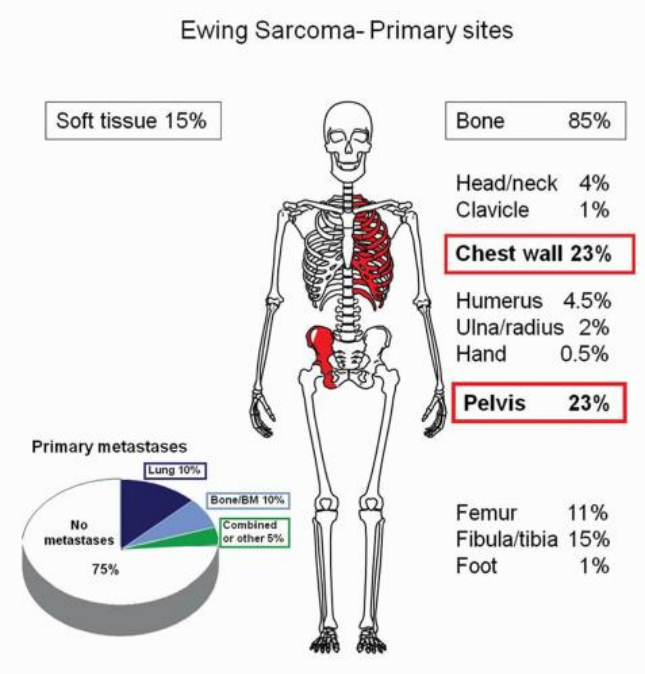

Figure 3.2-2: Ewing Sarcoma primary tumor and metastases sites. Primary tumor occurs in 85% of cases in bones, preferentially in the chest wall, in the pelvis and in the long bones of the lower part, and in 15% in soft tissues. Adapted from Ref. [187]

3.2.3. Current treatments of Ewing Sarcoma

This type of cancer has a quite good survival rate, near 70% [191], when the cancer is detected with no metastasis. Unfortunately, this survival rate falls at 20-30% [189], when diagnosis occurs after the spreading of metastases. Current treatment involves a systematic chemotherapy combined with either radiotherapy or surgery.

3.2.3.1. Local treatment: surgery and radiotherapy

Surgery and radiotherapy are used for a local control of the primary tumor. Surgery is preferred if the tumor is resectable after chemotherapy [190] but often implies amputation of limbs or resection that only delays the amputation. Radiotherapy has a larger area of action but is less specific to the tumor site and thus can induce secondary cancers such as leukemia. It can be given alone in case of tumors that are located in unfavorable locations (*e.g.* vertebral tumors) or that are too large to be resected by surgery. In those cases, it has been showed that patients had a poor prognosis and that in 26% of the patients treated with radiotherapy only, local and systemic failures were observed [187].

3.2.3.2. Chemotherapy

Systematic chemotherapy is used to treat primary tumor and distant metastases. The first drug investigated was cyclophosphamide, which was then combined with vincristine and radiotherapy, showing an outstanding result on five patients in 1968. Then began the modern multi-modality treatment of Ewing sarcoma. In 1974 the association of four drugs (vincristine, actinomycin D, cyclophosphamide, and doxorubicin) [188], the VACD scheme, was tested in combination with radiotherapy. This multi-modal therapy showed a great improvement of the survival rate in the patients tested. Indeed, this first trial showed an overall improvement of about 10% (96% vs. 86%) in terms of effectiveness of local control and of about 35% in event-free survival (60% vs. 24%) [187] compared to a three-drug regimen. More recently, it has been added two other drugs to this combination, Ifosfamide and Etoposide, given alternatively with the VADC scheme. This complement having showed its actual benefit in improving the survival rate, it is now considered as the standard-of-care in North-America [187].

Although this course of treatment greatly improved survival rates of the disease, the four drugs used induce adverse effects. Ifosfamide (IFO) has been extensively studied by Angelo PACI's team at UMR8203 in Gustave Roussy [192] to reduce the side effects induced by its use. This particular compound has been showed to induce urotoxicity, nephrotoxicity, encephalopathy, cardiotoxicity and neurotoxicity [193,194] in about 20% of patients.

The other prescribed compounds also induce side effects such as hair loss, inflammations, tissue damage at the site of injection, heart damage and peripheral neuropathy. All are more or less severe adverse effects, but none are equivalent to the long-term side effects as the urotoxicity and nephrotoxicity induced by Ifosfamide [193].

3.2.4. *EWS-Fli1* translocation as a target site for an innovative and personalized treatment

Fusion genes play a major role in certain types of cancer, particularly in sarcomas and leukemias [195]. Three types of fusion can occur: (i) an interstitial deletion, (ii) a chromosomal inversion or (iii) a translocation. The first is a mutation that leads to the loss of a part of a chromosome and thus to the deletion of a DNA sequence. This fusion type leads to genetic disorders, that are more or less fatal depending on the portion of gene that is deleted. For instance, the deletion of the interstitial genes between *TMPRSS2* and *ERG* promotes the progression of prostate cancer [196]. The second fusion type occurs when a portion of a

chromosome is inverted or rearranged within itself. This type can cause serious disorders, even if no DNA sequence is lost. In oncology, the EML-ALK fusion occurs after an inversion of chromosome 2p [Inv(2) (p21p23)] and presents an potent oncogenic activity, being one of the cause for Non-Small-Cell Lung Carcinoma emergence [197]. The third one is an abnormal rearrangement of parts of two fractured non-homologous chromosomes, on the same or on two different chromosomes, followed by a defective repair of those lesions. The newly created nucleic sequence often leads to the activation of oncogenes or the genesis of oncogenic fusion proteins. Two examples can be highlighted: chronic myelogenous leukemia, which is caused by the *BCR-ABL* fusion, and papillary thyroid cancer from the *RET-PTC* fusion [195]. In general, those phenomena interfere with the expression and the right functioning of transcription factors, leading to the deregulation of numerous genes often involved in cell cycle or in maintaining the integrity of DNA.

In the case of Ewing Sarcoma, it has been characterized that about 88-95% of the tumor cells present a characteristic translocation in t(11;22)(q24;q12) [198,199]. As presented in Figure 3.2-3, the 3' portion of the *Fli1* gene from chromosome 11 is translocated to the 5' portion of the *EWS* gene from chromosome 22. This translocation is characteristic from Ewing Sarcoma and the expressed protein plays the role of an aberrant transcriptional activator [200], meaning that it is involved in the over-expression of several genes. Its expression is partly responsible for the healthy cells transformation in tumor cells, and its continuous expression is necessary for tumor cells sustained growth.

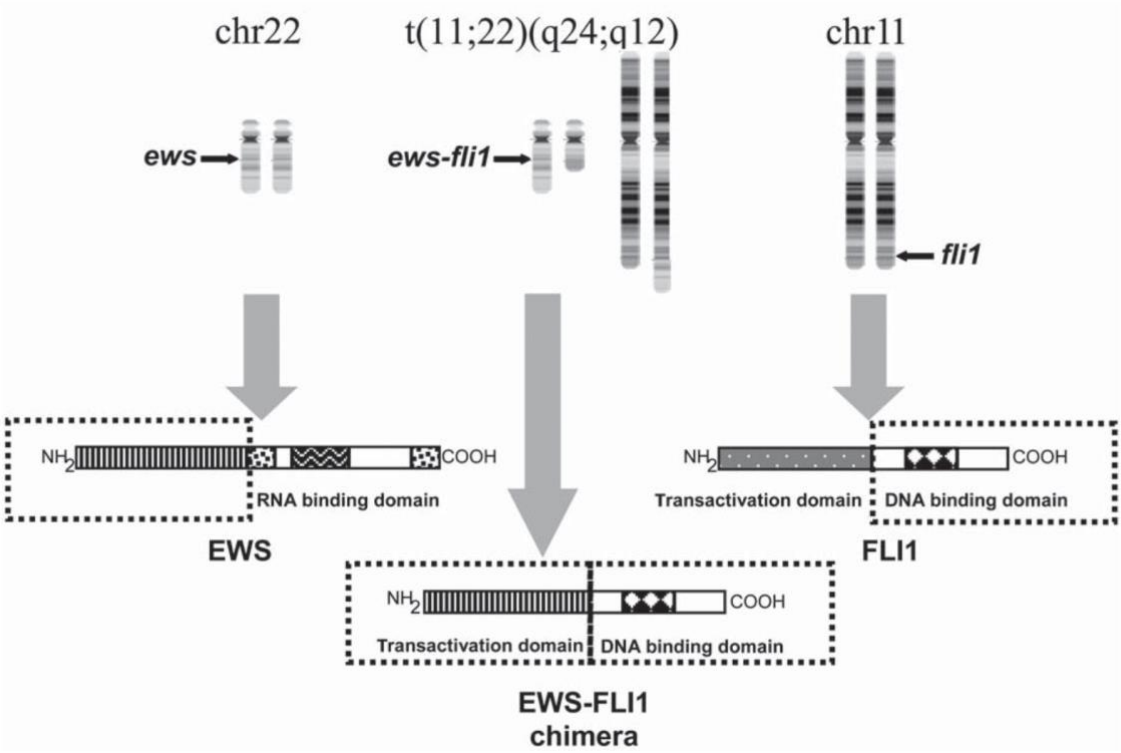

Figure 3.2-3: EWS-Fli1 translocation and oncogene junction formation. Translocation of the 3' portion of the Fli1 gene from chromosome 11 to the 5' portion of EWS gene on chromosome 22. From Ref. [187]

EWS gene encodes for a RNA-binding protein that can combine with components of the basal transcriptional machinery and post-transcriptional RNA processing [201]. It has been observed that mice with non-expressed *EWS* gene present a deficiency in homologous recombination and recombination repair. *Fli1* gene encodes for a member of the erythroblastosis transforming-virus-1 (ETS) transcription factors family, one of the largest families of transcription factors, often playing a role in cancer proliferation. It is important to note that *Fli1* gene can be substituted by another member of the ETS transcription factors family, such as *ERG*, *ETV1*, *ETV4* or *FEV*. This PhD project only focused on the most occurring case of these proto-oncogene activating translocations: *EWS-Fli1* translocation.

There are many different types of *EWS-Fli1* recombinations depending on the translocation sites of the *EWS* gene and the *Fli1* gene [202]. The most common translocation is Type 1, occurring in 60% of cases [203]. Type 2 is less frequent but still represents 25% of cases and is characterized by a greater clinical "aggressivity" [203]. As presented in Figure 3.2-4, Type 1 is characterized by a fusion between exon 7 of *EWS* to exon 6 of *Fli1*, whereas Type 2 appears after fusion of exon 7 of *EWS* to exon 5 of *Fli1* [204].

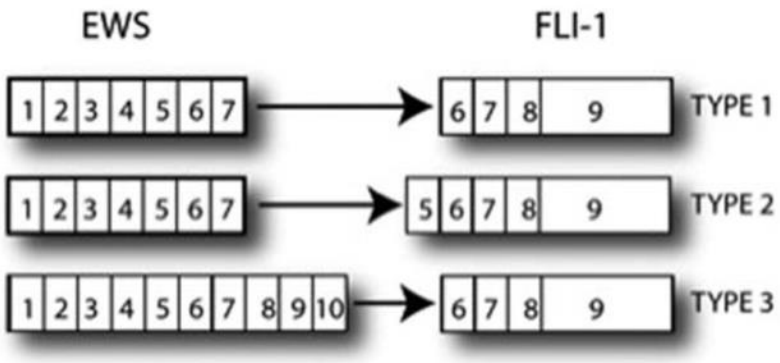

Figure 3.2-4: Schematic representation of the different types of EWS-Fli1 fusions. From Ref. [205]

The Type 1 fusion is the main focus of this project, because the rupture occurs in two introns, leading to the synthesis of mRNA with an homogenous junction sequence after the splicing of the pre-messenger [206]. This feature is more favorable to the design of an anti-sense strand, targeting this junction, and offering a specific targeting of the tumor cells exclusively. Furthermore, the project focused on Type 1 fusion, because it is the most common occurrence of the fusion gene, thus having the largest number of cases. The European project in which we took part also had the ambition to target the Type 2 fusion.

The encoded protein resulting from the *EWS-Fli1* gene is then very specific since the *EWS* RNA-binding domain is replaced by the DNA-binding domain from *Fli1*, thus creating a completely new ETS transcription factor possessing unique features. Indeed, it has been observed that a large number of genes are up-regulated by the fusion protein but also that an almost equal number of genes are constantly down-regulated. In particular, KOVAR *et al.* [201] showed that *EWS-Fli1* fusion protein had a double function in oncogenic transformation:

- it down-regulates the apoptosis activity of tumor cells by inhibiting proteins p21 and p53;
- it activates the IGF1 path that enhances cell proliferation.

This ability makes it the first driver of Ewing Sarcoma Family of Tumor (ESFT) oncogenesis and allows the tumor to grow and spread but also to be resistant to several chemotherapies.

3.2.5. Conclusion of Sub-section 3.2

Ewing Sarcoma is a rare pediatric cancer, induced by a specific fusion oncogene: *EWS-Fli1.* It has been mentioned that the conventional treatments of this disease have not evolved over the last three decades, inducing long-term major adverse effects, such as urotoxicity and

nephrotoxicity. Furthermore, Ewing Sarcoma presents a rather good 70% 5-year survival rate when diagnosed with no metastases, but this rate drops at 20-30% when metastases are found along with the primary tumor. New therapies are being studied, such as immunotherapy, in order to improve both long-term patient's live but also to improve the survival rate, in particular when metastases have occurred.

The *EWS-Fli1* fusion gene is highly specific to Ewing Sarcoma cells and it has been demonstrated that it was responsible for the down-regulation of the apoptosis activity, and for the up-regulation of cell proliferation. This specific fusion has thus become a perfect target for gene therapy. Indeed, over the last couple of decades, several teams studied the inhibition of expression of this fusion gene, as a potential therapy, in order to restore the apoptosis signal and to stop cell proliferation.

Our team has work on this gene target since the 2000's, inducing type 1 *EWS-Fli1* inhibition by using antisense oligonucleotides or siRNA, carried by various types of nanoparticles [40,152,207]. This PhD project focused on the use of siRNA to specifically target the fusion gene using a new technology. This technology is presented in the next section.

3.3. Gene silencing: a variety of tools

Gene silencing refers to the mechanism by which the expression of a specific gene is disabled, which can occur at different phases of the cell replication process. Indeed, cellular phenomena enable the silencing at the transcriptional or post-transcriptional levels but also during meiosis. Either way, it always results in the inhibition of the expression of the targeted gene encoded, and thus to the inhibition of the production of the associated protein. This phenomenon can be induced by natural agents such as viruses or transposons, but also by specifically engineered compounds. The later will be the main topic of this Section.

Gene silencing was for the first time observed in 1990 by the plant biologist Richard JORGENSEN and his team [208]. They indeed witnessed a post-transcriptional gene silencing during one of their experiments on petunia flowers. A purple pigment-producing transgene was supposed to deepen flowers' color when instead it whitened them or made appear a lack of pigmentation. This silencing phenomenon has been later more thoroughly described by FIRE, MELLO and colleagues in nematode worms, explaining the phenomenon behind gene silencing by showing that an endogenous double strand RNA (dsRNA) was responsible for gene silencing under a mechanism that they called Ribonucleic Acid interference (RNAi) [209].

There are several ways to silence or control the expression of a gene at the post-transcriptional level, among which oligonucleotide (ODN), ribozymes and RNAi. The main characteristics of each are summarized in Table 4. RNAi can be divided into four main categories: small interfering RNA (siRNA), micro-RNA (miRNA), short-hairpin RNA (shRNA) and piwi RNA (piRNA). Note that there are other types of RNAi, but they will not be detailed in this manuscript.

Table 4: Comparison of different silencing tools. Abbreviations: nt: nucleotides.

EFFECTOR	STRUCTURE	SILENCING MECHANISM	STABILITY IN SERUM	TRAITS	REFERENCES
ODNs	18-25 nt RNA or DNA; single-stranded	Binds to mRNA, RNaseH degradation or steric blocking mechanism	Few minutes if no chemical modifications	Less specific and efficient than siRNA	[210–212]
RIBOZYMES	Catalytic RNA; three helices	Hydrolysis or transesterification catalyze of self or other RNAs	10 seconds to a few minutes	Not stable enough to be used as a therapeutic	[210,212]
siRNA	21-22 nt RNA; double-stranded	Taken up by RISC complex and degradation of the complementary mRNA	Few hours	10 - 100 folds more potent than ODNs	[211,213–215]
miRNA	20-24 nt RNA; single-stranded	Control mRNA degradation and inhibition of its translation	No data	Crucial in animal development	[214,216,217]
shRNA	19-29 nt RNA; double-stranded	Transcripted from a plasmid introduced in the cell into a long RNA and then matured in siRNA	Constitutively expressed in cells, always at high concentrations even when degraded	Constitutively expressed in cells. More cumbersome to use than siRNA	[218–220]
piRNA	29-30 nt RNA; single-stranded	Binds to Piwi proteins that induce silencing by using transposons	No data	Highly abundant in mammalian testes	[221]

Considering all the options RNAi-based therapy can offer, only one is currently under extensive studies: siRNA. Indeed, as shown in Table 4, ODNs and ribozymes present more drawbacks than actual benefits, whereas siRNA presents good characteristics. Its mechanism as well as the miRNA-based gene silencing mechanism will be described in the following subsection.

3.3.1. RNAi: a focus on siRNA

RNAi mechanism is considered as an evolutionarily conserved phenomenon, stately present in cells and probably responsible for the genome integrity from exogenous nucleic acids [213]. Present in most lower eukaryotic cells in worms, plants and in embryonic cells of higher eukaryotes, it has been shown that RNAi was not only responsible for pathogen resistance but also for the regulation of endogenous genes and genomes [222]. Moreover, the introduction of a double stranded RNA in a cell induces a cellular stress response with interferons production, thus eventually leading to cell death. However, ELBASHIR *et al.* [223] showed that if a short dsRNA is introduced, then no or a very weak response is observed and silencing can be done. This is the reason why siRNA, which is a short dsRNA, can induce silencing while a longer dsRNA cannot. RNAi is more thoroughly described in Refs. [224], [225] and [226].

This technology is thus very attractive for medical applications as the down-regulation feature could be used in the treatment of multi-drug resistant diseases [227,228] or for personalized therapies. In particular, there is an increasing number of studies using RNAi in oncology, since cancer is closely linked to genome alteration, as presented in Section 3.1. RNAi encompasses several tools, such as siRNA and miRNA, which mechanisms will now be presented.

siRNAs are small dsRNA (21-23 nucleotides in length) taken up by cells and which need a carrier, either viruses or nanoparticles, as they show a very low stability in serum [229], due to a rapid degradations by serum nucleases. siRNA origin can be endogenous or exogenous, as presented in Figure 3.3-1.

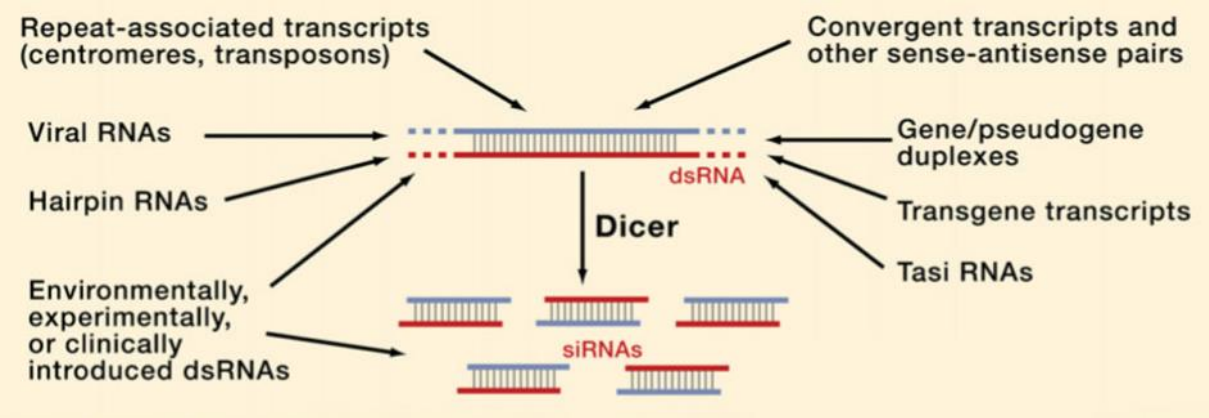

Figure 3.3-1: Various siRNA sources. Adapted from Ref. [222]

When siRNA is produced from an endogenous dsRNA, the later must first be catalyzed by the enzyme endoribonuclease III called Dicer, which then synthesizes siRNAs. The long dsRNA is cleaved and gives rise to a 21-23-nucleotides-long (nt) siRNA. This includes 2 free nt at the 3' extremity, that will interact with the Argonaute (Ago) protein, which will then assemble with the RNA-induced Silencing Complex (RISC) [222]. When siRNA is synthetically produced, it directly interacts with Ago and then is incorporated in RISC. siRNA is a double stranded RNA with a 'sense' strand and an 'antisense' strand. The sense strand is degraded by Ago whereas the antisense strand is used by RISC to target a specific mRNA, identified thanks to complementary Watson-Cricks base-paring. The mRNA is cleaved in a sequence-specific manner leading to its degradation by Ago component and to the translational repression of the targeted gene. The remaining mRNA fragments are then attacked by exonucleases from the cells to finalize the degradation [230]. RISC and siRNA are recycled and can process several other cleavage cycles [213]. Figure 3.3-2 illustrates the siRNA silencing process.

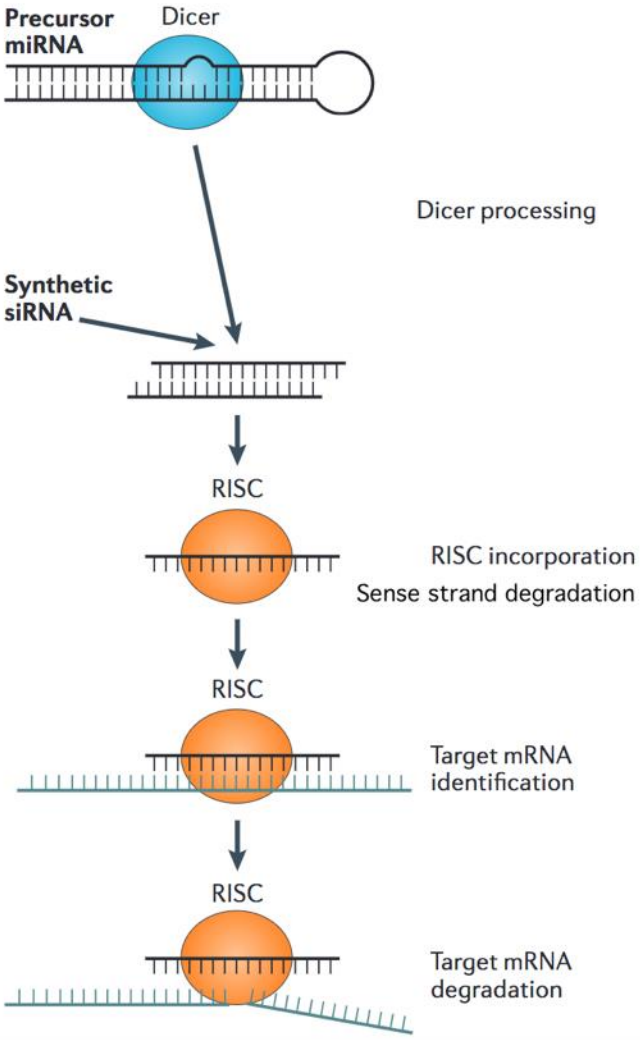

Figure 3.3-2: Gene silencing at post-transcriptional level using siRNA. dsRNA is first cleaved by Dicer to produce siRNA. In case of synthetic siRNA, this step is bypassed. siRNA then assembles with RISC. The sense strand of siRNA is degraded, and the antisense strand is used to guide RISC to the targeted mRNA and cleave it. siRNA and RISC are recycled to process other cleavage cycles. Adapted from Ref. [230]

The main benefit of gene therapy, and more particularly of siRNA mediated gene silencing, compared to conventional therapy, is the very high specificity in the selection of the targeted cell. siRNA mode of action being based on the very specific complementarity between the targeted sequence and the siRNA sequence, it should induce cytotoxicity only to the targeted cells. Nevertheless, three sources of toxicity have been identified:

- off-target effects: concentration dependent and sequence mediated, they lead to the silencing of non-targeted genes. It has been observed that these “off-target” effects could occur when a partial sequence complementarity exists, between the 5’ end of the

transfected siRNA guide strand and the non-targeted mRNA [231]. It is also non-negligible that the siRNA could inhibit another gene;

- Innate immune activation: the use of siRNA and more generally of dsRNA can activate innate immune receptors, triggering inflammatory and interferon responses. Thus, chemical modifications can help to avoid binding and activation of these receptors [230].

Gene silencing and more particularly siRNA is a great tool for gene therapy. The main hindrance of their clinical development is their very low stability in blood [232] and their low cellular uptake capacity [227]. siRNA thus needs a vector or a cell uptake promoter such as electroporation [233].

3.3.2. Vectors used for siRNA delivery

Although siRNA represents a lot of hope in gene silencing and thus personalized medicine, its wide use is still low mainly due to delivery difficulties and a lack of clinical positive results. Indeed, siRNA has a short half-life in serum, from a few minutes up to an hour when not modified or vectorized [233], and shows difficulties to go to the target through the systemic circulation because of nucleases-mediated degradation [211]. Furthermore, the various studies that have been performed showed that "naked" siRNA experienced a prompt renal excretion and did not readily enter cells. This behavior can be explained by the siRNA polyanionic property and macromolecular structure [234], which, by electrostatic forces induces a repulsion. Another important characteristic of RNAi-based therapy is that the desired gene has been observed to be silenced for three to five days [235]. Gene therapy should then include several administrations, depending on the expected outcome and the rationale of the therapy.

It is then important to develop an efficient protector to deliver siRNAs. Prof. MALVY and Dr. BERTRAND, from our team at *Laboratoire de Vectorologie et Thérapeutiques Anticancéreuses*, have been extensively studying and developing various types of nanovectors to carry siRNA. In 2000, LAMBERT *et al.* successfully developed nanocapsules composed of polyisobutylcyanoacrylate (PIBCA) to encapsulate (yielding efficiency of about 98% [236]) antisense oligonucleotides targeting *EWS-Fli1* oncogene [237], obtaining by this mean a consequent tumor growth inhibition *in vivo*. The same polymer was later used to encapsulate siRNA [238], displaying the same yield of encapsulation (≈97%), similar *in vitro EWS-Fli1* gene expression inhibition (≈60%) and *in vivo* tumor growth inhibition (≈43%), with

multiple intra-tumoral injections. A similar polymer was used for the inhibition of *RHOA* [239], which overexpression is responsible for an increased tumor cell proliferation and invasion and for tumor angiogenesis in an aggressive form of breast cancer. For this *in vivo* application, chitosan-coated polyisohexylcyanoacrylate (PIHCA) nanoparticles were used to encapsulate anti-RhoA siRNA, and administered intravenously every 3 days for 30 days, showing a total tumor growth inhibition all along the duration of the PIHCA-siRNA administration [239]. Chitosan-coated PIHCA-siRNA nanoparticles were also used for the inhibition of *EWS-Fli1* and *RET-PTC1* expression, in the treatment of Ewing Sarcoma [234] and of thyroid papillary carcinoma [240] xenografted tumors, respectively, in mice. By this mean, a tumor growth inhibition was again obtained, by the inhibition of *EWS-Fli1* expression for 11 days, with a total of 5 intravenous injections [234], and by the inhibition of *RET-PTC1* expression for 11 days, with a total of 5 intra-tumoral injections [240]. In our most recent work with organic nanoparticles, we used a squalenic component, able to self-organize in nanoparticles, and to complex with siRNA thanks to cationic charges at its surface. BERTRAND *et al.* obtained an *EWS-Fli1* gene expression inhibition *in vitro* [41], and URBINATI *et al.* obtained a consequent tumor growth inhibition in the case of prostate cancer, by targeting the *TMPRSS2-ERG* oncogene [241]. Since then, our team focused on the use of nanodiamonds to deliver siRNA.

Cationic polymers or nanoparticles are one of the most studied vectors for the delivery of siRNA, thanks to the electrostatic interactions with the negatively charged phosphate groups of the siRNA [37]. Some polymers have already been tested such as the natural polymers chitosan combined with PEI [242] or synthetic polymers such as polyethylenimine (PEI) [207] or dimethylaminoethyl methacrylate (DMAEMA).

Cationic lipoplexes or liposomes have also been studied [243,244]. Briefly a complex is spontaneously formed between siRNA and the polycationic polymers thanks to electrostatic forces between the two. The negative charges of the phosphate groups from siRNA and the polycationic groups from the liposome interact and can form NPs. This results in the entrapment of siRNA within the liposome [232]. HAMMOND *et al.* [245] used a multilayered liposome to encapsulate both the drug and siRNA, both being protected from blood stream and renal-excretion by a PEGylated outer layer.

Polymers and polycation-based vectors are also good engineered solutions for gene delivery. Although transfection efficiency and endosomal uptake and escape are low, they present very

low immunogenicity and no risk of chromosomal insertion, on the contrary of viral vectors. Also, they can carry a large amount and large-sized DNA and they can be easily synthesized. However, toxicity of those carriers must be considered, even though a majority of *in vivo* studies showed successful delivery, BEHLKE *et al.* in [233] cited different toxicities due to the cationic lipids, involving electrostatic effects.

Figure 3.3-3 presents a schematic representation of siRNA delivery by various cationic complexes or nanoparticles.

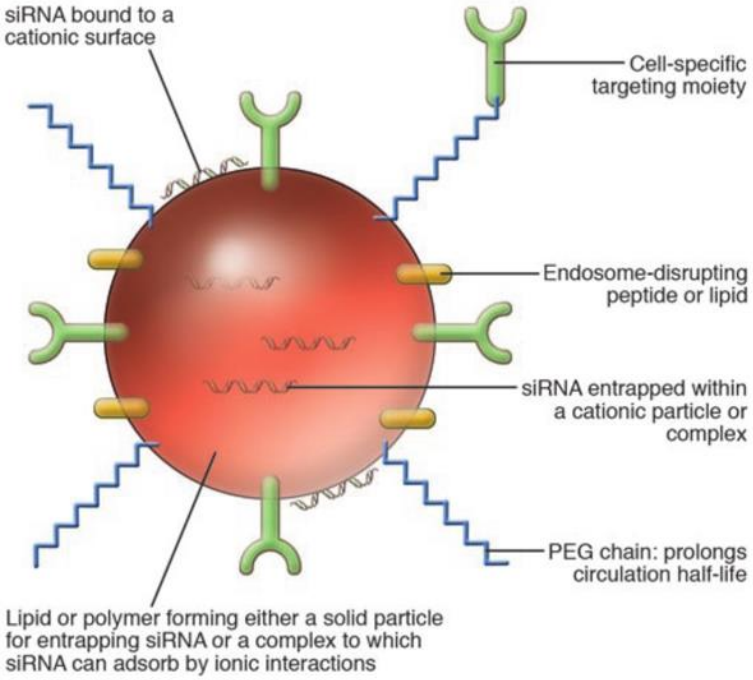

Figure 3.3-3: Schematic representation of siRNA delivery by biocompatible polymer complexes or nanoparticles. siRNA can be vectorized in different ways: (i) entrapped in the core of the particle, (ii) ionically adsorbed at the surface or (iii) the sense strand can be covalently attached to one of the surface components. A PEG polymer chains can be added to improve the pharmacokinetics and the biodistribution behavior but also to improve biocompatibility. Targeting materials, such as antibody or peptides, can also be added to the surface. From Ref. [244]

Another type of vectors also greatly used are the viral vectors. It is the most developed technique since they are widely used for gene therapy. Indeed, it is the easiest method to transfer genes of interest to desired cells and it is proven that it is a successful way. As a matter of fact, virus-based vectors get readily into the targeted cell and can even replicate itself. Among vectors that are used, one can cite adenovirus, retrovirus, vaccinia virus and

finally herpes simplex virus [246]. Although they can be very easy to use and have proven a great efficiency at delivering genes, viral vectors also present drawbacks such as a strong immune response [247]. Furthermore, even though the genes that are carried are carefully verified, viral vector use can cause chromosomal insertion and proto-oncogene activation. Finally, they can only carry a limited number of siRNA molecules and can be contaminated by another living viruses.

3.4. Conclusion of Chapter 3

RNAi therapy and more specifically siRNA showed great promises, but investments decreased over the years, because of a lack of clinical results. This technology could experience a revival, several pharmaceutical treatments based on this technology being at different stages of clinical trials, as indexed in the review in Ref. [248]. The leading company developing this technology, Alnylam, has four products, targeting hereditary ATTR amyloidosis, hypercholesterolemia, hemophilia and acute hepatic porphyrias, in late clinical stage (Phase III). All are siRNA, vectorized either by a lipid nanoparticle or by N-acetylgalactosamine (GalNAc) delivery platform[f].

siRNA has been shown to be an attractive tool for gene silencing and thus its application for new cancer therapies would represent a new paradigm in the treatment of certain diseases. Unfortunately, siRNA suffers from a low serum stability, a rapid renal clearance and a poor cellular uptake. In order to improve *in vivo* siRNA transfection, it is necessary to use a vector to either encapsulate it or load it on its surface for a better stability and an increased uptake.

The vector used for siRNA delivery during this PhD project was nanodiamond. The following chapters will present the different studies conducted on the nanodiamond-siRNA complexes. By using different types of nanodiamonds, *in vitro* studies and *in vivo* biodistribution were achieved.

[f] http://www.alnylam.com/alnylam-rnai-pipeline/#latestage

RESULTS

Chapter 4

Determining the optimal production method and the most effective surface modification for the *in vitro EWS-Fli1* expression inhibition: physico-chemical characterization and cell culture assays

As presented previously, nanodiamonds display very interesting characteristics to be used as drug delivery platforms, in particular for siRNA delivery to Ewing Sarcoma cells. In a previous work [249], which served as a proof-of-concept, detonation nanodiamonds were initially exposed to a micro-wave assisted hydrogen plasma, allowing an efficient cleaning of oxygen groups, a removal of the non-diamond carbon layer (graphite) and the formation of C-sp^3-H terminations at the surface of the nanoparticles [91]. A more detailed description of the used protocol is provided in Section 4.1.1. These hydrogenated detonation nanodiamonds (H-DND) were then suspended in de-ionized water, leading to a stable suspension with a high positive zeta potential of +50mV, very favorable for nucleic acid binding by electrostatic interactions. This study showed that siRNA was loaded on H-DND, then delivered to Ewing Sarcoma cell's cytoplasm, where it induced an efficient inhibition of *EWS-Fli1* gene expression, as presented in Figure 3.4-1.

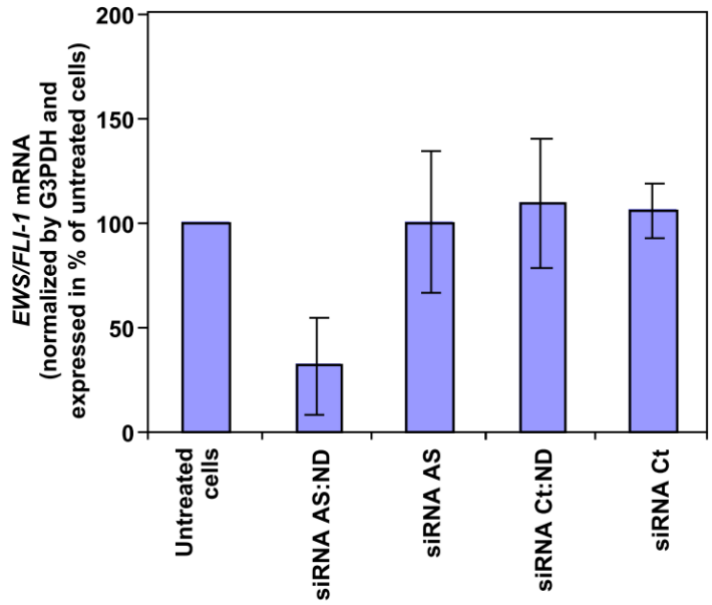

Figure 3.4-1: EWS-Fli1 inhibition after 24h of treatment with H-DND vectorized siRNA (antisense: siRNA AS; or control: siRNA Ct) on A673 Ewing cells. From Ref. [249]

This work demonstrated the proof-of-concept *in vitro*. A translation of these results to an *in vivo* pre-clinical model should be feasible and would represent a great hope for Ewing Sarcoma treatment. The European project DiamESTar, which has supported this PhD project, was funded to address: (i) the *in vitro* efficacy of such hydrogenation when applied to H-

DNDs of a size smaller than 5 nm; (ii) the *in vivo* efficacy, biodistribution and elimination of cationic ND:siRNA complexes. My work concerned the *in vitro* physico-chemical and biological (in terms of their ability to deliver an active siRNA in cultured cells) characterization of different cationic detonation nanodiamonds and functionalized HPHT nanodiamonds batches and the tissue distribution of the later when injected to a mouse.

To do so, different cationization strategies were used and tested: micro-wave plasma-assisted hydrogenation, annealing under hydrogen atmosphere, cationization by chemical treatment, and cationic polymer coating. The nanodiamond solutions were manufactured by different partners:

- Aqueous suspensions of DND (primary size ≈5 nm) hydrogenated by plasma or by annealing, were made in Jean-Charles ARNAULT's team at the Diamond Sensors Laboratory of CEA-LIST Saclay (Gif-sur-Yvette, France) for the former and in Gregory PIETER's team at the *Laboratoire de Marquage par le Tritium of Institut des sciences du vivant Frédéric Joliot*/CEA Saclay for the later;
- A chemically treated DND (primary size ≈3 nm) aqueous suspension of commercial solution NanoAmando®, was manufactured by NanoCarbon Research Institute, Ltd., Japan; a generous gift from Prof. Eiji OSAWA;
- A cationic polymer coated-HPHT diamonds (primary size ≈30 nm) suspension was prepared by Marek KINDERMANN, PhD student, in Peter CIGLER's Lab at the Institute of Organic Chemistry and Biochemistry (Czech Academy of Sciences, Prague, Czech Republic).

This chapter will present the physico-chemical characterizations that were conducted for each nanodiamond solution received. That includes size and electrophoretic mobility (zeta potential) measurements, siRNA binding capacity and colloidal stability over time. The ND:siRNA complexes were then tested *in vitro* for cytotoxicity, cell internalization, the ability to inhibit the junction oncogene *EWS-Fli1* and for apoptosis restoration. These preliminary assays were meant to determine the optimal cationization strategy, in order to then move to *in vivo* experiments. All the methods used for the experiments presented in this chapter are thoroughly described in Appendix A.

4.1. Plasma-assisted hydrogenation and hydrogenation by annealing of DND

4.1.1. Methods of production

4.1.1.1. Micro-wave plasma-assisted hydrogenation

The plasma-assisted hydrogenation of DND (P-DND-H) was conducted in Jean-Charles ARNAULT's and Hugues GIRARD's team at the *Diamond Sensors Laboratory* of CEA-LIST Saclay (Gif-sur-Yvette, France).

Briefly, a hydrogen plasma was created in a quartz tube resisting to high temperatures, in which 50-100 mg of ND powder was placed [134]. To initiate a plasma in the tube, a continuous flow of hydrogen (10 sccm) at a controlled low pressure of 12 mbar was made circulating with a pumping system, and the tube was placed in a wave-guide supplied with a micro-wave generator (frequency 2.45 GHz, Power: 250 W). This resulted in the formation of a hydrogen plasma, reaching a temperature of 700-1100°C. A schematic representation of the setup is presented in Figure 4.1-1.

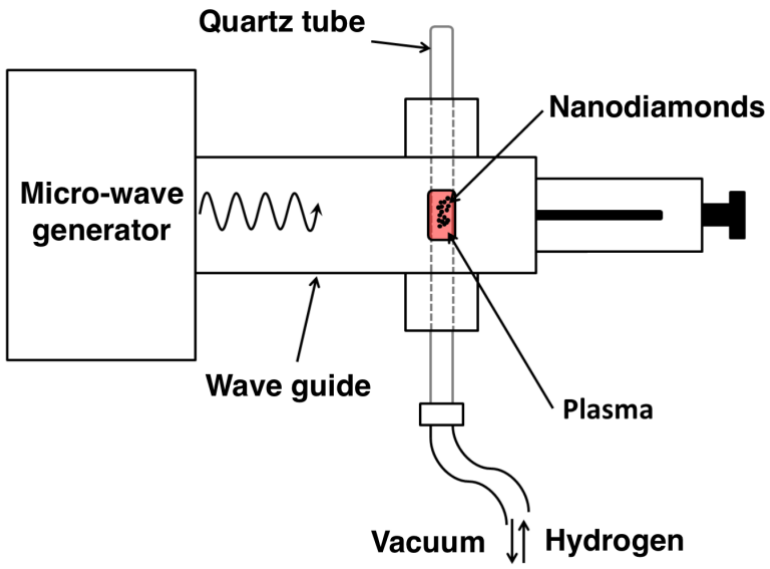

Figure 4.1-1: Schematic representation of the micro-wave plasma-assisted hydrogenation of NDs. From Ref. [91]

The sample was then exposed to the plasma for 20 minutes, and the quartz tube was rotated during the entire process in order to ensure the homogeneity of the hydrogenation over the whole surface of the DNDs. The resulting hydrogenated powder was then dispersed in deionized water, sonicated to disaggregate the clusters (Hielscher UP400s, 300W, 24 kHz, 1h

under cooling system) and finally centrifuged (2,300 *g*, 40 min) to only collect the small particles left in the supernatant.

4.1.1.2. Annealing under hydrogen atmosphere

The DND annealed under hydrogen atmosphere (A-DND-H) were produced at the *Laboratoire de Marquage par le Tritium of Institut des sciences du vivant Frédéric Joliot*/CEA Saclay in Gregory PIETER's team, by Emilie NEHLIG, post-doctoral fellow. As we intended to use tritium gas to study the biodistribution and the elimination of tritiated DND after injection in mice, the annealing method was adapted in order to work in a closed set up, as a flux could not be used because of the generated radioactivity.

The annealing treatment was performed at a lower temperature (450-550°C) than the plasma-assisted hydrogenation. Thermal annealing in the gas phase is a "simple and inexpensive process" suitable for surface reduction of DNDs, conferring them low surface contamination, good homogeneity of their surface, negative electron affinity, high positive zeta potential and narrow size distribution. This treatment was first set up by KOROLKOV *et al.* in 2007 [250] and performed at high temperature (800-850°C) for 5 h. A similar treatment was developed by WILLIAMS *et al.* in 2010 [130] at a lower temperature.

Briefly, a quartz tube was loaded with 30-35 mg of DND powder. The tube was then connected to the hydrogen set up, vacuum was made and the setup loaded with gas (200-250 mbar H_2). The tube containing the DND powder was placed in the oven, and connection was made with a trapping set up (round flask in dry ice and acetone bath). The sample was then let for 1h, at 550-560 °C. The tube was then closed and removed from the oven. The round flask was brought back to room temperature and vacuumed for 15 min. The DND powder was then vacuumed for 30 min before disconnection and air exposure. DNDs were placed in a glass vial in deionized water after 10 hours, sonicated and centrifuged (cf. previous method section 4.1.1.1), to only retrieve small particles from the supernatant.

Compared to micro-wave plasma-assisted hydrogenation, the annealing process allows a more homogeneous hydrogenation and renders a final solution with an increased colloidal stability, as it will be demonstrated in the following sections.

Moreover, this annealing method allowed the CEA team to graft tritium not only at the surface of DNDs, by replacing $^1H_2$ by $^3H_2$, but also in the core of the diamond nanocrystal, the tritium diffusing deep inside the nanoparticles, as demonstrated by GIRARD *et al.* [251]. The

method did not need much update: they placed DNDs in a quartz tube, with an isolation valve and in/out gas connections, including one connected to a cold trap. Fully reduced surface of DND's was obtained at 200 mbar and 550°C after a 4-hour exposure to a 100% Tritium gas. The labile ^{3}H were then removed thanks to a washing step with a protic solvent (methanol).

4.1.2. Physico-chemical characterization of nanodiamonds

4.1.2.1. Hydrogenated DND alone

The size and electrophoretic mobility (zeta potential) measurements were conducted with a Dynamic Light Scattering (DLS) NanoBrook 90Plus PALS device (Brookhaven Instruments Corporation, USA). More details about the different parameters and figure of merits used in DLS and described in this chapter, can be found in Appendix B.

From the different size and zeta potential measurements (Table 5), it appeared that there were disparities between the various batches, with more or less aggregation and fluctuation of the zeta potential, with no simple explanation for their causes. In Table 5, the *effective diameter* corresponds to the "Z-average" size. It is the most stable parameter produced by the DLS technique because it has a low sensitivity to noise. *Diameters in Number* results from a number distribution, where each particle has equal weighting. It allows to retrieve the contribution of small particles to the scattering, which signal intensity is dominated by the signal of the "large" particles or aggregates.

The *polydispersity Index* (PDI) provided by the DLS estimates the width of the particle size distribution. This value is dimensionless and fits between 0 and 1. Values between 0 and 0.2 are considered to be associated to well monodisperse distributions, values from 0.2 to 0.7 to mid-range polydisperse distribution and values greater than 0.7 to very polydisperse ones. The *baseline index* indicates the sample quality, *e.g.* presence of large particles/aggregates, by making the difference between the measured and the fitted baseline of the correlation function. The best quality solution should get the highest value at 10.

The *zeta potential* is inferred from the electrophoretic mobility measured by the apparatus (by Doppler velocimetry) via the Smoluchowski diffusion theory. It is the electrostatic potential at the boundary dividing the compact layer and the diffuse layer of the electrical double layer surrounding a charged colloidal nanoparticle. Its value provides information on the surface charge of the nanoparticles.

Nota bene: results from different batches and from different hydrogenation synthesis processes are gathered in this manuscript. Name coding was applied as follows:

P-	DND-	H-	1 to 3	1 to 5
Plasma-assisted	Detonation nanodiamond	hydrogenated	Producer: 1. NanoCarbon Institute; 2. PlasmaChem[g]; 3. Adamas[h]	Batch number
A-	DND-	H-	2	1 to 4
Annealed	Detonation nanodiamond	hydrogenated	Nanodiamond powder producer: PlasmaChem	Batch number

Example: sample P-DND-H-24 was a plasma-assisted hydrogenated detonation diamond produced by PlasmaChem, batch number 4.

*Table 5: Size and zeta potential of the different batches of plasma-assisted and annealing hydrogenation nanodiamonds. Effective diameter represents the average diameter inferred from Intensity (Z-average), diameter in Number is the mean value of measures in the Number distribution, PDI is the Polydispersity Index and the Baseline Index shows the aggregation level of the solution. *This sample is the same that was used in the proof-of-concept study* [249] *and was then considered as a reference in the following experiments.*

*** The calculation of the mean excluded the batch A-DND-H-21*

Sample ID	Effective diameter (nm)	Diameter in Number (nm)	PDI	Baseline Index	Zeta potential (mV)
P-DND-H-11*	58.1	27.7	0.22	0.00	+38.3
P-DND-H-12	247.5	57.1	0.16	0.00	+44.8
P-DND-H-13	376.7	39.3	0.25	0.00	+35.0
P-DND-H-21	161.8	53.9	0.26	6.8	+26.6
P-DND-H-22	230.5	93.2	0.22	4.1	+33.8
P-DND-H-23	242.7	53.0	0.20	0.00	+37.4
P-DND-H-24	192.3	39.2	0.24	0.00	+19.6
P-DND-H-25	116.7	72.9	0.14	9.7	+57.5
P-DND-H-31	286.2	48.1	0.20	0.5	+39.7
Mean	**241.8**	**57.5**	**0.20**	**2.0**	**+38.3**
A-DND-H-21	1430.5	78.2	0.16	4.0	+4.5

[g] PlasmaChem nanodiamond powder: PL-D-G02, average size: 4-6 nm.

[h] Adamas nanodiamond powder: information not provided

A-DND-H-22	171.1	65.6	0.24	5.5	+30.9
A-DND-H-23	71.7	31.3	0.21	9.0	+45.8
A-DND-H-24	63.4	55.7	0.18	9.7	+55.3
Mean**	**102.1**	**50.9**	**0.21**	**8.1**	**+44.0**

Table 5 shows a great difference between intensity (effective diameter) distribution and number (diameter in Number) distribution values. It is explained by the fact that the different solutions contained very small nanoparticles but also large aggregates. A positive point is that the PDI was around 0.2, meaning that our solutions were rather monodisperse, but the low baseline index suggested the presence of large aggregates. We can then assume that there were two populations: one composed of small aggregates (the single DND could not be measured in those conditions) and a second one constituted by large and very large aggregates.

Overall, DLS data showed that DND hydrogenated by annealing presented smaller effective diameters compared to those hydrogenated under plasma-assistance. The A-DND-H-21 sample had to be put aside for this analysis, as it obviously presented a very high degree of aggregation and a typical zeta potential associated to an unstable suspension [252]. The decrease of the effective diameter showed that there were less large aggregates, confirmed by the higher baseline index (close to 10). Finally, the annealing method induced a slightly larger zeta potential value.

4.1.2.2. Hydrogenated DND:siRNA complex

Figure 4.1-2 presents the size and zeta potential measurement of A-DND-H-22:siRNA complexes at increasing ND:siRNA mass ratio to obtain a behavioral study of the complex, for two different complexation protocols (*i.e.* with or without ultrasound sonication).

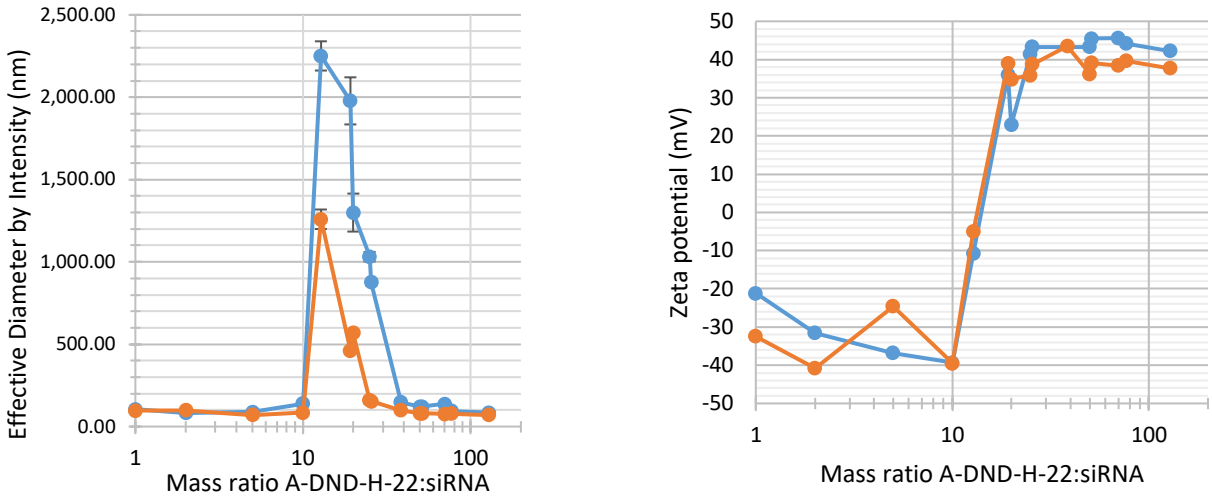

Figure 4.1-2: Size and zeta potential of A-DND-H-22:siRNA complex depending on the mass ratio, with (orange) or without (blue) ultrasound sonication during complexation. Left: Size. Right: Zeta potential

First, one can see that the mass ratio holds an important role and its variations induced three distinct regions on the complex size and zeta potential graphs:

- "Region 1": For mass ratio smaller than 10:1, the zeta potential was negative with values around -35 mV and the mean size was stable around 100 nm as a result of electrostatic repulsion. Considering that raw hydrogenated DND are positively charged (cf. Table 5), this negative zeta potential indicated that siRNAs, which are negatively charged, were in excess around DNDs and masked the positive charges of the DNDs.
- "Region 2": From mass ratio 10:1 to 25:1, the complexes experienced a transitory state with the formation of very large aggregates (size up to 2.3 µm) and a shift of zeta potential from negative to positive values. This state could represent the situation where the complexes carry no electric charge (similarly to the iso-electric point in a zeta-potential titration at varying pH) owing to an equilibrium of charges between nanodiamonds and siRNAs, inducing aggregation by short-range interaction forces (*e.g.* Van der Waals).
- "Region 3": For mass ratio larger than 25:1, DNDs were in excess, zeta potential was positive (≈+40mV), and complexes did not form aggregates thanks to electrostatic repulsion (like in "Region 1").

Secondly, one can observe a significant difference between the two methods of complexation. Indeed, during the transitory state where the largest aggregates are observed, the sonication allowed to reduce the size of the aggregates by two-fold. This aggregation state

of the complexes has an impact on the cell internalization. It has been observed that siRNA-loaded nanodiamonds (DND-H primary core size ≈ 7 nm, aggregates ≈ 30 nm) entered cells *via* the micropinocytosis and the clathrin-mediated endocytosis pathways [249]. Those two endocytosis pathways are typical for nanoscale particles, the former enabling the engulfment of particles of a size < 200 nm and the later engulfing particles with a size comprised between 200 nm and 1 μm [253]. Furthermore, surface charges have also been proved to influence internalization efficacy: cationic particles are better internalized than neutral or anionic charged particles [253]. One can thus understand that (i) mass ratios used in "Region 2", forming aggregates up to 2.3 μm with a neutral zeta potential, are not suited for our application since it would disable the internalization capacity of cells; (ii) mass ratios used in "Region 1" would not facilitate internalization because of negative charges at the surfaces of our complexes.

We chose to work at the 25:1 (DND-H:siRNA) mass ratio for two main reasons:

- This mass ratio is at the edge of two regions (2 and 3) where the zeta potential is at positive values (from + 35 mV) and the size of the aggregates (under the micrometer size when they are not sonicated and under 200 nm when they are) are compatible with a cell internalization. Also, we could not use larger mass ratios because it would have requested a too large amount of each product to deliver a sufficient quantity of siRNA to induce the oncogene inhibition;
- Our studies, former and present, show that this mass ratio was the best suited to obtain an inhibitory effect of *EWS-Fli1*, as it will be presented later.

Concerning the siRNA binding capacity of nanodiamonds, a comparison was made (i) between the samples hydrogenated with plasma assistance, for the three different DND providers (Figure 4.1-3); (ii) between the two methods of hydrogenation, *e.g.* plasma-assisted vs annealing (Figure 4.1-4); and (iii) between the two methods of complexation, *e.g.* with or without ultrasonic sonication during complexation (Figure 4.1-5).

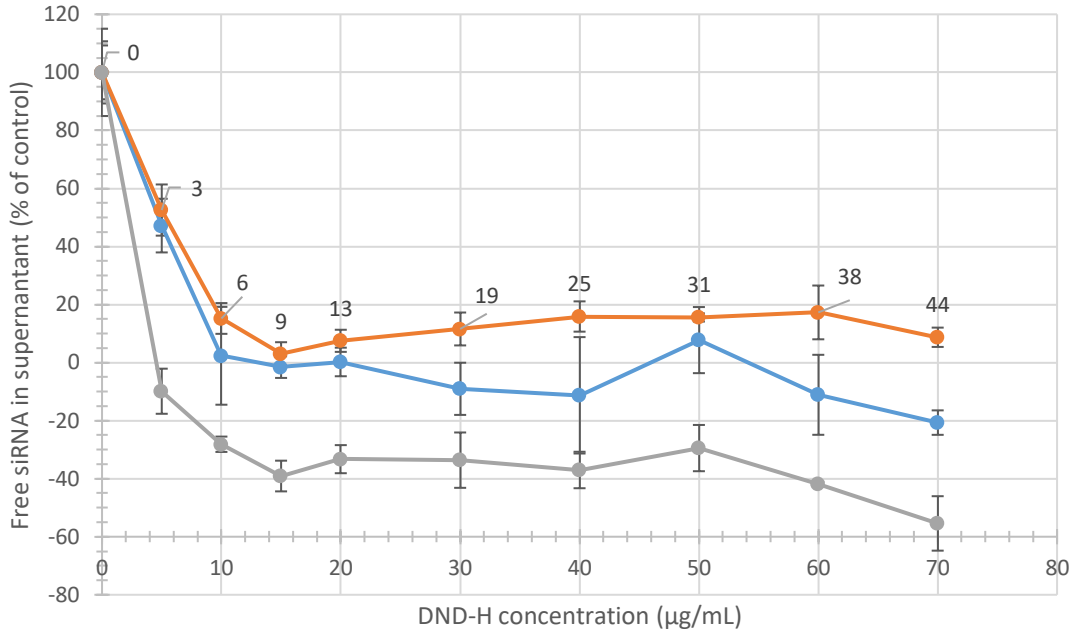

Figure 4.1-3: siRNA binding capacity to plasma-assisted hydrogenated NDs originating from three different nanodiamond powder producers. Blue: P-DND-H-13; Orange: P-DND-H-23; Grey: P-DND-H-31. Data label: mass ratio DND-H:siRNA. siRNA final concentration: 50 nM.

Figure 4.1-3 shows that the solutions resulting from three different nanodiamond powder providers display different behaviors. The saturation point (*i.e.* ND concentration for which all siRNA is bound to its surface) differs from one solution to another, even though zeta potential values of the three solutions are similar (≈+35mV, cf. Table 5). This difference has not been explained yet. For P-DND-H-13 and P-DND-H-31 (blue and grey curves respectively), one can see that the saturation curves go below 0% of free siRNA in the supernatant. These values are experimental artifacts, most probably coming from a problem with the blank values that were too low compared to the measured values. The important point to notice in this type of experiment is the shape of the curve and the value at which we reach the saturation point, *e.g.* at which we reach a plateau.

Figure 4.1-4 presents a comparison of the siRNA saturation curve for HND prepared by two methods of hydrogenation. It displays a difference of the saturation points, which can be explained by the zeta potential difference (A-DND=+44mV, P-DND=+38mV). The siRNAs were then more strongly bound to annealed DNDs than to plasma-assisted DNDs.

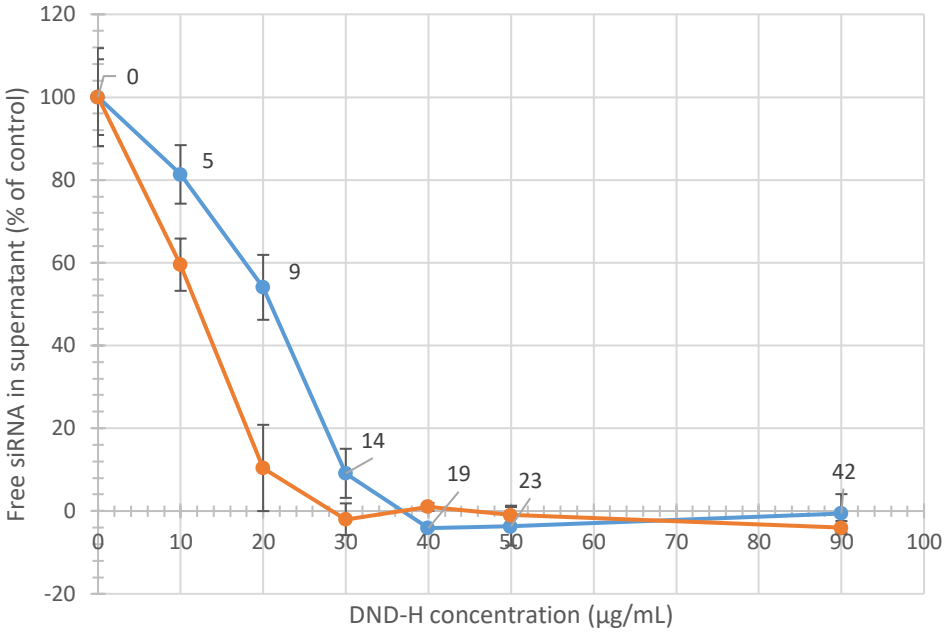

Figure 4.1-4: siRNA binding capacity to annealed under hydrogen (orange) or plasma-assisted (blue) hydrogenated nanodiamonds. Data label: mass ratio DND-H:siRNA. siRNA final concentration: 50 nM.

Finally, Figure 4.1-5 shows that the sonication during complexation does not induce any difference in the binding capacity of nanodiamonds indicating that aggregation during siRNA fixation onto DND have no influence on bonding capacity of hydrogenated diamonds.

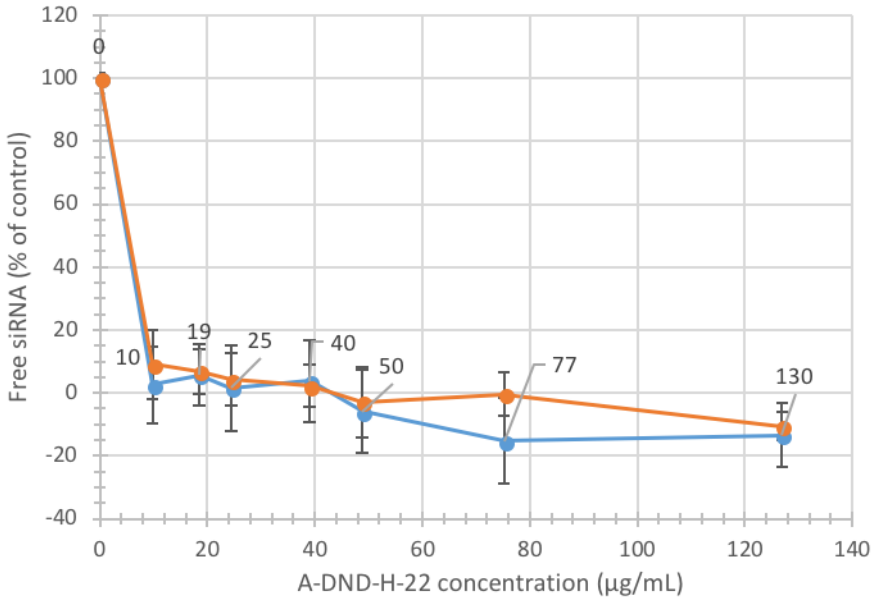

Figure 4.1-5: Dependence on the complexation method for siRNA binding capacity on DNDs hydrogenated by annealing. Orange curve: with ultrasonic sonication; Blue curve: without sonication. Data label: mass ratio DND-H:siRNA. siRNA final concentration: 50 nM.

One could see from the various experiments that there was a great variation in size and zeta potential values of the raw DNDs from the various batches available. Variations were also observed for siRNA binding saturation values, among the different batches tested and between the two methods of hydrogenation. Complexation with siRNA under sonication allowed to diminish by almost two-fold the aggregates' size but did not induce any variation in the titration of the binding of siRNA to DND. From this physico-chemical analysis, it appeared that the mass ratio (ND:siRNA) of 25:1 was the most suited, not inducing large aggregates (≈ 200 nm) and resulting in a positive zeta potential (≈ +35 mV).

4.1.3. *In vitro* efficacy on Human Ewing Sarcoma cells

After having characterized the received nanodiamond solutions and their behavior when complexed with siRNA, different *in vitro* assays were performed to determine (i) the cytotoxicity of DND-H solutions on cells, (ii) the DND-H:siRNA complex efficacy to inhibit *EWS-Fli1* expression, and (iii) the restoration capacity of cell apoptosis.

4.1.3.1. Hydrogenated DND cytotoxicity assay

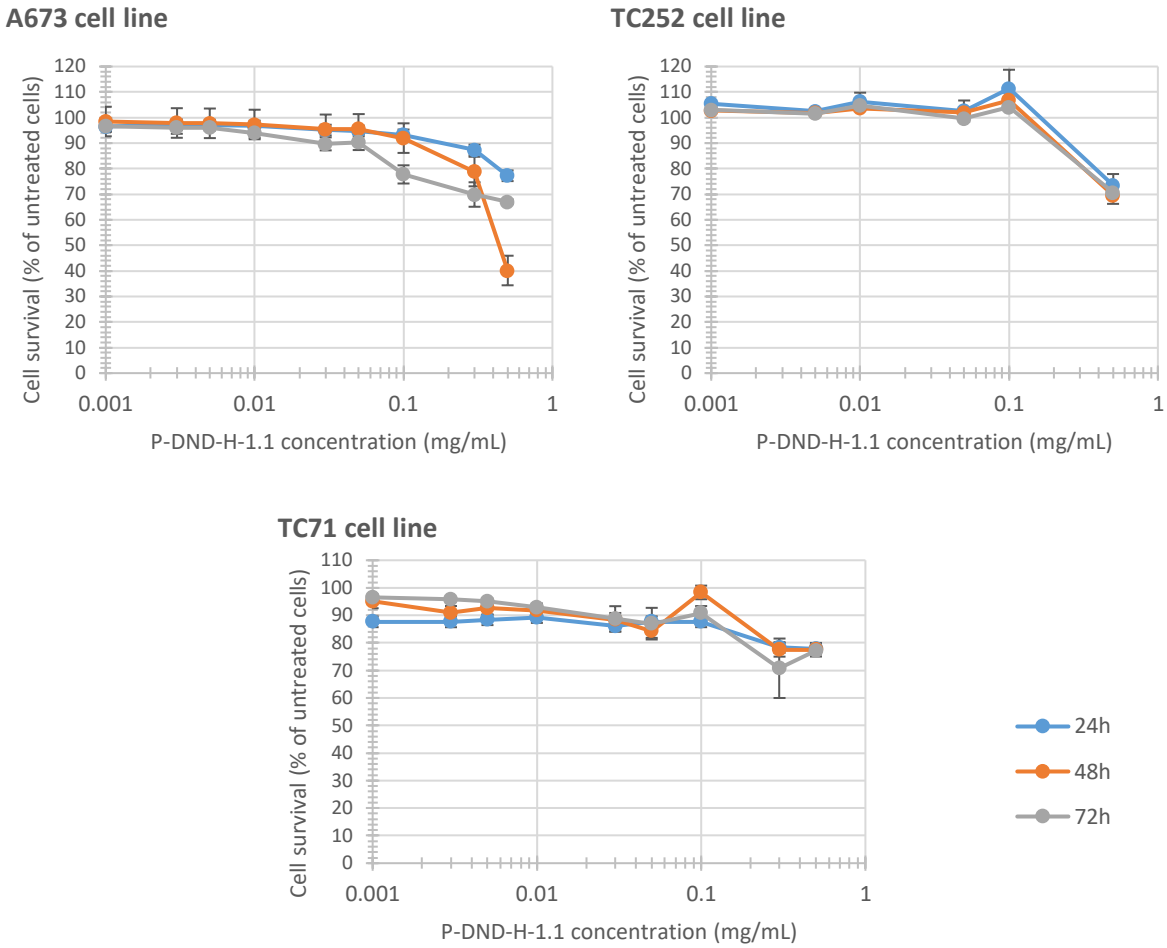

Figure 4.1-6: P-DND-H-11 cytotoxicity on 3 different Ewing Sarcoma human cell lines after 24 (blue curve), 48 (orange curve) and 72 h (grey curve) incubation time. MTS assay.

Figure 4.1-6 presents the cytotoxicity of P-DND-H on three different Ewing Sarcoma human cell lines: A673, TC252 and TC71, showing that a P-DND-H solution did not induce toxicity on cells at our working concentrations, *i.e.* between 0.01 and 0.05 mg/mL, and even after a 72h exposure. Similar assays were performed with other DND-H solutions, not presented here, and showed the same behavior with no induced toxicity. The results of the following assays will only be shown for A673 cell line, assays with TC71 and TC252 cell lines having shown similar results. Furthermore, A673 cell line is the most represented in Ewing Sarcoma literature.

4.1.3.2. Inhibition efficacy of *EWS-Fli1* expression with P-DND-H:siRNA

Inhibition efficacy was then tested, at different time points, at different siRNA concentrations and with different P-DND-H:siRNA mass ratios. First, Figure 4.1-7 presents the inhibition efficacy of the P-DND-H-11 solution, which served as a reference as it was successfully used in the proof-of-concept experiment published in 2015 by BERTRAND *et al.* [249]. One can see that we obtained an effective inhibition of the *EWS-Fli1* gene, modulated by the P-DND-H:siRNA mass ratio, set at 10:1 and 50:1. This result confirmed the inhibition early published in Ref. [249].

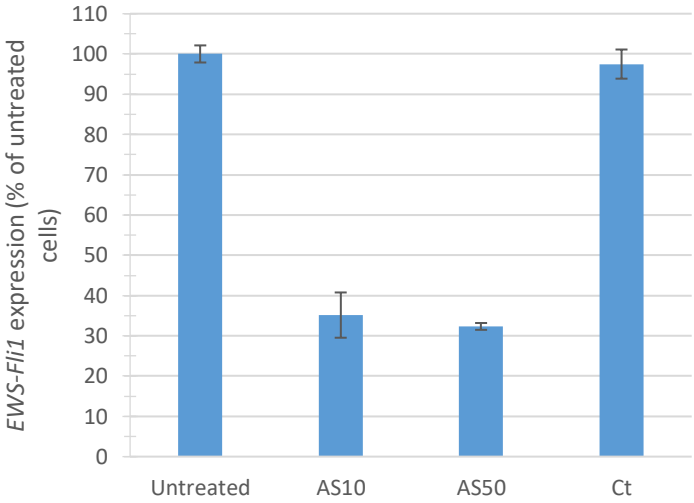

Figure 4.1-7: P-DND-H-11: siRNA inhibition efficacy after a 24h incubation. Final siRNA concentration: 50 nM. AS10: siRNA antisense used at a mass ratio P-DND-H:siRNA of 10:1; AS50: siRNA antisense used at a mass ratio 50:1; Ct: Control siRNA

Figure 4.1-8 presents the comparison of different batches of P-DND-H in their capacity to promote *EWS-Fli1* inhibition by siRNA. We observed that this inhibitory effect was not retrieved with newly prepared P-DND-H samples compared to P-DND-H-11 and the different

conditions show a disparity even between two batches from the same DND powder producer. Note that the Lipofectamine 2000 group was transfected in a medium without serum, as instructed by the producer, while all the other groups were incubated in a serum-containing medium. We thus obtained a very high inhibition rate with Lipofectamine 2000, but this platform cannot be used *in vivo*, as the transfectant would be degraded very quickly by the various proteins contained in the serum.

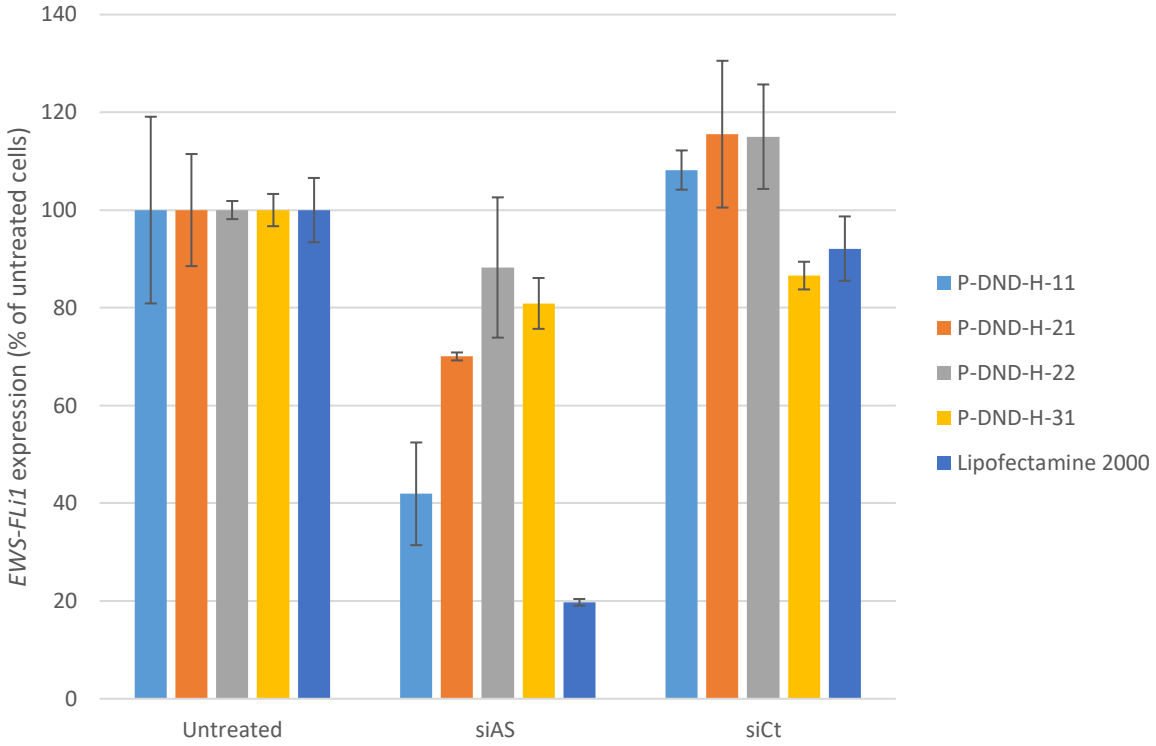

Figure 4.1-8: Comparison of the inhibition efficacy of different P-DND-H solutions, after a 24 h incubation. Mass ratio P-DND-H:siRNA: 25:1; final siRNA concentration: 50 nM.

To better understand the reasons of these negative results and determine new optimized parameters, we tested different siRNA final concentrations (Figure 4.1-9), and various P-DND-H:siRNA mass ratios (Figure 4.1-10).

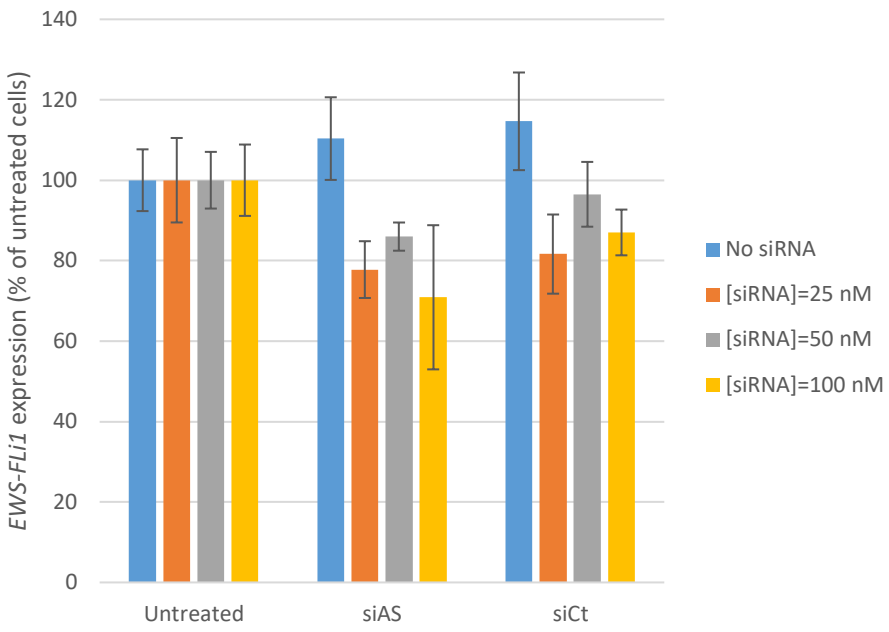

Figure 4.1-9: Inhibition efficacy optimization for different siRNA final concentration. For all curves, mass ratio P-DND-H:siRNA = 25:1; A673 cell line; P-DND-H-3.1 nanodiamonds.

Figure 4.1-9 shows that the variation of siRNA final concentration did not influence much the inhibition effect on A673 cells. Indeed, the inhibition efficacy varied between 18 and 22% and there was no significant difference with the control siRNA and with the untreated cells group in this specific experiment.

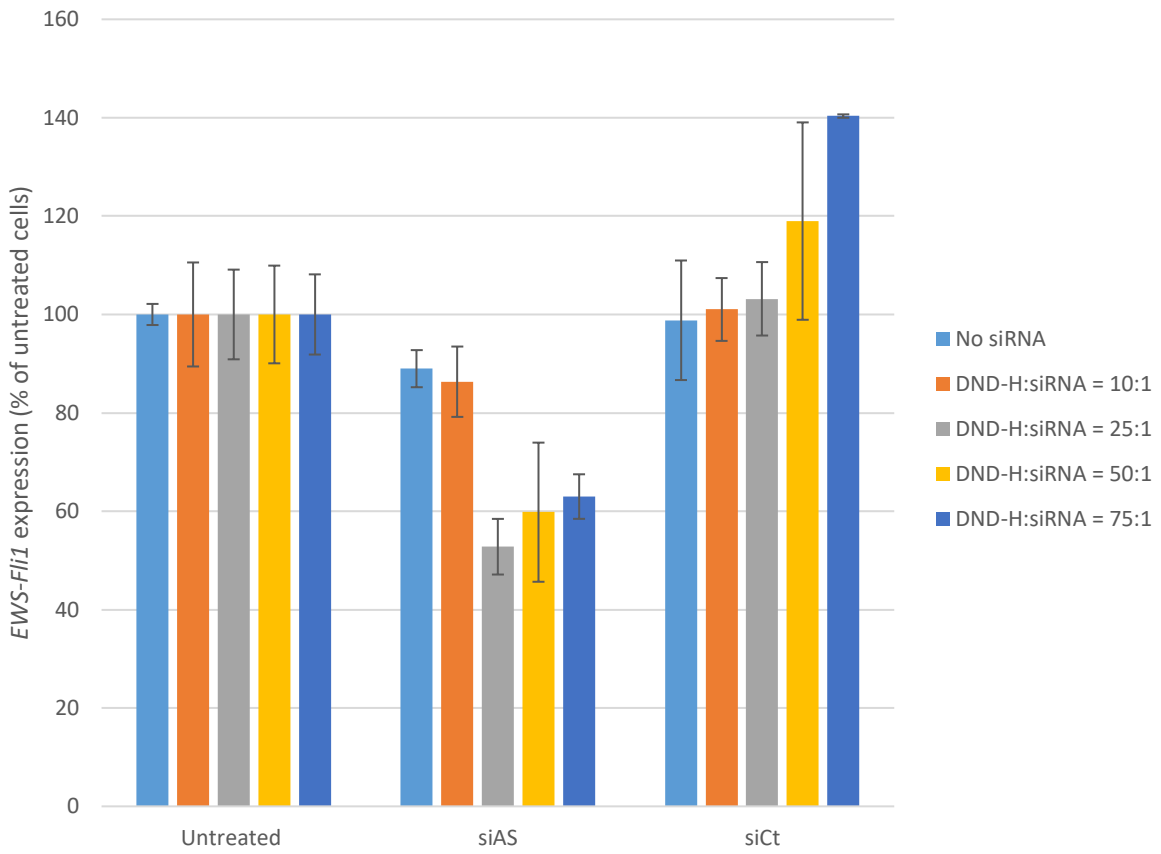

Figure 4.1-10: Inhibition efficacy parameters optimization - test of different mass ratio. P-DND-H-31, siRNA final concentration 50 nM, A673 cell line.

Figure 4.1-10 also shows that the inhibitory effect does not have a linear dependence to the mass ratio, and saturates at about 40% from mass ratio as low as 25:1. An interesting comparison can be made between the two similar conditions of Figure 4.1-9 and Figure 4.1-10, for final siRNA concentration of 50 nM and P-DND-H:siRNA mass ratio of 25:1. One can observe an important difference of inhibitory effect between the two biological replicates. This kind of variation was experienced several times all along my PhD project, making conclusions very hard to draw and highlighting the large variability of the different plasma-assisted DND solutions that were tested.

Nevertheless, despite the low replicability, the last two figures emphasize the fact that the initial experiments published by BERTRAND *et al.* [249] were already conducted in the optimal conditions and that a change in mass ratio or in final siRNA concentration could not improve the inhibition efficacy. However, one should note that the inhibition assays were only performed after a 24-hours incubation, and that we might have occulted a delayed effect.

4.1.3.3. Inhibition efficacy of *EWS-Fli1* expression with A-DND-H:siRNA

Previous results showed that hydrogenation by annealing treatment greatly improved the stability of the solution and the binding capacity of the nanodiamonds (see section 4.1.2). As for the plasma-assisted hydrogenation method, we tested several batches of the A-DND-H method, all produced with nanodiamond powder from the same producer. Since A-DND-H presented smaller aggregates than P-DND-H with a larger siRNA load per unit of mass, we hoped that the inhibition rate would also be increased. Unfortunately, as presented in Figure 4.1-11, the inhibition efficacy was not improved, with a value of only ≈35% inhibition.

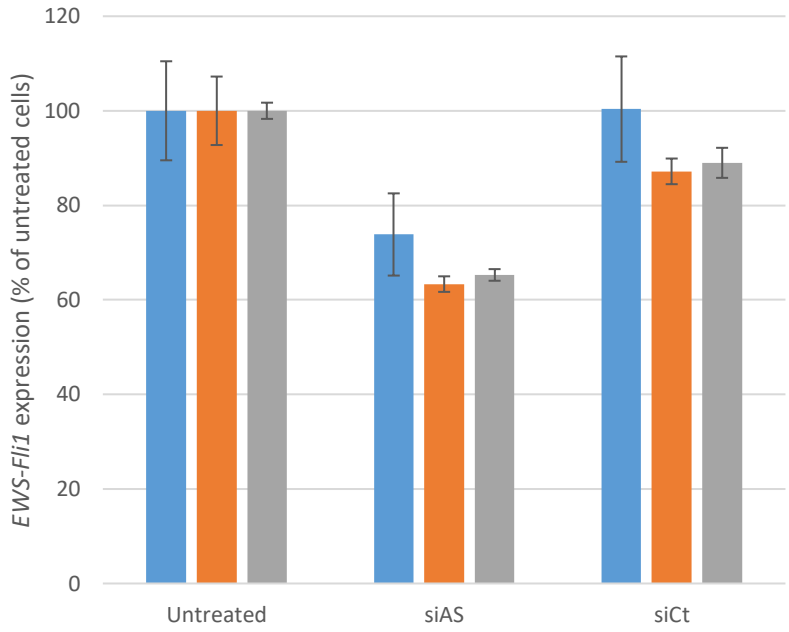

Figure 4.1-11: Inhibition efficacy of DND hydrogenated by annealing. Blue: A-DND-H-22; Grey: A-DND-H-23; Orange: A-DND-H-24. Mass ratio A-DND-H:siRNA=25:1

Moreover, we did not have sufficient amounts of each solution to repeat the experiments extensively. The low inhibitory effect and the small amounts of solution available are the reasons why the following results only present experiments conducted with P-DND-H.

4.1.3.4. Apoptotic recovery after P-DND-H:siRNA treatment

After having tested the inhibitory efficacy, we wanted to assess if the apoptotic response was restored after the light inhibition of the *EWS-Fli1* gene. This study was made using plasma-assisted hydrogenated NDs only and both apoptosis and cytotoxicity assays of the DND-H:siRNA complex were conducted. Furthermore, an association with Vincristine was made, acting as a trigger of the apoptosis.

Figure 4.1-12 shows the **cytotoxicity assay** conducted on A673 cell line, analyzed after a 48-h incubation with the different treatments. First, one can see that P-DND-H-22 alone and P-DND-H-22 associated with siRNA against *EWS-Fli1* (siAS) or with a control siRNA (siCt) did not induce significant toxicity. On the contrary, Vincristine at 1.5 and 2.5 ng/mL is toxic to cells after 48 h. However, when P-DND-H:siAS and Vincristine were associated, one can observe a strong and significant increase of the toxicity of about 50% for the concentration 1.5 ng/mL and of about 6-fold for the concentration 2.5 ng/mL compared to when Vincristine was applied alone on cells. One can also notice a significant difference (p<0.05) between the group treated with siAS and siCt at 2.5 ng/mL. One can assume that the siRNA sequence directed toward *EWS-Fli1* gene actually inhibited the gene, thus weakening even more the cells when treated with the cytotoxic agent Vincristine.

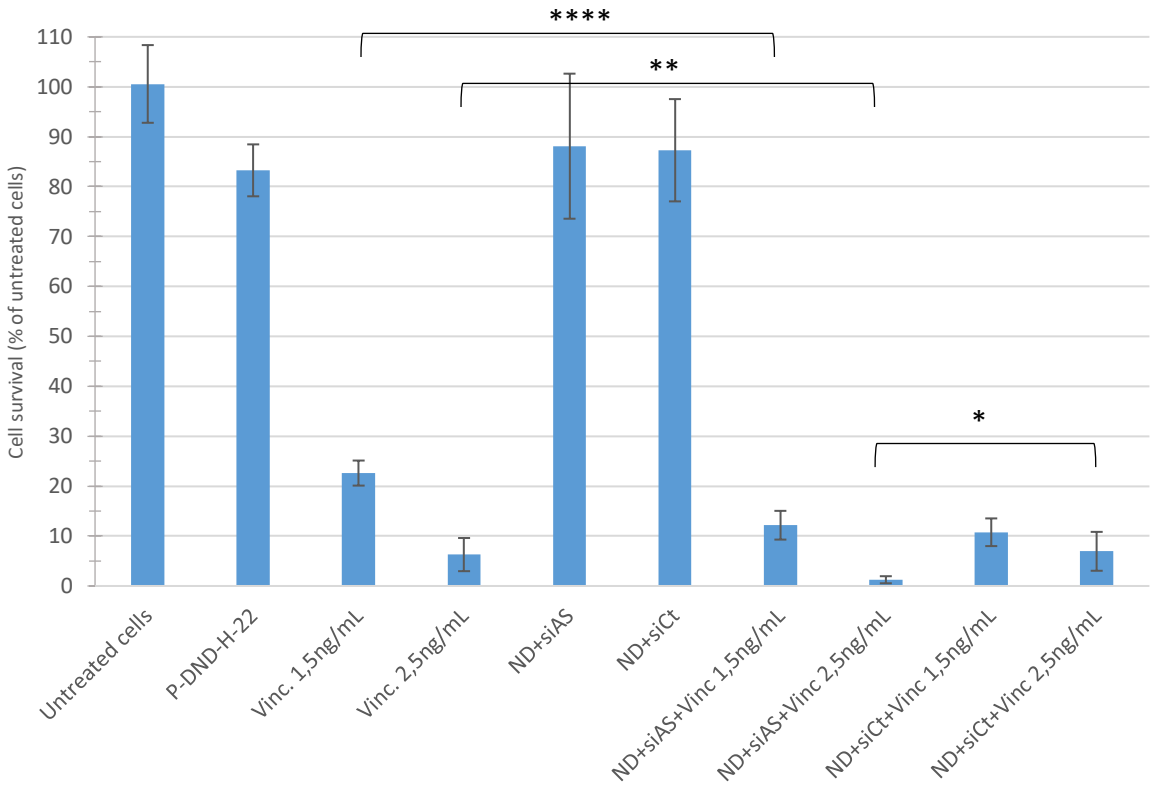

*Figure 4.1-12: Cell viability MTS assay of A673 cell line after a 48h incubation with P-DND-H-22, associated with siAS (toward EWS-Fli1), siCt (control) and/or Vincristine at different concentrations. T-test *: p<0.05, **: p<0.05, ****: p<10^{-4}.*

This very encouraging result needed to be complemented by an **apoptosis assay**, as presented in Figure 4.1-13. In this experiment, CellEvent Caspase 3/7 apoptosis kit was used. We tested

two Vincristine final concentrations, 2 and 3 ng/mL, both exhibiting about 30% apoptosis induction when applied on A673 cells. Nanodiamonds associated with siAS or siCt did not show any apoptosis induction. However, an interesting point is that when Vincristine was simultaneously applied to cells with P-DND-H or with P-DND-H:siRNA, the percentage of living cells was reduced and the part of apoptotic cell increased. Unfortunately, the assay showed that this toxicity was independent from the siRNA sequence used: the group "ND+siCt+Vinc [2]", which displayed a large fraction of living cells and almost no apoptotic cells, was most likely an experimental artefact, given the basal apoptosis induction of Vincristine at 2 ng/mL alone. Thus, we can assume that this increase in cell toxicity is not due to the restoration of the apoptotic pathway, which is stimulated by the addition of Vincristine, but most likely because of the association of the Vincristine molecules to P-DND-H:siRNA complexes, that might ease the cell entrance of Vincristine and thus increase its effect on cells.

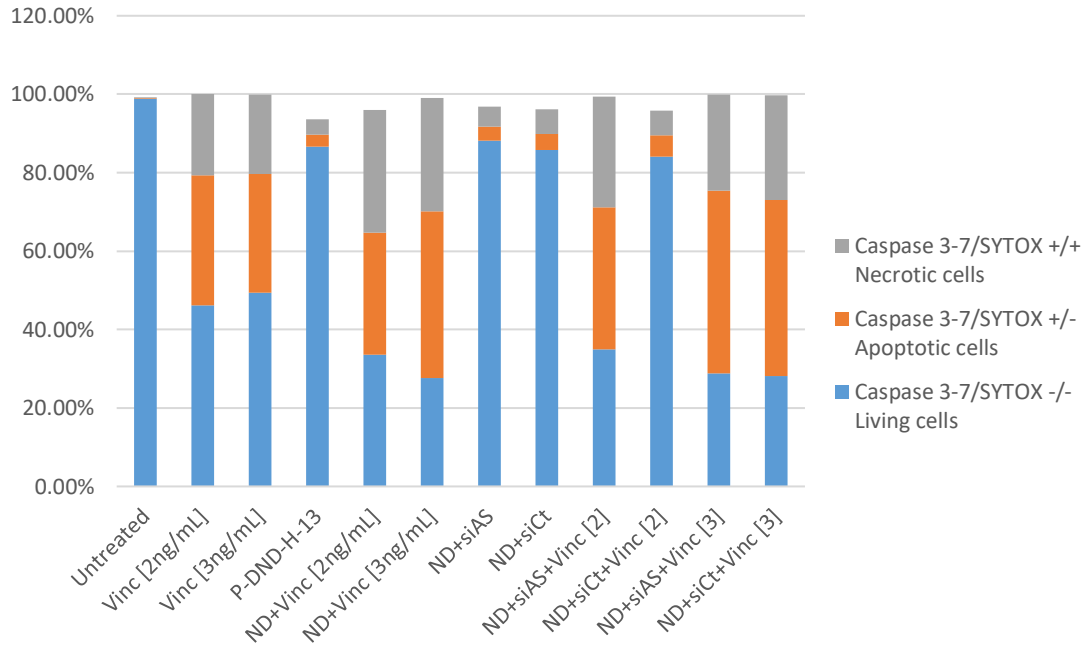

Figure 4.1-13: Apoptosis induction at 24h on A673 cells by P-DND-H-13 associated with siAS, siCt and/or Vincristine at final concentration of 2 or 3 ng/mL. siRNA final concentration = 50 nM.

4.1.4. Conclusion of Section 4.1

Numerous batches of plasma-assisted hydrogenation and hydrogenation by annealing of DND were tested. Plasma-assisted hydrogenation, which was well mastered by our collaborators of Diamond Sensor Lab (LIST/CEA Saclay), had worked successfully in the

proof-of-concept study [249]. However, the home-made system required an upgrade for automatization and, among other things, the micro-wave generator experienced a failure and needed to be replaced. It seems that the resulting setup modifications impacted the hydrogen termination synthesis and thus the properties of P-DND-H solutions, in particular their stability. The hydrogenation by annealing has, at least, improved this point. We speculate that the large variations in inhibition efficacy observed among different batches come from the setup modifications. Furthermore, we think that annealed DNDs were conferred a too high zeta potential, inducing a too strong binding of siRNA to these particles, preventing it from being released from the NDs to the cytoplasm.

The initial aim of our study was to use ultra-small nanodiamonds (primary particle size <5 nm), modified at their surface by different hydrogenation treatments that allowed siRNA electrostatic binding and further delivery in cell cytoplasm. We demonstrated that the different physical hydrogenation processes were not successful in reaching this goal, we then decided to test another cationization technique of DND by a "wet" chemical treatment.

4.2. Wet chemical hydrogenation: NanoAmando® solution

A commercial aqueous solution of NanoAmando was kindly provided by Professor Eiji OSAWA (Nano-Carbon Research Institute, Ltd, Japan), at a very large stock concentration of 20 mg/mL, with a nominal primary particle size of 3.1±0.6 nm and a positive zeta potential of +46.2 mV. The chemical cationization treatment is a long process, yielding to a stable solution, with a monodisperse size distribution and a positive zeta potential.

These nanodiamonds are produced by detonation reaction [92], then milled with zirconia beads [107] and purified by various chemical baths of HNO_3, a mixture of H_2SO_4 and HNO_3, $K_2Cr_2O_7$ in H_2SO_4, KOH/KNO_3, Na_2O_3, HNO_3/H_2O_2 under pressure, or $HClO_4$ [104]. They present cationic surface charges (+45 mV), acquired after a strong reduction chemical treatment [88]. This process has been described but not fully understood yet [252,254]. This commercial solution also presents a very good colloidal stability with no aggregates nor flocculation at stock concentration.

These DND have been tested for their physico-chemical properties and stability, once diluted, their siRNA binding capacity, and, of course, for the inhibition efficacy of the complex toward *EWS-Fli1* oncogene. Internalization studies by confocal microscopy were also conducted.

4.2.1. Physico-chemical characterization of NanoAmando solution

We started to verify the nominal size and zeta potential specifications of the provider with our DLS/zetameter system, as presented in Table 6.

Table 6: NanoAmando size and zeta potential characteristics as measured in our laboratory

Effective diameter (nm)	Diameter in Number (nm)	PDI	Baseline Index	Zeta potential (mV)
63.49	3.52	0.287	8.9	+50.96

One can see the major difference between effective diameter and diameter in Number. The later detects and favors ultra-small nanoparticle, when the former is mainly influenced by the few aggregates (cf. Appendix B). In this case, measurement in Number is the most suited. This highly concentrated solution is very stable over time, but it has to be diluted in order to be used in our *in vitro* assays.

We have conducted a study of the colloidal stability upon dilution in water and the results presented in Figure 4.2-1 show that the NanoAmando tend to aggregate. However, with the largest size at 52 nm, this aggregation is still compatible with cellular internalization and drug delivery. Moreover, this size is still below the aggregate's sizes we have obtained with P-DND-H and A-DND-H.

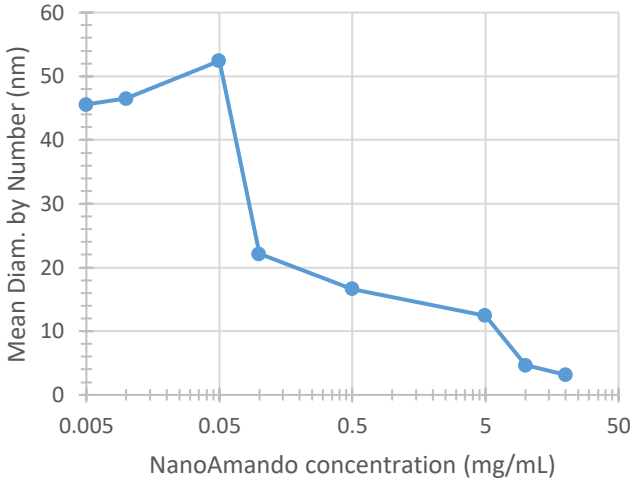

Figure 4.2-1: Hydrodynamic diameter measurement (by DLS, Number representation) of NanoAmando suspension after dilution at various concentrations.

The aggregation that we observed upon dilution, is in agreement with MCHEDLOV-PETROSSYAN *et al.* [128] reporting that when they are diluted, 3-nm nanodiamonds form

larger colloidal aggregates. This phenomenon could be explained by the fact that in concentrated solutions, the small particles interact through the surrounding water layer and tend to form periodic structures. When diluted, the distance between the particles is getting larger, inducing the formation of secondary aggregates, more separated and larger, because of the lack of close interactions through the particle's surrounding water layer.

siRNA binding capacity onto NanoAmando was also assessed (Figure 4.2-2) and displayed the same behavior as with the P-DND-H and A-DND-H, but with a full saturation in siRNA around a DND:siRNA mass ratio of 20:1. It is twice higher (cf. Figure 4.1-3 and Figure 4.1-4) than for the other solutions.

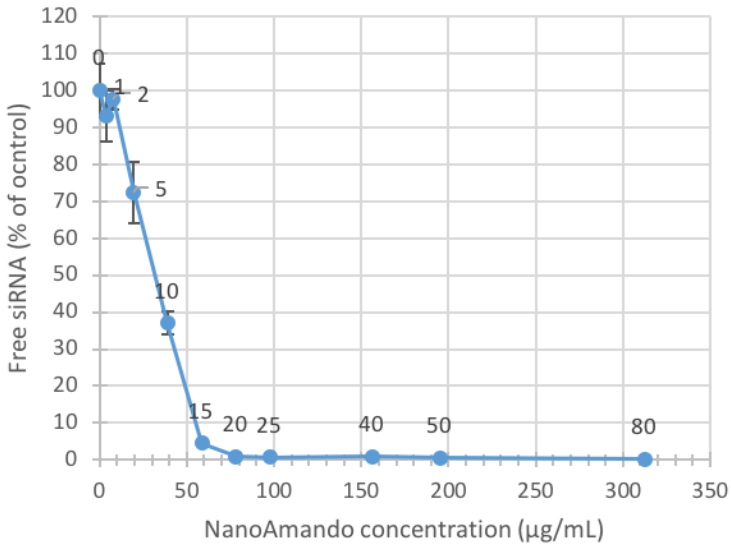

Figure 4.2-2: siRNA binding capacity of NanoAmando suspension. Data label: DND:siRNA mass ratio. Final siRNA concentration: 50 nM.

Apart from the siRNA binding, the size and zeta potential were also studied when NanoAmando DND were complexed with siRNA, as presented in Figure 4.2-3. Just as in Figure 4.1-2, one can observe three phases in the behavior of the complexes. Once again, two modes of complexation were compared: with or without ultrasound sonication during complexation. Briefly, small sizes were observed at DND:siRNA mass ratios between 1:1 and 15:1, with an average size of 70 nm for complexation with sonication and of about 150 nm without sonication. Then, at larger mass ratios, the complexes formed very large aggregates, in the range of 1800 nm with sonication and 2000 nm without sonication, for the largest sizes measured. The size of aggregates then slowly decreased but did not reach the values similar to those reached at small mass ratios. The highest mass ratio tested of 80:1 might have been too

low to reach this point, but from the trend of the curve, one can hypothesize that the size would have reached, at some point, the same plateau than at low mass ratios.

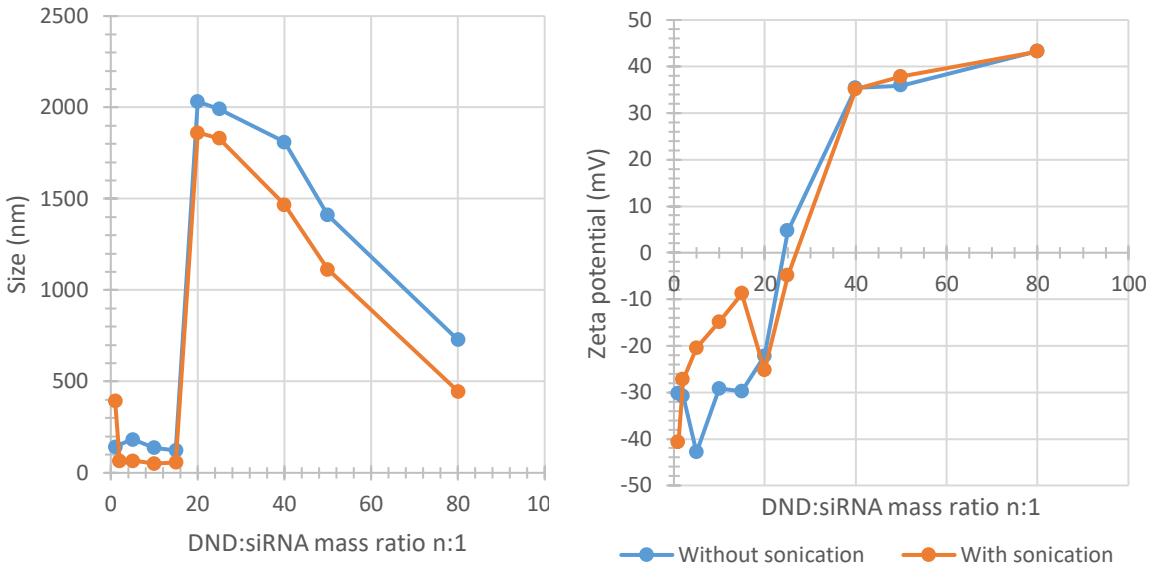

Figure 4.2-3: Size and zeta potential of NanoAmando:siRNA complex depending on mass ratio.

Zeta potential values experienced the same variations as described for the other cationic DNDs (cf. Figure 4.1-2):

- at low DND:siRNA mass ratios, siRNA was in excess compared to DNDs, zeta potential was thus negative;
- between mass ratio 20:1 and 40:1, the complexes experienced a transitory state, the zeta potential switching from negative to positive values through an isoelectric point (at mass ratio 25:1), eventually reaching +35 mV;
- at mass ratios higher than 40:1, DNDs were in excess, zeta potential was then positive, reaching +43 mV, approximately the value of zeta potential of the bare nanoparticle.

Once again, one can put in parallel the size stability of the complexes with the zeta potential variations. Indeed, zeta potential values between [-20;+20] mV are considered to be a sign of poor colloidal stability [252] leading to the aggregation of NanoAmando:siRNA complexes, just as for P/A-DND-H:siRNA complexes.

4.2.2. *In vitro* effects of NanoAmando:siRNA on Ewing Sarcoma cells

First the **cellular toxicity** of NanoAmando DNDs needed to be assessed, to ascertain that it could be used in our experimental conditions.

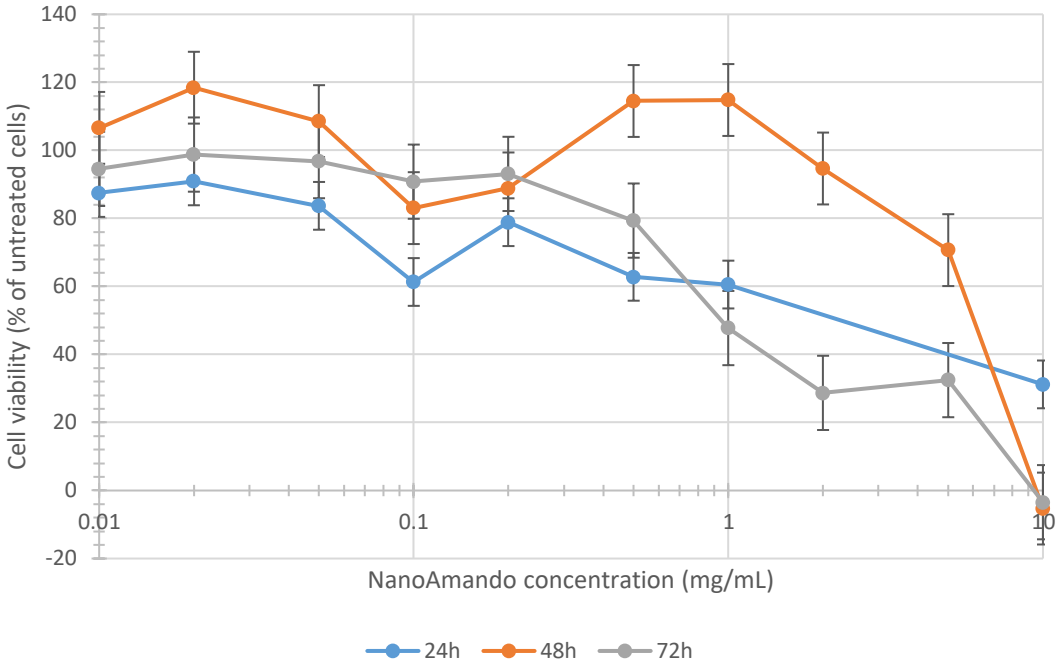

Figure 4.2-4: A673 cell viability when exposed to NanoAmando during 24, 48 and 72h. MTS assay.

Figure 4.2-4 shows a moderate toxicity of the solution on A673 cells starting from 0.2 mg/mL NanoAmando concentration. *EWS-Fli1* inhibition efficacy assays by NanoAmando:siRNA complexes were performed at siRNA final concentration from 10 to 150 nM, with a mass ratio DND:siRNA from 5:1 up to 50:1, setting the NanoAmando final concentration between ≈0.003 and 0.05 mg/mL, thus guaranteeing the absence of toxicity.

First, we tested different mass ratios, to control that the one determined for plasma-assisted and annealing hydrogenation was still adapted for NanoAmando suspension. We then tested three mass ratios, corresponding to the three zones observed in Figure 4.2-3, *e.g.* DND:siRNA mass ratio 5:1 (no aggregation, negative zeta potential), 25:1 (mass ratio used for P-DND and A-DND, but presenting a high aggregation) and 50:1 (less aggregation than 25:1 and a positive zeta potential). It was difficult to use higher mass ratios, because it would have had required to use a high quantity of siRNA, we then preferred to limit the study at a mass ratio of 50:1. The results displayed in Figure 4.2-5 demonstrate a mass ratio related inhibition efficacy of the expression of *EWS-Fli1* gene and a surprisingly high inhibitory effect up to 60% inhibition for DND:siRNA mass ratio of 25:1 and 50:1. This is the highest inhibition rate that we could obtain with this vector.

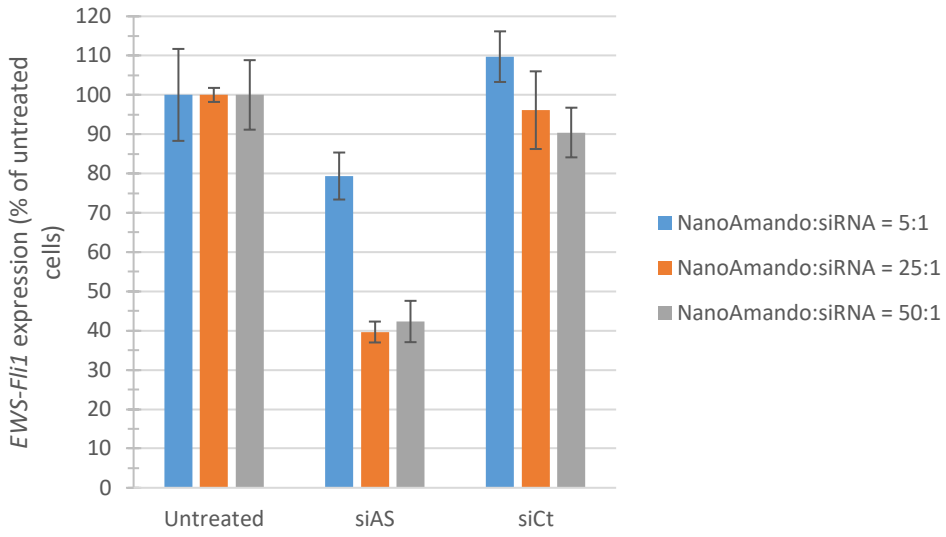

Figure 4.2-5: EWS-Fli1 inhibition by siRNA-AntiSense (siAS) or siRNA Control (siCt) [50 nM] delivered by NanaAmando on A673 cells after 24 h incubation, at different DND:siRNA mass ratios.

The effect of siRNA concentration on the inhibition efficacy was also assessed, at a fixed DND:siRNA mass ratio of 25:1. As shown in Figure 4.2-6, the inhibition efficacy increases with siRNA final concentration, after a 24-h incubation with A673 cells, but still remains below 40%. Considering the mixed results obtained in Figure 4.2-5 and Figure 4.2-6, with the same mass ratio of 25:1, one could only conclude for a great variability from an experiment to another, which was further confirmed by the fact that we could not obtain such a high inhibition again.

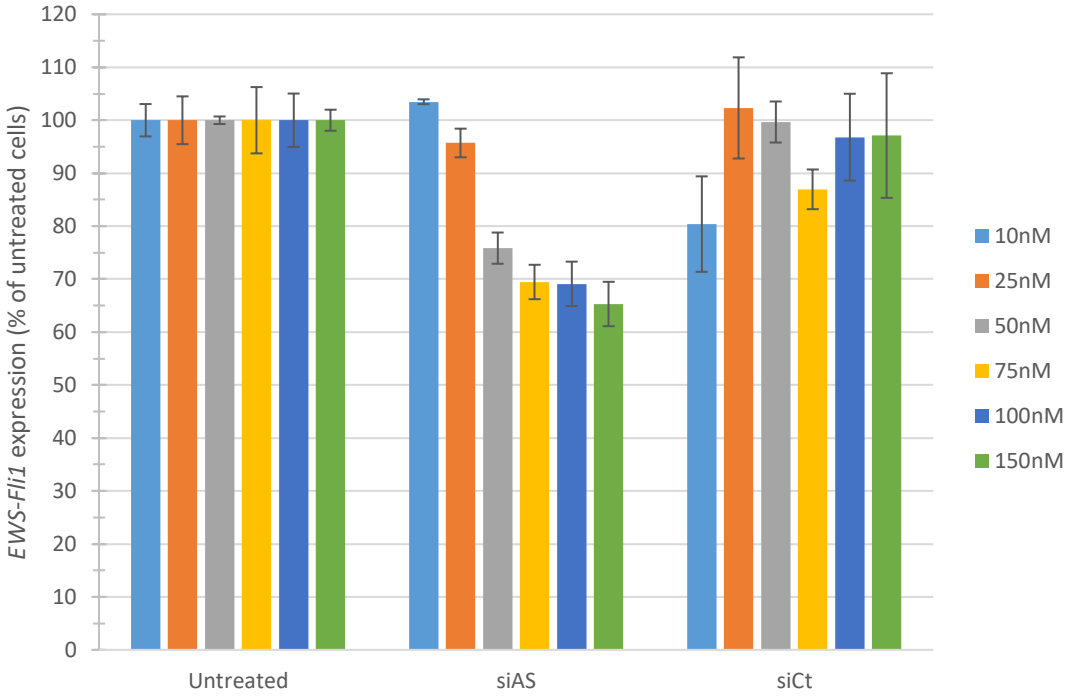

Figure 4.2-6: EWS-Fli1 gene expression inhibition depending on siRNA final concentration complexed with NanoAmando at mass ratio 25:1 (DND:siRNA) on A673 cells, after a 24 h incubation. siAS: siRNA AntiSense; siCT: siRNA Control.

We have established that siRNA binds efficiently to NanoAmando (see Figure 4.2-2). One possible reason of the low inhibition efficacy could be that the DND:siRNA complexes do not escape endosomes after endocytosis, thus preventing siRNA to reach cytoplasm and then the RISC complex. To test this hypothesis, we decided to treat the cells with chloroquine. This compound is known to promote endosomal escape [255] and it has already been used to improve gene transfer [256]. We tested this molecule at final concentrations of 100 and 200 µM, with a cell incubation of 3 hours at 37°C with chloroquine alone, prior to the addition of the NanoAmando:siRNA complexes (used at mass ratio of 25:1 and siRNA final concentration of 50 nM).

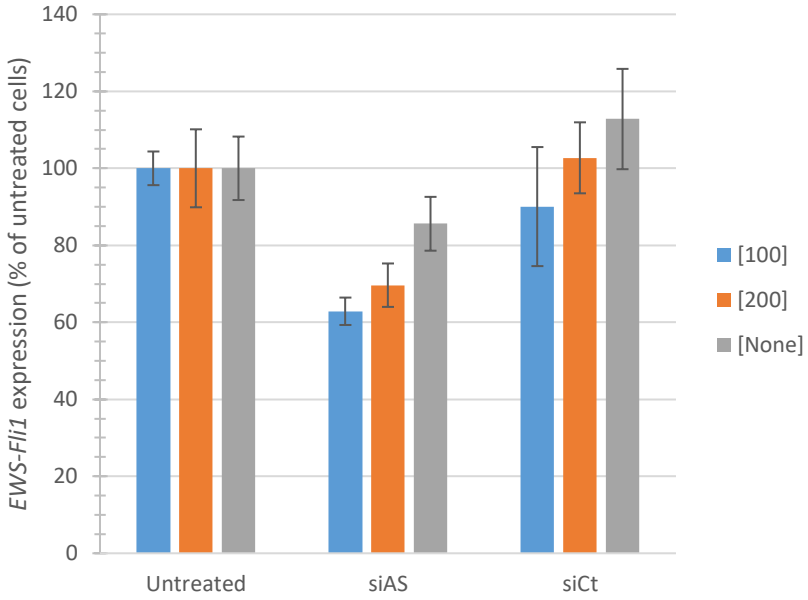

Figure 4.2-7: Effect of the addition of chloroquine prior to NanoAmando:siRNA (AS or Ct) treatment on A673 cells

Figure 4.2-7 shows that chloroquine only slightly increased *EWS-Fli1* inhibition when incubated with cells before a treatment by NanoAmando:siRNA complexes, with a final maximal inhibition of only 40%. Unexpectedly, we observed that the inhibition efficacy of *EWS-Fli1* expression seemed to decrease with an increase of chloroquine concentration, but the difference was indeed not significant. We suspect that this decrease is a toxic effect of chloroquine at the 200 µM concentration.

The potential entrapment in the vesicular compartments was examined by confocal imaging of A673 cells, after they had been incubated for 3 hours with NanoAmando:siRNA complexes, and then fixed. We used 3-color confocal microscopy to distinguish (i) the FITC-labeled siRNA in the green channel; (ii) the intrinsic fluorescence of DND (coming most likely from nitrogen-vacancies color centers) in the red channel; and (iii) the DAPI dye labeling of cell nucleus in the blue channel.

Figure 4.2-8 presents the XZ and YZ sections, at the bottom and at the right respectively, of the XY plane of the same cell. One can see the co-localization of the siRNA (green) and of NanoAmando (red) surrounding the cell nucleus under the form of aggregates (orange spots). Given the accumulation in confined dimensions, very close to the nucleus, and considering previous results [152,164], the complexes were most likely located in the endosomal or micropinocytosis compartments. A more detailed analysis by transmission electron

microscopy would be necessary to confirm this observation, but it was out of the scope of our study.

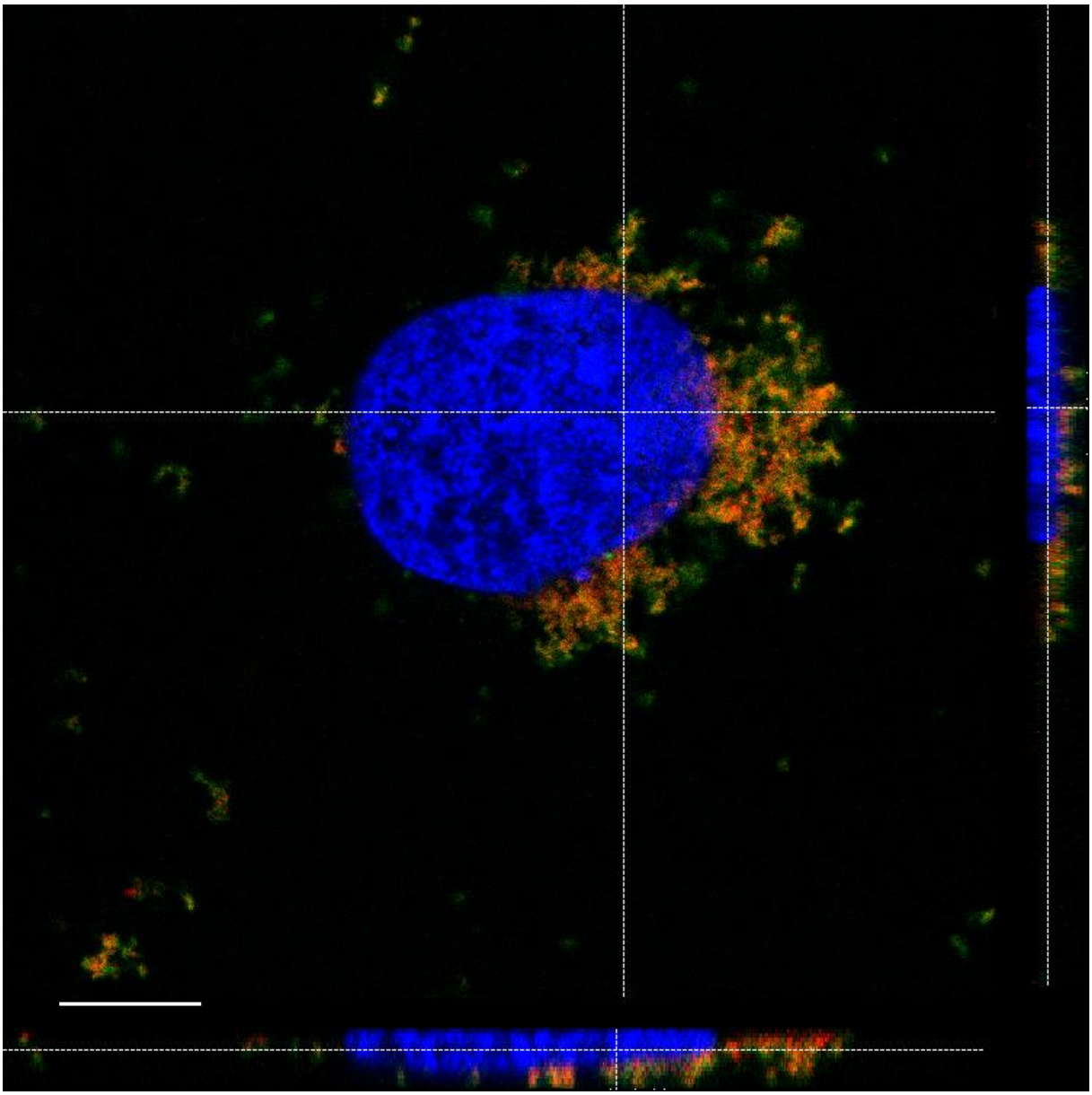

Figure 4.2-8: 3-colors staining confocal microscope image (63x magnification) of A673 cells treated with NanoAmando:siRNA-FITC. Cell nucleus: DAPI blue; NanoAmando: red; siRNA-FITC: green. Bottom: XZ section; Right: YZ section. Scale bar 10 µm

4.2.3. Conclusion of Section 4.2

We were kindly provided a commercial aqueous solution of NanoAmando®, which are DND with an ultra-small size of 3 nm that have been cationized by chemical treatment leading to a positive zeta potential of +46 mV. Thanks to their ultra-small primary size and high colloidal

stability in solution, we expected that these cationic DND would not suffer from a too high aggregation when complexed with siRNA.

Unfortunately, only a slight inhibition of the oncogene expression was observed. The reasons are not understood but this might be due to a poor desorption of the siRNA from the nanodiamonds, thus preventing the siRNA to get to the cytoplasm and to inhibit the oncogene. To test this hypothesis, it would be interesting to test different NanoAmando:siRNA mass ratios, but such developments could not be done during this PhD thesis.

Finally, a different cationization strategy was tested, relying on the covalent binding of a cationic co-polymer from the surface of nanodiamonds. For this approach, we had to switch to nanodiamond obtained by High Pressure High Temperature (HPHT) synthesis, which allows (i) more sophisticated surface functionalization methods, and (ii) to introduce a large number of nitrogen-vacancy color centers making the nanodiamonds strongly fluorescent. The downside of these improved properties is a primary size of ≈30 nm, the HPHT nanodiamonds being obtained by grinding HPHT faceted microdiamonds, and the fraction of size <30 nm being small.

4.3. Cationic polymer covalently coated to HPHT fluorescent nanodiamonds (Cop-FND)

The previous results showed that hydrogenated DNDs did not offer a good colloidal stability and that they were not able to induce a large and reproducible inhibition of the expression of *EWS-Fli1* when loaded with siRNA. A polymer-grafted HPHT nanodiamonds suspension has thus been tested to improve this low inhibition rate.

4.3.1. Methods

As a partner of the DiamESTar project, the organic chemist Petr CIGLER (Institute of Organic Chemistry and Biochemistry of the Czech Academy of Science, Prague) proposed to use a combination of silica and synthetic copolymer developed by his team [120] for the cationic functionalization of HPHT fluorescent nanodiamonds (Cop-FNDs).

Raw HPHT NDs (type Ib, with nitrogen impurity concentration of ≈200 ppm) supplied by Microdiamant Switzerland (MSY 0-0.05), were conferred **nitrogen-vacancies impurities** according to the published protocol [257]. Briefly, NDs were oxidized by air in a tube furnace, treated with a mixture of HNO_3 and HF and washed. NDs were irradiated with a 16.6 MeV proton beam to obtain a high density of vacancy, then an annealing step was carried to

form NV centers in the diamond lattice, followed by air oxidization. The resulting powder was again treated with a mixture of HNO_3 and HF and then washed. This procedure eventually provided a colloidal solution of **fluorescent ND**, with a high density of carboxyl groups at their surface, among other chemical functions.

The **silica shell** (hydrated SiO_2) was created using a modified Stöber procedure [257] which was previously described in Ref. [120,258]. Terminal methacrylate groups of the silica shell were used to grow a dense layer of **cationic copolymer**, which was synthetized via radical polymerization mainly from methacrylate monomers, as represented in Figure 4.3-1. This "grafting from" coating approach (polymer layer is polymerized from the surface of ND) leads to denser and better protecting coatings than the "grafting to" approach (polymer is synthetized in solution and then is attached on the surface) (cf. Subsection 2.3.3) [120].

Positive zeta potential value of polymeric NDs, of about +50mV (in pure deionized water), allows the binding of siRNA molecules on the surfaces via electrostatic bond. Moreover, due to electrosteric stabilization, this polymer coating better prevents NDs from rapid aggregation in biological solutions, improves colloidal stability, confers the ability to protect siRNA molecules against enzymatic cleavage and exhibits high binding capacity.

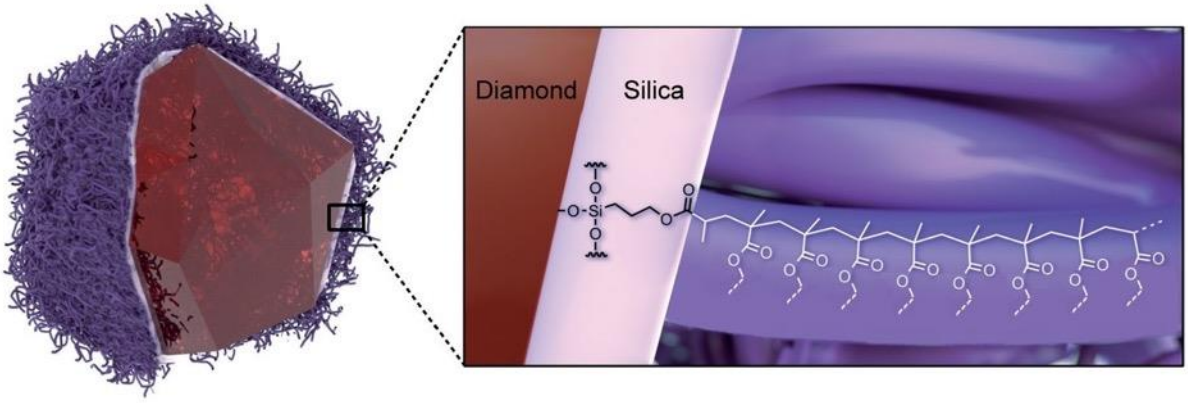

Figure 4.3-1: Schematic structure of the polymer coating on a fluorescent nanodiamond crystal. Redrawn from Ref. [120]

As we will show in the following sections, the combination of fluorescence and cationic polymer coating has allowed us (i) to deliver siRNA into Ewing sarcoma cells *in vitro* inducing a high inhibition of *EWS-Fli1* expression, and (ii) to track the ND:siRNA complexes *in vivo*.

4.3.2. *In vitro* efficacy of the Cop-FND:siRNA complex

The Cop-FND has been developed and fully studied by our partner in IOCB, Prague. Nevertheless, we carried complementary physico-chemical characterization assays. Furthermore, our Czech partners provided us with Cop-FND suspensions with a relative concentration. The following results will thus not be presented in function of concentrations but will be presented thanks to mass ratios between the relative Cop-FND concentration and the siRNA concentration.

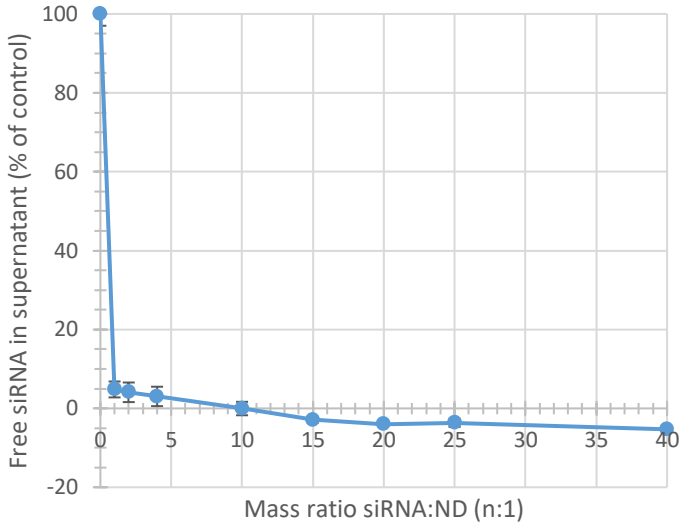

Figure 4.3-2: siRNA binding to Cop-FND depending on ND:siRNA mass ratio. Final siRNA concentration: 50 nM

After having observed a very good stability of the complex at different mass ratios (results not presented here) and after having shown that siRNA was well bound to Cop-FNDs (Figure 4.3-2) at the established ND:siRNA mass ratio of 3.9:1, the efficacy to inhibit *EWS-Fli1* gene expression needed to be assessed. We tested different final concentration of siRNA and different Cop-FND batches, as shown in Figure 4.3-3.

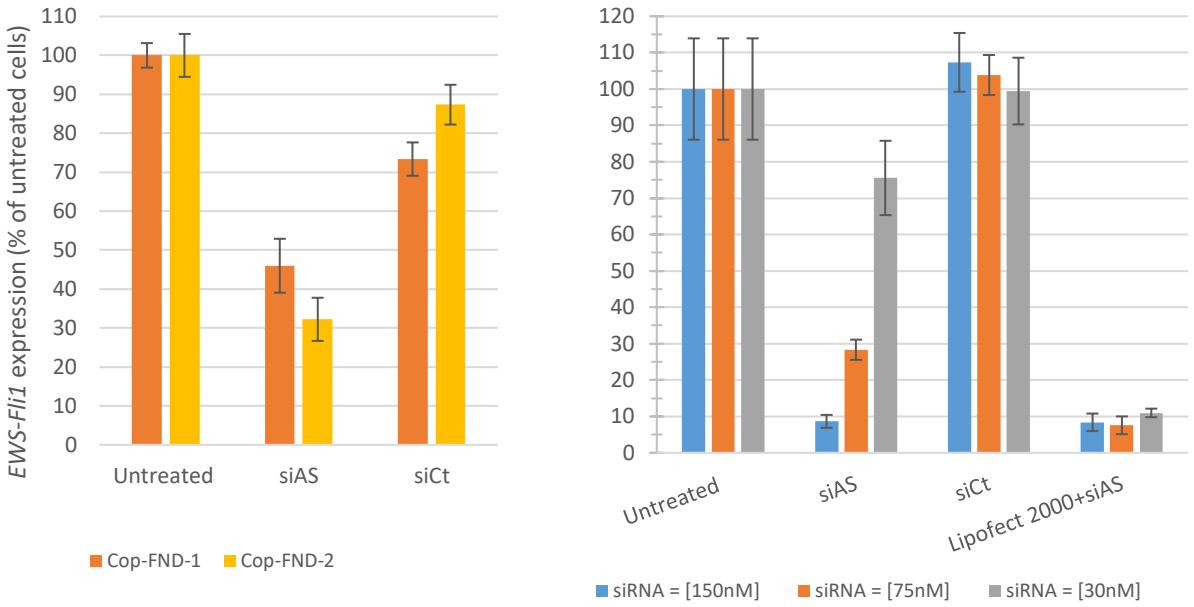

Figure 4.3-3: EWS-Fli1 inhibition by Cop-FND complexed with siRNA AntiSense (siAS) or Control (siCt). Left: comparison of two batches, siRNA final concentration 50 nM, 24 h incubation, Cop-FND:siRNA mass ratio = 3.9. Right: Dose/effect of siRNA final concentration with Cop-FND-1, 24 h incubation, Cop-FND:siRNA mass ratio = 3.9.

First, one can see a larger inhibition of *EWS-Fli1* gene expression and no dependence on the batch, on the contrary to cationic DNDs. Second, one can see a clear dose/effect relationship: when siRNA final concentration was increased, *EWS-Fli1* expression inhibition also increased. At 75 nM siRNA final concentration, we obtained a 70%-inhibition of *EWS-Fli1*, without having the trouble of a too high concentration inducing off-target effects. Interestingly, for the highest concentration of siRNA, the inhibition efficacy even reached the value obtained with Lipofectamine 2000, which has to be used in a serum-free medium, as instructed by the producer, while Cop-FND:siRNA was applied in presence of serum, allowing their use for *in vivo* purposes.

4.3.3. Conclusion of Section 4.3

The results presented in this section showed that the silica-copolymer functionalization enabled to obtain a gene expression inhibition efficacy as high as with commercial lipofectants, which however only work in serum-free conditions, contrary to the Cop-FND which works in full medium, closer to the *in vivo* situation.

Moreover, cationic Cop-FND is superior to previous cationic FND strategies published by our teams [152]. In the latter, Poly-Ethylene-Imine (PEI) cationic polymer chains were

adsorbed on FND, to obtain the cationic property required for siRNA electrostatic binding. This approach allowed to achieve *in vitro* a gene inhibition of 50%, but some ambiguity remained regarding the exact nature of the transfection agent. Indeed, PEI alone could act as a transfection agent for siRNA, and since it was not covalently linked to FNDs, one could not exclude that the transfection which led to the gene silencing resulted from PEI:siRNA complexes internalization, detached from FNDs and entering separately. The use of Cop-FND prevents such a scenario, and the high inhibition efficiency observed is a strong indication that the whole Cop-FND:siRNA complexes were internalized at once in cells. Therefore, we can ascertain that Cop-FND is the transfection agent leading to an effective delivery of siRNA directed against *EWS-Fli1* junction oncogene, in cultured Ewing sarcoma cells.

We therefore decided to use this vector for *in vivo* biodistribution assays, relying on FND intrinsic fluorescence properties. In my PhD work, I only focused on the tissue distribution of Cop-FND:siRNA complexes, after intravenous injection in mouse bearing human xenografted Ewing sarcoma cells; the *in vivo* efficacy experiments were carried out in a partner's laboratory. These results were complemented by biodistribution and elimination study of tritiated annealed-DND. The results we obtained *in vivo* are presented in the following chapter.

Chapter 5

Biodistribution of ^{3}H-DND and quantification of Cop-ND$_{HPHT}$ nanodiamonds in organ mice sections

The previous chapter presented the physico-chemical characterization and *in vitro* efficacy on Ewing Sarcoma cells of various types of nanodiamonds, whose surfaces were functionalized by different means. We demonstrated that only one platform exhibited a reliable inhibition efficacy, the Cop-FND. The Cop-FNDs are meant to be tested for their *in vivo* efficacy to deliver active siRNA. Such study needs to be accompanied by a tissue distribution investigation, in order to assess if these complexes would accumulate in a healthy organ, with possible toxic effects. Even though, no positive results on the inhibition of the oncogene were obtained *in vitro* with the annealing treatment, an *in vivo* study is still worth to be conducted as in some cases, nanovectors can deliver treatments that reveals to be active *in vivo* and not *in vitro* [259]. Moreover, owing to their radioactivity, annealed tritiated NDs bring new information on biodistribution and elimination of the DNDs.

This chapter will first present the biodistribution and elimination results obtained with the tritiated nanodiamonds, and then will present the innovative setup that was used to detect and quantify the Cop-FND in sections of mice's organs.

5.1. Tissue biodistribution of tritiated DND in mice

5.1.1. Methods

Nude mice were used for this assay, in accordance with the ethical project submitted and approved by the ethical committee regulating the animal facility in Gustave Roussy. One day before cells grafting, nude mice were gamma irradiated at a dose of 5 Gy. Mice were then injected subcutaneously with 3.10^6 A673 cells, on one flank, and treatment was not begun until the tumor had reached a volume of 200 mm^3. Radioactive DNDs were used for this study after an annealing treatment under tritium atmosphere, their preparation was presented in detail in Section 4.1.1.2. Tritium diffuses deep inside the nanoparticles as demonstrated by GIRARD *et al.* [251], and do not only form ^{3}H-C bonds at the surface. Labile tritium was removed by intensive washing in appropriate conditions [251], but no thermodesorption of weakly bond ^{3}H was done like in Ref. [251], since it would have resulted in DND that are no more cationic in aqueous suspension. The annealed tritiated DND (^{3}H-DND) were dispersed in water and then covered with siRNA via electrostatic interactions (see Appendix A-5). Specific measures were undertaken to contain the radioactivity of the ^{3}H-DND.

After the tumor had reached its optimal volume, the mice were injected in the caudal vein with 100 µL of a solution of ^{3}H-DND:siRNA (mass ratio= 4.9:1, siRNA final concentration 5 mg/kg) or with a solution of ^{3}H-DND. The high siRNA concentration injected, which previously showed a good inhibition rate [260], required us to use about the same mass ratio as the one established for Cop-FND complexation. This quantity of ^{3}H-DND corresponds to an injected radioactive dose of 2,425 µCi/mice. The animals were kept in a metabolism cage to collect urine and feces, and sacrificed 24h later by cervical dislocation, in accordance with the ethic committee regulations. Three mice were used for each condition.

The organs of interest (*i.e.* heart, lung, kidney, spleen, liver and tumor) were then collected and the urine and feces were retrieved from the time of injection until the sacrifice. The blood was collected after sacrifice in the pulmonary cavity. A part of each organ (100 mg) was then put in 1mL of Solvable (Perkin-Elmer, USA) for 4h at 60°C, 1h at 60°C for blood, in order to obtain a liquid phase. The feces were first put in 200 µL of H_2O at room temperature and then 1 mL of the Solvable solution was added for 2h at 60°C. Some samples (*i.e.* spleen, heart,

liver, lung, feces) were dark and opaque, making them difficult to analyze. Those samples were then treated by 100 µL of H_2O_2, to obtain a clear solution. Finally, 10 mL of a liquid scintillation cocktail, Ultima Gold (Perkin-Elmer), was added to each sample and the radioactivity was measured by liquid scintillation on a liquid scintillation counter Wallac 1409 (Perkin-Elmer).

One of the limitations of the tritium labeling method is the risk of ^{3}H exchange with water. Before injection, the ^{3}H-DND solution was ultracentrifuged for 3h at 40,000 rpm using a 50Ti rotor in a Beckman XL90 ultracentrifuge (Beckman Coulter, USA). The supernatant contained 3.6% of the total radioactivity. This fraction could correspond to either the ^{3}H exchanged with cold H from water or to a fraction of small DNDs that stayed in the supernatant despite these ultracentrifugation conditions. These parameters were taken into account for the interpretation of the results.

5.1.2. Biodistribution in organ mice

A first representation of the distribution of ^{3}H-DND in the different organs, feces and urine is given in Figure 5.1-1. The overall radioactivity measured in the different tissues and urine are represented, as counts per minute (cpm) given for one gram of tissue or one mL of urine. First, one can observe that almost no difference appeared between the injection of bare ^{3}H-DND and of ^{3}H-DND:siRNA. Second, one can see that the spleen, the liver and the lung displayed more than ten-fold more cpm/g than all the other organs. Almost the same level of radioactivity was detected in the heart, tumor and blood. Urine and feces presented the lowest levels.

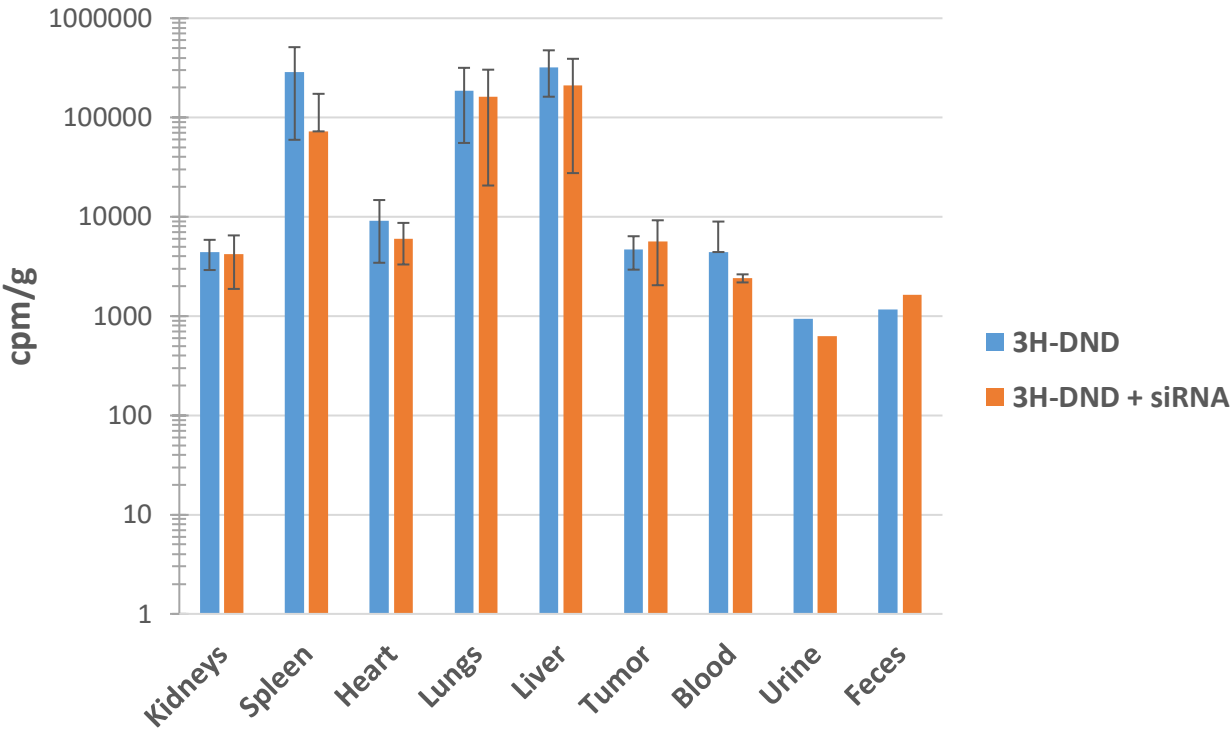

Figure 5.1-1: ^{3}H-DND distribution (counts per minutes/g; logarithmic scale) in the different organs, the feces and the urine of mice. n=3 mice for 3H-DND and n=2 for 3H-DND+siRNA. Error bars for urine and feces are not displayed because the urine and feces from the 3 mice, which were in the same cage, could not be differentiated and were then pooled in a single sample. Sacrifice 24h after injection. Error bars = standard deviation.

Moreover, by comparing the total amount of radioactivity collected in the different organs to the one of the injected solution, we estimated that we collected about 35% of the total injected radioactivity. We also measured the blood radioactivity, considering that we have collected only 10% of the total blood volume. The results can then be displayed differently: Figure 5.1-2 presents the amount of radioactivity extrapolated to the whole organ and expressed relatively to the injected dose. Owing to their larger mass, the liver and the lung exhibit an even more accentuated difference from the other organs in this representation. Despite a smaller size, the spleen also presents a high rate of radioactivity. Indeed, these three organs collected just by themselves almost the overall radioactivity that was measured. The liver was the organ where the highest amount of radioactivity was measured, with 26.4%±15.6% (without siRNA) of the total injected dose (24.2%±2.2% with siRNA), followed by the spleen (5%±3.7% without siRNA, 1.26%±1.4% with siRNA) and the lungs (3.4%±2.3% without siRNA, 3.5%±0.8% with siRNA).

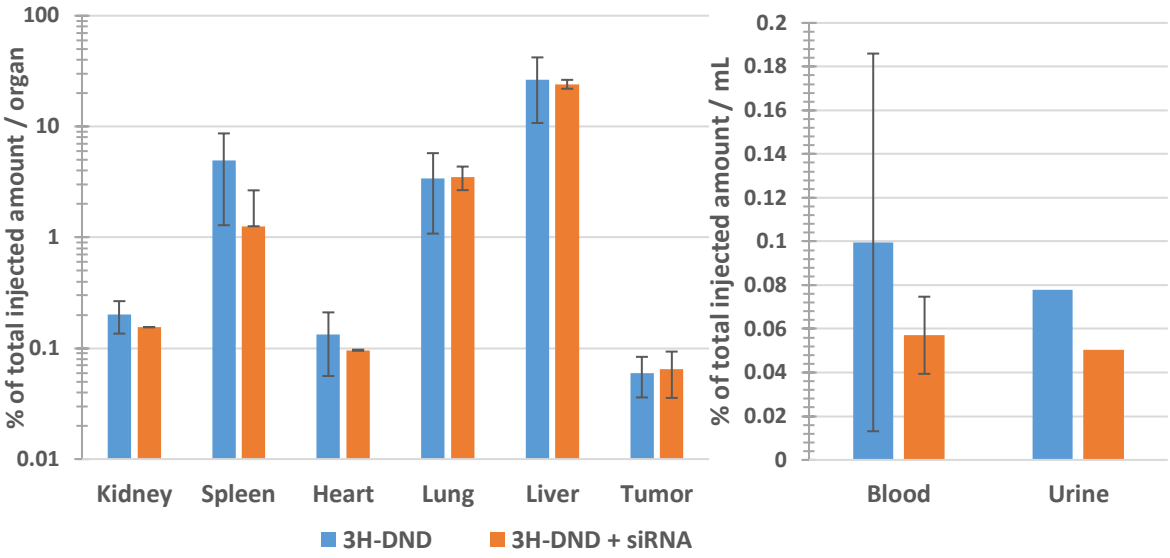

Figure 5.1-2: ^{3}H-DND distribution as a percentage of the total radioactivity injected relative to the whole organ (logarithmic scale, left graph) or to one mL or fluid (right graph). n=3 mice for 3H-DND and n=2 for 3H-DND+siRNA. Sacrifice 24h after injection. Error bars = standard deviation. No error bar is displayed for the urine, as it was collected for the 3 mice in the same cage.

This representation enables to distinguish in more details the difference of radioactivity between the kidneys, the heart and the tumor. It appeared that the kidneys presented twice higher radioactivity levels (0.2%±0.06 without siRNA, 0.15%±0.0003 with siRNA) compared to the heart (0.13%±0.08 without siRNA, 0.09%±0.001 with siRNA), and four-fold more than the tumor (0.06%±0.02 without siRNA, 0.06%±0.03 with siRNA). Some radioactivity was also detected in the urine but at low levels (0.08% without siRNA, 0.05% with siRNA).

5.1.3. Conclusion of Section 5.1

In this section, we performed a 24h-biodistribution assay of ^{3}H-DNDs injected in nude mice with or without siRNA attached to them.

It appeared from this preliminary *in vivo* assay that ^{3}H-DND preferentially accumulated in the liver, confirming previous studies [160]. Also, the levels detected in the feces are higher (1160 cpm/g without siRNA, 1629 cpm/g with siRNA) than in the urine (941 cpm/g without siRNA, 625 cpm/g with siRNA), showing that the liver excretion might be facilitated compared to the kidney excretion through the urine. Furthermore, the spleen is the second organ of choice in which the DND accumulated, correlating the observations of an uptake by the reticuloendothelial system [158]. Finally, the lung is the third organ in which the highest level of radioactivity was detected. The alveolar macrophages of this tissue are part of the

RES and could thus uptake the DNDs. Note that for each of these three organs, more than 3% of radioactivity of the injected solution was detected. This radioactivity was higher than the residual radioactivity detected in the supernatant of the injected solution (considered as the resulting from ^{3}H desorption from ^{3}H-DND), ensuring that the detected radioactivity cannot be entirely due to the desorption of ^{3}H in the suspension.

Interestingly, not much radioactivity was found in the kidneys, and even a lower level of radioactivity was detected in the urine. A medium speed centrifugation (90 min, 16,100 *g*, Eppendorf) was conducted on the urine. A solid pellet was obtained, and 23% of radioactive material was recovered in this pellet. This may represent the fraction of excreted DND by kidney filtration. Nevertheless, the very low radioactivity levels detected did not allow to conclude on the kidney excretion as a potential excretion pathway.

Finally, the tumor and the heart are the two organs with the lowest measured radioactivity. The DNDs may already have been gone through the tumor by the time of sacrifice, and hopefully, they might have dropped off their cargoes on the way. This could be studied by a gene expression assay to detect possible inhibition effect of *EWS-Fli1* expression induced by siRNA. Tissue distribution studies at shorter time analysis would also be useful. The heart was drained as much as possible from the blood present in the atrium and the ventricules, the sample was then mostly composed of the myocardium tissue and it seems that no diffusion in the muscle occurred.

The next section presents the organ distribution of Cop-FND, realized thanks to a fluorescence wide-field time-gated setup, which will be fully described, and the quantification of those FND in the different organs. Our setup also enabled us to identify in which cells the FNDs were accumulating in the liver.

5.2. Quantification of tissue distribution in mice by a high-throughput/high-content time-gated imaging setup

After having demonstrated the efficacy for the Cop-FND:siRNA complexes to inhibit the *EWS-Fli1* oncogene expression (cf. Section 4.3), the biodistribution of these complexes was investigated after injection in mice with an Ewing sarcoma xenografted tumor. The *in vivo* efficacy assays will be performed by Ibane ABASOLO-OLAORTUA's team at CIBBIM-Nanomedicine-VHIR laboratory, Barcelona, Spain, within the DiamESTar project consortium.

We took advantage of the "long" radiative lifetime of NV color centers that are responsible for FND fluorescence (cf. Section 2.2.3), to improve the signal-to-background imaging. To this aim, we developed an automatized time-gated fluorescence microscope capable of high-content imaging. This section describes the setup and the quantitative results obtained with it.

5.2.1. Methods

Nude mice were used for this assay, in accordance with the ethical project submitted and approved by the ethical committee regulating the animal facility in Gustave Roussy. The mice were injected subcutaneously with 5.10^6 A673 cells, on one flank, and treatment was not begun until the tumor had reached a volume of 200 mm^3. After reaching this point, 200 µL of Cop-FND coupled with siRNA, according to the protocol described in Appendix A-9, were injected intravenously in the mouse's caudal vein with a final siRNA concentration of 1 mg/kg and a FND:siRNA mass ratio of 3.9:1. Mice were sacrificed 24 h after the injection, by cervical dislocation in accordance with ethical procedures. Heart, lungs, liver, spleen, kidneys and tumor were collected and stored in paraformaldehyde 4%, then embedded in paraffin and sectioned (thickness ≈3 µm). Sections were either let without any staining or colored with Hematoxylin/Eosin/Saffron (HES) staining. Sections of organs were then observed under a 60x microscope objective from a "home-made" time-gated fluorescence microscope, developed by François TREUSSART'S team in collaboration with Xavier DELEN (*Laboratoire Charles Fabry*, Palaiseau) who built the pulsed laser source, and Alexander PAPINE (IMSTAR S.A., Paris) who designed the acquisition software. Fluorescence and 3-colors images of the entire organ were acquired under the form of a mosaic of fields of view, of size ≈110×110 µm each. The mosaic of the entire organ section was reconstructed using Imstar software.

5.2.2. Setup description

The characteristics and advantages of time-gated imaging has already been presented in Section 2.2.3, allowing an enhanced detection of fluorescence signal, emitted by the NV centers embedded in FNDs, compared to tissue autofluorescence. A schematic representation of our setup is presented in Figure 5.2-1. It relies on an inverted fluorescence microscope (Nikon Ti-E) with motorized stage and filter wheel. The excitation source is a home-made pulsed laser beam (emitting at 532 nm wavelength) expanded for wide-field illumination. The detection is made with an intensified CCD (ICCD) array detector (PI-Max3, Princeton Instruments, USA). The later contains a high precision oscillator that serves as the master

clock for acquisition timing and is used to trigger the laser pulses. The ICCD acquisition parameters (repetition rate, detection gate delay relative to the pulse, gate duration, and number of gates per image) are transferred to the ICCD through the software developed by IMSTAR which also manages the microscope motors, the white light illumination sources, collects the ICCD images, and finally analyzes the data. The acquisition time for each field of view was set at 350 ms, with an intensifier gain of 5 for the ICCD array detector.

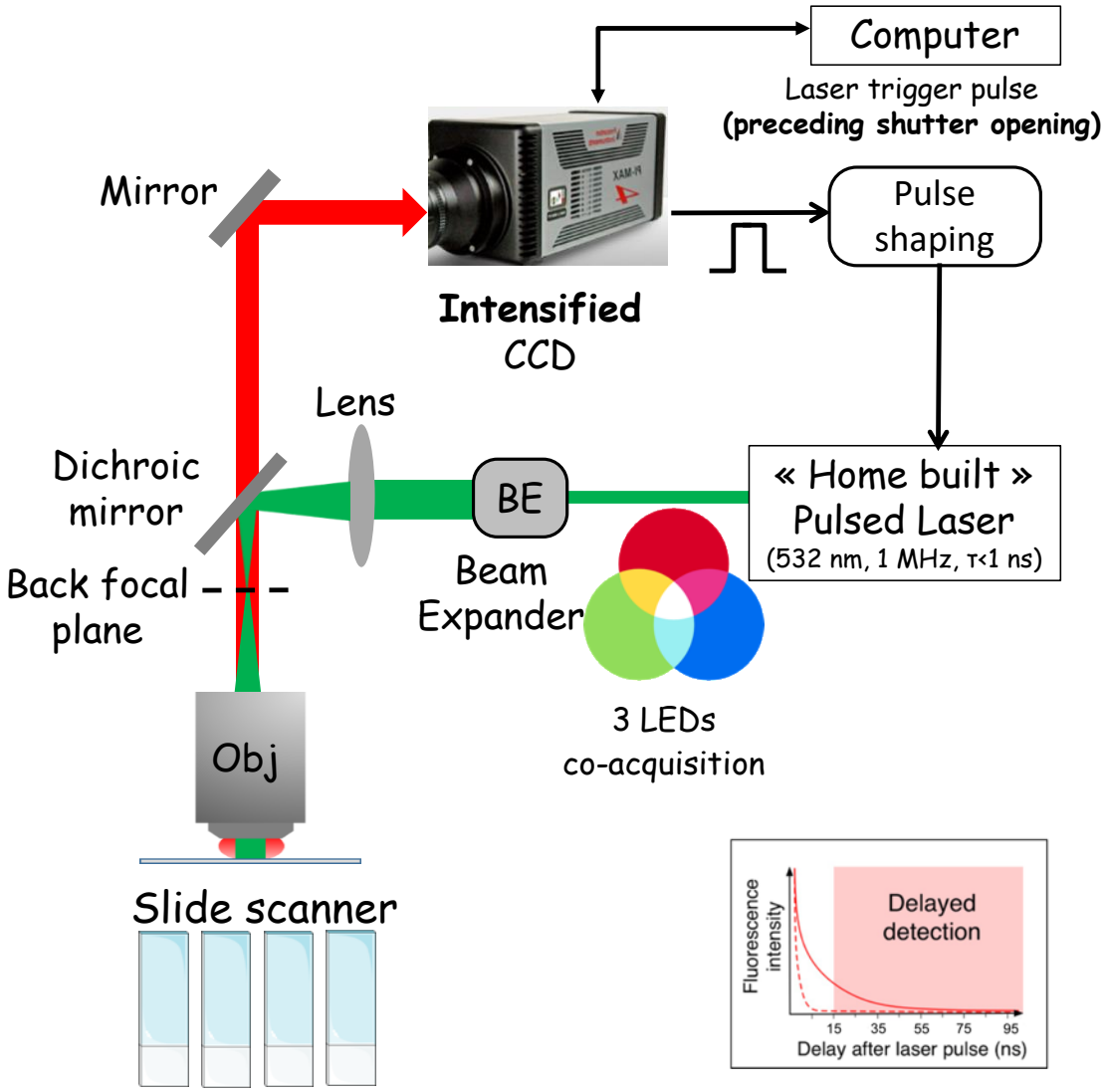

Figure 5.2-1: Schematic representation of the time-gated imaging setup. The setup allows a co-acquisition of both fluorescence and wide-field signal for each fields of view. The 'home-built' pulsed laser is set to emit at 532 nm to excite NV centers of FNDs, at a frequency of 1 MHz. The automated slide scanner allows to scan four slides in a row. The inset shows the detection gate delay, set at 15 ns to avoid collecting the autofluorescence signal of the tissue.

We made the choice to acquire two images at different focusing planes (total acquisition width set at 3 µm) in order to allow detection of all FNDs in the whole depth of the organ section. Thus, each fields of view were exposed twice during 350 ms. Furthermore, the acquisitions were made with a 60× magnification oil immersion objective (1 pixel ≈ 200 nm), Numerical Aperture=1.4, allowing to obtain a high optical resolution, still limited by diffraction to about 300 nm (considering 700 nm as the maximum of the emission spectrum of FNDs). This resolution makes possible to resolve sub-micrometer FNDs aggregates. In addition to the fluorescence acquisition, the microscope also recorded a white light bright-field image resulting from the successive acquisition of Red-Green-Blue images, each illuminated by a single-color LED embedded in a condenser. Both FND fluorescence and 3-LED images were acquired successively, so that they were intrinsically co-registered to the same field of view. This procedure allowed us to precisely localize FNDs relative to the tissue structure, with a subcellular resolution.

Regarding the home-built pulsed laser, a more detailed schematic is presented in Figure 5.2-2. It was used at 1 MHz repetition rate and could deliver a tunable average power, able to reach 1 W but we limited this power to only 25 mW. This value allowed us to clearly detect single FNDs, while avoiding the saturation of the signal due to aggregates, and without inducing too much photobleaching damage to the tissue. Note that some organs were acquired with a power of 50 mW, but thanks to the linearity of the acquisition setup, demonstrated in Appendix C, the fluorescence intensity measures were simply divided by two-fold to allow comparison to data acquired at 25 mW excitation power.

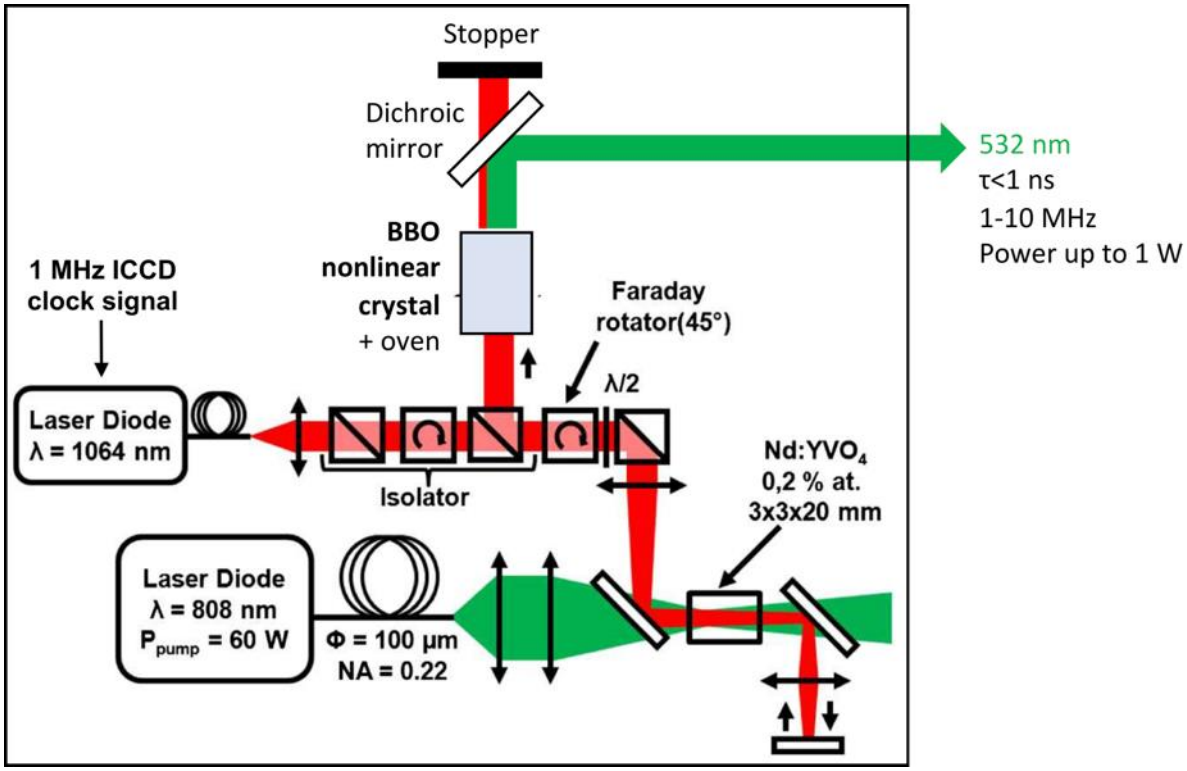

Figure 5.2-2: Schematic representation of the 532 nm pulsed laser setup. The laser rely on a 1064 nm laser source that can be triggered to deliver sub-nanosecond pulses, and that is injected in a neodymium doped vanadate crystal (Nd:YVO_4) pumped with a 60 W continuous wave diode laser at 808 nm, amplifying the 1064 nm beam after a double passage though the crystal. The amplified 1064 nm beam (power up to 4 W) is frequency doubled in a 532 nm beam, using a LBO nonlinear crystal (Type 2 non-critical phase-matching) placed in an oven (set at 151°C) to ensure the phase matching conditions required for optimal conversion. Adapted from Ref. [261].

For each organ section, we recorded up to 15,000 fields of view of ≈110x110 µm in size each. In addition, the motorized microscope stage accommodates a 4-slides charger mount so that we could launch the fully automatized acquisition of 4 organ sections at once. Overall, we could acquire an entire organ (size between 25 and 110 mm^2) in 6 to 10 hours, and it took up to three days to acquire four slides in the charger, with organs sizes between 25 and 110 mm^2.

Figure 5.2-3 shows one high-quality image obtained thanks to this setup. One can see that the entire organ (here liver) section, was acquired (size ≈100mm^2) and that it is possible to zoom in the picture, without any loss of resolution, and to go up to the cellular scale. This remarkable resolution is possible thanks to the high magnification that was utilized.

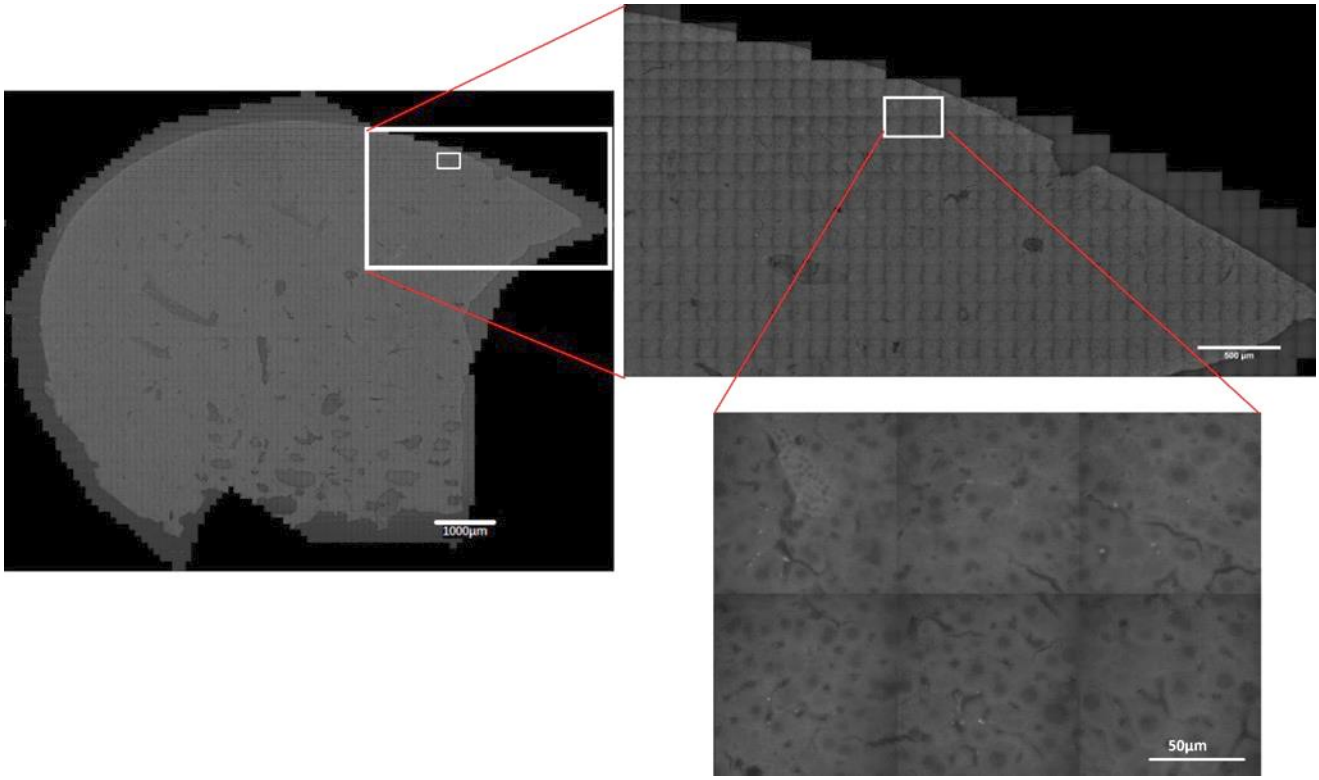

Figure 5.2-3: Fluorescence images of a mouse liver section, from the macroscopic scale up to the microscopic scale. The three images are extracted from the same scan, showing the high resolution while zooming in the image. Note that this acquisition was done on a HES-stained section, adding some fluorescence background despite the time-delayed detection.

5.2.3. Determining the optimal protocol for FND detection in tissue sections

For each organ, we had at our disposal two types of sections: some stained with Hematoxylin/Eosin/Saffron (HES) and others without any staining. The HES staining is one of the most used staining for histopathologic analysis, enabling the detection of the different structures and cells present in a sample. This specific staining allows to color the cells nuclei in blue, thanks to the hematoxylin. The eosin stains the eosinophilic structures, composed of extracellular or intracellular proteins, in various shades of red and purple. Typically, cytoplasm is stained with eosin. The saffron eases the coloration of collagen, thus staining the connective tissues in shades of orange.

We started acquiring fluorescence images using the HES-stained sections, so that we could get at the same time the bright field color image (through RGB illumination) and infer the FND subcellular location by superimposing the fluorescence to all channels. Figure 5.2-4 presents an example of field of view of the fluorescence channel of a HES-stained section.

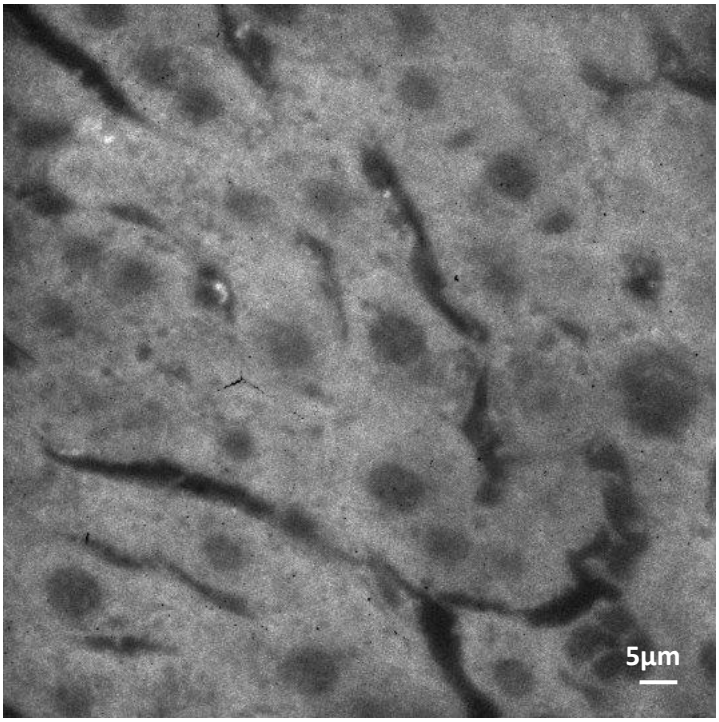

Figure 5.2-4: Time-gated fluorescence image of a HES-stained section of the liver. 60× magnification objective, 1 pixel ≈ 200 nm. White bright spots present in the image are Cop-FNDs.

Unfortunately, it appeared that the staining induced a very high level of auto-fluorescence, very hard to get rid of, even with the time-gated setup. We tried to bleach the tissue to reduce the fluorescence, by exposing it under a laser illumination for several minutes. Although it was efficient to greatly enhance the FND signal to background ratio, it could hardly be applied because it would have considerably increased the acquisition time. Indeed, the most practical method consisted in imposing two consecutive exposures of the same field of view. Despite the very short exposition time (2x350 ms, twice, because of the two-acquisitions in the Z-axis), this approach allowed to reduce the background fluorescence up to 40 %, as presented in Figure 5.2-5. One can see from the table included in Figure 5.2-5-C, that during the acquisition step, after a first bleaching step, the mean fluorescence intensity remained between 110 and 90% for FND sites, but it dropped down to 63% for the tissue. Note that for the already dark regions, the loss of signal is less important, explaining some of the high values for the column '% of the bleaching step signal after the acquisition'. The ambiguous spots from a single exposition were then more easily distinguishable, as their fluorescence did not vary between the two expositions. Indeed, if the fluorescence intensity value did not

decrease from one exposition to another, it showed that the spot most probably contained a FND. This parameter was included in our detection program, as described in Section 5.2.4.

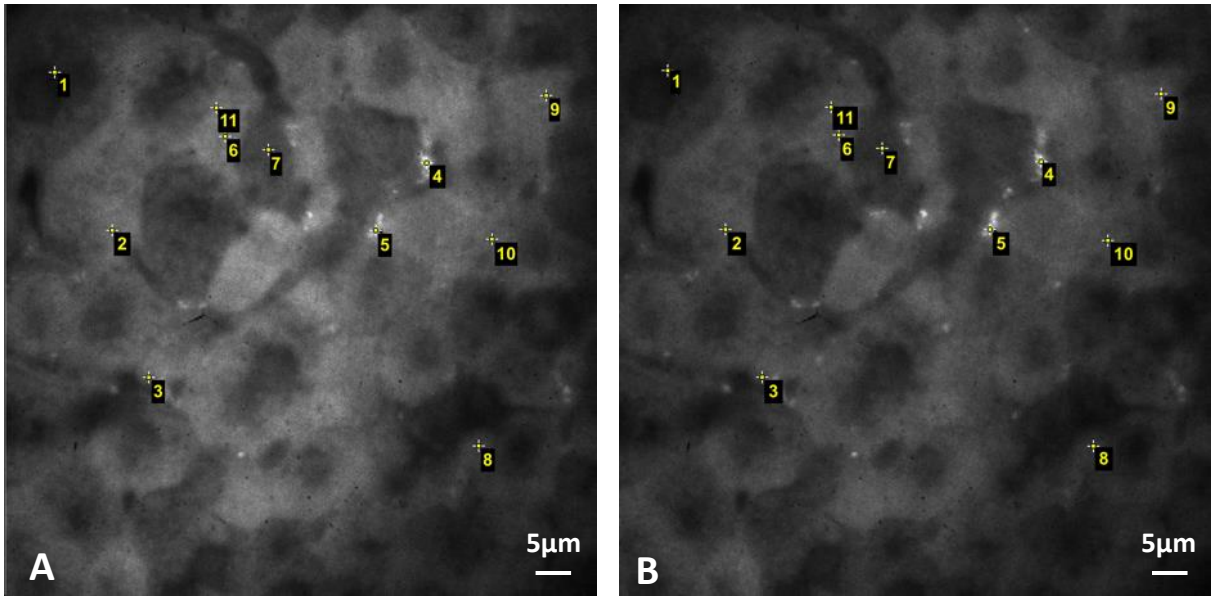

C

Point	Mean fluorescence intensity bleaching step	Mean fluorescence intensity acquisition step	% of the bleaching step signal after the acquisition
1	30	26	87
2	108	74	69
3	96	67	70
4	220	208	95
5	206	215	104
6	116	73	63
7	68	45	66
8	58	51	88
9	90	78	87
10	88	70	80
11	113	77	68

Figure 5.2-5: Time-gated fluorescence image of HES-stained liver section at 60× magnification. Images (A) and (B) present the same field of view. (A) Bleaching step image. (B) Acquisition step image. (C) Table showing the mean fluorescence intensity of various spots that can either be due to HES staining or tissue autofluorescence or to FNDs. Thanks to a comparison of the fluorescence intensity between the acquisition and bleaching steps we should be able to discriminate between FNDs and other source of localized fluorescence. ROI #4 and #5 fluorescence intensity was stable to ±5%, which is an indication that they correspond to FNDs.

We then acquired the FND signal on **non-HES-stained** organ sections, with the same process (*i.e.* two consecutive exposures of the same field of view). As presented in Figure 5.2-6, the absence of HES staining provided a much lower background fluorescence, allowing to distinguish more clearly FNDs in the complex organ sections, and to quantify them accurately.

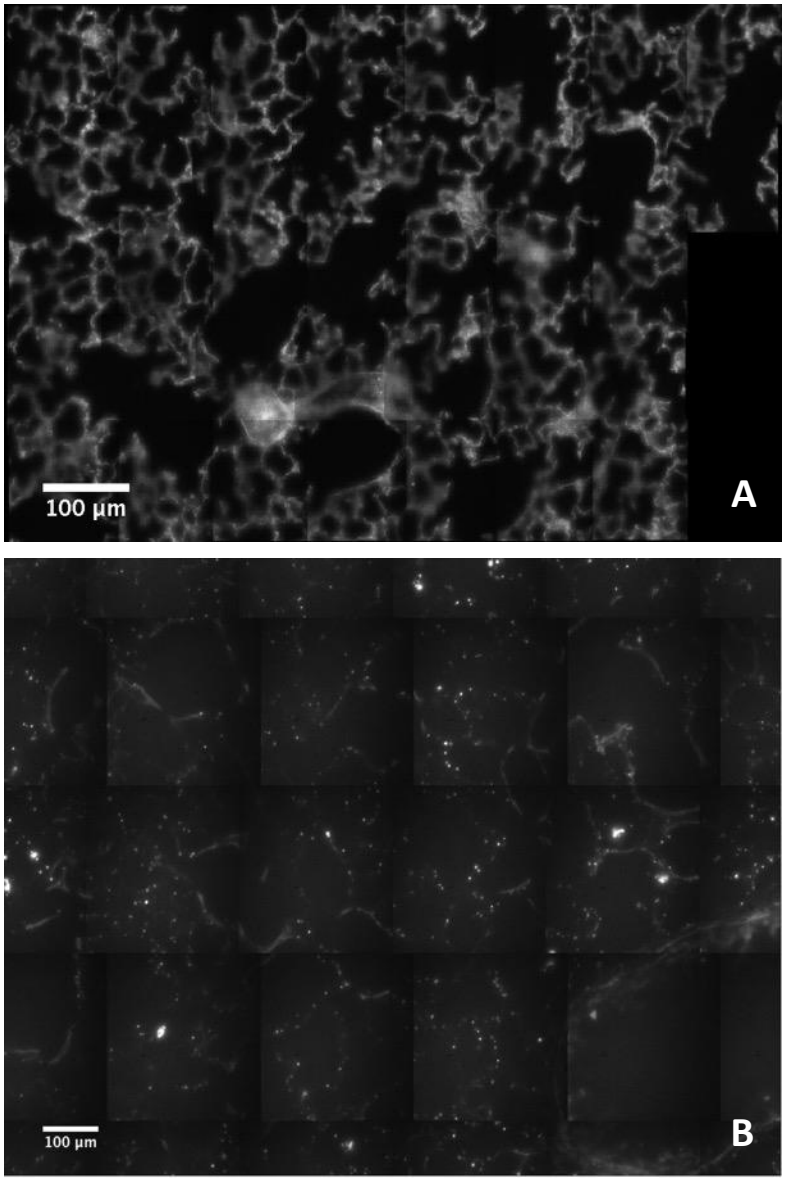

Figure 5.2-6: Comparison of FND fluorescence channel with or without HES staining for a lung section of the same mouse. (A) with HES staining; (B) Without staining. 60× magnification.

5.2.4. Automatic detection of the FNDs in the organ sections

The FNDs were automatically detected, thanks to an image analysis software developed by Alexandre PAPINE from Imstar S.A.. Briefly, small brighter elements and details were first detected by a Top-hat filter, and a ROI identifier was assigned to each of them, returning the elements being brighter than their surroundings. This first image processing did not include any size differentiation. Then, I tailored a filtering program for every organ, taking into account the fluorescence and the anatomy of each tissue, these parameters being different

from one another. This program included a filtering of the ROIs according to the following parameters:

- Value of the **ratio between the ROI's average intensity level and the average fluorescence level of the field of view (global contrast)**. This parameter can be associated to the contrast of the ROI compared to the global image. The ROIs were considered as FND only within a certain range of values;
- **Value of the local contrast**: a small ring (few pixels) was selected around the detected object and the ratio of the fluorescence levels was calculated between the average fluorescence within the object and the one of the ring. This allowed to eliminate the ROIs with low contrast, that were most probably false positives. Figure 5.2-7 illustrate the need of such parameter (same field of view on the three images): image A presents more ROIs, compared to image B, on which a threshold was applied. When compared to image C, the wrongly detected ROIs in A are most likely false positives;

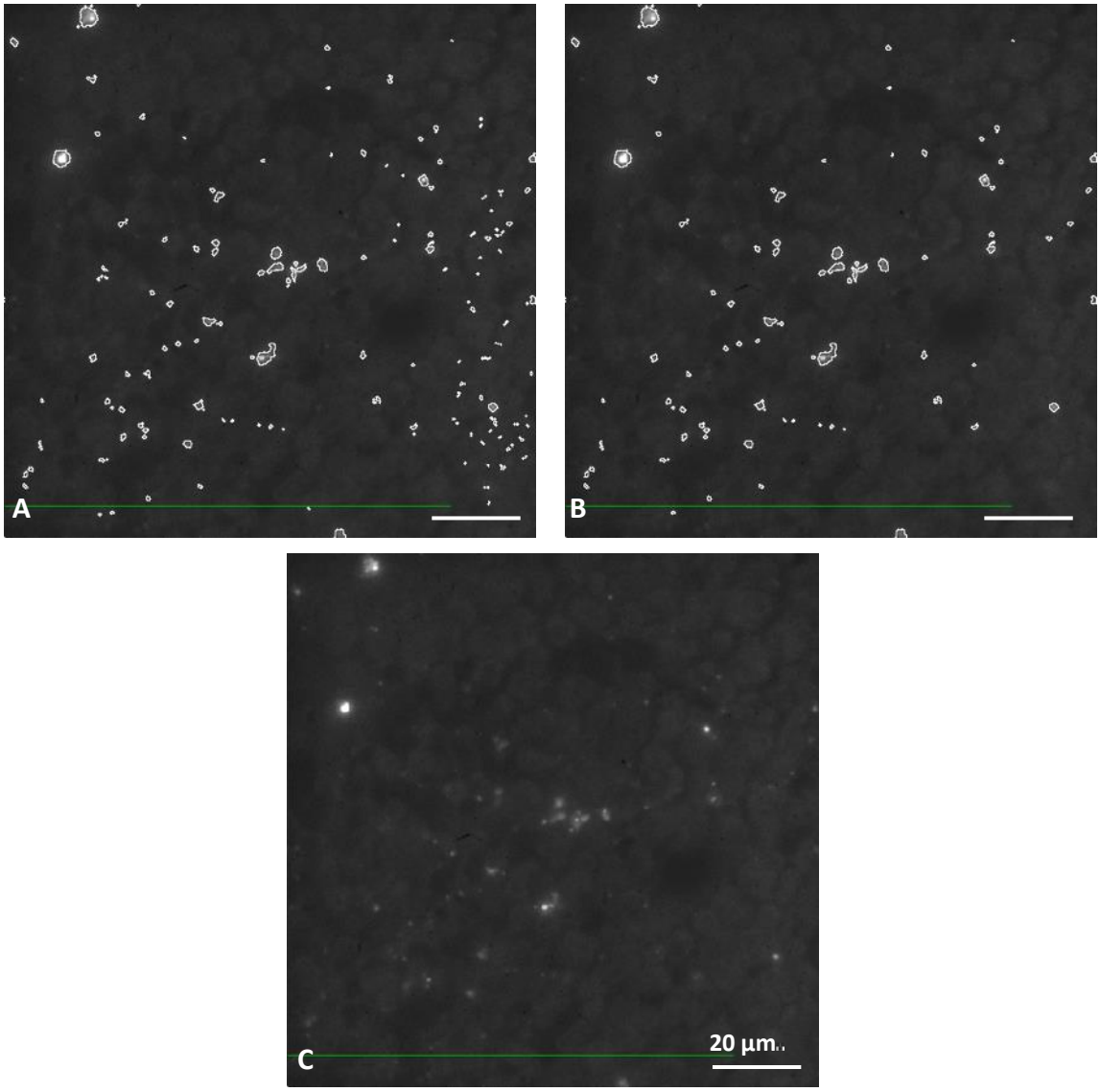

Figure 5.2-7: Importance of the local contrast ratio on the identification of the ROIs corresponding to FNDs. (A), (B) and (C) present the same field of view from a spleen section examined in FND fluorescence channel. (A) detection of the ROI (highlighted in white) without any threshold on the local contrast ratio; (B) detection of the ROI (highlighted in white) with a threshold specifically set for the spleen for the local contrast ratio. (C) same field of view without the highlighting of the ROIs. 60x magnification, non-HES staining

- **Value of the total intensity** of the object detected: below a specific threshold value, ROIs were considered as false positives;
- **Area of the ROI**: set to prevent the detection of a large part of the organ. In lung for instance, some parts of the organ were highly fluorescent and could be detected as FNDs if no size filter was applied. As presented in Figure 5.2-8, if no filter was applied (A), large portions of the tissue were incorrectly detected as FNDs, because of their high fluorescence intensity and high contrast.

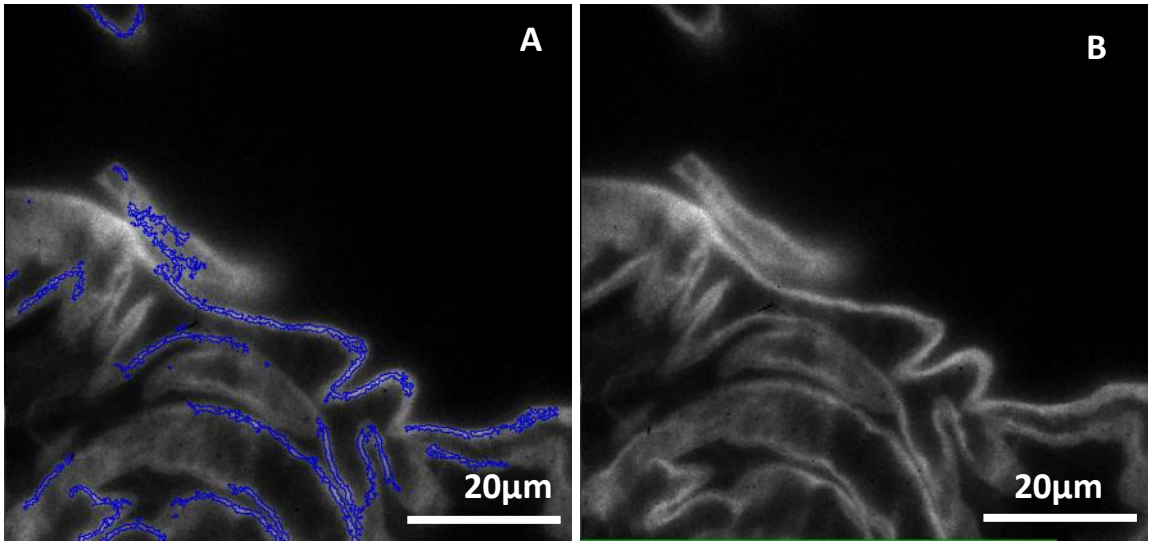

Figure 5.2-8: Importance of a filter based on the area of the ROI for the identification of ROIs corresponding to FNDs. (A) and (B) present the same field of view from a lung section examined in FND fluorescence channel, 60x magnification, non-HES staining. (A) without any threshold for the size of the ROI; (B) with a size threshold applied, specifically set for the lung.

- **Ratio of the fluorescence intensity between the first bleaching step and the acquisition step,** cf. Figure 5.2-5. When this ratio was within a specific range, the detected ROIs were considered as FNDs (the fluorescence of the FND should not decrease after the bleaching step).

The range of parameters set for each organ for which the ROIs were identified as FNDs are given in Table 7.

Table 7: Values of the range within which the detected ROIs were considered as FNDs, specific for each organ.

	Global contrast		Local contrast		Total intensity		Area		Ratio bleaching/acquisition steps	
Lung	1.3	1000	1.2	9999	30	9999	0.25	7.5	0.65	1.25
Heart	0.8	1000	1.27	9999	20	9999	0.4	9	0.75	1.25
Tumor	1.3	1000	1.13	9999	10	99999	0.25	60	0.65	1.25
Liver	1.3	1000	1.2	9999	30	99999	0.25	20	0.65	1.25
Spleen	1.3	1000	1.2	9999	30	99999	0.25	20	0.65	1.25
Kidney	1.3	1000	1.2	9999	30	99999	0.25	20	0.65	1.25

Figure 5.2-9 shows the result of the FND detection on an image of a liver section. One can see the high precision of the detection thanks to the applied thresholds.

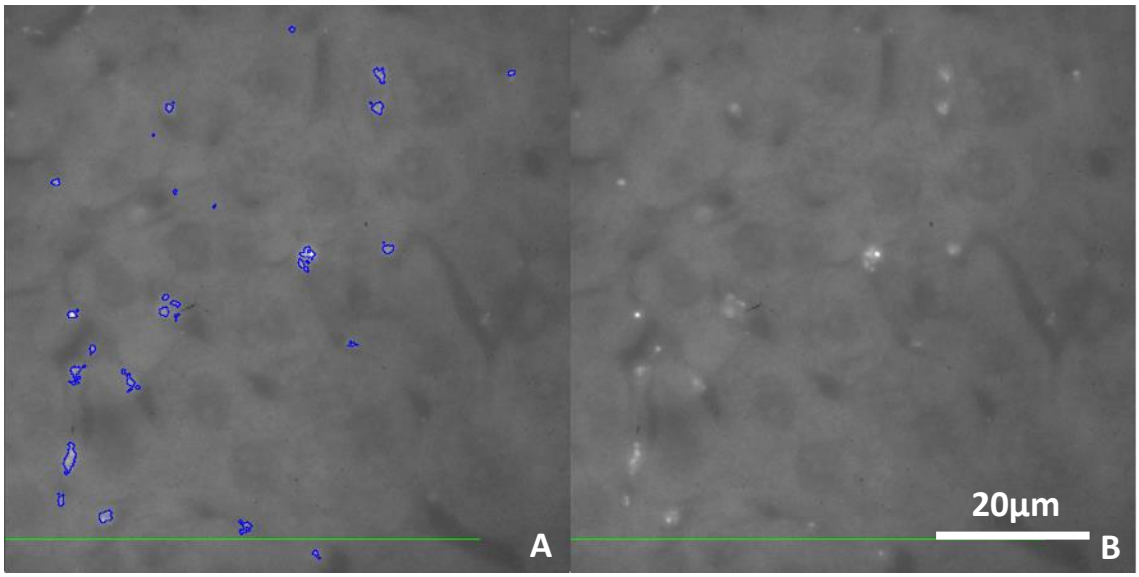

Figure 5.2-9: Visualization of the detection of FND in a section of the liver. Both images present the same field of view. (A) fluorescence image with FND detection as ROIs (blue lines); (B) Fluorescence without the ROIs displayed. 60x magnification, no HES staining.

The statistical results of the repartition of Cop-FND in each organ will now be presented. Note that the results are presented for two different mice having received the same treatment (Cop-FND:siRNA), and statistics were made on duplicates of organ sections originating from the same mouse.

5.2.5. Quantification of the FND in organ sections

Several parameters are presented in this section:

- The **number of ROI per mm²**, showing the density of ROI detected according to the surface acquired;
- The sum of all **ROIs fluorescence intensity** in an organ section **per unit of the section area**, which is considered as proportional to the **number of FNDs** present in each organ;
- The distribution of the **surface area of the detected ROI** for each organ, showing the state of aggregation of FNDs in each organ.

The number of detected ROIs gives a first information on the accumulation in the different organs. One can see from the numbers given in Figure 5.2-10 that, at 24h, the FNDs seem to have preferentially accumulated in the lung, the spleen and the liver. On the other hand, not

that much FNDs were found in the heart, in the tumor and in the kidneys. Nevertheless, the detection program has not been optimized yet to distinguish multiple aggregates within a ROI, meaning that ROI of size larger than the point spread function of the microscope (limited by diffraction to ≈300 nm) were detected as single events.

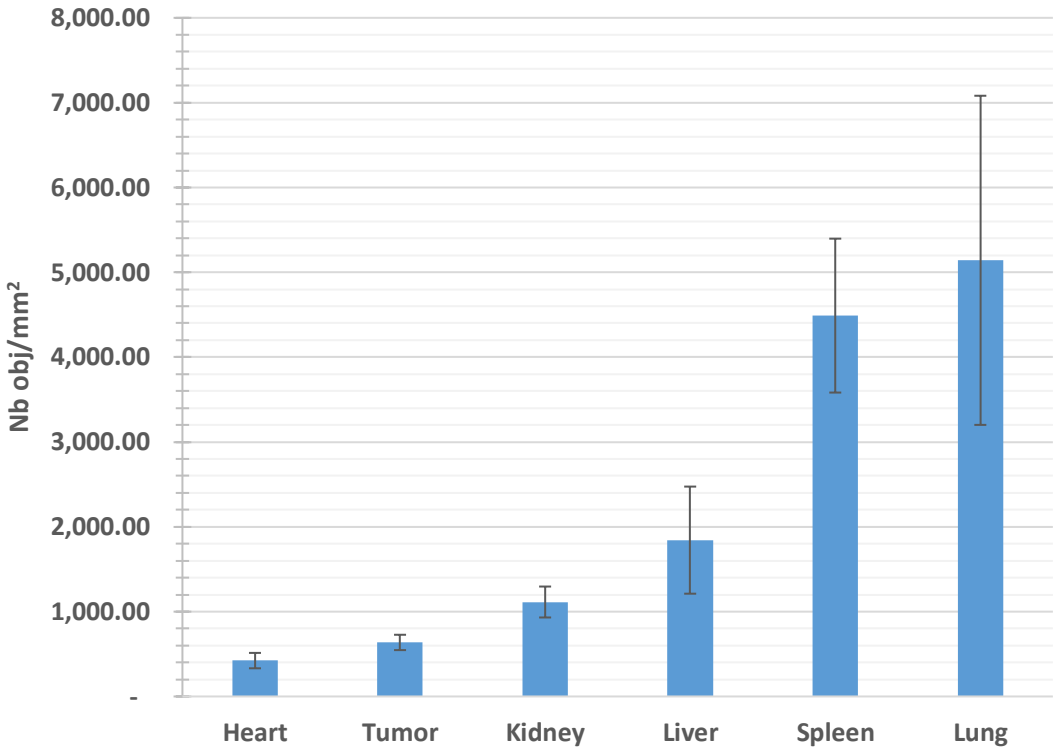

Figure 5.2-10: Number of ROIs detected in each organ per surface unit. Statistics were made from duplicates of sections originating from two different mice. Error bars = SEM.

In order to achieve a more realistic quantification of FNDs in each organ, we considered the fluorescence intensity of each ROI, which is expected to be proportional to the number of FNDs it contains, in the ideal case of identical particles. We then summed the intensity of all ROI detected in an organ and to be able to compare organ's distribution to each other's, we divided it over the total surface of the section (presented in photon counts/µm^2; pc/µm^2, Figure 5.2-11).

The organ section displaying the highest fluorescence intensity per unit area was not the lung as we could expect from the previous figure but the spleen (1.71±0.57 pc/µm^2), closely followed by the liver (1.37±0.64 pc/µm^2). The lung, which was the organ in which the largest number of ROIs had been detected, only comes third (0.75±0.35 pc/µm^2). Finally, the kidneys (0.2±0.04 pc/µm^2), the tumor (0.08±0.01 pc/µm^2) and the heart (0.05±0.01 pc/µm^2), presented much smaller accumulation of fluorescence.

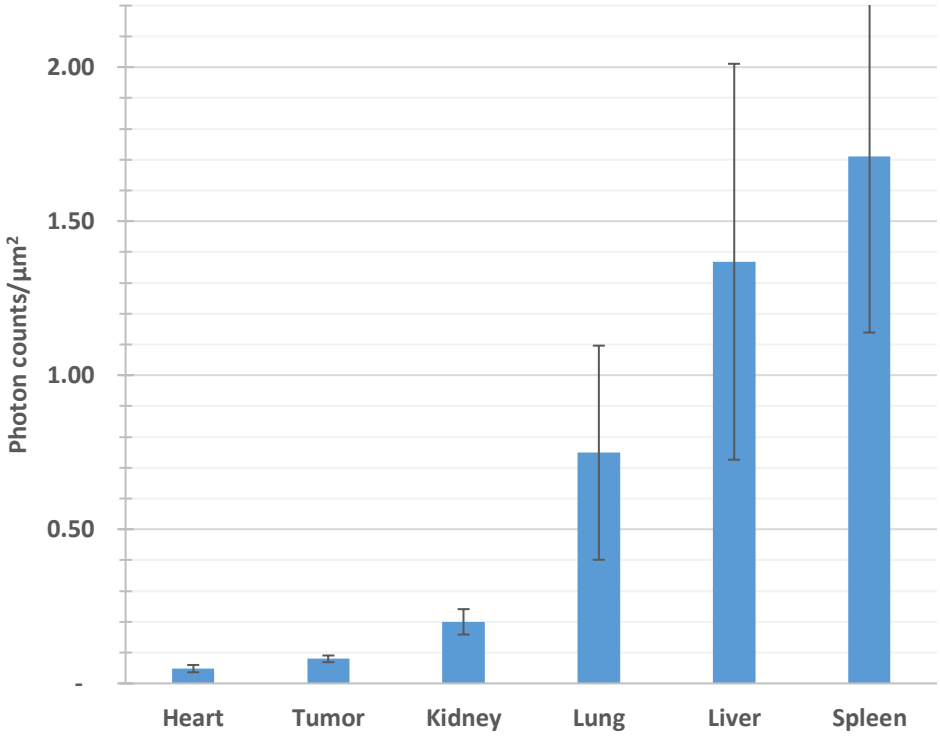

Figure 5.2-11: Total ROIs fluorescence intensity over the organ section area. Statistics were made from duplicates of organ sections, from two different mice. Error bars = SEM

The spleen, the liver and the lung remained the organs presenting the highest accumulation. In addition to gathering the highest density of fluorescence per unit area, spleen and liver also displayed the highest aggregation state, compared to the other organs, as it is presented in Figure 5.2-12. A box plot representation was preferred to display the wide distribution of the area of the detected ROIs [262] and revealed to be a great tool to compare the aggregation state in the different organs. The boxplot characterizes a sample using the 25th, 50th and 75th percentiles, also known as the lower quartile (25% of the population, represented at the bottom box extremity), the median of the distribution (middle line) and the upper quartile (75% of the distribution, top box extremities). The interquartile range covers 50% of the population, is independent from outliers and preserves the information of the center spread. The whiskers represent 90% and 10% of the population (top and bottom whiskers, respectively). The outliers were not presented here, in order not to make the graph too congested. Since the distribution of the ROI areas does not follow a normal law, the boxplot representation was the most adapted to characterize them and to compare FNDs aggregation state in the different organs. Furthermore, notches, giving the 95% confidence interval (CI) for the median, have been represented, but the number of ROIs being so large, this interval is

very small, and the median can be trusted with very high confidence. The ROI area distributions presented in Figure 5.2-12, show the broad distribution that can be found in some organs.

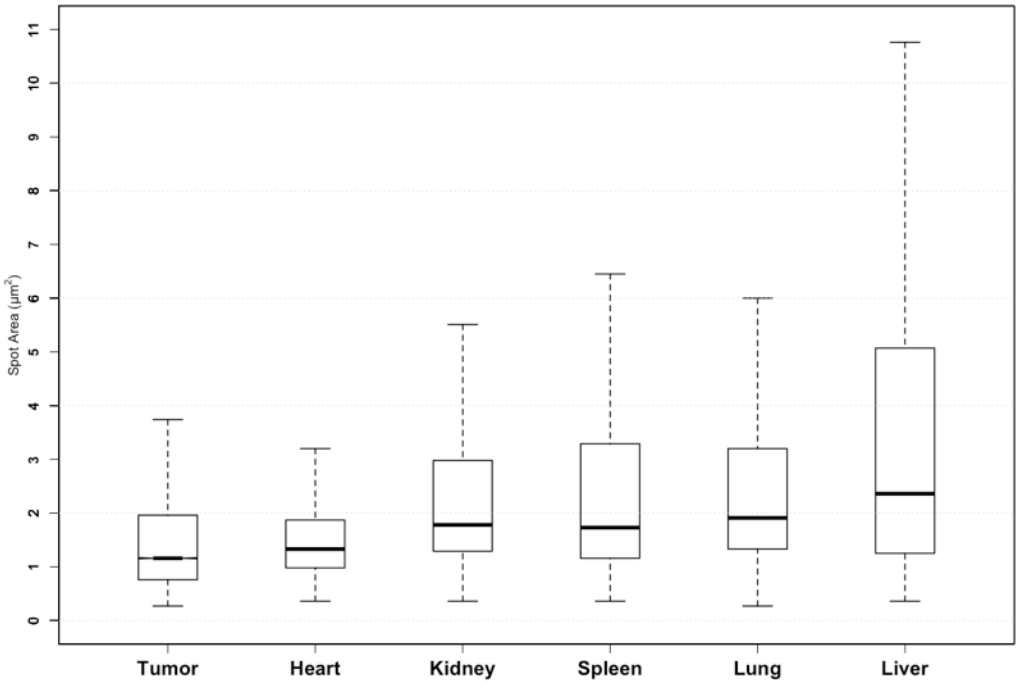

Figure 5.2-12: ROI Area distribution in the different organs. Statistics were made from duplicates of organ sections from two different mice. The central bars represent the median, the outer boxes represent 25 and 75% of the distribution and the whiskers represent 10 and 90% of the distribution.

The tumor presented the lowest ROI area median value (however with a rather large distribution), which tends to show a minor aggregation in this tissue. When correlated with the low value of density of fluorescence also observed for this organ, it is difficult to know if the complexes actually passed through the tumor and if so, if the siRNA was dropped to have its effects on cancerous cells. Interestingly, the tumor displayed a more spread ROI area distribution than the heart. The cardiac muscle only was analyzed, our protocol not allowing to analyze the circulating blood. Thus, it is only represented here the FNDs that entered the myocardium, and one can see that there is a limited aggregation rate in this tissue.

The kidney, the spleen and the lung presented similar ROI areas distributions. The median ROI area detected in spleen and kidney were very close, while the one in the lung was slightly higher. The aggregation in the lung was more spread, most probably because of the diversity of sizes of the different capillaries, in which the FNDs might have been trapped.

The liver presented the highest aggregation state of FNDs. The value of the median was the highest and the population was very spread, with a maximum at almost 11 μm^2. The liver is one of the organs, with the kidneys, which function is to filtrate the blood and to remove undesirable metabolites and xenobiotics from it. We can then assume that the observed high aggregation is a consequence of the accumulation of FNDs in the cells ensuring this filtrating function.

These results were consistent with previous studies that also localized nanodiamonds in the liver, the spleen and the lung, preferentially, 24h after the injection [158,161]. Nevertheless, the previous studies were carried thanks to radioactivity labeling of the NDs and to Raman spectrometry analysis and could not allow a precise localization at a subcellular resolution, as our setup enabled us to do. The next subsection presents this subcellular localization, in the case of the liver.

5.2.6. Cellular localization: case of the liver

In addition to the analysis of non-stained sections, HES-stained sections for all organs were analyzed in both fluorescence and bright-field. The HES-staining allowed us to determine in which cells or parts of the organ, the FNDs accumulated in, but with a diminished accuracy of FNDs detection.

Unfortunately, the analysis of such data is very time-consuming, thus it has only been conducted on the liver by the end of this manuscript's redaction. Nevertheless, kidney, spleen and lung should also be analyzed, later on, given the important role these organs seem to have in the clearance of FNDs.

Figure 5.2-13 shows a schematic representation of the hepatic structure, displaying the different cells and vessels present in the liver. Thanks to the help of Dr. Paule OPOLON, pathologist, we were able to identify in our scans, the different cells and structure, and thus identify the localization of FNDs aggregates.

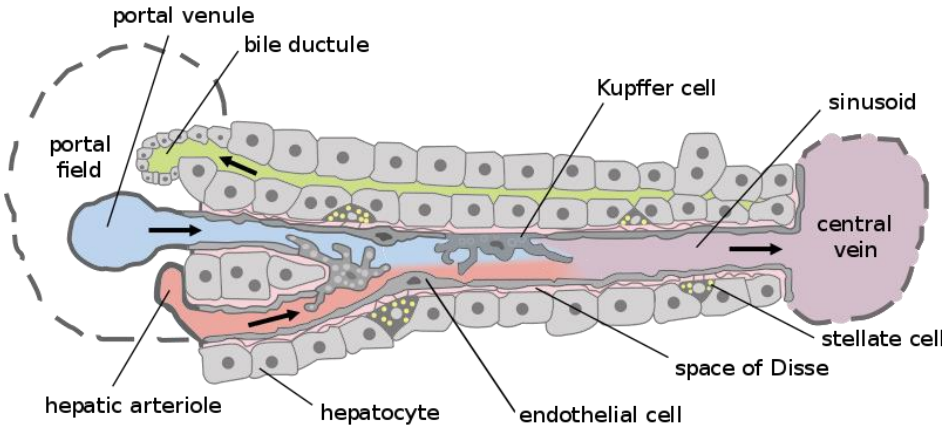

Figure 5.2-13: Illustration of part of the liver lobule, showing the hepatic structure. Adapted from [263]

The Figure 5.2-14 presents a mosaic of images, built from data acquired with our setup. It shows that the macro-image is well reconstructed allowing us to distinguish:

- An artery (A), which we can be differentiated from the vein (V) thanks to the endothelial cells surrounding the structure. Note that erythrocytes (RBC) are visible in both vein and artery;
- Bile ducts (BD) that serve as a canal for the bile circulation up to the duodenum;
- Sinusoids (S) that are the capillaries irrigating the hepatocytes with blood to filtrate;
- Hepatocytes (H) that are the main cells from the liver (square-like cells, circled in black in Figure 5.2-14), which function is to filtrate the blood from metabolites;
- Endothelial cells (E) composing the sinusoids vessels' wall, which are long and thin cells;
- Kupffer cells (K), that are macrophages, specific to the liver, long and large cells, typically composed of a triangular nucleus. Their major role is to transform into bile the pigments of the hemoglobin, released by disintegrated erythrocytes. They also phagocyte microbes that might have penetrated into the liver.

Note that the last two types of cells are not highlighted in Figure 5.2-14 because of the too wide field of view presented in this figure. Their observation is eased in the single fields of view presented in Figure 5.2-15. Nevertheless, their structures are very similar under HES staining, the distinction between the two types was then not straightforward and no distinction nor quantification of FNDs in the two types was performed.

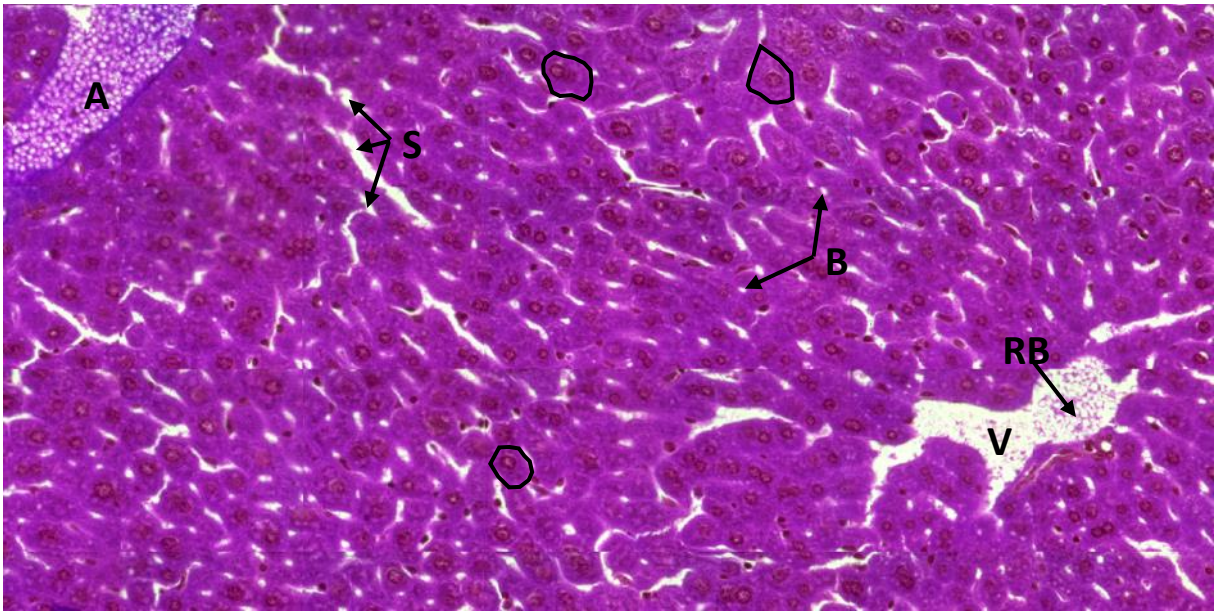

Figure 5.2-14: Mosaic of bright field images taken with a 60x magnification of a mouse liver section stained with HES. Annotations: A: artery; S: sinusoids; BD: bile duct; RBC: red blood cells e.g. erythrocytes; V: vein; three examples of hepatocytes are surrounded in black.

Thanks to a better knowledge of the liver structure, we could identify in which cells the FNDs preferentially accumulated. From different fields of view displayed in Figure 5.2-15, it seems that there was a privileged accumulation of FNDs, first in cells bordering the sinusoids, and second, most probably inside Kupffer cells or endothelial cells, as they were detected close to the nucleus. Kupffer cells are specific macrophages of the liver and one of the components of the reticulo-endothelial system. The phagocytosis of nanodiamonds by Kupffer cells has already been observed [158], and it has been established about a decade ago that NDs were rapidly captured by RES [158] by phagocytosis for their further excretion. Kupffer cells should thus play an important role in the removal of these nanoparticles from the organism. A staining specific to macrophages like F4/80 [264] would allow to unambiguously distinguish Kupffer cells from endothelial cells, so that we could have an accurate quantification of the distribution between the two cell types. Finally, no Cop-FND was detected in the hepatocytes.

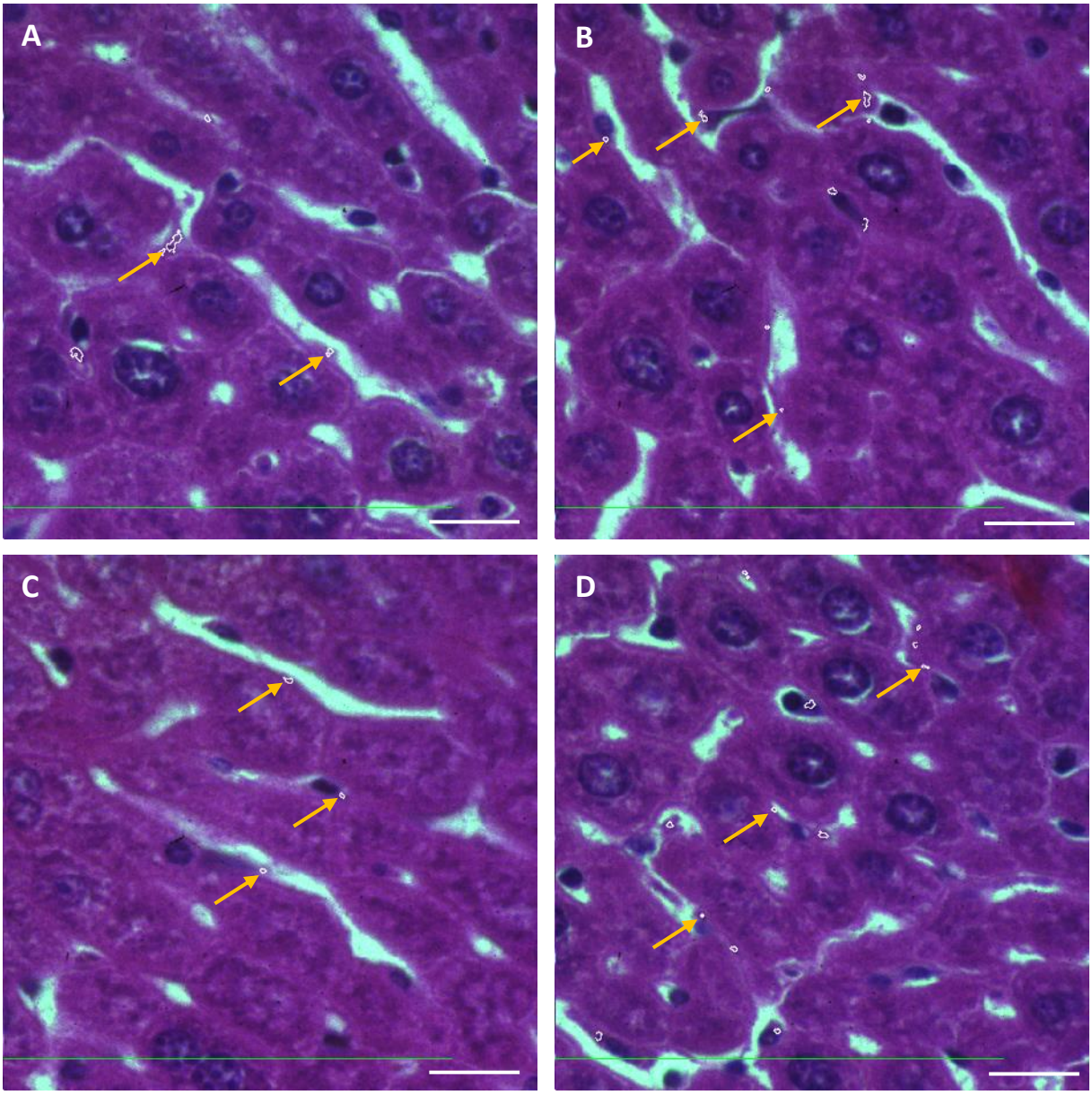

Figure 5.2-15: FND localization (indicated by white lined ROIs superimposed to the bright field) in the liver section. HES-stained sections, 60x magnification, scale bar 20 µm. Orange arrows point at FNDs detected on the border of sinusoids or in either Kupffer cells or endothelial cells. Only a macrophage specific staining will enable to distinguish Kupffer cells from endothelial cells.

5.2.7. Conclusion of Section 5.2

This section presented an innovative imaging setup, based on time-gated imaging used for the assessment of Cop-FND$_{HPHT}$ biodistribution in mice, that were xenografted with an Ewing Sarcoma tumor. The mice were injected in the caudal vein with Cop-FND$_{HPHT}$:siRNA complexes, and sacrificed 24 hours later. The heart, the kidney, the liver, the spleen, the lung

and the tumor were collected, fixed and sectioned. Some organ sections were stained with HES.

We established the optimal scanning protocol, showing that despite the time-gating setup, allowing to reject the autofluorescence signal from the tissue, a first bleaching step was needed prior to the acquisition step to make the analysis process more accurate. Furthermore, it was essential in order not to miss any Cop-FND detection, to run the quantification process on non-stained sections. Indeed, the fluorescence of the HES staining was too strong and seemed to hide the fluorescence signal from the Cop-FNDs.

It appeared that 24h after the injection, most of the Cop-FNDs were accumulated and aggregated in the liver, in the spleen and in the lung (Figure 5.2-11 and Figure 5.2-12), confirming previous studies [265]. The accumulation in those specific organs is consistent with an uptake of the nanodiamonds by the reticuloendothelial system, partly composed of the macrophages from the liver (Kupffer cells), from the lungs (alveolar macrophages) and from the spleen (red pulp macrophages), which will try to degrade and eliminate NDs from the organism. The cellular localization study conducted in the liver, thanks to our high-content imaging setup, tends to show that we might be in this configuration, but still needs to be confirmed by a more thorough study and to be completed by a macrophage specific staining (F4/80 staining). Cellular localization studies also have to be conducted on spleen and lung sections.

The aggregation state in the kidney, the tumor and the heart was lower (Figure 5.2-12). The low accumulation in the kidney is potentially explained by the fact that, at 24h, Cop-FNDs were preferentially processed by the liver and the spleen, in view of their excretion, and that the residual FNDs were then, a few days later, directed to the kidneys, as it has been reported in Ref. [265]. Our methodology did not allow to image the blood contained in the atrium or the ventricles of the heart at the time of the sacrifice. We thus only studied the myocardium and observed that almost no Cop-FNDs from the blood circulation aggregated in the heart muscle. Finally, the low aggregation state observed in the tumor might be explained by the fact that at 24h, a certain quantity of FNDs had already passed through it, but did not stay in this tissue. This only can be confirmed by a study at a shorter time-point, and by a gene expression analysis of the tumor at 24h.

Conclusion and perspectives

Nanomedicine is a promising route for the development of innovative biomedical applications. Among the very large number of drug delivery nanoparticle vehicle candidates, nanodiamonds (NDs) have emerged as original vectors that provide a slow release of the drug and a long circulation time. These results stem from (i) the broad variety of surface modifications allowing to bind different types of drugs, and from (ii) the very low toxicity of nanodiamonds. During this PhD thesis, I tested different types of diamond nanoparticles as vehicles for a gene therapy molecule: siRNA. Some of these NDs were also fluorescent (owing to embedded NV defects), enabling us to track their fate in mouse organism after injection of the treatment. Functionalized detonation or high pressure high temperature synthesis NDs were provided by collaborators. We realized the biodistribution assays thanks to a home-built time-gated imaging setup, allowing to acquire high-content images of entire organ sections post-sacrifice, including a bright field color image in addition to the fluorescence image. The later, combined with large magnification imaging, enabled us to detect single ND at a subcellular resolution, providing information on which cellular type preferentially engulfed them.

The testing of the various surface functionalizations revealed a certain disparity between the different samples and highlighted the importance of the method of functionalization. The experiment at the origin of the project, had involved the use of plasma-assisted hydrogenated detonation nanodiamonds, produced by Jean-Charles ARNAULT's team at CEA-LIST, Paris-Saclay. Our team at *Laboratoire de Vectorologie et Thérapeutiques Anticancéreuses* had demonstrated that this platform could be successfully used to vectorize siRNA up to the cytoplasm of the cells, where it could have its effect, inducing an inhibitory effect of 50% to 60%. During this project, we tested the same process, but we could not reproduce the high inhibitory effect of the proof-of-concept experiments. It also emerged that the colloidal

stability of the new nanodiamond suspensions was degraded. We attributed these negative results to the modification of the plasma hydrogenation setup.

We then tested detonation nanodiamond hydrogenation by an annealing under a dihydrogen atmosphere at 550-560°C, produced by the CEA-LIST. This method yielded more stable colloidal hydrogenated ND solution, most probably thanks to a more homogeneously hydrogenated surface. Unfortunately, the use of these H-DND to deliver siRNA, did not result in a larger inhibition of *EWS*-Fli1 expression *in vitro*. Nevertheless, the same annealing setup also enabled the exposition of nanodiamonds to tritium gas, yielding tritium terminated nanoparticles (^{3}H-DND), used to study the *in vivo* tissue distribution and elimination of nanodiamonds, after injection in mice.

It appeared that the physico-chemical gas hydrogenation was not optimized for our application. The originality of this project relied on the use of ultra-small nanodiamonds (DND ≈ 3-7nm) so that they could be more easily excreted, in particular by the renal path. We thus kept going with detonation diamonds, offering smaller sizes than HPHT synthesis. We tested a suspension of DND functionalized with a wet chemical treatment. This highly stable colloidal suspension displayed NDs of 3 nm size and with a zeta potential of +45-50mV. Although these cationic DND allowed us to achieve up to 60% inhibition, we did not have enough reproducibility to carry on with this system for *in vivo* assays.

The last nanodiamonds suspension we tested originated from High Pressure High Temperature synthesis, with a larger primary size of about 70 nm. These NDs were irradiated by high energy particles to generate Nitrogen-Vacancy fluorescent defects, yielding fluorescent NDs. These FNDs were then functionalized with an atomically thin silica shell on which a cationic copolymer was covalently grown (Cop-FND$_{HPHT}$), allowing the siRNAs to be electrostatically bound to the particles. Cop-FND$_{HPHT}$ showed a great efficacy to bind siRNA and to release it in the cytoplasm of the cells, inducing one of the highest inhibition rate of 70% ever obtained on the expression of *EWS-Fli1*, in a serum-containing medium. This surface coating appeared to be the optimal functionalization and was the one selected for *in vivo* efficacy assay. The latter will be conducted soon, but after the end of my PhD.

In parallel, I have focused my experiments on the tissue distribution of NDs, 24 hours after injection in mice bearing an Ewing Sarcoma xenografted tumor. Indeed, the fate of nanoparticle vectors in the organism is a central question of nanomedicine and is one of the

hurdles to their broad use. We tested two types of NDs for the *in vivo* tissue distribution: the ^{3}H-DND (small single particle size) and the Cop-FND$_{HPHT}$ (larger single particle size). The intrinsic fluorescence conferred by the NV centers to the FND$_{HPHT}$ and the surface-tritiation of the ^{3}H-DND then appeared to be a real advantage, as no fluorophore needed to be added to the complexes to track them. Furthermore, the long fluorescence excited state life-time of NV centers in nanodiamonds allowed a background-reduced imaging of Cop-FND$_{HPHT}$ in tissue section. To this aim I have used a home-built time-gated imaging system, with exclusive features of large magnification (60×) and numerical aperture (1.4), pulsed-laser with high excitation power, and 3-color LED for bright field imaging. This setup has enabled to obtain high-content (fluorescence + 3-color) and high-resolution images of macro(millimeter)-sized organ sections collected on mice that were xenografted with a tumor and on which we injected in the caudal vein the FND:siRNA complexes. From these images, we could precisely quantify FND$_{HPHT}$ fluorescence, which we consider as proportional to the number of nanoparticles. By this mean, we assessed that the FNDs preferentially accumulated in the reticuloendothelial system, more precisely in the liver, spleen and lung. Indeed, our high-resolution setup with co-registration of fluorescence and bright field images allowed us to resolve Cop-FNDs in Kupffer cells and/or endothelial cells of the liver. A smaller fraction was found in the kidneys, potentially indicating that 24h after injection, some FNDs were already excreted through the urine. Finally, the last two smaller fractions were found, first in the myocardium, indicating that the blood circulation limited a penetration in the heart muscle, and second in the tumor, unfortunately. In the latter case, one cannot exclude that at 24h, the majority of the FND that had entered the tumor was already flushed out of it, leaving the possibility for the siRNA to have reached its target. This distribution has also been observed with the ^{3}H-DND, with an additional information on the urine and feces, in which some radioactivity was measured, with higher levels for the feces. These observations tend to confirm the uptake and excretion of the complexes through the liver.

These two biodistribution experiments will be repeated at shorter sacrifice time-points, to get the kinetics. Also, urine and feces will be collected when using the Cop-FND, in order to evaluate how efficiently these ND are eliminated. Moreover, the caudal injection is known to induce a rapid accumulation in the liver, if the injection is performed too quickly. Thus, to avoid this bias, a retro-orbital injection could be tested. Nevertheless, the limiting points of this mode of injection are that it is a manipulator-dependent procedure, and that it is less and

less approved by ethical committees, thus difficult to implement. To conclude, both ^{3}H-DND and Cop-FND revealed to be useful tools for the biodistribution study, and both showed similar tissue distribution.

An extension of the project will be to direct the ND:siRNA complexes towards the cancer cells, and limit unwanted distribution in off target organs. To this aim, the team plan to take advantage of the membrane protein CD99 (also called MIC2) known to be highly expressed on the surface of cancerous cells, and in particular of Ewing Sarcoma cells [266]. Therefore, CD99 can be considered as an antigen enabling active targeting of the Ewing Sarcoma cells, to optimize siRNA delivery. This strategy has been successful applied by LVTA team *in vivo* using polymer nanoparticles as siRNA delivery vehicles [260]. In this experiment the expression of *EWS-Fli1* was inhibited at 78% by associating the siRNA with the CD99-targeted nanoparticles compared with an inhibition of only 41% achieved with the non-targeted nanoparticles. To extend this approach to the case of NDs, the chemist team of Petr CIGLER (IOCB, Prague) with whom we collaborate, plans to graft antiCD99 covalently to the copolymer of Cop-FND. This experiment will require a "large" amount (10 mg) of a specific clone of antiCD99 selected to be non-toxic, and which is fortunately commercially available from a Czech company.

As another important and direct continuation of the project, we will be able to use soon a metastatic model of Ewing Sarcoma currently developed by Oscar TIRADO-MARTINEZ's team at IDIBELL (Barcelona). This stage of the disease is the most fatal to patients, there is then an urge to develop a more efficient treatment.

Furthermore, our strategy of using traceable cationic NDs as siRNA therapy delivery, is not siRNA-sequence specific. It can thus be used to vectorize a plethora of siRNA-sequence. As a natural extension of our project, one could use cationic ND to transport a siRNA directed against Type 2 *EWS-Fli1* junction which represents about 25% of the cases. Among the other diseases that could benefit from our strategy, we can mention papillary thyroid carcinomas, which is caused by the expression of the *RET/PTC1* oncogene. Finally, siRNA therapy should not be considered as a substitute to chemotherapy but more like an additive to it, inducing a synergetic effect between the two. This would allow to obtain less toxic treatments than the current one used, but despite the promising results obtained during this PhD project, there is still a long way before this kind of treatment to reach the bedside of patients.

APPENDICES

Appendix A: Methods

1. Size and electro-mobility (zeta potential) measurements:

Size and zeta potential were measured by Dynamic Light Scattering (DLS) with a NanoBrook 90Plus PALS from Brookhaven Instruments (Long Island, USA) with a light scattered collected at 90°. The measurements were made right after reception of the solutions, on a 150-fold dilution of the stock solution in distilled water. Another measurement of the size and zeta potential was conducted on the nanodiamond:siRNA complex. For this purpose, a fixed concentration of siRNA was used while the nanodiamond concentration was increased, resulting in the study of the size and zeta potential of the complex depending on the mass ratio between DND and siRNA.

2. siRNA binding assay:

This study was made to assess the siRNA binding capacity of nanodiamonds depending on the mass ratio between DND and siRNA, at a fixed siRNA concentration and with an increasing DND concentration. Briefly, siRNA and DND were mixed at room temperature, in a mixed solution of distilled water and 100 mM Hepes (pH 7.2) + 100 mM NaCl buffer. After a 10-min incubation, the solution was centrifuged at 16,100 *g*, for 15 min at 15°C. Then 30 µL of the supernatant was mixed with 30 µL of 1 µg/mL ethidium bromide (EtBr, Sigma Aldrich, USA) and the fluorescence resulting only from EtBr intercalated in RNA grooves was recorded with a fluorescence plate reader (GloMax®-Multi, Promega, USA; excitation wavelength: 525 nm, and detection range 580-640 nm). Experiments were performed in triplicate.

3. Stability study:

The colloidal stability was assessed by size measurement (NanoBrook 90Plus PALS, Brookhaven Instruments) and visual checking over time.

4. Cytotoxicity assay:

A673 and TC71 human Ewing Sarcoma cell lines were generous gifts from Dr. Elizabeth R. LAWLOR (University of Michigan, USA) and TC252 human Ewing Sarcoma cell line was kindly provided by Oscar MARTINEZ TIRADO (*Institut d'Investigacio Biomedica de Bellvitge*, Barcelona). All cell lines were grown in DMEM medium (Gibco, USA) supplemented with

10% fetal bovine serum (Gibco) and 1% penicillin-streptomycin antibiotics (Gibco). Cells were plated one day before treatment in 96-wells plates at 10^3 cells per well and incubated at 37°C, 5% CO_2 in a moistly atmosphere. The medium was then removed and replaced by 100 µL medium containing increasing concentrations of P-DND-H-11, from 0 to 0.5 mg/mL. Cells were incubated for 24, 48 or 72 h, cell viability was then assessed thanks to a MTS assay. Briefly, 10 µL of MTS (Biovision, USA) were added to each well and incubated for 3 h at 37°C. The produced formazan was then quantified by absorbance measurement at the wavelength of 490 nm using a microplate reader (ELx808, BioTek, USA). Each condition was performed in 8 replicates. Results are expressed as % of untreated cells.

5. Inhibition of *EWS-Fli1* gene expression:

A673 cells were seeded at 2.10^5 cells/mL on a 12-wells plate in DMEM medium (Gibco) containing 10% bovine calf serum and 1% penicillin/streptomycin (Gibco) and incubated at 37°C, 5% CO_2 in moistly atmosphere one day before treatment. Medium was then replaced by 450 µL of same medium and 50 µL of 10 mM Hepes pH 7.2, 100 mM NaCl containing P-DND-H or A-DND-H bound to siRNA targeted toward *EWS-Fli1* (Sense strand: GCA GCA GAA CCC UUC UUA Ud(GA); Antisense strand: AUA AGA AGG GUU CUG CUG Cd(CC)) or a control sequence (RP1: Sense strand: CGU UAC CAU CGA GGA UCC Ad(AA); Antisense strand: UGG AUC CUC GAU GGU AAC Gd(CT)) at 50 nM final concentration. DND-H:siRNA mass ratio was 50:1, 25:1 or 10:1. A positive control was also tested, by using Lipofectamine2000 (Invitrogen, USA) to deliver siRNA. Note that for this condition, serum-free medium, *e.g.* Opti-MEM, was used, according to the producer protocol. Cells were incubated for 24 h and total RNA was extracted by Trizol (Invitrogen, USA) method. Briefly, the cell culture medium was discarded, cells were then washed with PBS and lysed with 400 mL of Trizol solution. Finally, the lysates were collected and 60 µL of chloroform:isoamylic alcohol (49:1) was added. The solution was then centrifuged at 16,100 *g* for 15 min at 4°C. 150 µL of the supernatant containing the RNA were added to the same volume of isopropanol and RNA precipitation was obtained after 15 min at room temperature. The solutions were then centrifuged at 16,100 *g* for 15 min at 4°C and the pellet washed twice with 70% ethanol and dried. The total extracted RNA was dissolved in 10 µL of water containing 0.5 U of RNasin (Promega, USA) and RNA concentration was determined by spectrophotometry at the wavelength of 260 nm (Nanodrop, Thermo Fisher Scientific, USA).

The reverse transcription was performed on 1.5 µg of total RNA by adding 2 µL of random hexamers 50 µg/mL (Promega), and heating at 70°C for 3 min. RNA was then incubated with 0.5 mL M-MLV reverse transcriptase 200 U/µL (Promega), 0.5 µL DNTP 20 mM, 0.5 µL RNasin (40 U/µL) and 4 µL of MMLV RT buffer (Promega) for 15 min at room temperature followed by 1 h at 42°C, in a final volume of 20 µL. PCR quantification was carried out with a KAPA SYBR FAST ABI Prism kit (KAPA Biosystems, South Africa). The *EWS-Fli1* gene was amplified with the *EWS*- Forward Primer: 5'-AGC AGT TAC TCT CAG CAG AAC ACC -3' and *Fli1*-reverse primer: 5'-CCA GGA TCT GAT ACG GAT CTG GCT G-3' (Eurogentec, Belgium). We mixed 0.4 µL of each primer 10 µM, with 5 µL of cDNA diluted 1/20 (v/v) and 10 µL of KAPA SYBR Mix FAST Mix, in a final volume of 20 µL. The samples were amplified over 40 cycles, in a Step One Plus Real Time PCR-systems (Applied Biosystems, USA), as follows: 20 s at 95°C, followed by 40 cycles of 95°C for 3 s, 60 °C for 30 s, melting curve were then obtained. The human 18S rRNA gene and GAPDH gene were used as controls and were amplified with the 18S Forward Primer 5'-CGT TCA GCC ACC CGA GAT-3', and 18S Reverse Primer 5'-TAA TGA TCC TTC CGC AGG TT-3'. GAPDH: Forward Primer: 5'-CAA GGT CAT CCATGA CAA CTT TG-3', and Reverse Primer: 5'GTC CAC CAC CCT GTT GCT GTA G-3'. Comparative CT (threshold cycle) methods were used to normalize the target CT by the 18S or GAPDH control gene CT.

6. Apoptosis assay:

A673 cells were seeded at 2.10^5 cells/mL in 6-well plates the day prior treatment. The CellEvent Caspase 3/7 Green flow cytometry assay kit (ThermoFisher, USA) was used to conduct this assay. Different conditions were tested but 5 control conditions (*i.e.* without DND-H:siRNA) were essentials: 1) untreated cells without staining, 2) untreated cells with CellEvent green solution only, 3) untreated cells with SYTOX AADvanced solution only, 4) untreated cells with both staining, and 5) positive control (Etoposide at 25 µM or Vincristine at 2 ng/mL). Cells were incubated with P-DND-H or A-DND-H loaded or not with antisense siRNA or control siRNA, combined or not with Vincristine at various concentrations. The mass ratio used DND-H:siRNA was 25:1. After 24, 48 or 72 h incubation time, the medium was collected and cells were harvested thanks to TripLE Express Enzyme 1X (ThermoFisher, USA) and then centrifuged for 5 min at 200 *g*. Supernatant was discarded and the cell pellet was re-suspended in DMEM at a concentration of 10^6 cells/mL. For 1 mL of the solution,

1 µL of the CellEvent solution was added and incubated for 30 min at 37°C. 1 µL of SYTOX AADvanced solution was then added to the 1 mL solution and the mix was then incubated again 5 min at 37°C. The analysis was finally performed within the hour by flow cytometry on a BD Accuri C6 flow cytometer (BD, USA). The untreated group was used to draw a region (gating) around the population presenting the typical characteristics of cells (concerning forward scatter and side scatter parameters) and to distinguish them from cell debris and large particles. Analysis was then made based on this gating and results are presented in % of this population. **Living cells** appeared as non-stained (**CellEvent/SYTOX -/-**), **apoptotic** cells appeared as stained by CellEvent Caspase 3/7 green only (**CellEvent/SYTOX +/-**) and **necrotic** cells appeared as stained by SYTOX AAdvanced only (**CellEvent/SYTOX -/+**). However, this assay does not distinguish between cells that have already undergone an apoptotic cell death and those that have died as a result of necrotic pathway. In both cases, the **dead** cells were stained with both CellEvent Caspase 3/7 green and SYTOX AADvanced (**CellEvent/SYTOX +/+**). The typical result obtained by flow cytometry if presented in Figure A-1.

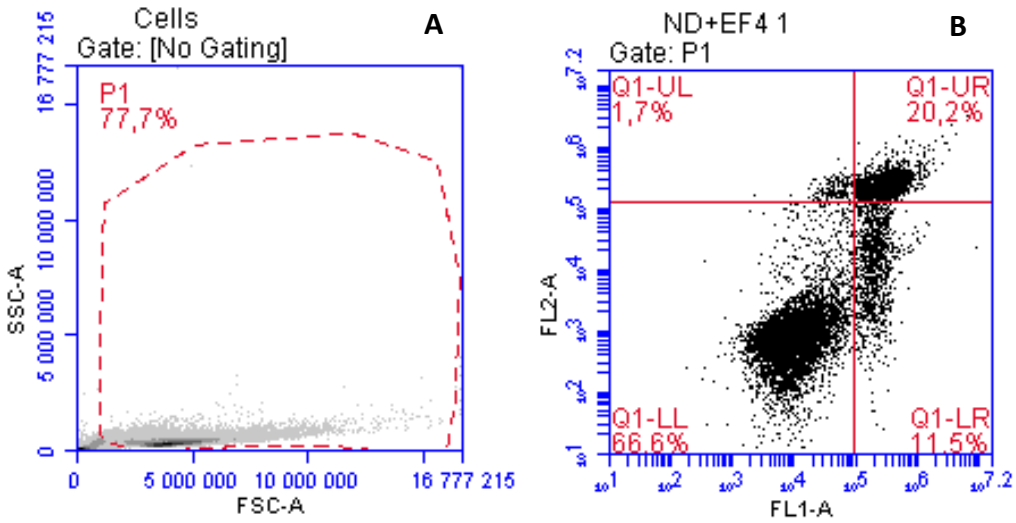

Figure A-1: Classical results of an apoptosis assay analyzed with flow cytometry. (A) presents the untreated cells, with no staining. A gating, P1, was done on this group and considered as the population on which the analysis can be run. FSC (Forward Scatter) displays the size of cells and SSC (Side Scatter) displays the granularity of the cells. The cells at the bottom left corner are debris and are thus not included in the gating. The data showed in B are composed of 10,000 events detected in the defined gating from A. FL1-A is used to detect the CellEvent channel (laser emission: 488 nm, excitation: 530/30 nm) and FL2-A to detect the SYTOX channel

(laser emission: 488 nm, excitation: 585/40 nm). Q1-LL = living cells, Q1-LR = apoptotic cells, Q1-UL: necrotic cells, Q1-UR: dead, late apoptotic cells.

7. Cell internalization microscopy:

A673 cells were seeded one day prior treatment at 2.10^5 cells/mL on a cover glass placed at the bottom of the well, in a 12-wells plate. Cells were then treated with P-DND-H and/or FITC-siRNA for a 3-hours incubation at 37°C. It is essential to have the three following controls to be able to set imaging parameters the more accurately: cells with no DND and no siRNA; cells with DND only, cells with FITC-siRNA only. After the incubation, a first wash of each well was performed with PBS. Then, 750 µL of a 4% formalin PBS solution was added to each well and let for 20 min at RT in the dark. After this incubation time, two PBS washings were made, before slide fixation with DAPI Fluoromount-G (eBioscience, USA), for cell nucleus staining. Final slides were then let at RT in the dark for 72 h for polymerization. Observations were then made with an epifluorescence microscope, Zeiss Observer Z1, or with a confocal microscope, Leica, HR-SP8.

8. *EWS-Fli1* gene expression inhibition with the addition of chloroquine:

Same protocol as in 5, with an extra incubation of 3 hours with chloroquine on A673 cells, prior to treatment with NanoAmando:siRNA. Final concentration of chloroquine tested were 100 and 200 µM, directly diluted in DMEM and then added to cells.

9. Cop-FND:siRNA complexation:

Before complexation with siRNA, the Cop-FND solution was sonicated 15 seconds in an ultra-sound bath. Then, the diluted Cop-FND solution was added to the diluted siRNA solution at a mass ratio of ND:siRNA of 3.9:1, and the mixed solution was put again in the ultra-sound bath for 20 seconds. This protocol, and more particularly mass ratio, has been optimized to provide very stable colloidal suspensions and to strongly limit aggregation at all stages of the complex formation. The success of the complexation step was characterized by a clear and translucent final suspension, while a failure resulted in a milky suspension that flocculates.

Appendix B: Particle Size Measurement by Dynamic Light Scattering (DLS): an explicative note of the different values

Dynamic Light Scattering measures the variation of intensity of light scattered by particles in solution (due to their Brownian motion) and relates it to the size of the particles. More precisely, DLS measures the time dependent fluctuations of the scattered intensity (dependent upon particle size, see Figure B-1), from which the translational diffusion coefficient (D) and subsequently the hydrodynamic diameter (D_H) are deduced, taken into account the solvent viscosity at the experiment temperature.

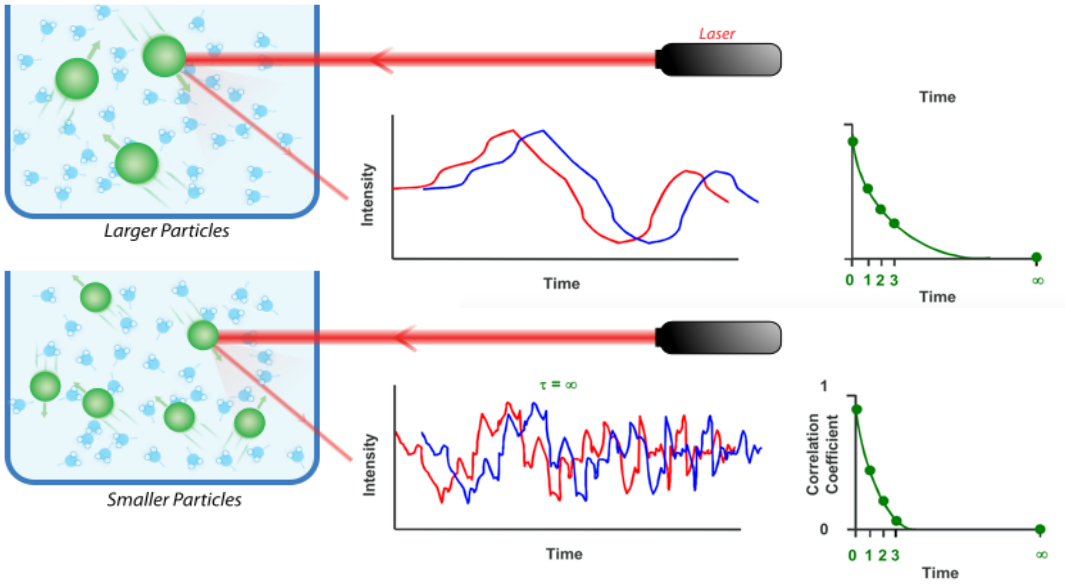

Figure B-1: Fluctuations in diffused intensity measured by DLS and construction of the correlation coefficient curve, comparison of the collected signal from large and small particles. Adapted from Malvern technical datasheet and Creative commons image by Mike Jones (CC BY-SA 3.0)

Auto-correlation function: inferred from the scattered intensities collected over time, according to:

$$G(\tau) = \langle \frac{I(t).I(t+\tau)}{I(t)^2} \rangle$$

Where: I = intensity,

t = time,

τ = the delay time

Figure B-2 shows the correlation function, with a qualitative description of information that can be extracted from the shape of the curve. The intercept is used to evaluate the signal-to-noise ratio from a measured sample and is often used to judge the quality of the data. The baseline should go to zero and be as flat as possible, if not, it is an indication for the presence of large particles, contaminants or aggregates.

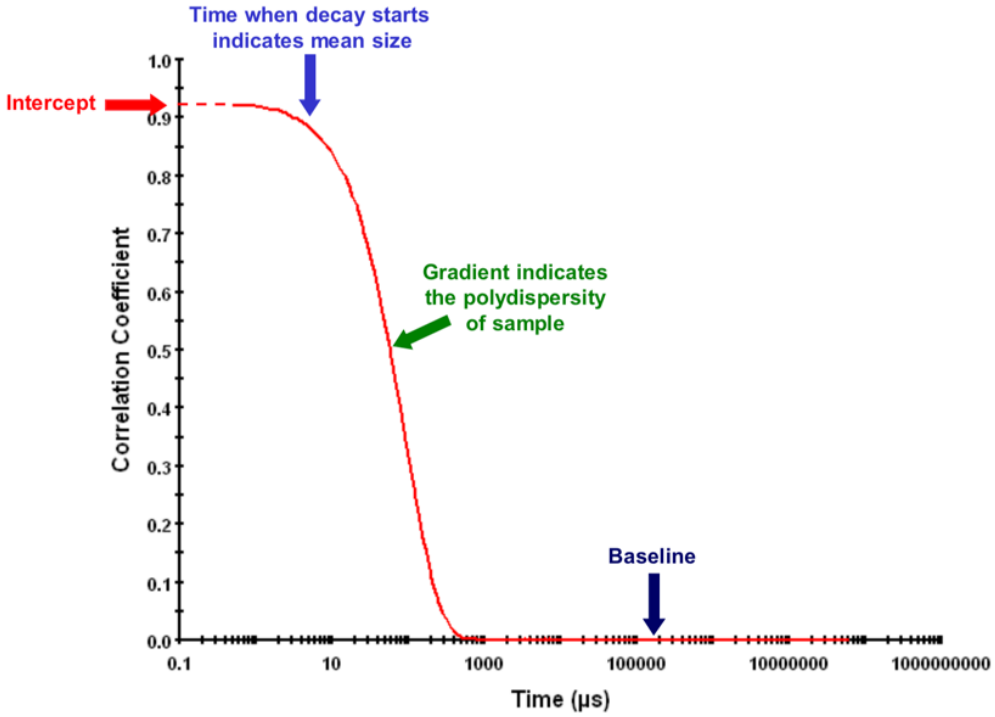

Figure B-2: Auto-correlation function description. From Malvern technical support datasheet

The intercept and the baseline are used in the equation for modelling the correlation function such as:

$$G(\tau) = B + A\sum e^{-2q^2D\tau}$$

Where: B = baseline at infinite time,

A = amplitude or intercept,

q = scattering vector = $\left(\frac{4\pi n}{\lambda_0}\right).\sin(\theta/2)$

n = dispersant refractive index,

λ_0 = laser wavelength,

θ = detection angle

D = diffusion coefficient,

τ = the delay time

The sum has to be understood as the contribution of different sizes, considered as discrete or continuous.

The auto-correlation function also contains the diffusion coefficient information, required to be entered in the STOKES-EINSTEIN equation, used to calculate the hydrodynamic diameter. The diffusion coefficient D describes the Brownian motion of the nanoparticle in a particular solvent environment. It depends not only on the size of the particle core but also on surface structures, the concentration and the types of ions in the medium. D is obtained by fitting the correlation function with a suitable algorithm: cumulants analysis or distribution analysis.

Cumulants analysis: simple method to analyze the correlation function of a DLS measurement. The algorithm fits the logarithm of the intensity correlation function to a 3rd order polynomial (ISO22412:2017), giving a mean particle size (Z-average) and an estimate of the width of the distribution (polydispersity index). This analysis method is perfectly suited for monodispersed population but becomes less descriptive for samples moving further away from monomodal distribution.

Effective diameter or "Z-average": mathematically, the harmonic intensity means of the particle sizes, derived from the **cumulants** methods[i]. It is the most stable parameter produced by DLS technique because it has a low sensitivity to noise (considering it is inferred from a least square fit of the intensity correlation function). Nevertheless, it is very sensitive to the presence of aggregates or large contaminants (*e.g.* dusts) due to its inherent intensity weighting.

Diameter by Number: this distribution is inferred by MIE scattering theory, from the intensity measurement, where each particle has equal weighting. It requires the index of refraction of the material composing the nanoparticle and relies on the hypothesis of spherical nanoparticles. It allows to retrieve the contribution of small particles to the scattering, which signal is dominated – in intensity – by the largest particles or aggregates, owing to the Rayleigh scattering cross section scaling as d^6, with d the particle diameter. Figure B-3 shows the difference of distribution representation depending on number, volume or intensity representation.

[i] https://www.azonano.com/article.aspx?ArticleID=3098

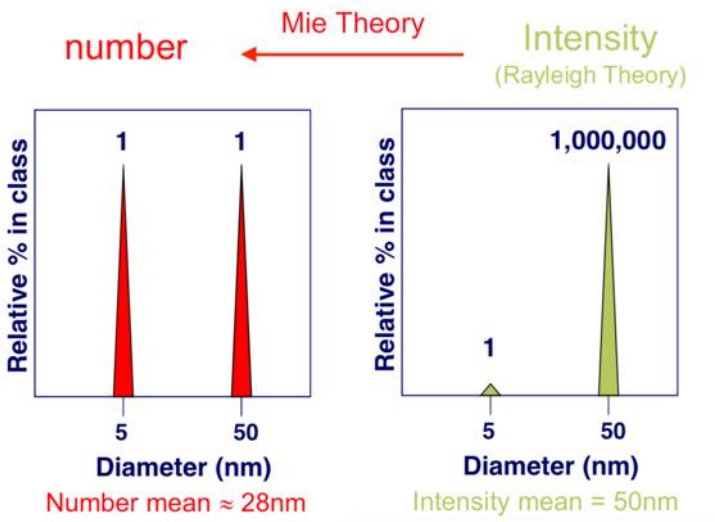

Figure B-3: Number, Volume and Intensity distribution representations, for a mixture composed of equal number of 5 nm and 50 nm spherical nanoparticles. From Malvern technical support datasheet

Polydispersity Index: is extracted from the correlation function from the cumulants analysis: a single particle size distribution is assumed and a single exponential fit is applied to the autocorrelation function. The polydispersity describes the width of the assumed Gaussian distribution. This value is dimensionless and fits between 0 and 1. Values between 0 and 0.2 are considered to be associated to highly monodisperse distributions, values from 0.2 to 0.7 to mid-range polydisperse distribution and values greater than 0.7 to very polydisperse ones.

Baseline Index: indicates the sample quality, *e.g.* presence of large particles/aggregates, by making the difference between the measured and the fitted baseline of the correlation function.

Hydrodynamic Diameter: diameter of a hypothetical hard sphere diffusing at the same speed and fashion as that of the particle being measured, as represented in Figure B-4. This value is indicative of the dynamic hydrated/solvated particle and is dependent upon shape, surface structure and ions surrounding the particle. It is calculated thanks to the Stokes-Einstein equation.

Where: D_H = hydrodynamic diameter,
k = Boltzmann's constant,
T = absolute temperature,
η = viscosity coefficient,

$$\text{Stokes} - \text{Einstein equation:}$$

$$D_H = \frac{kT}{3\,\pi\,\eta\,D}$$

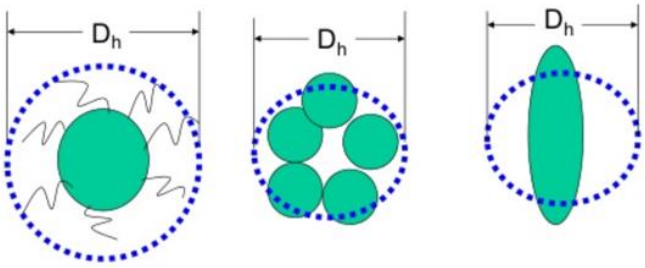

Figure B-4: Representation of the hydrodynamic diameter. From Horiba technical support datasheet

Appendix C: linearity of the intensity detected in time-gated microscopy with the excitation laser power

The first time-gated microscopy measurements were made at a laser excitation power of 50 mW, to facilitate the detection of Cop-FNDs, but in some cases (organ section with large aggregates) this power led to the saturation of the signal from large aggregates, which biases the final representation of the sum of total intensity. However, in most cases we did not observe such saturation, and the data could be processed.

For the organ sections displaying fluorescence saturation, the acquisitions were done at the lower excitation power of 25 mW. In order to be able to include all data (acquired at either 25 or 50 mW) in the same analysis, we checked whether we could simply apply a linear correction.

To this aim we compared the total intensity from 100 scenes of a Cop-FND-containing organ section. The sum of the total intensity over the surface for each detection power is displayed in Table C-1.

Table C-1: Sum of total intensity over surface area for an increasing detection power.

Power (mW)	15	25	37,5	50
Sum of total intensity/surface	1,34	2,34	3,59	4,49

The graphic representation of those data (Figure C-2) shows that the linear regression fits well the data. This is confirmed by the value of (i) the slope (close to 0.1), and (ii) of the correlation coefficient R^2, very close to 1, reinforcing the postulate that the fluorescence intensity evolves linearly with the excitation power.

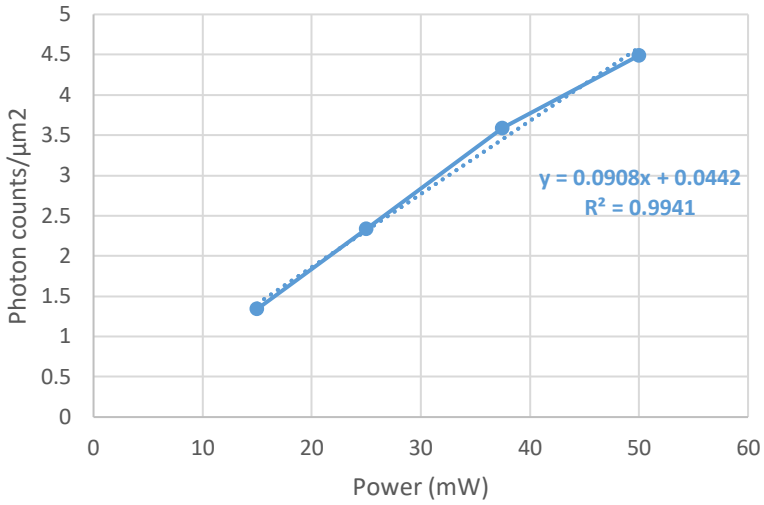

Figure C-1: Sum of total intensity over the organ section surface vs laser excitation power. The evolution can be fitted with a line (dashed line).

Fluorescence images that would have been obtained at P=25 mW were extrapolated from P=50 mW real acquisition by applying a global factor of 2.

***

REFERENCES

1. Gartia, M. R.; Hsiao, A.; Pokhriyal, A.; Seo, S.; Kulsharova, G.; Cunningham, B. T.; Bond, T. C.; Liu, G. L. Colorimetric Plasmon Resonance Imaging Using Nano Lycurgus Cup Arrays. *Advanced Optical Materials* **2013**, *1*, 68–76, doi:10.1002/adom.201200040.

2. Lambertson, R. H.; Lacy, C. A.; Gillespie, S. D.; Leopold, M. C.; Coppage, R. H. Gold nanoparticle colorants as traditional ceramic glaze alternatives. *Journal of the American Ceramic Society* **2017**, *100*, 3943–3951, doi:10.1111/jace.14928.

3. Jin, R.; Cao, Y.; Mirkin, C. A.; Kelly, K. L.; Schatz, G. C.; Zheng, J. G. Photoinduced conversion of silver nanospheres to nanoprisms. *Science* **2001**, *294*, 1901–1903, doi:10.1126/science.1066541.

4. Feynman, R. P. There's Planty of Room at the Bottom. *Engineering and Science* **1960**, *23*, 22–36, doi:10.1109/84.128057.

5. Takagahara, T.; Takeda, K. Theory of the quantum confinement effect on excitons in quantum dots of indirect-gap materials. *Physical Review B* **1992**, *46*, 15578–15581, doi:10.1103/PhysRevB.46.15578.

6. Boisseau, P.; Loubaton, B. Nanomedicine, nanotechnology in medicine. *Comptes Rendus Physique* **2011**, *12*, 620–636, doi:10.1016/j.crhy.2011.06.001.

7. Hassan, S.; Prakasha, G.; Bal Ozturk, A.; Saghazadeh, S.; Farhan Sohail, M.; Seo, J.; Remzi Dokmeci, M.; Zhang, Y. S.; Khademhosseini, A. Evolution and clinical translation of drug delivery nanomaterials. *Nano Today* **2017**, *15*, 91–106, doi:10.1016/j.nantod.2017.06.008.

8. Verdun, C.; Couvreur, P.; Vranckx, H.; Lenaerts, V.; Roland, M. Development of a nanoparticle controlled-release formulation for human use. *Journal of Controlled Release* **1986**, *3*, 205–210, doi:10.1016/0168-3659(86)90081-7.

9. Verdun, C.; Brasseur, F.; Vranckx, H.; Couvreur, P.; Roland, M. Tissue distribution of doxorubicin associated with polyisohexylcyanoacrylate nanoparticles. *Cancer Chemotherapy and Pharmacology* **1990**, *26*, 13–18, doi:10.1007/BF02940287.

10. Anselmo, A. C.; Mitragotri, S. Nanoparticles in the clinic. *Bioengineering & Translational Medicine* **2016**, *1*, 10–29, doi:10.1002/btm2.10003.

11. Fukumori, Y.; Ichikawa, H. Nanoparticles for cancer therapy and diagnosis. *Advanced Powder Technology* **2006**, *17*, 1–28, doi:10.1163/156855206775123494.

12. Freitas, R. A. What is nanomedicine? *Nanomedicine: Nanotechnology, Biology, and Medicine* 2005, *1*, 2–9.

13. Lécuyer, T.; Teston, E.; Ramirez-Garcia, G.; Maldiney, T.; Viana, B.; Seguin, J.; Mignet, N.; Scherman, D.; Richard, C. Chemically engineered persistent luminescence nanoprobes for bioimaging. *Theranostics* **2016**, *6*, 2488–2524, doi:10.7150/thno.16589.

14. Kucsko, G.; Maurer, P. C.; Yao, N. Y.; Kubo, M.; Noh, H. J.; Lo, P. K.; Park, H.; Lukin, M. D. Nanometer scale thermometry in a living cell. *Nature* **2013**, *500*, 54–8, doi:10.1038/nature12373.

15. Kyprianou, D.; Guerreiro, A. R.; Chianella, I.; Piletska, E. V.; Fowler, S. A.; Karim, K.; Whitcombe, M. J.; Turner, A. P. F.; Piletsky, S. A. New reactive polymer for protein immobilisation on sensor surfaces. *Biosensors and Bioelectronics* **2009**, *24*, 1365–1371, doi:10.1016/j.bios.2008.07.070.

16. Whitlow, J.; Pacelli, S.; Paul, A. Multifunctional nanodiamonds in regenerative medicine: Recent advances and future directions. *Journal of Controlled Release* 2017, *261*, 62–86.

17. Shi, J.; Kantoff, P. W.; Wooster, R.; Farokhzad, O. C. Cancer nanomedicine: Progress, challenges and opportunities. *Nature Reviews Cancer* 2017, *17*, 20–37.

18. Hong, C. C.; Lin, C. C.; Hong, C. L.; Lin, Z. X.; Chung, M. H.; Hsieh, P. W. Handheld analyzer with on-chip molecularly-imprinted biosensors for electrical detection of propofol in plasma samples. *Biosensors and Bioelectronics* **2016**, *86*, 623–629, doi:10.1016/j.bios.2016.07.032.

19. Hou, W.; Toh, T. B.; Abdullah, L. N.; Yvonne, T. W. Z.; Lee, K. J.; Guenther, I.; Chow, E. K. H. Nanodiamond–Manganese dual mode MRI contrast agents for enhanced liver tumor detection. *Nanomedicine: Nanotechnology, Biology, and Medicine* **2017**, *13*, 783–793, doi:10.1016/j.nano.2016.12.013.

20. Garcia, J.; Tang, T.; Louie, A. Y. Nanoparticle-based multimodal PET/MRI probes. *Nanomedicine* **2015**, *10*, 1343–1359, doi:10.2217/nnm.14.224.

21. Ashton, J. R.; West, J. L.; Badea, C. T. In vivo small animal micro-CT using nanoparticle contrast agents. *Frontiers in Pharmacology* 2015, *6*, 256.

22. Ramírez-García, G.; Martínez-Alfaro, M.; D'Orlyé, F.; Bedioui, F.; Mignet, N.; Varenne, A.; Gutiérrez-Granados, S.; Richard, C. Photo-stimulation of persistent luminescence nanoparticles enhances cancer cells death. *International Journal of Pharmaceutics* **2017**, *532*, 696–703, doi:10.1016/j.ijpharm.2017.07.009.

23. Wang, X.; Liu, K.; Yang, G.; Cheng, L.; He, L.; Liu, Y.; Li, Y.; Guo, L.; Liu, Z. Near-infrared light triggered photodynamic therapy in combination with gene therapy using upconversion nanoparticles for effective cancer cell killing. *Nanoscale* **2014**, *6*, 9198, doi:10.1039/C4NR02495H.

24. Singh, R.; Lillard, J. W. Nanoparticle-based targeted drug delivery. *Experimental and Molecular Pathology* 2009, *86*, 215–223.

25. Longmire, M.; Choyke, P. L.; Kobayashi, H. Clearance properties of nano-sized particles and molecules as imaging agents: considerations and caveats. *Nanomedicine* **2008**, *3*, 703–717, doi:10.2217/17435889.3.5.703.

26. Soo Choi, H.; Liu, W.; Misra, P.; Tanaka, E.; Zimmer, J. P.; Itty Ipe, B.; Bawendi, M. G.; Frangioni, J. V Renal clearance of nanoparticles. *Nature Biotechnology* **2007**, *25*, 1165–1170, doi:10.1038/nbt1340.

27. Skocaj, M.; Filipic, M.; Petkovic, J.; Novak, S. Titanium dioxide in our everyday life; is it safe? *Radiology and Oncology* **2011**, *45*, 227–247.

28. W. Lem, K.; Choudhury, A.; A. Lakhani, A.; Kuyate, P.; R. Haw, J.; S. Lee, D.; Iqbal, Z.; J. Brumlik, C. Use of Nanosilver in Consumer Products. *Recent Patents on Nanotechnology* **2012**, *6*, 60–72, doi:10.2174/187221012798109318.

29. Bawa, R. Regulating nanomedicine - can the FDA handle it? *Current Drug Delivery* 2011, *8*, 227–234.

30. Shi, J.; Kantoff, P. W.; Wooster, R.; Farokhzad, O. C. Cancer nanomedicine: progress, challenges and opportunities. *Nature Reviews Cancer* **2016**, *17*, 20–37, doi:10.1038/nrc.2016.108.

31. Bobo, D.; Robinson, K. J.; Islam, J.; Thurecht, K. J.; Corrie, S. R. Nanoparticle-Based Medicines: A Review of FDA-Approved Materials and Clinical Trials to Date. *Pharmaceutical Research* 2016, *33*, 2373–2387.

32. Dawidczyk, C. M.; Russell, L. M.; Searson, P. C. Nanomedicines for cancer therapy: state-of-the-art and limitations to pre-clinical studies that hinder future developments. *Frontiers in Chemistry* **2014**, *2*, 1–13, doi:10.3389/fchem.2014.00069.

33. Puri, A.; Loomis, K.; Smith, B.; Lee, J.-H.; Yavlovich, A.; Heldman, E.; Blumenthal, R. Lipid-Based Nanoparticles as Pharmaceutical Drug Carriers: From Concepts to Clinic. *Critical Reviews in Therapeutic Drug Carrier Systems* **2009**, *26*, 523–580, doi:10.1615/CritRevTherDrugCarrierSyst.v26.i6.10.

34. Lee, V. H. L.; Ghandehari, H.; Allen, T. M.; Cullis, P. R. Liposomal drug delivery systems: From concept to clinical applications. *Advanced Drug Delivery Reviews* **2013**, *65*, 36–48.

35. Bei, D.; Meng, J.; Youan, B.-B. C. Engineering nanomedicines for improved melanoma therapy: progress and promises. *Nanomedicine (London, England)* **2010**, *5*, 1385–99, doi:10.2217/nnm.10.117.

36. Dineshkumar, B.; Krishnakumar, K.; John, A.; Paul, D.; Cherian, J.; Panayappan, L. Nanocapsules : A Novel Nano-Drug Delivery System. *International Journal of Research in Drug Delivery* **2013**, *3*, 1–3.

37. Devulapally, R.; Paulmurugan, R. Polymer nanoparticles for drug and small silencing RNA delivery to treat cancers of different phenotypes. *Wiley interdisciplinary reviews. Nanomedicine and nanobiotechnology* **2014**, *6*, 40–60, doi:10.1002/wnan.1242.

38. Danhier, F.; Ansorena, E.; Silva, J. M.; Coco, R.; Le Breton, A.; Préat, V. PLGA-based nanoparticles: an overview of biomedical applications. *Journal of controlled release : official journal of the Controlled Release Society* **2012**, *161*, 505–22, doi:10.1016/j.jconrel.2012.01.043.

39. Larson, N.; Ghandehari, H. Polymeric conjugates for drug delivery. *Chemistry of Materials* 2012, *24*, 840–853.

40. Toub, N.; Bertrand, J.-R.; Tamaddon, A.; Elhamess, H.; Hillaireau, H.; Maksimenko, A.; Maccario, J.; Malvy, C.; Fattal, E.; Couvreur, P. Efficacy of siRNA nanocapsules targeted against the EWS-Fli1 oncogene in Ewing sarcoma. *Pharmaceutical research* **2006**, *23*, 892–900, doi:10.1007/s11095-006-9901-9.

41. Bertrand, J.-R.; Lucas, C.; Pham, N. M.; Durieu, C.; Couvreur, P.; Malvy, C. P.; Desmaële, D. Turning Squalene into Cationic Lipid Allows a Delivery of siRNA in Cultured Cells. *Nucleic Acid Therapeutics* **2015**, *25*, 121–129, doi:10.1089/nat.2014.0504.

42. Neburkova, J.; Vavra, J.; Cigler, P. Coating nanodiamonds with biocompatible shells for applications in biology and medicine. *Current Opinion in Solid State and Materials Science* 2017, *21*, 43–53.

43. Correa, S.; Dreaden, E. C.; Gu, L.; Hammond, P. T. Engineering nanolayered particles for modular drug delivery. *Journal of controlled release : official journal of the Controlled Release Society* **2016**, doi:10.1016/j.jconrel.2016.01.040.

44. Mody, N.; Tekade, R. K.; Mehra, N. K.; Chopdey, P.; Jain, N. K. Dendrimer, Liposomes, Carbon Nanotubes and PLGA Nanoparticles: One Platform Assessment of Drug Delivery Potential. *AAPS PharmSciTech* **2014**, 1–12, doi:10.1208/s12249-014-0073-3.

45. Leiro, V.; Duque Santos, S.; Lopes, C. D. F.; Paula Pêgo, A. Dendrimers as Powerful Building Blocks in Central Nervous System Disease: Headed for Successful Nanomedicine. *Advanced Functional Materials* 2017, 1700313.

46. He, Q.; Shi, J. Mesoporous silica nanoparticle based nano drug delivery systems: synthesis, controlled drug release and delivery, pharmacokinetics and biocompatibility. *Journal of Materials Chemistry* **2011**, *21*, 5845, doi:10.1039/c0jm03851b.

47. Gibson, J. D.; Khanal, B. P.; Zubarev, E. R. Paclitaxel-functionalized gold nanoparticles. *Journal of the American Chemical Society* **2007**, *129*, 11653–61, doi:10.1021/ja075181k.

48. Finlay, J.; Roberts, C. M.; Dong, J.; Zink, J. I.; Tamanoi, F.; Glackin, C. A. Mesoporous silica nanoparticle delivery of chemically modified siRNA against TWIST1 leads to reduced tumor burden. *Nanomedicine: Nanotechnology, Biology and Medicine* **2015**, doi:10.1016/j.nano.2015.05.011.

49. Rehor, I.; Slegerova, J.; Kucka, J.; Proks, V.; Petrakova, V.; Adam, M.-P.; Treussart, F.; Turner, S.; Bals, S.; Sacha, P.; Ledvina, M.; Wen, A. M.; Steinmetz, N. F.; Cigler, P. Fluorescent nanodiamonds embedded in biocompatible translucent shells. *Small (Weinheim an der Bergstrasse, Germany)* **2014**, *10*, 1106–15, doi:10.1002/smll.201302336.

50. Cortajarena, A. L.; Ortega, D.; Ocampo, S. M.; Gonzalez-García, A.; Couleaud, P.; Miranda, R.; Belda-Iniesta, C.; Ayuso-Sacido, A. Engineering Iron Oxide Nanoparticles for Clinical Settings. *Nanobiomedicine* **2014**, *1*, 2, doi:10.5772/58841.

51. Wadajkar, A. S.; Menon, J. U.; Kadapure, T.; Tran, R. T.; Yang, J.; Nguyen, K. T. Design and Application of Magnetic-based Theranostic Nanoparticle Systems. *Recent patents on biomedical engineering* **2013**, *6*, 47–57, doi:10.2174/1874764711306010007.

52. Maier-Hauff, K.; Ulrich, F.; Nestler, D.; Niehoff, H.; Wust, P.; Thiesen, B.; Orawa, H.; Budach, V.; Jordan, A. Efficacy and safety of intratumoral thermotherapy using magnetic iron-oxide nanoparticles combined with external beam radiotherapy on patients with recurrent glioblastoma multiforme. *Journal of Neuro-Oncology* **2011**, *103*, 317–324, doi:10.1007/s11060-010-0389-0.

53. Duguet, E.; Vasseur, S.; Mornet, S.; Devoisselle, J.-M. Magnetic nanoparticles and their applications in medicine. *Nanomedicine* **2006**, *1*, 157–168, doi:10.2217/17435889.1.2.157.

54. Colombo, M.; Carregal-Romero, S.; Casula, M. F.; Gutiérrez, L.; Morales, M. P.; Böhm, I. B.; Heverhagen, J. T.; Prosperi, D.; Parak, W. J. Biological applications of magnetic nanoparticles. *Chemical Society Reviews* **2012**, *41*, 4306, doi:10.1039/c2cs15337h.

55. Ghasempour, S.; Shokrgozar, M. A.; Ghasempour, R.; Alipour, M. Investigating the cytotoxicity of iron oxide nanoparticles in in vivo and in vitro studies. *Experimental and Toxicologic Pathology* **2015**, *67*, 509–515, doi:10.1016/j.etp.2015.07.005.

56. Kievit, F. M.; Zhang, M. Cancer nanotheranostics: improving imaging and therapy by targeted delivery across biological barriers. *Advanced materials (Deerfield Beach, Fla.)* **2011**, *23*, H217-47, doi:10.1002/adma.201102313.

57. Giljohann, D. A.; Seferos, D. S.; Prigodich, A. E.; Patel, P. C.; Mirkin, C. A. Gene regulation with polyvalent siRNA-nanoparticle conjugates. *Journal of the American Chemical Society* **2009**, *131*, 2072–3, doi:10.1021/ja808719p.

58. Pan, Y.; Leifert, A.; Ruau, D.; Neuss, S.; Bornemann, J.; Schmid, G.; Brandau, W.; Simon, U.; Jahnen-Dechent, W. Gold nanoparticles of diameter 1.4 nm trigger necrosis by oxidative stress and mitochondrial damage. *Small (Weinheim an der Bergstrasse, Germany)* **2009**, *5*, 2067–76, doi:10.1002/smll.200900466.

59. Pan, Y.; Bartneck, M.; Jahnen-Dechent, W. Cytotoxicity of gold nanoparticles. *Methods in Enzymology* **2012**, *509*, 225–242, doi:10.1016/B978-0-12-391858-1.00012-5.

60. Wu, Y.-N.; Wu, P.-C.; Yang, L.-X.; Ratinac, K. R.; Thordarson, P.; Jahn, K. A.; Chen, D.-H.; Shieh, D.-B.; Braet, F. The anticancer properties of iron core–gold shell nanoparticles in colorectal cancer cells. *International Journal of Nanomedicine* **2013**, *8*, 3321–3331, doi:10.2147/IJN.S47742.

61. Cheng, L.-C.; Chen, H. M.; Lai, T.-C.; Chan, Y.-C.; Liu, R.-S.; Sung, J. C.; Hsiao, M.; Chen, C.-H.; Her, L.-J.; Tsai, D. P. Targeting polymeric fluorescent nanodiamond-gold/silver multi-functional nanoparticles as a light-transforming hyperthermia reagent for cancer cells. *Nanoscale* **2013**, *5*, 3931, doi:10.1039/c3nr34091k.

62. Cadeddu, J. A.; Haley, B.; Frenkel, E. Nanoparticles for drug delivery in cancer treatment. *Urologic Oncology: Seminars and Original Investigations* **2008**, *26*, 57–64.

63. Rallapalli, H.; Smith, B. R. Carbon Nanotubes for Enhanced Biopharmaceutical Delivery. *Reviews in Cell Biology and Molecular Medicine* **2016**, *2*, 281–305, doi:10.1002/3527600906.MCB.201600006.

64. Das, K.; Madhusoodan, A.; Mili, B.; Kumar, A.; Saxena, A. C.; Kumar, K.; Sarkar, M.; Singh, P.; Srivastava, S.; Bag, S. Functionalized carbon nanotubes as suitable scaffold materials for proliferation and differentiation of canine mesenchymal stem cells. *International Journal of Nanomedicine* **2017**, *12*, 3235–3252, doi:10.2147/IJN.S122945.

65. Lalwani, G.; Gopalan, A.; D'Agati, M.; Srinivas Sankaran, J.; Judex, S.; Qin, Y. X.; Sitharaman, B. Porous three-dimensional carbon nanotube scaffolds for tissue engineering. *Journal of Biomedical Materials Research - Part A* **2015**, *103*, 3212–3225, doi:10.1002/jbm.a.35449.

66. Patlolla, A.; Knighten, B.; Tchounwou, P. Multi-walled carbon nanotubes induce cytotoxicity, genotoxicity and apoptosis in normal human dermal fibroblast cells. *Ethnicity & disease* **2010**, *20*, S1-65–72, doi:10.1016/j.ydbio.2004.09.001.

67. Kumarathasan, P.; Breznan, D.; Das, D.; Salam, M. A.; Siddiqui, Y.; Mackinnon-Roy, C.; Guan, J.; De Silva, N.; Simard, B.; Vincent, R. Cytotoxicity of carbon nanotube variants: A comparative in vitro exposure study with A549 epithelial and J774 macrophage cells. *Nanotoxicology* **2015**, *9*, 148–161, doi:10.3109/17435390.2014.902519.

68. Bawarski, W. E.; Chidlowsky, E.; Bharali, D. J.; Mousa, S. A. Emerging nanopharmaceuticals. *Nanomedicine : nanotechnology, biology, and medicine* **2008**, *4*, 273–82, doi:10.1016/j.nano.2008.06.002.

69. Prabhakar, N.; Näreoja, T.; von Haartman, E.; Karaman, D. Sen; Jiang, H.; Vlasov, D. I.; Jiang, H.; Koho, S.; Dolenko, T. A.; Pekka, E. H.; Ralchenko, V. G.; Hosomi, S.; Vlasov, I. I.; Sahlgren, C.; Rosenholm, J. M. Core–shell designs of photoluminescent nanodiamonds with porous silica coatings for bioimaging and drug delivery II: application. *Nanoscale* **2013**, *5*, 3713–3722, doi:10.1039/c3nr33926b.

70. Rehor, I.; Slegerova, J.; Kucka, J.; Proks, V.; Petrakova, V.; Adam, M. P.; Treussart, F.; Turner, S.; Bals, S.; Sacha, P.; Ledvina, M.; Wen, A. M.; Steinmetz, N. F.; Cigler, P. Fluorescent nanodiamonds embedded in biocompatible translucent shells. *Small* **2014**, *10*, 1106–1115, doi:10.1002/smll.201302336.

71. Mahipal, A.; Nguyen, D. Risks and benefits of phase 1 clinical trial participation. *Cancer control : journal of the Moffitt Cancer Center* **2014**, *21*, 193–9, doi:10.1177/107327481402100303.

72. Eisenhauer, E. A.; O'Dwyer, P. J.; Christian, M.; Humphrey, J. S. Phase I Clinical Trial Design in Cancer Drug Development. *Journal of Clinical Oncology* **2000**, *18*, 684–684, doi:10.1200/JCO.2000.18.3.684.

73. Umscheid, C. A.; Margolis, D. J.; Grossman, C. E. Key concepts of clinical trials: A narrative review. *Postgraduate Medicine* 2011, *123*, 194–204.

74. Suvarna, V. Phase IV of Drug Development. *Perspectives in Clinical Research* **2010**, *1*, 57–60.

75. Zhang, X.; Zhang, Y.; Ye, X.; Guo, X.; Zhang, T.; He, J. Overview of phase IV clinical trials for postmarket drug safety surveillance: A status report from the ClinicalTrials.gov registry. *BMJ Open* 2016, *6*, e010643.

76. Fournier, A.; Zureik, M. Estimate of deaths due to valvular insufficiency attributable to the use of benfluorex in France. *Pharmacoepidemiology and Drug Safety* **2012**, *21*, 343–351, doi:10.1002/pds.3213.

77. Greener, M. First do no harm. *EMBO reports* **2008**, *9*, 221–224, doi:10.1038/embor.2008.17.

78. Beiranvand, S.; Eatemadi, A.; Karimi, A. New Updates Pertaining to Drug Delivery of Local Anesthetics in Particular Bupivacaine Using Lipid Nanoparticles. *Nanoscale Research Letters* **2016**, *11*, 307, doi:10.1186/s11671-016-1520-8.

79. Zatsepin, T. S.; Koteliansky, V. Lipid nanoparticles for targeted siRNA delivery – going from bench to bedside. *Int J Nanomedicine.* **2016**, *11*, 3077–3086, doi:10.2147/IJN.S106625.

80. Roberts, M. S.; Mohammed, Y.; Pastore, M. N.; Namjoshi, S.; Yousef, S.; Alinaghi, A.; Haridass, I. N.; Abd, E.; Leite-Silva, V. R.; Benson, H. A. E.; Grice, J. E. Topical and cutaneous delivery using nanosystems. *Journal of Controlled Release* **2017**, *247*, 86–105, doi:10.1016/j.jconrel.2016.12.022.

81. Gao, W.; Chen, Y.; Zhang, Y.; Zhang, Q.; Zhang, L. Nanoparticle-based local antimicrobial drug delivery. *Advanced Drug Delivery Reviews* 2017.

82. Lin, Q.; Chen, J.; Zhang, Z.; Zheng, G. Lipid-based nanoparticles in the systemic delivery of siRNA. *Nanomedicine* **2014**, *9*, 105–120, doi:10.2217/nnm.13.192.

83. Tsoulfas, G. The impact of the European financial crisis on clinical research within the European union or “when life gives you lemons, make lemonade.” *Hippokratia* **2012**, *16*, 6–10.

84. Tinkle, S.; Mcneil, S. E.; Mühlebach, S.; Bawa, R.; Borchard, G.; Barenholz, Y. C.; Tamarkin, L.; Desai, N. Nanomedicines: Addressing the scientific and regulatory gap. *Annals of the New York Academy of Sciences* **2014**, *1313*, 35–56, doi:10.1111/nyas.12403.

85. Ray, P. C.; Yu, H.; Fu, P. P. Toxicity and environmental risks of nanomaterials: Challenges and future needs. *Journal of Environmental Science and Health - Part C Environmental Carcinogenesis and Ecotoxicology Reviews* 2009, *27*, 1–35.

86. Neuman, D.; Chandhok, J. N. Patent Watch: Nanomedicine patents highlight importance of production methods. *Nature Reviews Drug Discovery* 2016, *15*, 448–449.

87. Venditto, V. J.; Szoka, F. C. Cancer nanomedicines: So many papers and so few drugs! *Advanced Drug Delivery Reviews* 2013, *65*, 80–88.

88. Krueger, A. New carbon materials: Biological applications of functionalized nanodiamond materials. *Chemistry - A European Journal* **2008**, *14*, 1382–1390, doi:10.1002/chem.200700987.

89. Bundy, F. P.; Hall, H. T.; Strong, H. M.; Wentorf, R. H. Man-Made Diamonds. *Nature* **1955**, *176*, 51–55.

90. Zheng, W.-W.; Hsieh, Y.-H.; Chiu, Y.-C.; Cai, S.-J.; Cheng, C.-L.; Chen, C. Organic functionalization of ultradispersed nanodiamond: synthesis and applications. *Journal of Materials Chemistry* **2009**, *19*, 8432, doi:10.1039/b904302k.

91. Arnault, J. C.; Girard, H. A. Hydrogenated nanodiamonds: Synthesis and surface properties. *Current Opinion in Solid State and Materials Science* **2016**, 1–7, doi:10.1016/j.cossms.2016.06.007.

92. Ōsawa, E. Monodisperse single nanodiamond particulates. *Pure and Applied Chemistry* **2008**, *80*, 1365–1379, doi:10.1351/pac200880071365.

93. Nunn, N.; Torelli, M.; McGuire, G.; Shenderova, O. Nanodiamond: A high impact nanomaterial. *Current Opinion in Solid State and Materials Science* 2017, *21*, 1–9.

94. Moore, L.; Yang, J.; Lan, T. T. H.; Osawa, E.; Lee, D. K.; Johnson, W. D.; Xi, J.; Chow, E. K. H.; Ho, D. Biocompatibility Assessment of Detonation Nanodiamond in Non-Human Primates and Rats Using Histological, Hematologic, and Urine Analysis. *ACS Nano* **2016**, *10*, 7385–7400, doi:10.1021/acsnano.6b00839.

95. Chang, Y.-R.; Lee, H.-Y.; Chen, K.; Chang, C.-C.; Tsai, D.-S.; Fu, C.-C.; Lim, T.-S.; Tzeng, Y.-K.; Fang, C.-Y.; Han, C.-C.; Chang, H.-C.; Fann, W. Mass production and dynamic imaging of fluorescent nanodiamonds. *Nature Nanotechnology* **2008**, *3*, 284–288, doi:10.1038/nnano.2008.99.

96. Ivanov, M.; Mahbooba, Z.; Ivanov, D.; Smirnov, S.; Pavlyshko, S.; Osawa, E.; Brenner, D.; Shenderova, O. Nanodiamond-Based Oil Lubricants on Steel-Steel and Stainless Steel – Hard Alloy High Load Contact: Investigation of Friction Surfaces. *Nanosystems: Physics, Chemistry, Mathematics* **2014**, *5*, 160–166.

97. Prawer, S.; Greentree, A. D. Diamond for Quantum Computing. *Science* **2008**, *320*, 1601–1602, doi:10.1126/science.1158340.

98. Petit, T. Modifications de surface des nanodiamants : compréhension des mécanismes d'échanges électroniques et mise en évidence d'un effet thérapeutique, Ecole Normale Supérieur de Cachan, 2013.

99. Dufour, P.; Liebert, J.; Fontaine, G.; Behara, N. White dwarf stars with carbon atmospheres. *Nature* **2007**, *450*, 522–524, doi:10.1038/nature06318.

100. Danilenko, V. V. On the history of the discovery of nanodiamond synthesis. *Physics of the Solid State* **2004**, *46*, 595–599, doi:10.1134/1.1711431.

101. Neu, E.; Steinmetz, D.; Riedrich-Möller, J.; Gsell, S.; Fischer, M.; Schreck, M.; Becher, C. Single photon emission from silicon-vacancy colour centres in chemical vapour deposition nano-diamonds on iridium. *New Journal of Physics* **2011**, *13*, 025012, doi:10.1088/1367-2630/13/2/025012.

102. Yang, G.-W.; Wang, J.-B.; Liu, Q.-X. Preparation of nano-crystalline diamonds using pulsed laser induced reactive quenching. *Journal of Physics: Condensed Matter* **1999**, *10*, 7923–7927, doi:10.1088/0953-8984/10/35/024.

103. Mochalin, V. N.; Shenderova, O.; Ho, D.; Gogotsi, Y. The properties and applications of nanodiamonds. *Nature Nanotechnology* **2011**, *7*, 11–23, doi:10.1038/nnano.2011.209.

104. Dolmatov, V. Y. Detonation-synthesis nanodiamonds: synthesis, structure, properties and applications. *Russian Chemical Reviews* **2007**, *76*, 339–360, doi:10.1070/RC2007v076n04ABEH003643.

105. Chen, X.; Zhang, W. Diamond nanostructures for drug delivery, bioimaging, and biosensing. *Chem. Soc. Rev.* **2017**, *46*, 734–760, doi:10.1039/C6CS00109B.

106. Paci, J. T.; Man, H. B.; Saha, B.; Ho, D.; Schatz, G. C. Understanding the surfaces of nanodiamonds. *Journal of Physical Chemistry C* **2013**, *117*, 17256–17267, doi:10.1021/jp404311a.

107. Osawa, E. Recent progress and perspectives in single-digit nanodiamond. *Diamond and Related Materials* **2007**, *16*, 2018–2022, doi:10.1016/j.diamond.2007.08.008.

108. Stehlik, S.; Varga, M.; Ledinsky, M.; Jirasek, V.; Artemenko, A.; Kozak, H.; Ondic, L.; Skakalova, V.; Argentero, G.; Pennycook, T.; Meyer, J. C.; Fejfar, A.; Kromka, A.; Rezek, B. Size and Purity Control of HPHT Nanodiamonds down to 1 nm. *Journal of Physical Chemistry C* **2015**, *119*, 27708–27720, doi:10.1021/acs.jpcc.5b05259.

109. Rehor, I.; Cigler, P. Precise estimation of HPHT nanodiamond size distribution based on transmission electron microscopy image analysis. *Diamond and Related Materials* **2014**, *46*, 21–24, doi:10.1016/j.diamond.2014.04.002.

110. Shenderova, O. A.; McGuire, G. E. Science and engineering of nanodiamond particle surfaces for biological applications (Review). *Biointerphases* **2015**, *10*, 030802, doi:10.1116/1.4927679.

111. Walker, J. Optical absorption and luminescence in diamond. *Reports on Progress in Physics* **1979**, *42*, 1605, doi:10.1088/0034-4885/42/10/001.

112. Aharonovich, I.; Greentree, A. D.; Prawer, S. Diamond photonics. *Nature Photonics* 2011, *5*, 397–405.

113. Rondin, L.; Dantelle, G.; Slablab, A.; Grosshans, F.; Treussart, F.; Bergonzo, P.; Perruchas, S.; Gacoin, T.; Chaigneau, M.; Chang, H.-C.; Jacques, V.; Roch, J.-F. Surface-induced charge state conversion of nitrogen-vacancy defects in nanodiamonds. *Physical Review B - Condensed Matter and Materials Physics* **2010**, *82*, doi:10.1103/PhysRevB.82.115449.

114. Yu, S. J.; Kang, M. W.; Chang, H. C.; Chen, K. M.; Yu, Y. C. Bright fluorescent nanodiamonds: No photobleaching and low cytotoxicity. *Journal of the American Chemical Society* **2005**, *127*, 17604–17605, doi:10.1021/ja0567081.

115. Haziza, S. Quantification of intraneuronal transport by fluorescent nanodiamond tracking . Application to the screening of the functional impact of neuropsychiatric disease-related genetic risk factors ., 2015.

116. Boudou, J.-P.; Curmi, P. A.; Jelezko, F.; Wrachtrup, J.; Aubert, P.; Sennour, M.; Balasubramanian, G.; Reuter, R.; Thorel, A.; Gaffet, E. High yield fabrication of fluorescent nanodiamonds. *Nanotechnology* **2009**, *20*, 235602, doi:10.1088/0957-4484/20/23/235602.

117. Dantelle, G.; Slablab, A.; Rondin, L.; Lain, F.; Carrel, F.; Bergonzo, P.; Perruchas, S.; Gacoin, T.; Treussart, F.; Roch, J. F. Efficient production of NV colour centres in nanodiamonds using high-energy electron irradiation. In *Journal of Luminescence*; 2010; Vol. 130, pp. 1655–1658.

118. Su, L. J.; Fang, C. Y.; Chang, Y. T.; Chen, K. M.; Yu, Y. C.; Hsu, J. H.; Chang, H. C. Creation of high density ensembles of nitrogen-vacancy centers in nitrogen-rich type Ib nanodiamonds. *Nanotechnology* **2013**, *24*, 315702, doi:10.1088/0957-4484/24/31/315702.

119. Treussart, F.; Vlasov, I. I. Photoluminescence of color centers in nanodiamonds. In *Nanodiamonds*; Arnault, J. C., Ed.; Elsevier, 2017; pp. 155–181 ISBN 9780323430326.

120. Rehor, I.; Mackova, H.; Filippov, S. K.; Kucka, J.; Proks, V.; Slegerova, J.; Turner, S.; Van Tendeloo, G.; Ledvina, M.; Hruby, M.; Cigler, P. Fluorescent nanodiamonds with bioorthogonally reactive protein-resistant polymeric coatings. *ChemPlusChem* **2014**, *79*, 21–24, doi:10.1002/cplu.201300339.

121. Hsiao, W. W. W.; Hui, Y. Y.; Tsai, P. C.; Chang, H. C. Fluorescent Nanodiamond: A Versatile Tool for Long-Term Cell Tracking, Super-Resolution Imaging, and Nanoscale Temperature Sensing. *Accounts of Chemical Research* 2016, *49*, 400–407.

122. Rittweger, E.; Han, K. Y.; Irvine, S. E.; Eggeling, C.; Hell, S. W. STED microscopy reveals crystal colour centres with nanometric resolution. *Nature Photonics* **2009**, *3*, 144–147, doi:10.1038/nphoton.2009.2.

123. Arroyo-Camejo, S.; Adam, M. P.; Besbes, M.; Hugonin, J. P.; Jacques, V.; Greffet, J. J.; Roch, J. F.; Hell, S. W.; Treussart, F. Stimulated emission depletion microscopy resolves individual nitrogen vacancy centers in diamond nanocrystals. *ACS Nano* **2013**, *7*, 10912–10919, doi:10.1021/nn404421b.

124. Beveratos, A.; Brouri, R.; Gacoin, T.; Poizat, J.-P.; Grangier, P. Nonclassical radiation from diamond nanocrystals. *Physical Review A* **2001**, *64*, 061802, doi:10.1103/PhysRevA.64.061802.

125. Faklaris, O.; Garrot, D.; Joshi, W.; Druon, F.; Boudou, J. P.; Sauvage, T.; Georges, P.; Curmi, P. A.; Treussart, F. Detection of single photoluminescent diamond nanoparticles in

cells and study of the internalization pathway. *Small* **2008**, *4*, 2236–2239, doi:10.1002/smll.200800655.

126. Kuo, Y.; Hsu, T. Y.; Wu, Y. C.; Chang, H. C. Fluorescent nanodiamond as a probe for the intercellular transport of proteins in vivo. *Biomaterials* **2013**, *34*, 8352–8360, doi:10.1016/j.biomaterials.2013.07.043.

127. Hui, Y. Y.; Su, L.-J.; Chen, O. Y.; Chen, Y.-T.; Liu, T.-M.; Chang, H.-C. Wide-field imaging and flow cytometric analysis of cancer cells in blood by fluorescent nanodiamond labeling and time gating. *Scientific reports* **2014**, *4*, 5574, doi:10.1038/srep05574.

128. Mchedlov-Petrossyan, N. O.; Kamneva, N. N.; Marynin, A. I.; Kryshtal, A. P.; Ōsawa, E. Colloidal properties and behaviors of 3 nm primary particles of detonation nanodiamonds in aqueous media. *Phys. Chem. Chem. Phys.* **2015**, *17*, 16186–16203, doi:10.1039/C5CP01405K.

129. Krüger, A.; Kataoka, F.; Ozawa, M.; Fujino, T.; Suzuki, Y.; Aleksenskii, A. E.; Vul', A. Y.; Osawa, E. Unusually tight aggregation in detonation nanodiamond: Identification and disintegration. *Carbon* **2005**, *43*, 1722–1730, doi:10.1016/j.carbon.2005.02.020.

130. Williams, O. A.; Hees, J.; Dieker, C.; Jäger, W.; Kirste, L.; Nebel, C. E. Size-dependent reactivity of diamond nanoparticles. *ACS Nano* **2010**, *4*, 4824–4830, doi:10.1021/nn100748k.

131. Morita, Y.; Takimoto, T.; Yamanaka, H.; Kumekawa, K.; Marino, S.; Aonuma, S.; Kimura, T.; Komatsu, N. A facile and scalable process for size-controllable separation of nanodiamond particles as small as 4 nm. *Small* **2008**, *4*, 2154–2157, doi:10.1002/smll.200800944.

132. Girard, H. A.; Perruchas, S.; Gesset, C.; Chaigneau, M.; Vieille, L.; Arnault, J. C.; Bergonzo, P.; Boilot, J. P.; Gacoin, T. Electrostatic grafting of diamond nanoparticles: A versatile route to nanocrystalline diamond thin films. *ACS Applied Materials and Interfaces* **2009**, *1*, 2738–2746, doi:10.1021/am900458g.

133. Krueger, A.; Lang, D. Functionality is key: Recent progress in the surface modification of nanodiamond. *Advanced Functional Materials* **2012**, *22*, 890–906, doi:10.1002/adfm.201102670.

134. Arnault, J.-C.; Petit, T.; Girard, H.; Chavanne, A.; Gesset, C.; Sennour, M.; Chaigneau, M. Surface chemical modifications and surface reactivity of nanodiamonds

hydrogenated by CVD plasma. *Physical Chemistry Chemical Physics* **2011**, *13*, 11481, doi:10.1039/c1cp20109c.

135. Dolmatov, V. Y. Detonation-synthesis nanodiamonds: synthesis, structure, properties and applications. *Russian Chemical Reviews* **2007**, *76*, 339–360, doi:10.1070/RC2007v076n04ABEH003643.

136. Wolcott, A.; Schiros, T.; Trusheim, M. E.; Chen, E. H.; Nordlund, D.; Diaz, R. E.; Gaathon, O.; Englund, D.; Owen, J. S. Surface structure of aerobically oxidized diamond nanocrystals. *Journal of Physical Chemistry C* **2014**, *118*, 26695–26702, doi:10.1021/jp506992c.

137. Krueger, A.; Ozawa, M.; Jarre, G.; Liang, Y.; Stegk, J.; Lu, L. Deagglomeration and functionalisation of detonation diamond. In *Physica Status Solidi (A) Applications and Materials Science*; WILEY-VCH Verlag, 2007; Vol. 204, pp. 2881–2887.

138. Martín, R.; Heydorn, P. C.; Alvaro, M.; Garcia, H. General strategy for high-density covalent functionalization of diamond nanoparticles using fenton chemistry. *Chemistry of Materials* **2009**, *21*, 4505–4514, doi:10.1021/cm9012602.

139. Shenderova, O.; Panich, A. M.; Moseenkov, S.; Hens, S. C.; Kuznetsov, V.; Vieth, H. M. Hydroxylated detonation nanodiamond: FTIR, XPS, and NMR studies. *Journal of Physical Chemistry C* **2011**, *115*, 19005–19011, doi:10.1021/jp205389m.

140. Krueger, A. The structure and reactivity of nanoscale diamond. *Journal of Materials Chemistry* **2008**, *18*, 1485, doi:10.1039/b716673g.

141. Liu, Y.; Gu, Z.; Margrave, J. L.; Khabashesku, V. N. Functionalization of nanoscale diamond powder: Fluoro-, alkyl-, amino-, and amino acid-nanodiamond derivatives. *Chemistry of Materials* **2004**, *16*, 3924–3930, doi:10.1021/cm048875q.

142. Ray, M. A.; Shenderova, O.; Hook, W.; Martin, A.; Grishko, V.; Tyler, T.; Cunningham, G. B.; McGuire, G. Cold plasma functionalization of nanodiamond particles. *Diamond and Related Materials* **2006**, *15*, 1809–1812, doi:10.1016/j.diamond.2006.06.003.

143. Spitsyn, B. V.; Denisov, S. A.; Skorik, N. A.; Chopurova, A. G.; Parkaeva, S. A.; Belyakova, L. D.; Larionov, O. G. The physical-chemical study of detonation nanodiamond application in adsorption and chromatography. *Diamond and Related Materials* **2010**, *19*, 123–127, doi:10.1016/j.diamond.2009.10.020.

144. Mochalin, V. N.; Neitzel, I.; Etzold, B. J. M.; Peterson, A.; Palmese, G.; Gogotsi, Y. Covalent incorporation of aminated nanodiamond into an epoxy polymer network. *ACS Nano* **2011**, *5*, 7494–7502, doi:10.1021/nn2024539.

145. Chang, B. M.; Lin, H. H.; Su, L. J.; Lin, W. Der; Lin, R. J.; Tzeng, Y. K.; Lee, R. T.; Lee, Y. C.; Yu, A. L.; Chang, H. C. Highly fluorescent nanodiamonds protein-functionalized for cell labeling and targeting. *Advanced Functional Materials* **2013**, *23*, 5737–5745, doi:10.1002/adfm.201301075.

146. Wang, D.; Li, Y.; Tian, Z.; Cao, R.; Yang, B. Transferrin-conjugated nanodiamond as an intracellular transporter of chemotherapeutic drug and targeting therapy for cancer cells. *Therapeutic delivery* **2014**, *5*, 511–524, doi:10.4155/tde.14.17.

147. Huang, L. C. L.; Chang, H. C. Adsorption and immobilization of cytochrome c on nanodiamonds. *Langmuir* **2004**, *20*, 5879–5884, doi:10.1021/la0495736.

148. Shimkunas, R. A.; Robinson, E.; Lam, R.; Lu, S.; Xu, X.; Zhang, X. Q.; Huang, H.; Osawa, E.; Ho, D. Nanodiamond-insulin complexes as pH-dependent protein delivery vehicles. *Biomaterials* **2009**, *30*, 5720–5728, doi:10.1016/j.biomaterials.2009.07.004.

149. Perevedentseva, E.; Cai, P.-J.; Chiu, Y.-C.; Cheng, C.-L. Characterizing Protein Activities on the Lysozyme and Nanodiamond Complex Prepared for Bio Applications. *Langmuir* **2011**, *27*, 1085–1091, doi:10.1021/la103155c.

150. Chen, M.; Pierstorff, E. D.; Lam, R.; Li, S. Y.; Huang, H.; Osawa, E.; Ho, D. Nanodiamond-mediated delivery of water-insoluble therapeutics. *ACS Nano* **2009**, *3*, 2016–2022, doi:10.1021/nn900480m.

151. Chen, M.; Zhang, X.-Q.; Man, H. B.; Lam, R.; Chow, E. K.; Ho, D. Nanodiamond Vectors Functionalized with Polyethylenimine for siRNA Delivery. *The Journal of Physical Chemistry Letters* **2010**, *1*, 3167–3171, doi:10.1021/jz1013278.

152. Alhaddad, A.; Adam, M.-P.; Botsoa, J.; Dantelle, G.; Perruchas, S.; Gacoin, T.; Mansuy, C.; Lavielle, S.; Malvy, C.; Treussart, F.; Bertrand, J.-R. Nanodiamond as a vector for siRNA delivery to Ewing sarcoma cells. *Small* **2011**, *7*, 3087–95, doi:10.1002/smll.201101193.

153. Keremidarska, M.; Ganeva, A.; Mitev, D.; Hikov, T.; Presker, R.; Pramatarova, L.; Krasteva, N. Comparative study of cytotoxicity of detonation nanodiamond particles with an osteosarcoma cell line and primary mesenchymal stem cells. *Biotechnology and Biotechnological Equipment* **2014**, *28*, 733–739, doi:10.1080/13102818.2014.947704.

154. Paget, V.; Sergent, J. A.; Grall, R.; Altmeyer-Morel, S.; Girard, H. A.; Petit, T.; Gesset, C.; Mermoux, M.; Bergonzo, P.; Arnault, J. C.; Chevillard, S. Carboxylated nanodiamonds are neither cytotoxic nor genotoxic on liver, kidney, intestine and lung human cell lines. *Nanotoxicology* **2014**, *8*, 46–56, doi:10.3109/17435390.2013.855828.

155. Mohan, N.; Chen, C.-S. S.; Hsieh, H.-H. H.; Wu, Y.-C. C.; Chang, H.-C. C. In vivo imaging and toxicity assessments of fluorescent nanodiamonds in caenorhabditis elegans. *Nano Letters* **2010**, *10*, 3692–3699, doi:10.1021/nl1021909.

156. Kurzyp, M.; Girard, H. A.; Cheref, Y.; Brun, E.; Sicard-Roselli, C.; Saada, S.; Arnault, J.-C. Hydroxyl radical production induced by plasma hydrogenated nanodiamonds under X-ray irradiation. *Chem. Commun.* **2017**, *53*, 1237–1240, doi:10.1039/C6CC08895C.

157. Brož, A.; Bačáková, L.; Štenclová, P.; Kromka, A.; Potocký, Š. Uptake and intracellular accumulation of diamond nanoparticles – a metabolic and cytotoxic study. *Beilstein Journal of Nanotechnology* **2017**, *8*, 1649–1657, doi:10.3762/bjnano.8.165.

158. Yuan, Y.; Chen, Y.; Liu, J. H.; Wang, H.; Liu, Y. Biodistribution and fate of nanodiamonds in vivo. *Diamond and Related Materials* **2009**, *18*, 95–100, doi:10.1016/j.diamond.2008.10.031.

159. Zhang, X.; Yin, J.; Kang, C.; Li, J.; Zhu, Y.; Li, W.; Huang, Q.; Zhu, Z. Biodistribution and toxicity of nanodiamonds in mice after intratracheal instillation. *Toxicology Letters* **2010**, *198*, 237–243, doi:10.1016/j.toxlet.2010.07.001.

160. Rojas, S.; Gispert, J. D.; Martin, R.; Abad, S.; Menchon, C.; Pareto, D.; Victor, V. M.; Alvaro, M.; Garcia, H.; Herance, J. R. Biodistribution of amino-functionalized diamond nanoparticles. in vivo studies based on 18F radionuclide emission. *ACS Nano* **2011**, *5*, 5552–5559, doi:10.1021/nn200986z.

161. Qi, W.; Li, Z.; Bi, J.; Wang, J.; Wang, J.; Sun, T.; Guo, Y.; Wu, W. Biodistribution of co-exposure to multi-walled carbon nanotubes and nanodiamonds in mice. *Nanoscale Research Letters* **2012**, *7*, 473, doi:10.1186/1556-276X-7-473.

162. Huang, H.; Pierstorff, E.; Osawa, E.; Ho, D. Active nanodiamond hydrogels for chemotherapeutic delivery. *Nano Letters* **2007**, *7*, 3305–3314, doi:10.1021/nl071521o.

163. Zhang, X. Q.; Chen, M.; Lam, R.; Xu, X.; Osawa, E.; Ho, D. Polymer-functionalized nanodiamond platforms as vehicles for gene delivery. *ACS Nano* **2009**, *3*, 2609–2616, doi:10.1021/nn900865g.

164. Alhaddad, A.; Durieu, C.; Dantelle, G.; Le Cam, E.; Malvy, C.; Treussart, F.; Bertrand, J.-R. Influence of the internalization pathway on the efficacy of siRNA delivery by cationic fluorescent nanodiamonds in the Ewing sarcoma cell model. *PloS one* **2012**, *7*, e52207, doi:10.1371/journal.pone.0052207.

165. Zhang, X. Q.; Lam, R.; Xu, X.; Chow, E. K.; Kim, H. J.; Ho, D. Multimodal nanodiamond drug delivery carriers for selective targeting, imaging, and enhanced chemotherapeutic efficacy. *Advanced Materials* **2011**, *23*, 4770–4775, doi:10.1002/adma.201102263.

166. Liu, K.-K.; Zheng, W.-W.; Wang, C.-C.; Chiu, Y.-C.; Cheng, C.-L.; Lo, Y.-S.; Chen, C.; Chao, J.-I. Covalent linkage of nanodiamond-paclitaxel for drug delivery and cancer therapy. *Nanotechnology* **2010**, *21*, 315106, doi:10.1088/0957-4484/21/31/315106.

167. Grall, R.; Girard, H.; Saad, L.; Petit, T.; Gesset, C.; Combis-Schlumberger, M.; Paget, V.; Delic, J.; Arnault, J.-C.; Chevillard, S. Impairing the radioresistance of cancer cells by hydrogenated nanodiamonds. *Biomaterials* **2015**, *61*, 290–8, doi:10.1016/j.biomaterials.2015.05.034.

168. Rehor, I.; Lee, K. L.; Chen, K.; Hajek, M.; Havlik, J.; Lokajova, J.; Masat, M.; Slegerova, J.; Shukla, S.; Heidari, H.; Bals, S.; Steinmetz, N. F.; Cigler, P. Plasmonic Nanodiamonds: Targeted Core-Shell Type Nanoparticles for Cancer Cell Thermoablation. *Advanced Healthcare Materials* **2015**, *4*, 460–468, doi:10.1002/adhm.201400421.

169. Fu, C.-C.; Lee, H.-Y.; Chen, K.; Lim, T.-S.; Wu, H.-Y.; Lin, P.-K.; Wei, P.-K.; Tsao, P.-H.; Chang, H.-C.; Fann, W. Characterization and application of single fluorescent nanodiamonds as cellular biomarkers. *Proceedings of the National Academy of Sciences* **2007**, *104*, 727–732, doi:10.1073/pnas.0605409104.

170. Zvyagin, A. V.; Manson, N. B. Optical and Spin Properties of Nitrogen-Vacancy Color Centers in Diamond Crystals, Nanodiamonds, and Proximity to Surfaces. In *Ultrananocrystalline Diamond: Synthesis, Properties and Applications: Second Edition*; Elsevier, 2012; pp. 327–354 ISBN 9781437734652.

171. Doherty, M. W.; Manson, N. B.; Delaney, P.; Jelezko, F.; Wrachtrup, J.; Hollenberg, L. C. L. The nitrogen-vacancy colour centre in diamond. *Physics Reports* 2013, *528*, 1–45.

172. Toyli, D. M.; Christle, D. J.; Alkauskas, A.; Buckley, B. B.; Van de Walle, C. G.; Awschalom, D. D. Measurement and control of single nitrogen-vacancy center spins above 600 K. *Physical Review X* **2012**, *2*, 031001, doi:10.1103/PhysRevX.2.031001.

173. Turcheniuk, K.; Mochalin, V. Biomedical Applications of Nanodiamond (Review). *Nanotechnology* **2017**, *28*, doi:10.1088/1361-6528/aa6ae4.

174. Glenn, D. R.; Zhang, H.; Kasthuri, N.; Schalek, R.; Lo, P. K.; Trifonov, A. S.; Park, H.; Lichtman, J. W.; Walsworth, R. L. Correlative light and electron microscopy using cathodoluminescence from nanoparticles with distinguishable colours. *Scientific Reports* **2012**, *2*, 865, doi:10.1038/srep00865.

175. Nawa, Y.; Inami, W.; Lin, S.; Kawata, Y.; Terakawa, S.; Fang, C.-Y.; Chang, H.-C. Multi-Color Imaging of Fluorescent Nanodiamonds in Living HeLa Cells Using Direct Electron-Beam Excitation. *ChemPhysChem* **2014**, *15*, 721–726, doi:10.1002/cphc.201300802.

176. Lien, Z.-Y.; Hsu, T.-C.; Liu, K.-K.; Liao, W.-S.; Hwang, K.-C.; Chao, J.-I. Cancer cell labeling and tracking using fluorescent and magnetic nanodiamond. *Biomaterials* **2012**, *33*, 6172–6185, doi:10.1016/j.biomaterials.2012.05.009.

177. Polyak, K.; Hahn, W. C. Roots and stems: stem cells in cancer. *Nature Medicine* **2006**, *12*, 296–300, doi:10.1038/nm1379.

178. Lin, H. H.; Lee, H. W.; Lin, R. J.; Huang, C. W.; Liao, Y. C.; Chen, Y. T.; Fang, J. M.; Lee, T. C.; Yu, A. L.; Chang, H. C. Tracking and Finding Slow-Proliferating/Quiescent Cancer Stem Cells with Fluorescent Nanodiamonds. *Small* **2015**, *11*, 4394–4402, doi:10.1002/smll.201500878.

179. Haziza, S.; Mohan, N.; Loe-Mie, Y.; Lepagnol-Bestel, A.-M.; Massou, S.; Adam, M.-P.; Le, X. L.; Viard, J.; Plancon, C.; Daudin, R.; Koebel, P.; Dorard, E.; Rose, C.; Hsieh, F.-J.; Wu, C.-C.; Potier, B.; Herault, Y.; Sala, C.; Corvin, A.; Allinquant, B.; Chang, H.-C.; Treussart, F.; Simonneau, M. Fluorescent nanodiamond tracking reveals intraneuronal transport abnormalities induced by brain-disease-related genetic risk factors. *Nature Nanotechnology* **2016**, *12*, 322–328, doi:10.1038/nnano.2016.260.

180. Organization, W. H. WHO, Cancer. *WHO* 2017.

181. Hanahan, D.; Weinberg, R. The Hallmarks of Cancer (Review). *Cell* **2000**, *100*, 57–70, doi:10.1016/S0092-8674(00)81683-9.

182. Fouad, Y. A.; Aanei, C. Revisiting the hallmarks of cancer. *American Journal of Cancer Research* 2017, *7*, 1016–1036.

183. Hanahan, D.; Weinberg, R. A. Hallmarks of cancer: The next generation. *Cell* 2011, *144*, 646–674.

184. Kurt, Straif Aaron, Cohen Jonathan, S. *Air pollution and cancer.*; International Agency for Research on Cancer, 2010; ISBN 978-92-832-2166-1.

185. Soto, A. M.; Sonnenschein, C. Environmental causes of cancer: Endocrine disruptors as carcinogens. *Nature Reviews Endocrinology* 2010, *6*, 363–370.

186. World Health Organization WHO | Genes and human disease Available online: http://www.who.int/genomics/public/geneticdiseases/en/index3.html (accessed on Jan 3, 2018).

187. Bernstein, M.; Kovar, H.; Paulussen, M.; Randall, R. L.; Schuck, A.; Teot, L. A.; Juergens, H. Ewing's sarcoma family of tumors: current management. *The oncologist* **2006**, *11*, 503–19, doi:10.1634/theoncologist.11-5-503.

188. Balamuth, N. J.; Womer, R. B. Ewing's sarcoma. *The lancet oncology* **2010**, *11*, 184–92, doi:10.1016/S1470-2045(09)70286-4.

189. Lahl, M.; Fisher, V. L.; Laschinger, K. Ewing's sarcoma family of tumors: an overview from diagnosis to survivorship. *Clinical journal of oncology nursing* **2008**, *12*, 89–97, doi:10.1188/08.CJON.89-97.

190. Iwamoto, Y. Diagnosis and treatment of Ewing's sarcoma. *Japanese journal of clinical oncology* **2007**, *37*, 79–89, doi:10.1093/jjco/hyl142.

191. Yu, H.; Ge, Y.; Guo, L.; Huang, L.; Yu, H.; Ge, Y.; Guo, L.; Huang, L. Potential approaches to the treatment of Ewing's sarcoma. *Oncotarget* **2015**, *5*, 5523–5539, doi:10.18632/oncotarget.12566.

192. Skarbek, C.; Lesueur, L. L.; Chapuis, H.; Deroussent, A.; Piochedurieu, C.; Daville, A.; Caron, J.; Rivard, M.; Martens, T.; Bertrand, J. R.; Le Cam, E.; Vassal, G.; Couvreur, P.; Desmaele, D.; Paci, A. Preactivated oxazaphosphorines designed for isophosphoramide mustard delivery as bulk form or nanoassemblies: Synthesis and proof of concept. *Journal of Medicinal Chemistry* **2015**, *58*, 705–717, doi:10.1021/jm501224x.

193. Hanly, L.; Chen, N.; Rieder, M.; Koren, G. Ifosfamide nephrotoxicity in children: a mechanistic base for pharmacological prevention. *Expert opinion on drug safety* **2009**, *8*, 155–68, doi:10.1517/14740330902808169.

194. Lowenberg, D.; Thorn, C. F.; Desta, Z.; Flockhart, D. A.; Altman, R. B.; Klein, T. E. PharmGKB summary: ifosfamide pathways, pharmacokinetics and pharmacodynamics. *Pharmacogenetics and genomics* **2014**, *24*, 133–8, doi:10.1097/FPC.0000000000000019.

195. Aman, P. Fusion oncogenes in tumor development. *Seminars in cancer biology* **2005**, *15*, 236–43, doi:10.1016/j.semcancer.2005.01.009.

196. Linn, D. E.; Penney, K. L.; Bronson, R. T.; Mucci, L. A.; Li, Z. Deletion of interstitial genes between TMPRSS2 and ERG promotes prostate cancer progression. *Cancer Research* **2016**, *76*, 1869–1881, doi:10.1158/0008-5472.CAN-15-1911.

197. Yong, W. P.; Soo, R.; Innocenti, F. Pharmacogenomics and Personalized Medicines in Cancer Treatment. In *Cancer Drug Design and Discovery: Second Edition*; Elsevier, 2013; pp. 55–90 ISBN 9780123965219.

198. Mateo-Lozano, S.; Gokhale, P. C.; Soldatenkov, V. A.; Dritschilo, A.; Tirado, O. M.; Notario, V. Combined transcriptional and translational targeting of EWS/FLI-1 in Ewing's sarcoma. *Clinical cancer research : an official journal of the American Association for Cancer Research* **2006**, *12*, 6781–90, doi:10.1158/1078-0432.CCR-06-0609.

199. Owen, L. A.; Kowalewski, A. A.; Lessnick, S. L. EWS/FLI mediates transcriptional repression via NKX2.2 during oncogenic transformation in Ewing's sarcoma. *PloS one* **2008**, *3*, e1965, doi:10.1371/journal.pone.0001965.

200. Matsumoto, Y.; Tanaka, K.; Nakatani, F.; Matsunobu, T.; Matsuda, S.; Iwamoto, Y. Downregulation and forced expression of EWS-Fli1 fusion gene results in changes in the expression of G(1)regulatory genes. *British journal of cancer* **2001**, *84*, 768–75, doi:10.1054/bjoc.2000.1652.

201. Kovar, H. Downstream EWS/FLI1 - upstream Ewing's sarcoma. *Genome medicine* **2010**, *2*, 8, doi:10.1186/gm129.

202. Janknecht, R. EWS-ETS oncoproteins: the linchpins of Ewing tumors. *Gene* **2005**, *363*, 1–14, doi:10.1016/j.gene.2005.08.007.

203. Lin, P. P.; Brody, R. I.; Hamelin, A. C.; Bradner, J. E.; Healey, J. H.; Ladanyi, M. Differential transactivation by alternative EWS-FLI1 fusion proteins correlates with clinical heterogeneity in Ewing's sarcoma. *Cancer research* **1999**, *59*, 1428–32.

204. Desai, S. S.; Jambhekar, N. A. Pathology of Ewing's sarcoma/PNET: Current opinion and emerging concepts. *Indian journal of orthopaedics* **2010**, *44*, 363–8, doi:10.4103/0019-5413.69304.

205. Huang, H. J.; Angelo, L. S.; Rodon, J.; Sun, M.; Kuenkele, K.-P.; Parsons, H. A.; Trent, J. C.; Kurzrock, R. R1507, an anti-insulin-like growth factor-1 receptor (IGF-1R)

antibody, and EWS/FLI-1 siRNA in Ewing's sarcoma: convergence at the IGF/IGFR/Akt axis. *PloS one* **2011**, *6*, e26060, doi:10.1371/journal.pone.0026060.

206. Delattre, O.; Zucman, J.; Plougastel, B.; Desmaze, C.; Melot, T.; Peter, M.; Kovar, H.; Joubert, I.; de Jong, P.; Rouleau, G.; Aurias, A.; Thomas, G. Gene fusion with ETS DNA-binding domain caused by chromosome translocation in human tumours. *Nature* **1992**, *359*, 162–165.

207. de Martimprey, H.; Vauthier, C.; Malvy, C.; Couvreur, P. Polymer nanocarriers for the delivery of small fragments of nucleic acids: oligonucleotides and siRNA. *European journal of pharmaceutics and biopharmaceutics : official journal of Arbeitsgemeinschaft für Pharmazeutische Verfahrenstechnik e.V* **2009**, *71*, 490–504, doi:10.1016/j.ejpb.2008.09.024.

208. Napoli, C. Introduction of a Chimeric Chalcone Synthase Gene into Petunia Results in Reversible Co-Suppression of Homologous Genes in trans. *THE PLANT CELL* **1990**, *2*, 279–289, doi:10.1105/tpc.2.4.279.

209. Fire, A.; Xu, S.; Montgomery, M. K.; Kostas, S. A.; Driver, S. E.; Mello, C. C. Potent and specific genetic interference by double-stranded RNA in Caenorhabditis elegans. *Nature* **1998**, *391*, 806–11, doi:10.1038/35888.

210. Reischl, D.; Zimmer, A. Drug delivery of siRNA therapeutics: potentials and limits of nanosystems. *Nanomedicine: Nanotechnology, Biology and Medicine* **2009**, *5*, 8–20.

211. Bertrand, J.-R.; Pottier, M.; Vekris, A.; Opolon, P.; Maksimenko, A.; Malvy, C. Comparison of antisense oligonucleotides and siRNAs in cell culture and in vivo. *Biochemical and biophysical research communications* **2002**, *296*, 1000–4.

212. Yao, Y.; Wang, C.; Varshney, R. R.; Wang, D.-A. Antisense makes sense in engineered regenerative medicine. *Pharmaceutical research* **2009**, *26*, 263–75, doi:10.1007/s11095-008-9772-3.

213. Novina, C. D.; Sharp, P. A. The RNAi revolution. *Nature* **2004**, *430*, 161–4, doi:10.1038/430161a.

214. Carthew, R. W.; Sontheimer, E. J. Origins and Mechanisms of miRNAs and siRNAs. *Cell* **2009**, *136*, 642–55, doi:10.1016/j.cell.2009.01.035.

215. Mello, C. C.; Conte, D. Revealing the world of RNA interference. *Nature* **2004**, *431*, 338–42, doi:10.1038/nature02872.

216. Eulalio, A.; Huntzinger, E.; Izaurralde, E. Getting to the root of miRNA-mediated gene silencing. *Cell* **2008**, *132*, 9–14, doi:10.1016/j.cell.2007.12.024.

217. BARTEL, D. MicroRNAsGenomics, Biogenesis, Mechanism, and Function. *Cell* **2004**, *116*, 281–297, doi:10.1016/S0092-8674(04)00045-5.

218. Paddison, P. J.; Caudy, A. A.; Bernstein, E.; Hannon, G. J.; Conklin, D. S. Short hairpin RNAs (shRNAs) induce sequence-specific silencing in mammalian cells. *Genes & development* **2002**, *16*, 948–58, doi:10.1101/gad.981002.

219. Grimm, D. Small silencing RNAs: state-of-the-art. *Advanced drug delivery reviews* **2009**, *61*, 672–703, doi:10.1016/j.addr.2009.05.002.

220. Rao, D. D.; Vorhies, J. S.; Senzer, N.; Nemunaitis, J. siRNA vs. shRNA: similarities and differences. *Advanced drug delivery reviews* **2009**, *61*, 746–59, doi:10.1016/j.addr.2009.04.004.

221. Malone, C. D.; Hannon, G. J. Small RNAs as guardians of the genome. *Cell* **2009**, *136*, 656–68, doi:10.1016/j.cell.2009.01.045.

222. Carthew, R. W.; Sontheimer, E. J. Origins and Mechanisms of miRNAs and siRNAs. *Cell* **2009**, *136*, 642–55, doi:10.1016/j.cell.2009.01.035.

223. Elbashir, S. M.; Harborth, J.; Lendeckel, W.; Yalcin, A.; Weber, K.; Tuschl, T. Duplexes of 21-nucleotide RNAs mediate RNA interference in cultured mammalian cells. *Nature* **2001**, *411*, 494–8, doi:10.1038/35078107.

224. Fire, A. RNA-triggered gene silencing. *Trends in Genetics* **1999**, *15*, 358–363, doi:10.1016/S0168-9525(99)01818-1.

225. Sharp, P. A. RNAi and double-strand RNA. *Genes and Development* 1999, *13*, 139–141.

226. Hunter, C. P. Genetics: A touch of elegance with RNAi. *Current Biology* **1999**, *9*, R440-2, doi:10.1016/S0960-9822(99)80276-0.

227. Watts, J. K.; Corey, D. R. Silencing disease genes in the laboratory and the clinic. *The Journal of pathology* **2012**, *226*, 365–79, doi:10.1002/path.2993.

228. Stege, A.; Kruhn, A.; Lage, H. Overcoming multidrug resistance by RNA interference. *Methods in molecular biology (Clifton, N.J.)* **2010**, *596*, 447–465, doi:10.1007/978-1-60761-416-6_20.

229. Hickerson, R. P.; Vlassov, A. V; Wang, Q.; Leake, D.; Ilves, H.; Gonzalez-Gonzalez, E.; Contag, C. H.; Johnston, B. H.; Kaspar, R. L. Stability study of unmodified siRNA and relevance to clinical use. *Oligonucleotides* **2008**, *18*, 345–54, doi:10.1089/oli.2008.0149.

230. Wittrup, A.; Lieberman, J. Knocking down disease: A progress report on siRNA therapeutics. *Nature Reviews Genetics* 2015, *16*, 543–552.

231. Jackson, A. L. Widespread siRNA "off-target" transcript silencing mediated by seed region sequence complementarity. *RNA* **2006**, *12*, 1179–1187, doi:10.1261/rna.25706.

232. Resnier, P.; Montier, T.; Mathieu, V.; Benoit, J.-P.; Passirani, C. A review of the current status of siRNA nanomedicines in the treatment of cancer. *Biomaterials* **2013**, *34*, 6429–6443.

233. Behlke, M. A. Progress towards in vivo use of siRNAs. *Molecular therapy : the journal of the American Society of Gene Therapy* **2006**, *13*, 644–70, doi:10.1016/j.ymthe.2006.01.001.

234. Elhamess, H.; Bertrand, J.-R.; Maccario, J.; Maksimenko, A.; Malvy, C. Antitumor vectorized oligonucleotides in a model of ewing sarcoma: unexpected role of nanoparticles. *Oligonucleotides* **2009**, *19*, 255–64, doi:10.1089/oli.2009.0197.

235. Aagaard, L.; Rossi, J. J. RNAi therapeutics: principles, prospects and challenges. *Advanced drug delivery reviews* **2007**, *59*, 75–86, doi:10.1016/j.addr.2007.03.005.

236. Toub, N.; Bertrand, J.-R.; Malvy, C.; Fattal, E.; Couvreur, P. Antisense Oligonucleotide Nanocapsules Efficiently Inhibit EWS-Fli1 Expression in a Ewing Sarcoma Model. *Oligonucleotides* **2006**, *16*, 158–168, doi:10.1089/oli.2006.16.158.

237. Lambert, G.; Bertrand, J. R.; Fattal, E.; Subra, F.; Pinto-Alphandary, H.; Malvy, C.; Auclair, C.; Couvreur, P. EWS Fli-1 antisense nanocapsules inhibits Ewing sarcoma-related tumor in mice. *Biochemical and Biophysical Research Communications* **2000**, *279*, 401–406, doi:10.1006/bbrc.2000.3963.

238. Toub, N.; Bertrand, J. R.; Tamaddon, A.; Elhamess, H.; Hillaireau, H.; Maksimenko, A.; Maccario, J.; Malvy, C.; Fattal, E.; Couvreur, P. Efficacy of siRNA nanocapsules targeted against the EWS-Fli1 oncogene in Ewing sarcoma. *Pharmaceutical Research* **2006**, *23*, 892–900, doi:10.1007/s11095-006-9901-9.

239. Pillé, J.-Y.; Li, H.; Blot, E.; Bertrand, J.-R.; Pritchard, L.-L.; Opolon, P.; Maksimenko, A.; Lu, H.; Vannier, J.-P.; Soria, J.; Malvy, C.; Soria, C. Intravenous Delivery of Anti-RhoA Small Interfering RNA Loaded in Nanoparticles of Chitosan in Mice: Safety and Efficacy in Xenografted Aggressive Breast Cancer. *HUMAN GENE THERAPY* **2006**, *17*, 1019–1026, doi:10.1089/hum.2006.17.ft-248.

240. De Martimprey, H.; Bertrand, J. R.; Malvy, C.; Couvreur, P.; Vauthier, C. New core-shell nanoparticules for the intravenous delivery of sirna to experimental thyroid papillary carcinoma. *Pharmaceutical Research* **2010**, *27*, 498–509, doi:10.1007/s11095-009-0043-8.

241. Urbinati, G.; de Waziers, I.; Slamiç, M.; Foussignière, T.; Ali, H. M.; Desmaële, D.; Couvreur, P.; Massaad-Massade, L. Knocking Down TMPRSS2-ERG Fusion Oncogene by siRNA Could be an Alternative Treatment to Flutamide. *Molecular Therapy - Nucleic Acids* **2016**, *5*, e301, doi:10.1038/mtna.2016.16.

242. Huh, M. S.; Lee, S. Y.; Park, S.; Lee, S.; Chung, H.; Lee, S.; Choi, Y.; Oh, Y. K.; Park, J. H.; Jeong, S. Y.; Choi, K.; Kim, K.; Kwon, I. C. Tumor-homing glycol chitosan/polyethylenimine nanoparticles for the systemic delivery of siRNA in tumor-bearing mice. *Journal of Controlled Release* **2010**, *144*, 134–143, doi:10.1016/j.jconrel.2010.02.023.

243. Miele, E.; Spinelli, G. P.; Miele, E.; Di Fabrizio, E.; Ferretti, E.; Tomao, S.; Gulino, A. Nanoparticle-based delivery of small interfering RNA: challenges for cancer therapy. *International journal of nanomedicine* **2012**, *7*, 3637–57, doi:10.2147/IJN.S23696.

244. Akhtar, S.; Benter, I. F. Nonviral delivery of synthetic siRNAs in vivo. *The Journal of clinical investigation* **2007**, *117*, 3623–32, doi:10.1172/JCI33494.

245. Hammond, P. T. Polyelectrolyte multilayered nanoparticles: using nanolayers for controlled and targeted systemic release. *Nanomedicine (London, England)* **2012**, *7*, 619–22, doi:10.2217/nnm.12.47.

246. Young, L. S.; Searle, P. F.; Onion, D.; Mautner, V. Viral gene therapy strategies: from basic science to clinical application. *The Journal of pathology* **2006**, *208*, 299–318, doi:10.1002/path.1896.

247. Nayak, S.; Herzog, R. W. Progress and prospects: Immune responses to viral vectors. *Gene Therapy* 2010, *17*, 295–304.

248. Gao, Y.; Liu, X.-L.; Li, X.-R. Research progress on siRNA delivery with nonviral carriers. *International journal of nanomedicine* **2011**, *6*, 1017–25, doi:10.2147/IJN.S17040.

249. Bertrand, J.-R.; Pioche-Durieu, C.; Ayala, J.; Petit, T.; Girard, H. A.; Malvy, C. P.; Le Cam, E.; Treussart, F.; Arnault, J.-C. Plasma hydrogenated cationic detonation nanodiamonds efficiently deliver to human cells in culture functional siRNA targeting the Ewing sarcoma junction oncogene. *Biomaterials* **2015**, *45*, 93–8, doi:10.1016/j.biomaterials.2014.12.007.

250. Korolkov, V. V.; Kulakova, I. I.; Tarasevich, B. N.; Lisichkin, G. V. Dual reaction capacity of hydrogenated nanodiamond. *Diamond and Related Materials* **2007**, *16*, 2129–2132, doi:10.1016/j.diamond.2007.07.018.

251. Girard, H. A.; El-Kharbachi, A.; Garcia-Argote, S.; Petit, T.; Bergonzo, P.; Rousseau, B.; Arnault, J.-C. Tritium labeling of detonation nanodiamonds. *Chemical Communications* **2014**, *50*, 2916–2918, doi:10.1039/C3CC49653H.

252. Gibson, N.; Shenderova, O.; Luo, T. J. M.; Moseenkov, S.; Bondar, V.; Puzyr, A.; Purtov, K.; Fitzgerald, Z.; Brenner, D. W. Colloidal stability of modified nanodiamond particles. *Diamond and Related Materials* **2009**, *18*, 620–626, doi:10.1016/j.diamond.2008.10.049.

253. Canton, I.; Battaglia, G. Endocytosis at the nanoscale. *Chemical Society Reviews* **2012**, *41*, 2718, doi:10.1039/c2cs15309b.

254. Gines, L.; Mandal, S.; Ahmed, A.-I.; Cheng, C.-L.; Sow, M.; Williams, O. Positive Zeta Potential of Nanodiamonds. *Nanoscale* **2017**, *9*, 12549–12555, doi:10.1039/C7NR03200E.

255. Liang, W.; Lam, J. K. W. Endosomal Escape Pathways for Non-Viral Nucleic Acid Delivery Systems. *Molecular Regulation of Endocytosis* **2012**, 429–456, doi:10.5772/46006.

256. Erbacher, P.; Roche, A. C.; Monsigny, M.; Midoux, P. Putative Role of Chloroquine in Gene Transfer into a Human Hepatoma Cell Line by DNA/Lactosylated Polylysine Complexes. *EXPERIMENTAL CELL RESEARCH* **1996**, *225*, 186–194, doi:10.1006/excr.1996.0169.

257. Rendler, T.; Neburkova, J.; Zemek, O.; Kotek, J.; Zappe, A.; Chu, Z.; Cigler, P.; Wrachtrup, J. Optical imaging of localized chemical events using programmable diamond quantum nanosensors. *Nature Communications* **2017**, *8*, 14701, doi:10.1038/ncomms14701.

258. Slegerova, J.; Hajek, M.; Rehor, I.; Sedlak, F.; Stursa, J.; Hruby, M.; Cigler, P. Designing the nanobiointerface of fluorescent nanodiamonds: highly selective targeting of glioma cancer cells. *Nanoscale* **2015**, *7*, 415–420, doi:10.1039/C4NR02776K.

259. Maksimenko, A.; Polard, V.; Villemeur, M.; Elhamess, H.; Couvreur, P.; Bertrand, J. R.; Aboubakar, M.; Gottikh, M.; Malvy, C. In vivo potentialities of EWS-Fli-1 targeted antisense oligonucleotides-nanospheres complexes. *Annals of the New York Academy of Sciences* **2005**, *1058*, 52–61, doi:10.1196/annals.1359.010.

260. Ramon, A. L.; Bertrand, J. R.; de Martimprey, H.; Bernard, G.; Ponchel, G.; Malvy, C.; Vauthier, C. siRNA associated with immunonanoparticles directed against cd99 antigen improves gene expression inhibition in vivo in Ewing's sarcoma. *Journal of molecular recognition : JMR* **2013**, *26*, 318–29, doi:10.1002/jmr.2276.

261. Délen, X.; Balembois, F.; Georges, P. Direct amplification of a nanosecond laser diode in a high gain diode-pumped Nd:YVO4 amplifier. *Optics letters* **2014**, *39*, 997–1000, doi:10.1364/OL.39.000997.

262. Krzywinski, M.; Altman, N. Visualizing samples with box plots. *Nature Methods* **2014**, *11*, 119–120, doi:10.1038/nmeth.2813.

263. Frevert, U.; Engelmann, S.; Zougbédé, S.; Stange, J.; Ng, B.; Matuschewski, K.; Liebes, L.; Yee, H. Intravital observation of plasmodium berghei sporozoite infection of the liver. *PLoS Biology* **2005**, *3*, 1034–1046, doi:10.1371/journal.pbio.0030192.

264. Lopez, B. G.; Tsai, M. S.; Baratta, J. L.; Longmuir, K. J.; Robertson, R. T. Characterization of Kupffer cells in livers of developing mice. *Comparative Hepatology* **2011**, *10*, 2, doi:10.1186/1476-5926-10-2.

265. Yakovlev, R. Y.; Solomatin, A. S.; Leonidov, N. B.; Kulakova, I. I.; Lisichkin, G. V. Detonation diamond—A perspective carrier for drug delivery systems. *Russian Journal of General Chemistry* **2014**, *84*, 379–390, doi:10.1134/S1070363214020406.

266. Ambros, I. M.; Ambros, P. F.; Strehl, S.; Kovar, H.; Gadner, H.; Salzer-Kuntschik, M. MIC2 is a specific marker for Ewing's sarcoma and peripheral prinitive neuroectodermal tumors. *Cancer* **1991**, *67*, 1886–1893.

Résumé de la thèse en français

Nanodiamants fluorescents pour la vectorisation de siRNA : évaluation *in vitro* et quantification haut-débit/haute-résolution *in vivo*

Sandra Claveau

Laboratoire Vectorologie et Thérapeutiques Anticancéreuses, UMR8203, CNRS, Univ. Paris-Sud, Institut Gustave Roussy, Université Paris-Saclay, 94805 Villejuif cedex

Laboratoire Aimé Cotton, UMR9188, CNRS, Univ. Paris-Sud, ENS Paris-Saclay, Université Paris-Saclay, 91405 Orsay cedex

Le nanodiamant (ND) est largement utilisé pour diverses applications, notamment biomédicales, tirant avantage de sa faible cytotoxicité et d'une bonne biocompatibilité. De plus, les modifications de surface des diamants ont fait l'objet de nombreux travaux qui sont en train de déboucher sur la fixation maîtrisée de biomolécules. Lors de cette thèse, des nanodiamants cationiques ont été utilisés pour vectoriser des siRNAs dans le cadre du développement d'une thérapie génique ciblant le Sarcome d'Ewing. Notre étude a été menée sur des cultures de cellules tumorales, ainsi que sur un modèle murin pré-clinique.

Les petits ARN interférents (ou siRNA pour *small interfering RNA*) sont des outils d'inhibition de l'expression de gènes qui représentent un grand espoir pour le traitement de certaines maladies mais qui sont rapidement dégradés dans l'organisme par les nucléases. Ces molécules ont donc besoin d'un vecteur pour les protéger des dégradations et les amener jusqu'au cytoplasme des cellules cibles. Le Sarcome d'Ewing est un cancer pédiatrique rare dont la formation est due, dans 85% des cas, à une translocation chromosomique qui produit l'oncogène de jonction *EWS-Fli1*. Cette translocation confère toutes les caractéristiques de la cellule cancéreuse, avec notamment une perte de la fonction d'apoptose et l'induction d'une prolifération incontrôlée des cellules. Jean-Rémi Bertrand et son équipe (Gustave Roussy, UMR8203, Villejuif) ont déjà proposé et validé une séquence siRNA ciblant spécifiquement *EWS-Fli1* et permettant son inhibition, vectorisée par différentes plateformes.

Lors de mes travaux de thèse, j'ai utilisé des nanodiamants issus de différents modes de production : détonation (DND, très petite taille ≈3-10 nm) ou Haute Pression Haute

Température (ND_{HPTH}, taille ≈70 nm). Ils ont été fonctionnalisés par quatre méthodes différentes : (i) hydrogénation par plasma ou (ii) par recuit thermique, (iii) rendus cationiques par traitement chimique ou (iv) par greffage covalent d'un polymère cationique (COP-ND_{HPHT}). Les charges positives ainsi créées à la surface des ND permettent l'adsorption électrostatique des siRNA.

Mes travaux ont été articulé autour de deux axes de recherche :

(i) Etude *in vitro* des complexes (Gustave Roussy, UMR8203, Villejuif) : j'ai comparé les **caractéristiques physico-chimiques** (taille, potentiel zêta et capacité d'adsorption des siRNA) des différents ND et mis en évidence que l'**efficacité d'inhibition de l'oncogène** par les siRNA dépend du mode production et de la fonctionnalisation des ND cationiques précédemment décrits. Le vecteur le plus efficace dans l'inhibition d'*EWS-Fli1* s'est avéré être le COP-ND_{HPHT}, avec lequel nous avons obtenu près de 70% d'inhibition. Leur biodistribution dans les organes de la souris a ensuite été explorée.

(ii) Distribution tissulaire (Laboratoire Aimé Coton, UMR 9188, Orsay) : pour cette étude nous avons eu recours à des **ND_{HPHT} rendus fluorescents** (FNDs) par la création dans leur maille cristalline de centres colorés azote-lacune (NV pour *Nitrogen-Vacancy*). Ceux-ci ont pu être détectés par un système optimisé d'imagerie de fluorescence plein champ à fort grossissement (x60) utilisant une excitation laser impulsionnelle. Ce dispositif utilise une porte temporelle retardée par rapport à l'excitation pour tirer profit de la longue durée de vie (30 ns) du niveau excité des centres NV, par rapport à celle de l'autofluorescence (≈2 ns). Il permet ainsi de faire ressortir les NDs dans des coupes très autofluorescentes des organes des souris. Le fort grossissement permet de distinguer les FND individuels des agrégats au sein de l'environnement tissulaire, tout en ayant une très bonne résolution des sous-structures de l'organe total. Nous avons observé qu'après 24h les FND se trouvaient principalement dans le foie, la rate, le poumon et le rein.

Ces travaux ont permis d'une part d'identifier le mode de production et de fonctionnalisation optimal des nanodiamants pour la vectorisation efficace de siRNA, et d'autre part de déterminer, par une nouvelle méthode de microscopie de fluorescence, la biodistribution de ces vecteurs dans les organes de souris portant une tumeur xénogreffée sous-cutanée. L'étude d'efficacité thérapeutique des complexes ND:siRNA sur ces souris,

ainsi que sur un modèle plus avancé de tumeur orthotopiques avec métastases, est en cours dans deux équipes partenaires. De plus, il est possible d'augmenter l'efficacité du traitement en dirigeant les complexes plus spécifiquement vers les cellules du Sarcome d'Ewing. En effet, ces dernières surexpriment l'antigène de surface CD99, si bien qu'en greffant sur les ND un fragment (Fab) d'anticorps ciblant CD99, il doit être possible d'augmenter l'internalisation des complexes ND:siRNA dans la tumeur.

***

Titre : Nanodiamants fluorescents pour la vectorisation de siRNA : évaluation *in vitro* et quantifications haut-débit/haute-résolution *in vivo*

Mots clés : nanodiamant, siRNA, Sarcome d'Ewing, biodistribution

Résumé : Le Sarcome d'Ewing est un cancer pédiatrique rare, principalement dû à l'expression de l'oncogène de jonction EWS-Fli1, et dont les traitements médicamenteux ont peu évolué au cours des dernières décennies. Nous nous intéressons à une nouvelle approche thérapeutique utilisant des siRNA, ciblant spécifiquement l'oncogène EWS-Fli1, et permettant l'inhibition de la croissance tumorale. Durant mon travail de thèse, j'ai utilisé des nanocristaux de diamant issus soit de détonation (DND), soit de synthèse haute pression haute température (ND_{HPHT}) pour vectoriser les siRNA, accrochés par interaction électrostatique. Pour ce faire, les NDs ont été rendus cationiques par différentes méthodes: (i) hydrogénation assistée par plasma, (ii) par recuit thermique, ou (iii) par traitement chimique pour les DNDs, ou (iv) greffage covalent d'un polymère cationique sur des ND_{HPHT} (COP-NDHPHT). Mes travaux ont comporté deux axes: (i) étude *in vitro* des complexes ND:siRNA (caractérisation physico-chimiques des NDs et étude de l'efficacité d'inhibition de l'oncogène par le complexe); (ii) distribution tissulaire de COP-ND_{HPHT}, injectés dans des souris, grâce à des ND_{HPHT} fluorescents, contenant des défauts azote-lacune. Pour les détecter individuellement dans des coupes d'organes de souris portant une tumeur xénogreffée sous-cutanée, nous avons développé un système d'imagerie en épifluorescence à grande ouverture numérique, et résolu en temps afin de rejeter l'autofluorescence tissulaire (de durée de vie plus courte que celle des NDs). Nous avons quantifié le nombre, l'état d'agrégation et la localisation cellulaire (grâce à un marquage histopathologique imagé simultanément) de ces vecteurs 24h après injection. Les NDs ont été clairement détectés dans les différents organes, dont la tumeur, ouvrant la voie à un contrôle de la progression tumoral grâce au siRNA.

Title : Fluorescent nanodiamonds as siRNA vectors: *in vitro* evaluation and high-content-high-resolution quantifications *in vivo*

Keywords : nanodiamond, siRNA, Ewing Sarcoma, biodistribution

Abstract : Ewing Sarcoma is a rare pediatric cancer, caused in the majority of the cases by the expression of the fusion oncogene *EWS-Fli1*. Current treatments have not much evolved over the past decades. We are investigating a new therapy based on siRNA specifically targeting the oncogene and inhibiting the tumor growth. During my PhD thesis, I have tested different types of synthetic nanodiamonds (ND) used to vectorize siRNA electrostatically bound at their surface: ND produced by detonation (DND) and by High Pressure High Temperature synthesis (ND_{HPTH}). Their surfaces have been cationized by various processes: (i) plasma or (ii) thermal hydrogenation, (ii) chemical treatment, or (iv) covalent grafting of a copolymer (COP-ND_{HPHT}). My PhD work included two main axis: (i) *in vitro* study of ND:siRNA complexes (NDs physico-chemical characterization and oncogene inhibition efficacy by the complex); (ii) tissue distribution of COP-ND_{HPHT}, injected into mice, using fluorescent ND_{HPHT} containing nitrogen-vacancy defects. To detect them individually in sections of mouse organs carrying a subcutaneous xenograft tumor, we developed an epifluorescence imaging system with large numerical aperture and resolved in time to reject tissue autofluorescence (of a shorter lifetime than NDs). We quantified the number, the aggregation state and the cell localization (thanks to simultaneous histopathological imaging) of these vectors 24 hours after injection. NDs have been clearly detected in different organs, including the tumor, paving the way for tumor progression control with siRNA.